UNIVERSIDAD POLITÉCNICA DE MADRID
Escuela Técnica Superior de Ingenieros de Caminos, Canales y Puertos

Influence of the microstructure on the deformation mechanisms of wrought Mg alloys

DOCTORAL THESIS

Submitted for the degree of Doctor by:

Biaobiao Yang
Master in Material Science and Engineering

Madrid, 2025

UNIVERSIDAD POLITÉCNICA DE MADRID
Escuela Técnica Superior de Ingenieros de Caminos, Canales y Puertos

Doctoral Degree in Engineering of Structures, Foundations and Materials

Influence of the microstructure on the deformation mechanisms of wrought Mg alloys

DOCTORAL THESIS

Submitted for the degree of Doctor by:

Biaobiao Yang
Master in Material Science and Engineering

Under the supervision of:
Dr. Javier LLorca

Madrid, 2025

Title: Influence of the microstructure on the deformation mechanisms of wrought Mg alloys

Author: Biaobiao Yang

Doctoral Programme: Engineering of Structures, Foundations and Materials

Thesis Supervision:

Dr. Javier LLorca, University Professor, Universidad Politécnica de Madrid

External Reviewers:

Thesis Defense Committee:

Thesis Defense Date:

For Chenying

Acknowledgement

El tiempo presente, al mentarlo, ya es ausente.

Typing this doctoral thesis, time to say goodbye to my doctoral period.

Firstly, I would like to express my gratitude to the People's Republic of China, who gave me necessary living expenses in Spain via China Scholarship Council (CSC). I sincerely hope my mother country can be more prosperous, strong, and beautiful in the future!

Secondly, I want to ask my family, especially my wife, Chenying Shi for pardon, given I did not accompany them in the past years. I am grateful for their unconditional understanding and love, and I hope I can be with them asap.

Thirdly, I would like to thank my supervisor, Javier Llorca. He provided me with many sound and valuable suggestions in the investigation. Following him, I embarked on scientific research regarding the deformation behavior of alloys, and what I have learned from him is my most precious treasure academically and also in my whole life.

Fourthly, I want to say thanks to my collaborators during the investigation, who gave me a lot of valuable instructions. They are Yunping Li, Matthew Barnett, Akihito Chiba, Guoqiang Xie, Jun Wang, Yujie Cui, Xu Xu, David Lunt, Michael Titus, Alberto Orozco Caballero, Valentin Vassilev, Anxin Ma, Dikai Guan, Fan Zhang, Gaoming Zhu, Jingya Wang, Meijuan Zhang, Dongfeng Shi, Feiyu Zhao, et al.

Fifthly, I am grateful to receive help and encouragement from my friends and colleagues, including Tian Xie, Wei Shao, Abbas Jamali, Maral Sarebanzadeh, Eugenia Nieto, Ignacio Escobar, Victoria Tucker, Guillermo Santos, Juan Alberto Meza, Lodyk Warzanskyj Prieto, Alireza Rezaei, Mahdi Sabbaghian, Yi Yang, Yidi Li, Nafiseh Mollaei, Jinling Yang, Yuyao Liu, Jun Hu, Xiang Ao, Xiaolu Li, Xuebao Lin, Shuanglan Du, Xiaomei Yang, Mingyang Zhang, Meihui Zhou, Junchen Xiao, Qi Chen, Mingdi Yu, Jie Xu, et al.

Here, I sincerely wish all of them all the best!

Biaobiao Yang

Abstract

Wrought magnesium (Mg) and Mg alloys have emerged as competitive alternatives for structural components in transportation, aerospace, and medical industries due to their low density, high specific stiffness, and good biocompatibility. Designing high-performance wrought Mg alloys requires understanding the relationship between microstructure and deformation mechanisms (slip and twinning), especially at room temperature, which has not been fully established.

This thesis studies experimentally the deformation mechanisms of various wrought Mg alloys with different microstructures at ambient temperature, using state-of-the-art techniques such as electron backscatter diffraction, transmission electron microscopy, slip trace analysis, slip trace - modified lattice rotation analysis, grain reference orientation deviation, as well as machine learning.

Chapter 3 explores the deformation mechanisms of an as-extruded Mg-6.5Zn alloy with dual texture and limited yield asymmetry under tension and compression. Compressive deformation in grains with standard prismatic texture is accommodated by <a> basal slip and extension twinning, while tensile deformation promotes <a> basal and non-basal slips, leading to the typical yield asymmetry. Rotated grains, however, exhibit stronger yield asymmetry, with tensile deformation absorbed by <a> basal slip and extension twinning, and compression relying on <a> basal slip and compression twinning. Moreover, activation of <a> non-basal slips can suppress compression twinning transforming into double twinning.

Chapter 4 studies the influence of prismatic precipitates on the deformation mechanisms of Mg-4.5Zn alloys with a strong prismatic texture during tensile deformation. In samples without precipitates, 92% of grains with slip traces are planar, primarily involving <a> basal slip and <c + a> II pyramidal slip. In samples with precipitates, 76% of grains with slip traces are non-planar, with <a> prismatic slip being most active, followed by <c + a> II pyramidal slip. Precipitation-induced hardening of <a> basal slip favored cross-slip to the prismatic plane, progressing deformation via <a> prismatic slip dislocations parallel to precipitates.

Chapter 5 examines the deformation of a Mg-1Al alloy with a strong prismatic texture, focusing on the nucleation and growth of anomalous extension twins during tension. These twins nucleated at the onset of plastic deformation near

grain boundary triple junctions due severe strain incompatibility between neighbor grains as a result of different <a> basal slip-induced lattice rotations. Anomalous twins grew with applied strain due to continuous activation of <a> basal slip in adjacent grains, increasing strain incompatibility.

Chapter 6 investigates the influence of microstructure on extension twinning behavior using a large grain dataset (> 3000 grains × 28 features) and machine learning. Twin nucleation was favored in larger grains and grains with high twinning Schmid factors, but twins also formed in grains with very low or negative Schmid factors if they had at least one smaller, or more rigid, neighbor grain. Twinning in small grains with high twinning Schmid factors was favored if they had low basal slip Schmid factors and at least one neighbor with high basal slip Schmid factors that deformed easily.

All these results reveal the complex deformation mechanisms of wrought Mg alloys with different microstructures and help to advance in the microstructural design of high-performance Mg alloys.

Resumen

El magnesio (Mg) fabricado por extrusión y sus aleaciones han surgido como alternativas competitivas para componentes estructurales en las industrias del transporte, aeroespacial y médica debido a su baja densidad, alta rigidez específica y buena biocompatibilidad. El diseño de aleaciones de Mg de forja de alto rendimiento requiere comprender la relación entre la microestructura y los mecanismos de deformación (deslizamiento de dislocaciones y maclado), especialmente a temperatura ambiente, lo cuales no han sido completamente establecidos.

Esta tesis estudió experimentalmente los mecanismos de deformación de diversas aleaciones de Mg extruidas con diferentes microestructuras a temperatura ambiente, utilizando técnicas como la difracción de electrones retrodispersados, la microscopía electrónica de transmisión, el análisis de bandas de deslizamiento, el análisis de rotación de la red cristalina y de la desviación en la orientación de los granos, así como herramientas de aprendizaje automático.

El capítulo 3 explora los mecanismos de deformación de una aleación Mg-6.5Zn extruida con una textura dual y una asimetría en el límite elástico entre tensión y compresión muy reducida. La deformación en compresión de los granos con textura prismática habitual se acomoda mediante deslizamiento en el plano <a> basal y maclado de extensión, mientras que la deformación a tracción promueve deslizamientos en el plano <a> basal y no <a> basal, lo que lleva a la típica asimetría en el límite elástico en tracción y compresión. Sin embargo, los granos rotados presentan una asimetría más fuerte, ya que la deformación a tracción se absorbe mediante deslizamiento <a> basal y maclado de extensión, mientras que la compresión depende del deslizamiento <a> basal y del maclado de compresión. La activación de deslizamientos no basales también puede suprimir la transformación de las maclas de compresión en maclas doble.

El capítulo 4 estudia la influencia de los precipitados paralelos a los planos prismáticos en los mecanismos de deformación en tracción de aleaciones de Mg-4.5Zn con una fuerte textura prismática. En los materiales sin precipitados, se encontraron bandas de deslizamiento planas en el 92% de los granos, involucrando principalmente el deslizamiento <a> basal y el deslizamiento piramidal II <c + a>. En los materiales con precipitados, se observaron bandas de deslizamiento no planas en el 76% de los granos, con el deslizamiento prismático <a> mostrando

mayor actividad, seguido por el deslizamiento piramidal II <c + a>. El endurecimiento inducido por la precipitación del deslizamiento <a> basal favoreció el deslizamiento cruzado hacia el plano prismático, progresando la deformación a través del deslizamiento prismático <a> paralelo a los precipitados.

El capítulo 5 examina la deformación de una aleación Mg-1Al con una fuerte textura prismática, enfocándose en la nucleación y crecimiento de maclas de extensión anómalas durante la deformación en tracción. Estas maclas se nuclearon al inicio de la deformación plástica cerca de las uniones triples de los límites de grano a causa de la incompatibilidad severa de la deformación entre los granos vecinos debido a las diferentes rotaciones de la red cristalina inducidas por el deslizamiento <a> basal. Las maclas anómalas crecieron con la deformación aplicada debido a la activación continua del deslizamiento <a> basal en los granos vecinos, aumentando la incompatibilidad de deformación.

El capítulo 6 investiga la influencia de la microestructura en el comportamiento del maclado de extensión, utilizando una base de datos de más de 3000 granos con 28 características cada uno, aplicando un modelo de aprendizaje automático. Se encontró que la nucleación de maclas se favorece en granos más grandes y con altos valores de Schmid factor para maclado, pero también que las maclas pueden formarse en granos con valores del factor de Schmid muy bajos o negativos si tienen al menos un grano vecino más pequeño o más rígido. El maclado en granos pequeños con altos valores de Schmid factor para maclado se favorece si tienen valores bajos del factor de Schmid para deslizamiento basal y al menos un vecino con valor de factor de Schmid alto y que se deforme fácilmente.

Esta tesis revela la relación entre la microestructura y los mecanismos de deformación de las aleaciones de Mg extruidas en diversas condiciones y ayudará para desarrollar nuevas aleaciones de Mg con altas prestaciones.

Table of Contents

List of Figures

List of Tables

Abbreviations and Acronyms

Acronym	Definition
g	Orientation matrix calculated from the Bunge Euler angles in the region near the observed slip traces before deformation
g'	Orientation matrix, calculated from the Bunge Euler angles in the region near the observed slip traces after deformation
rot	Rotation Matrix between the **g'** and the **g**
$\boldsymbol{o_{x,y}}$	Orientation matrix at position (x,y)
$\boldsymbol{o_g}$	Mean orientation matrix of a grain
$\boldsymbol{o_{t\_the}}$	Theoretical orientation matrix of a twinned grain
$\boldsymbol{GROD_{x,y}}$	Rotation matrix between the $\boldsymbol{o_{x,y}}$ and the $\boldsymbol{o_g}$
$\overrightarrow{GROD\_axis}$	Misorientation axis of the grain reference orientation deviation
$GROD\_angle$	Misorientation angle of the grain reference orientation deviation
ϑ_i	Electron backscatter diffraction-derived in-plane lattice rotation
$\overrightarrow{A_i}$	Unit vector along the i direction (either X, Y or Z)
$\vec{b}$	Slip dislocation Burgers vector, used in Transmission Electron Microscope
d	Average grain size
d_s	Spacing between diffracting planes
$\vec{g}$	Diffraction vector in transmission electron microscopy images
ε_1	Longitudinal strain along the loading direction
L_g^0	Grain length along the loading direction before deformation
L_g	Grain length along the loading direction after deformation
m'	Geometric compatibility factor (Luster-Morris parameter)
ψ	Angle between the slip / twin plane normal directions of two slip / twin systems adjacent to a grain boundary
κ	Angle between the Burgers vectors / shear directions of two slip / twin systems adjacent to a grain boundary

φ	Angle between the loading direction and the slip or twin plane normal vector
ω	Angle between the loading direction and the slip or twin direction
k_s	Strengthening parameter in the Hall-Petch relationship
k_t	Twin plane normal
η	Twin shear direction
λ	Twin rotation axis, calculated by $\lambda = k_t \times \eta$
λ_w	Wavelength of the electrons
σ_y	Yield strength of polycrystal material
σ_0	Yield or flow stress of single-crystal or bulk large-grain-size polycrystalline material
δ	Angle of incidence of the electrons on the diffracting plane
θ	Rotation angle used in the slip trace - modified lattice rotation analysis
$\vec{N}$	Vector normal to sample surface
$\overrightarrow{RA}_{cc}$	Rotation axis vector in the crystal coordinate system
$\overrightarrow{RA}_{sc}$	Rotation axis vector in the sample coordinate system
$\overrightarrow{SP}_{cc}$	Slip plane normal vector in the crystal coordinate system
$\overrightarrow{SP}_{sc}$	Slip plane normal vector in the sample coordinate system
$\overrightarrow{SD}_{cc}$	Slip direction vector in the crystal coordinate system
$\overrightarrow{SD}_{sc}$	Slip direction vector in the sample coordinate system
$\vec{T}$	Slip trace vector on the sample surface
AE	As-extruded
BC	Band Contrast
BN	Bayesian Network
CRSS	Critical Resolved Shear Stress
CT	Compression Twin

CV	Cross-validation, used in machine learning
CYS	Compressive Yield Strength
DT	Double Twin
EBSD	Electron Backscatter Diffraction
ED	Extrusion Direction
ET	Extension Twin
FCC	Face Centered Cubic
GB	Grain Boundary
GDB	Gradient Boosting, an algorithm used in machine learning
GROD	Grain Reference Orientation Deviation
HCP	Hexagonal Close-Packed
HRDIC	High Resolution Digital Image Correlation
IPF	Inverse Pole Figure
MB	Markov Blanket, used in machine learning
Mg	Magnesium
ML	Machine Learning
mrd	Multiples of Random Distribution
ND	Normal Direction in rolled Mg plates
NSS	Number of Slip Systems
NTV	Number of Twin Variants
PA	Peak-aged
RA	Rotation Axis
RD	Rolling Direction in rolled Mg plates
RE	Rare Earth
ROC AUC	Area Under the Receiver Operating Characteristic Curve
SE	Secondary Electron

SEM	Scanning Electron Microscope
SF or m	Schmid Factor
ST-MLRA	Slip Trace - Modified Lattice Rotation Analysis
TCA	Tension-Compression Asymmetry
TD	Transverse Direction in rolled Mg plates
TEM	Transmission Electron Microscopy
TYS	Tensile Yield Strength
VPSC	Visco-Plastic Self-Consistent
XRD	X-ray Diffraction

1. Introduction

1.1. Mg and its applications

Due to their low density, high specific strength and specific stiffness, magnesium (Mg) alloys are very promising for applications in transportation (cf. Figure 1.1). Mg alloys also have an elastic modulus closer to that of human bones than other metals (Table 1.1), excellent biocompatibility and biodegradability, thus have an excellent potential for applications in hard tissue (bone) engineering within the biomedical field (cf. Figure 1.1(B)). In addition, Mg alloys have good thermal conductivity, electromagnetic shielding, and damping capabilities, and they have been widely used in the field of computer, communication, and consumer electronic products.

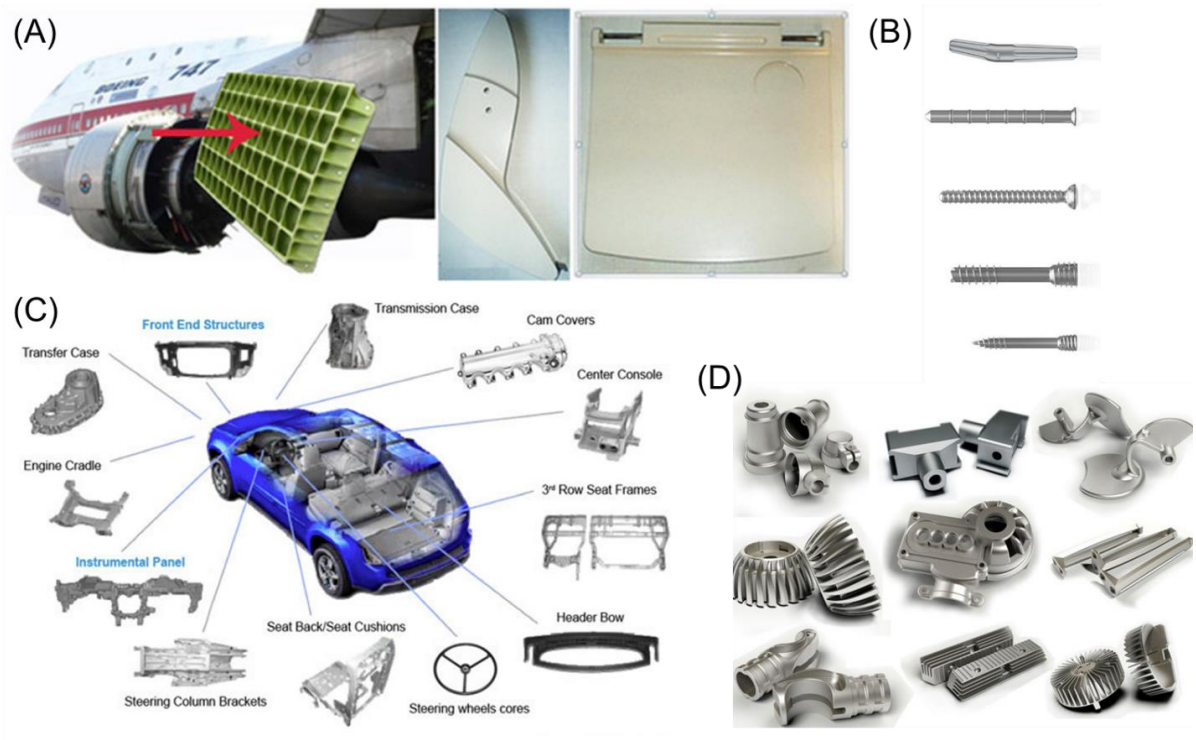

Figure 1.1: Present applications of Mg alloys [1]: (A) Boeing 747 Mg alloy wings and seats, (B) bio-absorbable Mg alloy implants, (C) Mg alloy components in the automotive industry and (D) other Mg alloy industrial products.

Notwithstanding the potential of Mg alloys, their large-scale market application still needs to overcome a series of difficulties, such as limited strength, poor formability, and very low corrosion resistance. The mechanical properties of metallic materials are closely related to their microstructure and the deformation mechanism activated during plastic deformation. Therefore, understanding and mastering the plastic deformation behavior of Mg alloys with different microstructures under different loading conditions is of paramount importance in science and engineering to optimize the mechanical performance of Mg alloys and pave the way for many applications.

Table 1.1: Properties of pure Mg at room temperature [2–4].

Properties	Values
Crystallographic axial ratio (c/a)	1.624
Density	1.738 g/cm^3
Atomic number	12
Relative atomic weight	24.3050
Atomic radius	0.160 nm
Atomic volume	14.0 cm^3/mol
Melting point	650 ± 0.5 °C
Boiling point	1090 °C
Recrystallization temperature	423 °C
Specific heat capacity	1.05 kJ/(kg·°C)
Heat of fusion	195 kJ/kg
Thermal conductivity	156 W/(m·°C)
Elastic modulus	45 GPa
Shear modulus	17 GPa
Fracture elongation	1-12%
Maximum tensile strength	80-180 MPa
Standard electrode potential	-2.37 V
Solidification shrinkage	4.2%

1.2. Deformation modes of Mg

Pure Mg presents a hexagonal close-packed (HCP) crystallographic lattice. The atomic occupancy in the unit cell of a HCP Mg alloy, and the main crystallographic coordinate axes, are depicted in Figure 1.2. The unit cell contains three layers of atoms stacked in the order ABABABA… along the $\vec{c}$ axis. The atoms on each corner of the A layer in the unit cell are shared by 6 unit cells, the atoms

in the core of the A layer are shared by the upper and lower unit cells, and the three atoms inside the unit cell are not shared with other cells. There are three coordinate axes at the base of the hexagonal cell, $\overrightarrow{a_1}$, $\overrightarrow{a_2}$, $\overrightarrow{a_3}$, and one $\vec{c}$ axis parallel to the vertical direction, which satisfy the following spatial geometric relationship: (1) the angle between $\overrightarrow{a_1}$, $\overrightarrow{a_2}$, $\overrightarrow{a_3}$ is 120°; (2) $\vec{c}$ is always perpendicular to the other three axes. The lattice parameters at room temperature of pure Mg are a = 0.321 nm, c = 0.521 nm, and the c/a axial ratio is 1.624.

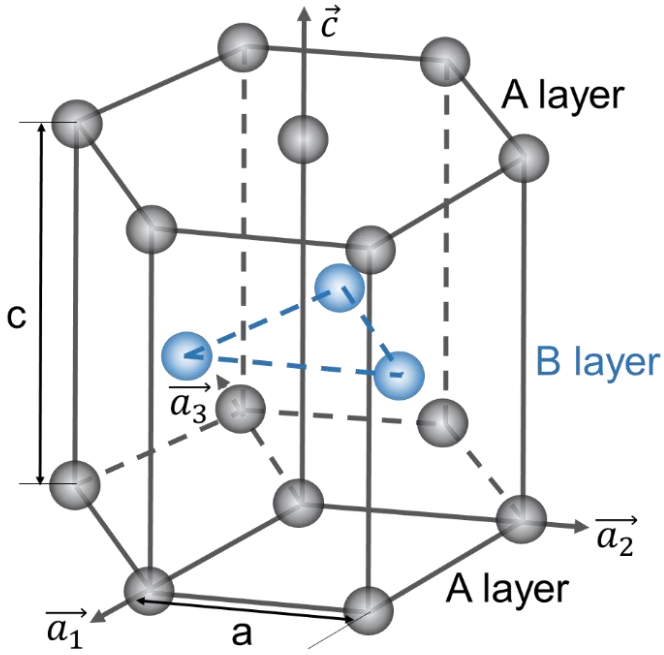

Figure 1.2: Schematic diagram of the HCP lattice.

Dislocation slip is the most common plastic deformation mechanism in crystalline metals. The shear stress required for dislocation slip is generally the lowest when the slip plane is parallel to the close-packed plane (the largest interplanar distance), and the Burgers vector is parallel to the close-packed direction (the interatomic distance is the shortest). The Miller-Bravais indexes and the corresponding CRSS values of the different slip systems in pure Mg at room temperature are summarized in Table 1.2. In Mg alloys, the {0001} <11$\bar{2}$0> (<a> basal) slip exhibits the lowest critical resolved shear stress (CRSS) to promote dislocation slip and this soft mechanism is responsible for the limited strength of

Mg alloys. <a> basal slip can only accommodate deformation along the basal plane because the three slip directions (SDs) are parallel to the three coordinate axes of the basal plane, as shown in Figure 1.3. Thus, <a> basal slip can only provide two independent slip systems. Similarly, $\{1\bar{1}00\}$ $<11\bar{2}0>$ (<a> prismatic) slip and $\{1\bar{1}01\}$ $<11\bar{2}0>$ (<a> pyramidal) slip can only provide two independent slip systems along the basal plane. They have the same slip direction on the basal plane, but different sliding planes, which are located on the prismatic plane and the I pyramidal plane, respectively (Figure 1.3).

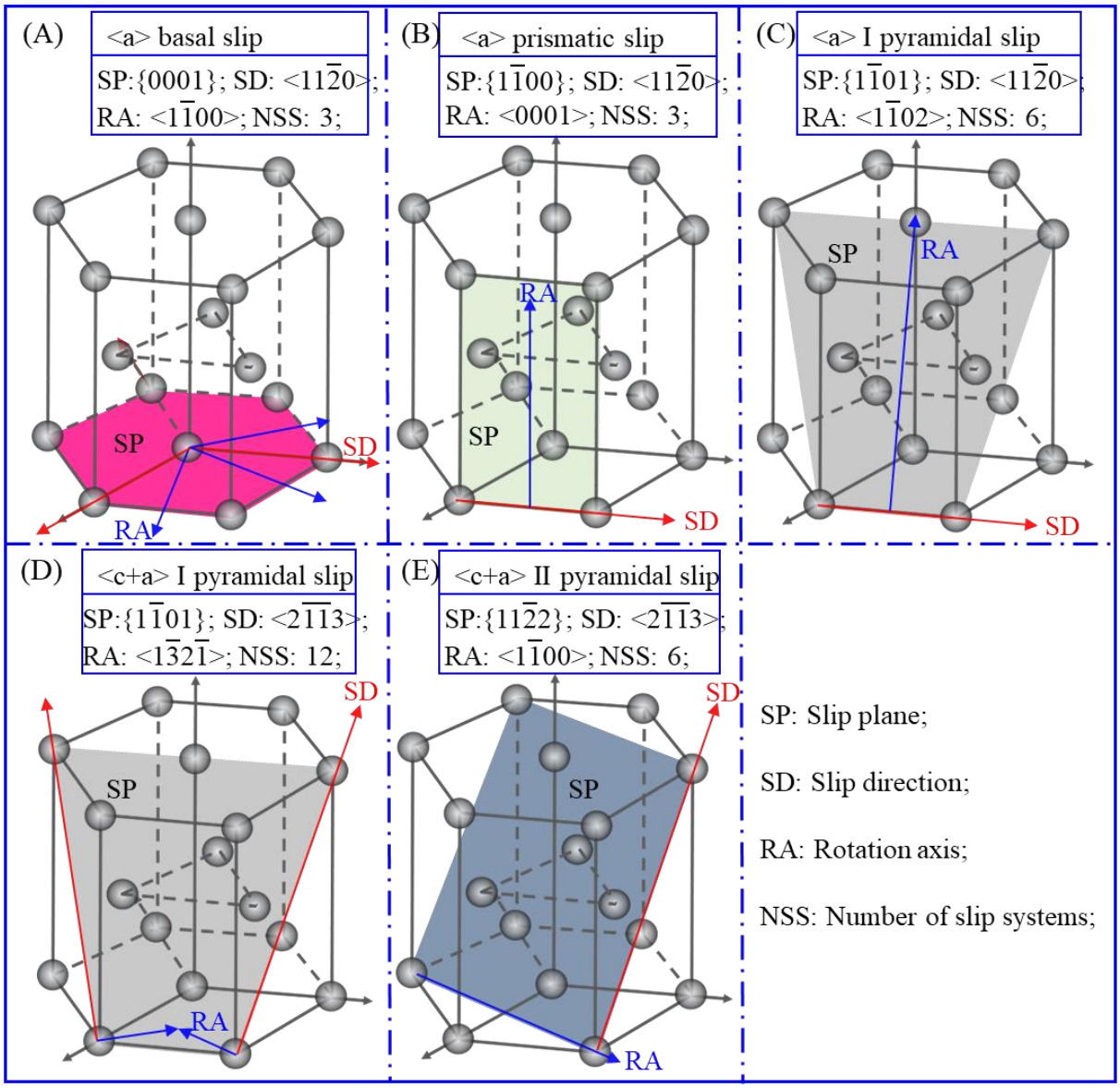

Figure 1.3: Principal slip systems in Mg alloys: (A) <a> basal slip, (B) <a> prismatic slip, (C) <a> I pyramidal slip, (D) <c + a> I pyramidal slip, and (E) <c + a> II pyramidal slip.

Table 1.2: Miller-Bravais notations and CRSS values of slip and twinning mechanisms in pure Mg at room temperature.

Plastic deformation mechanism	Miller-Bravais notation	CRSS (MPa)
<a> basal slip	{0001} <11$\bar{2}$0>	0.5 [5,6]
<a> prismatic slip	{1$\bar{1}$00} <11$\bar{2}$0>	39 [7]
<c + a> I pyramidal slip	{10$\bar{1}$1} <$\bar{1}\bar{1}$23>	54 [8]
<c + a> II pyramidal slip	{11$\bar{2}$2} <$\bar{1}\bar{1}$23>	98 [9]
Extension twin	{10$\bar{1}$2} <$\bar{1}$011>	12 [10]
Compression twin	{$\bar{1}$011} <10$\bar{1}$2>	114-185 [11,12]

Von Mises [13] has pointed out that each grain must have at least five independent slip systems to ensure unconstrained plastic deformation in any direction. The combination of <a> basal slip, <a> prismatic slip and <a> I pyramidal slip does not satisfy the Von Mises criterion because their slip directions are identical and are found within the basal plane. They cannot accommodate deformation along the $\vec{c}$ axis and thus other slip systems, such as {10$\bar{1}$1} <$\bar{1}\bar{1}$23> (<c + a> I pyramidal) slip and {11$\bar{2}$2} <$\bar{1}\bar{1}$23> (<c + a> II pyramidal) slip, which can provide 12 and 6 independent slip systems, respectively (Figure 1.3), have to be active to absorb plastic strains in the $\vec{c}$ axis direction.

Nevertheless, the CRSS values to activate <c + a> non-basal slips are very high, and this leads to the activation of twinning in Mg to accommodate the deformation along the $\vec{c}$ axis. The most common twinning mechanisms in Mg alloys are the {10$\bar{1}$2} (twin plane) <$\bar{1}$011> (twin direction) extension twin (ET) and the {$\bar{1}$011} <10$\bar{1}$2> compression twin (CT) [14,15]. Twinning occurs by the rotation of the crystal around the <1$\bar{2}$10> direction and the rotation angles are 86.30° (ET) and 56.15° (CT) (Figure 1.4). Moreover, twinning is a polar mechanism associated with the shearing of the crystal lattice along one direction but not along the opposite one. ETs appear in Mg under the application of tensile stress along the $\vec{c}$ axis or compression perpendicular to the $\vec{c}$, axis, while CTs develop under compression along the $\vec{c}$ axis or tension perpendicular to the $\vec{c}$ axis [16]. Each type of twin is associated with different twin shear strains: 0.129 for ETs and 0.138 for CTs [16].

Twinning deformation is described by the twinning plane and the twinning direction (Figure 1.4), and the shearing of the crystal lattice leads to a mirror image of the parent grain in the twinned region across the twin plane. There are 6 possible ET variants and another 6 CT variants, which have different twinning planes and twinning directions. Moreover, ETs often appear within the CTs during deformation, leading to the formation of double twins (DTs). The combination of 6 possible ET variants and another 6 CT variants leads to 36 theoretical DT variants, which can be classified into 4 main variants: D30, D38, D67, and D70. Their rotation axis (RA) - rotation angle pairs are <$2\bar{1}\bar{1}0$> & 30.1°, <$2\bar{1}\bar{1}0$> & 37.5°, <$34\bar{7}\bar{2}$> or <$34\bar{7}\bar{2}$> & 66.5°, and <$\bar{1}\bar{4}77\bar{3}$> or <$\bar{1}\bar{4}773$> & 69.9°, respectively [17].

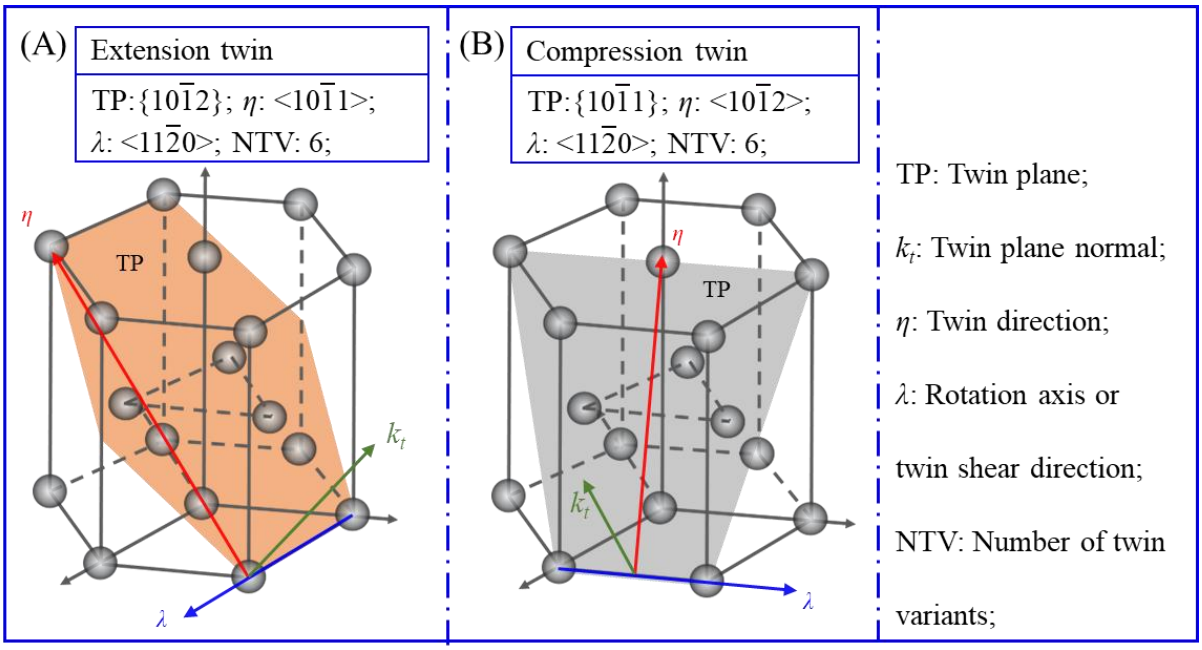

Figure 1.4: Twinning mechanisms in Mg alloys: (A) {10$\bar{1}$2} <$\bar{1}$011> ET and (B) {$\bar{1}$011} <10$\bar{1}$2> CT [18].

The CRSS values to activate ET and CT in Mg are very different (cf. Table 1.2) and, in particular, the CRSS for ET is much lower than that for <c + a> pyramidal slip. As a result, <a> basal slip and ET are the dominant deformation mechanisms in Mg and Mg alloys, particularly at ambient temperature. CT is less common and is often accompanied by large stress concentrations. Moreover, CTs are much thinner than ETs [19].

Deformation twins are three-dimensional structures, and their appearance involves the nucleation of an embryo (habitually at a grain boundary, GB) followed the propagation of the twin boundaries along three directions: twin shear direction (η), twin plane normal (k_t) and the direction $\lambda = k_t \times \eta$.

Nucleation and growth are two principal processes involved in twinning. Several theories have been advanced to explain the nucleation of ETs and CTs. In earlier works, the classical theory treated twinning as a homogeneous simple shear on the first invariant plane, which is accomplished by gliding of twinning dislocations or disconnections on the twinning plane [16]. Thus, the parent crystal and the twin are related by a rotation. However, not all sites are shifted to the correct positions by the shear transformation when the primitive unit cell contains more than one atom, and atomic shuffling is necessary [16,20].

Twin nucleation is a heterogeneous process that takes place in regions with large stress concentrations in the microstructure, such as GBs in polycrystal Mg alloys [21,22]. The nucleation of ETs has been widely studied [22–26] but a definitive theory is still lacking. Several models for ET nucleation were proposed in the past, including the pole mechanism of Thompson and Millard [27], the slip dislocation dissociation mechanism of Mendelson [28], and the disconnection mechanism proposed by Serra, Bacon and Pond [29–32]. Later, a zonal-twinning mechanism based on atomistic simulations was proposed by Wang et al. [33,34], in which a stable twin nucleus was created by simultaneous nucleation of a partial dislocation with a Burgers vector of -50/107 $[10\bar{1}1]$ and multiple twinning dislocations with a Burgers vector of 1/15 $[10\bar{1}1]$. In addition, Wang et al. [35] presented a pure-shuffle mechanism for twin nucleation in Mg at GBs due to the stress concentration and to the presence of GB dislocations. Besides, He et al. [23] experimentally reported a dual-step mechanism for ET nucleation through in-situ high-resolution transmission electron microscope (TEM). The nucleation of ETs was initiated by disconnections on the prismatic | basal interfaces which establish the lattice correspondence of the twin with a minor deviation from the ideal orientation. Subsequently, the formation of coherent twin boundaries was achieved

through the rearrangement of the disconnections at the prismatic | basal interface [23].

The nucleation of CTs has been studied less, but there is still a controversy on the twinning mechanism [36–44]. For example, atomistic simulations of Wang et al. [39] reported that 2-layer twinning dislocations are the commonly active twinning dislocations, rather than other twinning dislocations. However, the TEM observations of Kim et al. [41] in HCP Ti showed that various twinning dislocations were activated to produce twins that accommodated the imposed shear strain during equal channel angular pressing.

Once the CT or ET has been formed, it is generally accepted that twin thickening is mediated by the glide of twinning dislocations along the twin planes [23,30,45–47], and this process is controlled by the resolved shear stress on the twin plane along the twin shear direction.

From the polycrystal viewpoint, the most common criterion used to explain twin nucleation in one grain is the global Schmid factor (SF), based on the hypothesis that the stress state in one grain is identical to the macroscopic applied stress [48–50]. This criterion is supported, for instance, by the micro-tensile tests in pure Mg single crystals by Ventura et al. [51] who reported that the appearance of ETs followed the SF criteria [51]. Similar results were found in an extruded AZ31 alloy deformed in compression along the extrusion direction (ED) [52] and in a hot rolled AZ31 alloy during successive in-plane compression tests along two different directions [53]. However, recent works have revealed that other microstructural features, besides the SF, also have a remarkable influence on twin nucleation [54–57]. Beyerlein et al. reported that the GB misorientation angle can affect twin nucleation in polycrystalline pure Mg, when it comes to twin pairs nucleated at a GB [58]. Guan et al. revealed, for a WE43 Mg alloy, that the Luster-Morris geometric compatibility factor (m') between <a> basal slip of neighbor grains and the active ET variant plays a more critical role in twin nucleation than the global SF of the ET [59]. A similar conclusion was also drawn by Zhou et al. in their analysis of the ET variant selection in Mg-5Y (wt.%) alloy by means of in-situ electron backscatter diffraction (EBSD) [60]. Finally, Koike et al. [61] found that

the intragranular localized <a> basal slip was responsible for the formation of anomalous ETs with low or even negative SFs in rolled AZ31 Mg alloy sheets deformed in tension along the rolling direction (RD) [61].

Furthermore, ET was also found to be very sensitive to the grain size of Mg alloys [62,63]. Ghaderi and Barnett studied the effect of grain size on ET in an extruded AZ31 Mg alloy and found that the macroscopic stress required for the activation of ETs decreased as the grain size increased [64] and a similar behavior was observed by Dobroň et al. [65]. Thus, there is still no consensus on the underlying factors leading to twin nucleation [22–25] because ETs not necessarily occur in all large grains, at all GBs, or in all grains with favorably oriented for twinning [66,67] and it is important to ascertain the main microstructural features that lead to the nucleation of ETs because of the relevance of this mechanism in the deformation and fracture of Mg alloys.

It should be noted that the shear strain provided by twinning is limited, and the main roles of twinning are to change the crystal orientation, relief the stress concentrations, and further activate new slip and twinning within the twinned region. In fact, the continuous plastic deformation of the polycrystal can assist to the reactivation of ETs inside the ETs, forming $\{10\bar{1}2\}$-$\{10\bar{1}2\}$ secondary twins [68], and nucleate secondary ETs inside the CTs, forming $\{\bar{1}011\}$-$\{10\bar{1}2\}$ DTs [69,70].

1.3. Wrought Mg alloys

Wrought Mg alloys, compared to the cast counterparts, present higher ductility and mechanical strength resulting from the refined and homogeneous microstructures as well as from the reduced porosity because of thermomechanical processes. Based on the different processing techniques, wrought Mg alloys can be classified into rolled, forged, and extruded.

Rolling is a conventional process to produce sheets. The influence of various processing parameters during rolling on the microstructure and mechanical properties of Mg alloys were thoroughly investigated [71,72], and rolled Mg alloys of high quality are produced. Rolled Mg alloy sheets generally present a strong

basal texture, with the (0001) basal planes perpendicular to the normal direction (ND) and parallel to the rolling plane. This hinders the activation of (0001) [11$\bar{2}$0] basal slip during tensile deformation, limiting the room temperature formability. Therefore, recent developments have been mainly focused on the control of the microstructure and of the crystallographic orientation [73]. Different rolling techniques have been reported to improve the formability, including -but not limited to- hard plate rolling [74], differential speed rolling [75], and accumulative roll bonding [76]. For example, Mg-9Al-1Zn (AZ91) plates processed by hard plate rolling technique, -which achieves a large reduction during a single rolling pass-, are made up of coarse grains of 30-60 μm with a typical basal texture and fine grains of 1-5 μm and ultrafine (sub) grains of 200-500 nm with a weakened basal texture [74]. More importantly, the AZ91 Mg alloy prepared by this technique exhibited a simultaneous high strength and uniform ductility, i.e., ~371 MPa and ~23%, respectively [74].

Forging is a manufacturing process where a metal is shaped under high pressure, typically using a press or a hammer, to produce components with enhanced mechanical properties due to the refined microstructure resulting from the process. In practice, triaxial or multidirectional forging was frequently applied to Mg alloys to attain a refined microstructure and superior mechanical properties [77–79]. In triaxial forging, the process utilizes a die that presses the alloy to a particular strain, then releases and rotates it to 90° and presses it again along a different axis to a near-identical strain. This process is carried out along each of the three sample axes, x, y, and z, when rotated 90° which allows to apply a uniform strain to the material [80]. For example, a AZ61 Mg alloy was multi-directionally forged at room temperature to a cumulative strain of 2.0 with the forging axis changing by 90° from pass to pass, i.e. z → x → y → z → x, during the forging [81]. The coarse initial grains were gradually subdivided into ultrafine ones by mechanical twins, and the forged AZ61 Mg alloy displayed an excellent balance of mechanical properties: yield stress of 480 MPa, ultimate tensile strength of 525 MPa and a plastic strain to fracture of 5% [81]. In addition, some Mg alloy forgings,

such as automobile wheels, missile casings, etc., can be used in industrial applications directly or with only a small amount of machining [82].

Extrusion is an economic process to produce long slabs that can be used for structural components. Compared to forging and rolling, extrusion involves a more intense triaxial compressive stress state. Extrusion is better suited for achieving large plastic deformations of Mg alloys, and extruded Mg alloys also tend to have more uniform microstructures [83]. However, these conditions lead to the development of strong crystallographic textures. Commercial Mg alloys usually develop a strong prismatic texture (or ring-fiber texture with the (0001) basal planes aligned parallel to the ED) during hot extrusion process, which accounts for the unsatisfactory formability and ductility at room temperature [84]. Various extrusion technologies including, but not limited to, equal channel angular extrusion [85], asymmetric extrusion [86,87], and on-line twist extrusion [88], were developed to randomize the texture of extruded Mg alloys. For example, the (0002) basal texture intensity of AZ31 Mg alloy sheets processed by asymmetric extrusion was weakened due to the asymmetry shear deformation, and the crystallographic orientation of basal plane was tilted about 12° toward the ED [86].

Considering the poor room-temperature formability of Mg alloys, they are typically processed at higher temperatures, relying on the activation of non-basal slip systems at medium to high temperatures (usually > 300°C) as well as to recrystallization [73,89]. Nie et al. [18] summarized the CRSS values of <a> basal slip, <a> prismatic slip, <c + a> pyramidal slip, ET, and CT in single-crystal pure Mg at different temperatures (see Figure 1.5). As the temperature increases the CRSS of <a> prismatic slip, <c + a> pyramidal slip, and CT decrease continuously, indicating a strong temperature dependence for the activation of these three deformation mechanisms. However, the CRSS for <a> basal slip and ET only changes slightly with temperature, suggesting that these two deformation mechanisms are not thermally activated. In addition, the CRSS ratios between non-basal slip to basal slip, gradually decrease with increasing temperature [18]. This indicates that more deformation mechanisms are available in Mg alloys at

high temperatures, leading to more homogeneous deformation and better formability of Mg alloys.

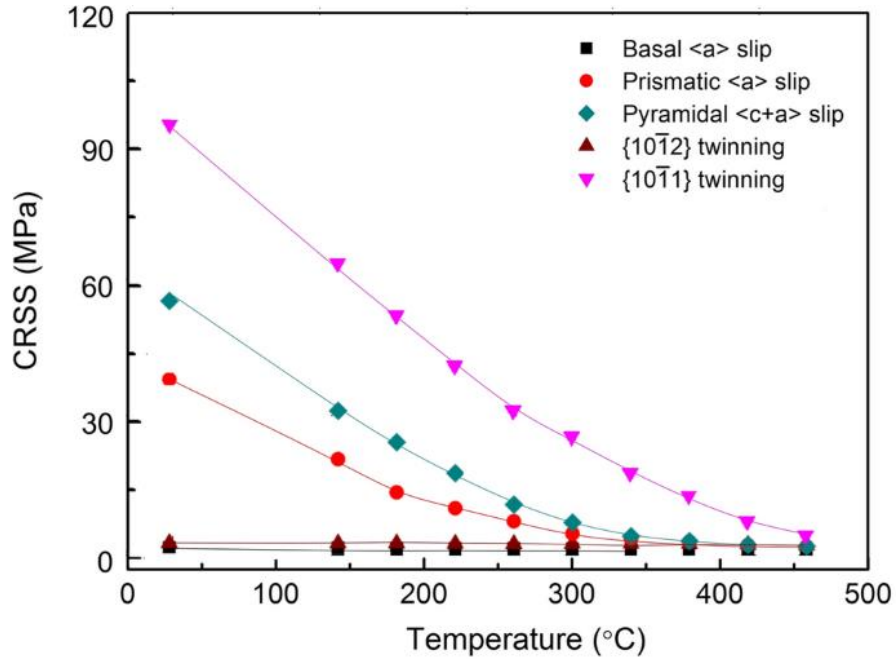

Figure 1.5: CRSS values for different slip and twinning modes in Mg single crystals as a function of temperature [18].

After rolling, forging, or extrusion, wrought Mg alloys can undergo heat treatments to induce static recrystallization or precipitation, optimize texture, reduce anisotropy, and lower residual stresses [90,91]. Despite that, wrought Mg alloys often exhibit strong textures, leading to significant anisotropy. Strong anisotropy can be advantageous for Mg alloy components subjected to uniaxial loads, but most engineering scenarios require Mg alloys that exhibit similar or near mechanical properties along different loading directions. Thus, the development of low-cost, high-performance wrought Mg alloys still needs more effort.

1.4. Deformation mechanisms of wrought Mg alloys

The deformation mechanisms of wrought Mg alloys with different microstructures subjected to diverse loading conditions have been analyzed in detail in the past. In particular, the studies have addressed the effect of grain size

[62–65], alloying elements and content [92–97], volume fraction, size and distribution of precipitates [98–107], texture [108–112], temperature [113–116], and strain rate [117–122]. All these factors impact the relative activity of slip and twinning modes during deformation and, thus, the mechanical properties of Mg alloys. The main investigations are summarized in the following sections.

1.4.1. Texture

The texture of a polycrystal describes the orientation distribution of crystallographic orientation of the grains within the aggregate. The typical textures of wrought Mg alloys are basal texture, commonly found in rolled Mg plates, and the extrusion texture (or prismatic texture), generally associated with extruded Mg bars.

The likelihood that one particular plastic deformation mode (either slip or twinning) is active in a crystal of the polycrystalline aggregate under a given external load is assessed - in a first approximation- through the SF. The SF is a constant that links the applied external stress with the resolved shear stress that determines the activation of a given slip system or twinning variant in one crystal [123]. For a given slip plane (or the twinning system) that shares the same value of the CRSS, the slip directionslip direction (or the twinning variant) with the highest SF will be activated first as the external load increases.

In the case of uniaxial loading, the SF is given by the product of the cosine of the angle (φ) between the loading direction and the slip or twin plane normal vector and the cosine of the angle (ω) between the loading direction and the slip or twin direction [123]:

$$m = \cos(\varphi) * \cos(\omega). \quad (1.1)$$

Thus, the SF for slip ranges between 0 and 0.5. However, twinning is a polar mechanism that only occurs in one direction. Accordingly, the twinning SF ranges between -0.5 and 0.5 [16].

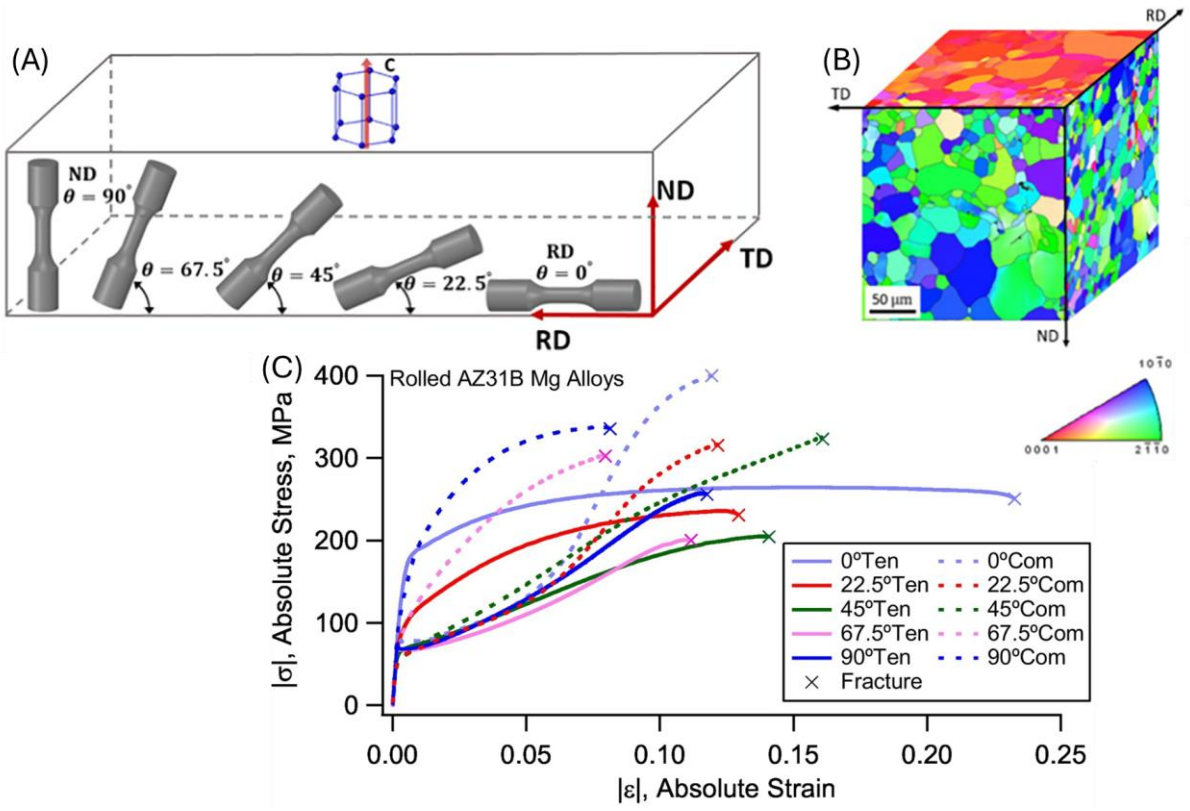

Figure 1.6: Rolled AZ31B Mg plate: (A) specimen orientations in the rolled plate, and (B) three-dimensional stereograph of the original microstructure. (C) engineering stress-engineering strain curves of rolled AZ31B Mg alloy under monotonic tension and monotonic compression for five material orientations at room temperature. TD: transverse direction [109].

The strong texture of wrought Mg alloys generally leads to severe asymmetry in mechanical properties, e.g. tension-compression asymmetry (TCA), because ET is a polar mechanism that is only active in the crystals in which the external load tends to extend the $\vec{c}$ axis. In rolled Mg plates with a basal texture, the $\vec{c}$ axis of most grains is oriented parallel to the ND (Figure 1.6). When compression is applied along the ND on a rolled Mg alloy with a strong basal texture, the SF for basal slip is low and is negative for ET, while the SF for the other deformation modes with large CRSS values is high. This inevitably results in a high yield strength during compression, ~170 MPa for the rolled AZ31B Mg alloy (Figure 1.6(C)) because <c + a> pyramidal slip (that has a high CRSS) has to be active to accommodate the deformation of the crystals along the $\vec{c}$ axis. However, tensile loading along the ND is associated with a low for SF for basal slip but the SF for ET is high, leading to a low yield strength of ~75 MPa because of the initial

accommodation of plastic strain by twinning (Figure 1.6(C)). Similarly, the SFs for basal slip and ET are low during tensile deformation along the RD or TD, whilst the SF for ET is high during compression along the RD or TD. This leads to changes in the activity of ET at the yield point when the material is deformed along different orientation and to a significant tension-compression yield asymmetry of rolled Mg alloy along the RD or TD. The obvious asymmetry in deformation mechanisms and mechanical properties was also reported in other rolled pure Mg and Mg alloys with a strong basal texture [18,124–126].

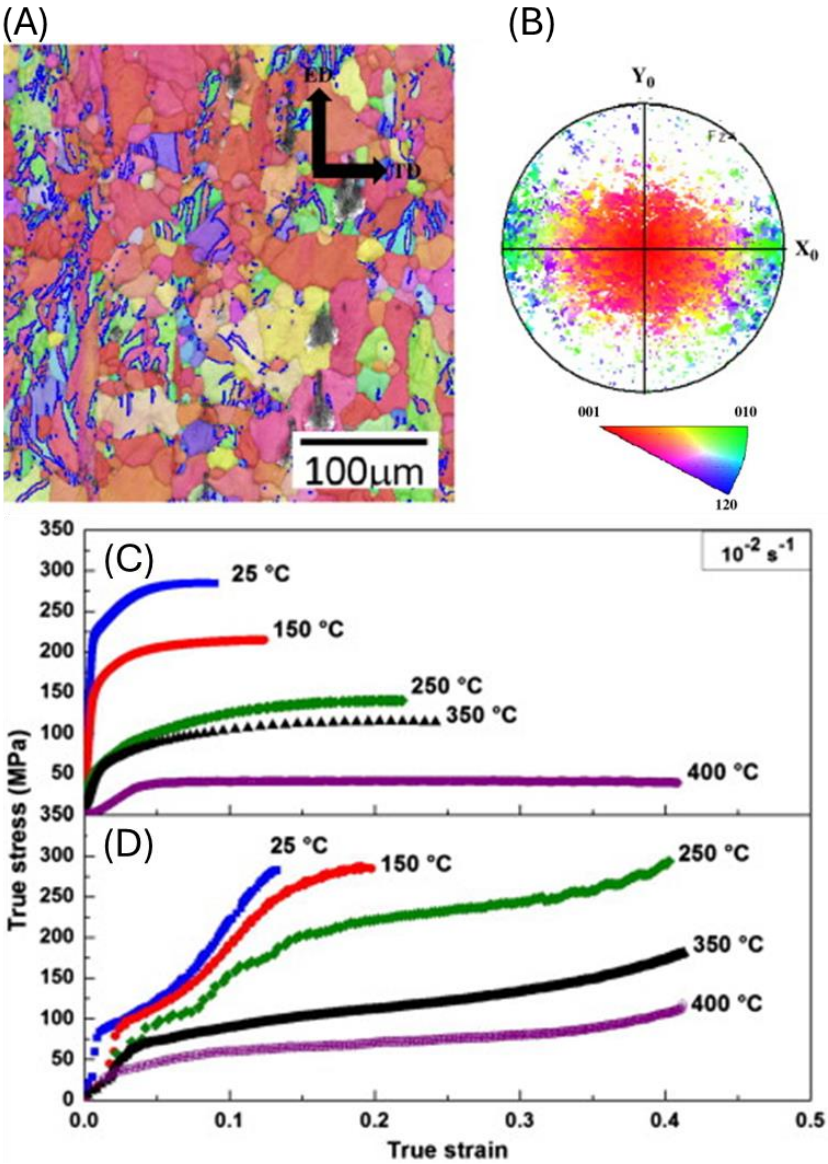

Figure 1.7: (A) Inverse pole figure (IPF) map, and (B) {0001} pole figure of the extruded AM30 Mg alloys. True stress-true strain responses of the alloy in uniaxial (C) tension and (D) compression at different temperatures but at a fixed strain rate of 10^{-2} s^{-1} [127].

In extruded Mg bars with a prismatic texture, the $\vec{c}$ axis of most grains is oriented perpendicular to the ED, as illustrated by the basal pole figure (Figure 1.7(B)). When an extruded Mg alloy is deformed in tension along the ED, the SFs for basal slip and ET are low, leading to a high yield strength, ~225 MPa for the extruded AM30 Mg alloy at room temperature (Figure 1.7(C)). However, the SF for basal slip is low but the SF for ET is high when compression is applied along the ED, leading to high activity of ET near the yield point and, accordingly, to a low yield strength, ~80 MPa for the extruded AM30 Mg alloy at ambient temperature (Figure 1.7D). That demonstrates that the extruded Mg alloys also exhibit a marked tension-compression yield asymmetry along the ED at room temperature. Similar yield asymmetry phenomena were also observed in other extruded Mg alloys with prismatic texture [125,128–132].

Various strategies, including but not limited to the alloying with rare earths (RE), were used to weaken the texture and improve the formability of wrought Mg alloys [133–135]. The addition of RE elements was reported to effectively improve the strength and reduce the TCA. The strength improvement is associated with the solute strengthening of <a> basal slip and the refined grain size in Mg alloys containing RE elements [136]. The reduced asymmetry could be ascribed to the combined roles of reduced grain size, weakened texture, suppression twinning, and enhancement of the activity of non-basal slip systems, i.e. the pyramidal <c + a> slip [95,137]. Although the alloying of RE can greatly improve the mechanical properties of wrought Mg alloys, the increased cost significantly limits their application.

1.4.2. Precipitates

Apart from the pronounced asymmetry in mechanical properties, the other key challenge hindering the practical application of wrought Mg alloys is their relatively low mechanical strength. One of the most effective methods to enhance the strength of Mg alloys is through alloying and heat treatment, which leads to the formation of a dispersion of nm-sized precipitates within the matrix [138–144]. These precipitates interact with dislocations and twins and increase the CRSS to

promote plastic deformation. The most widely used wrought Mg alloys as structural materials are Mg-Al and Mg-Zn based alloys, whose common precipitates and their influence on the mechanical properties were extensively investigated [98–107].

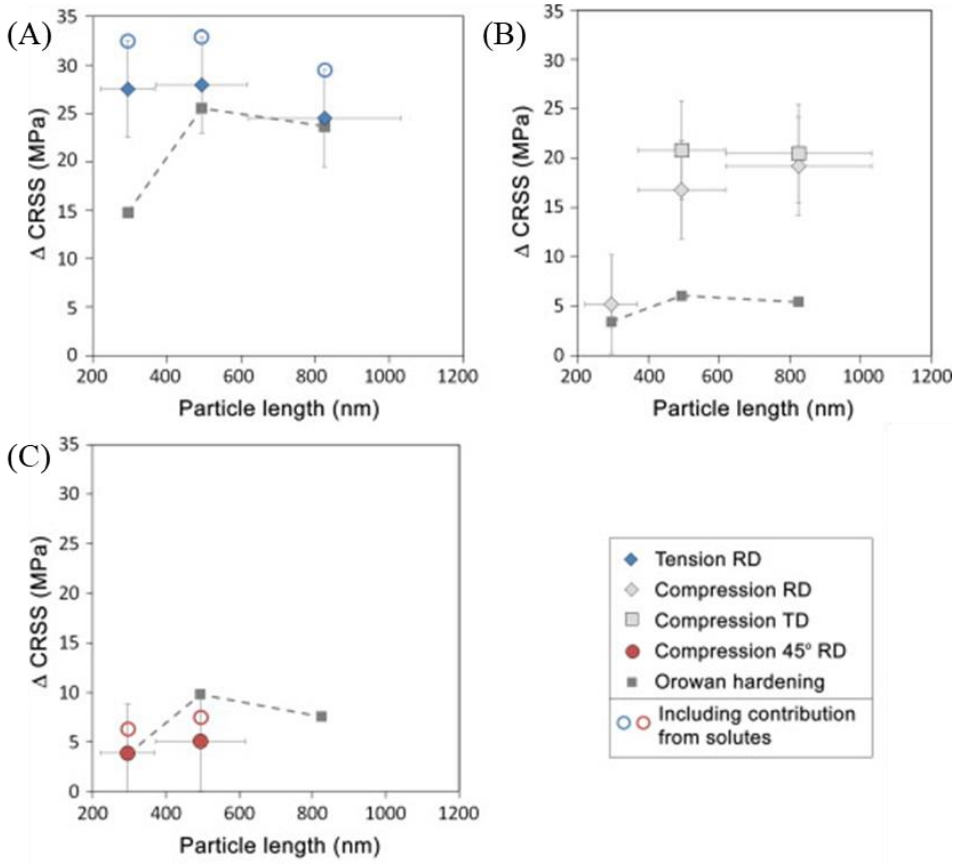

Figure 1.8: Increase in estimated CRSS of (A) <a> prismatic slip, (B) ET, and (C) <a> basal slip resulting from different ageing treatments in Mg-Al alloys. The predicted hardening from Orowan looping for each case is shown as a dotted grey line. The open circles represent the increased hardening results if solid-solution strengthening is taken into account [145].

Ageing of Mg-Al alloys at high temperature leads to the precipitation of the β-$Mg_{17}Al_{12}$ phase (with a body-centered cubic crystal structure, space group of 143m, and a lattice constant of 1.057 nm) which appears in the form of plates parallel to the basal plane [146]. Stanford et al. [145] established the correlation between the CRSS values of different deformation mechanisms and the precipitate size for rolled AZ31 plates. They showed that these precipitates only had a mild influence on the CRSS for <a> basal and <a> prismatic slip as well as for ET (Figure 1.8). In particular, the increase in CRSS was below 10 MPa for <a> basal slip because the

$Mg_{17}Al_{12}$ plates parallel to the basal plane are not a strong obstacle for the motion of <a> basal dislocations. Thus, the strengthening effect of ß-$Mg_{17}Al_{12}$ precipitates is limited [122, 124].

Stanford et al. [145] also showed that the CRSS values for <a> basal slip and <a> prismatic slip are not sensitive to the size of the ß-$Mg_{17}Al_{12}$ precipitates. However, the CRSS for deformation twinning increased as the size of the ß-$Mg_{17}Al_{12}$ precipitates grew from 300 nm to 500 nm, but further growth of the precipitates did not lead to additional increase in the CRSS for deformation twinning (see Figure 1.8). As a result, aged AZ91 Mg alloy exhibits a higher compressive-to-tensile yield strength ratio of 0.91, compared to the solution-treated state (0.75). Similar conclusions were drawn by Jain et al. [147] for the Mg-8Al-0.5Zn (wt.%) alloy.

Mg-Zn alloys stand for one of the best age-hardenable wrought Mg alloys. The precipitation sequence follows the path: supersaturated solid solution → Guinier-Preston zones → rod-shaped β_1' (monoclinic Mg_4Zn_7 and/or hexagonal $MgZn_2$) parallel to the $\vec{c}$ axis → coarse basal plate β_2' (hexagonal $MgZn_2$) → equilibrium phase β (monoclinic MgZn) [148–151]. The rod-shaped β_1' precipitates grow along the $\vec{c}$ and stand as effective obstacles for the propagation of <a> basal dislocation because of their small diameter and high number density [148]. The β_1' Mg_4Zn_7 precipitates have a monoclinic structure (space group of B/2m, a = 2.596 nm, b = 1.428 nm, c = 0.524 nm, Y = 102.5°), and the β_1' $MgZn_2$ precipitates have a hexagonal structure (space group of P63/mmc, a = 0.522 nm, c = 0.857 nm) [148].

The presence of rod-shaped β_1' precipitates increases the CRSS of <a> basal slip in Mg-Zn alloys [152,153]. Robson et al. [154] and Stanford and Barnett [155] have calculated the Orowan strengthening of <a> basal slip to be 43 MPa due to the presence of β_1' precipitates when Mg-5Zn (wt.%) alloy is aged at 150°C for 192 h. Similar increment on the CRSS for <a> basal slip was also experimentally reported by Alizadeh and LLorca [156] on Mg-4Zn (wt.%) alloy using the micropillar compression experiments (44.6 ± 5.5 MPa; aged at 149 °C for 100 h).

The hardened basal slip improves the mechanical strength of Mg-Zn alloys after ageing. However, contrary to extruded Mg-Al alloys [145], the presence of precipitates increase the tension-compression yield asymmetry in extruded Mg-5Zn (wt.%) alloys along the ED [154]. Robson et al. [157] hold that the mechanical asymmetry in a Mg alloy extrusion with a strong prismatic texture along ED is largely determined by the relative ease with which ET occurs (controlling yield in axial compression for extruded Mg alloys) compared to <a> prismatic slip (controlling yield in axial tension). Following this, the influence of precipitates on the CRSS for twin growth and <a> prismatic slip, i.e. the ratio of the increase in CRSS for twin growth to that for <a> prismatic slip, is relevant. In the case of ß-$Mg_{17}Al_{12}$ basal plates, the precipitates hinder twin growth, as compared to <a> prismatic slip, thus the tension-compression yield asymmetry is decreased. The reduced volume fraction of ETs due to the presence of ß-$Mg_{17}Al_{12}$ plates parallel to the basal plane was also experimentally reported by Jain et al. [147] in a cast Mg-8Al-0.5Zn (wt.%) alloy after 2% compression. However, the rod-shaped β_1' precipitates preferentially increase the CRSS for <a> prismatic slip and they have lower influence on twin growth. Thus, aged Mg-Zn alloys exhibit an increased tension-compression yield asymmetry.

Note that not all $\vec{c}$ axis rod-shaped precipitates will cause the increased tension-compression yield asymmetry of Mg alloys. For instance, Hidalgo-Manrique et al. [158] reported that the introduction of the rod-shaped Mg_3Nd precipitates, whose longer axis is parallel to the $\vec{c}$ axis, promoted <a> prismatic alloy, as compared to ET, on a extruded Mg-1Mn-1Nd (wt.%) alloy, thus contributing to the development of a reversed yield stress asymmetry, i.e. the compressive yield strength (CYS) being higher than the tensile yield strength (TYS).

1.4.3. Grain size

Grain refinement is an important strategy to increase the strength of wrought Mg alloys (Figure 1.9). The GBs hinder the dislocation propagation and create stress concentrations at GBs. The back stresses associated with these stress

concentrations increase the resolved shear stress necessary to move dislocations. This leads to the Hall-Petch relationship for metallic polycrystals, that relates the yield strength, σ_y with the average grain size d according to [159,160]:

$$\sigma_y = \sigma_0 + k_s \cdot d^{-1/2} \tag{1.2}$$

where σ_0 is yield or flow stress of single-crystal or bulk large-grain-size polycrystalline material, and k_s the strengthening parameter. The slope k_s in the Hall-Petch relationship for wrought Mg alloys can be as high as 200 ~ 300 MPa·μm$^{1/2}$ [161], which is 3 ~ 5 times higher than that of Al alloys (only 40 ~ 70 MPa·μm$^{1/2}$) [162]. Generally, the value of k_s is determined by the intrinsic strength of each grain and the ease of deformation transfer between neighbor grains. The higher value of k_s for Mg alloys with respect to Al alloys could be ascribed to the fact that HCP Mg alloys have lower number of easy slip systems than face centered cubic (FCC) Al alloys [163,164]. Thus, prismatic and pyramidal slip systems have to be activated at GBs in Mg alloys to accommodate the local strains, as shown by Armstrong et al. [163,164]. Note that the Hall-Petch relationship can be applied for Mg alloys with grain sizes in the micron-meter range and above.

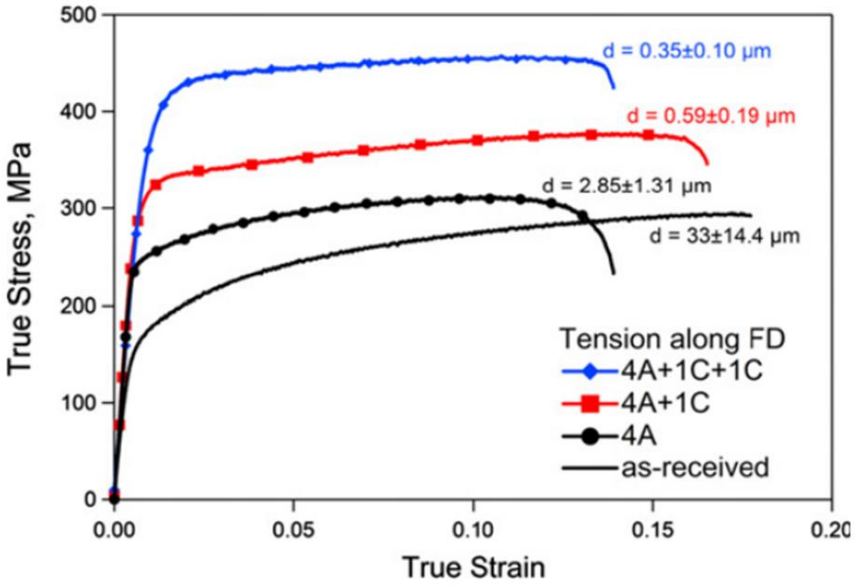

Figure 1.9: Room temperature true stress vs. strain curves for wrought AZ31 Mg alloy samples with different grain sizes in tension along the flow direction during the equal-channel angular pressing [165].

In addition, grain refinement in Mg alloys reduces the tension-compression yield asymmetry, because ET is favored in large grains thus the contribution of ET to plastic slip decreases with the decreased grain size [126,166,167]. A typical example can be found in an extruded AZ31 Mg alloys with different grain sizes [168]. The AZ31 Mg alloy extruded at 400°C has an average grain size of 5.3 μm and exhibits a TYS and CYS of 218 MPa and 165 MPa, respectively, at room temperature. However, the AZ31 Mg alloy extruded at 175°C has an average grain size of 0.65 μm, and exhibits a comparable TYS and CYS of ~380 MPa at room temperature [168]. Therefore, grain refinement not only increases the yield strength of wrought Mg alloys but also reduces the tension-compression yield asymmetry.

The influence of grain size on the dominant deformation mechanisms (slip and twinning) in wrought Mg alloys has also attracted much attention. Cepeda-Jiménez et al. [169] analyzed pure Mg manufactured by rolling and found that ET and <c + a> pyramidal slip dominate the deformation in the sample with the largest grain size (36 μm), during tension along the RD at 50°C and at 10^{-3} s^{-1}. Note that the ETs have low SFs, and their nucleation was ascribed to the local stress accommodation. ET activity decreased significantly in the sample with intermediate grain size (19 μm) and, instead, <c + a> pyramidal and <a> basal slip prevailed. In the sample with the smallest grain size (5 μm), both ET and non-basal slip become severely hindered and, thus, deformation was localized along bands of grains with misorientations <35°. Similar suppression of ET behavior via grain refinement was reported in other wrought Mg alloys [62–65,170]. This was ascribed to the higher k_s value for ET than that for slip [171,172]. Quantitatively, the k_s value for ET under compression along the ED in an extruded AZ31 alloy is 1.58 times higher than that for dislocation slip under tension along the ED (282 MPa·$\mu m^{1/2}$ and 178 MPa·$\mu m^{1/2}$ for ET and slip, respectively) [173]. However, there is not yet a consensus on the evolution of dominant slip system as a result of grain refinement. For example, Kang et al. [174] reported that the dominant slip systems in wrought, weak-textured pure Mg samples, prepared by high pressure torsion and post annealing treatments, changed from <a> basal slip to non-basal slip

(including <c> and <c + a> dislocations) as the grain size was reduced from 125 to 5.5 μm, which is contrary to the work of Cepeda-Jiménez et al. [169].

Although grain refinement can effectively strengthen Mg alloys and reduce the tension-compression yield asymmetry, it usually leads to a reduction of ductility / elongation [175], an important parameter when considering formability of the materials. Strain hardening of fine-grained Mg alloys is very limited and the Consideré criterion -that controls the onset of plastic instability in tension- is reached at very low strains [176,177]. As extreme cases, ultrafine-grained and nanostructured materials can be many times stronger than their coarse-grained counterparts, but their ductility is typically lower than 5% at room temperature [175]. For example, the yield strength of the wrought Mg-6.2Zn-0.5Zr-0.2Ca (wt.%) alloys increased from 107 ± 4 to 311 ± 3 MPa whilst the ductility was reduced from 16.5 ± 0.7% to 1.2 ± 0.1% as the grain size was reduced from 57 to 0.1 μm [178].

1.5. Motivation and objectives

Wrought Mg alloys, due to their low density, high specific strength, and homogeneous microstructures, are increasingly used in automotive, aerospace, and electronic applications. However, the plastic deformation mechanisms of Mg alloys are notably complex due to their HCP crystal structure, which leads to the activation and interaction of different slip and twinning systems. This complexity, combined with the strong texture in wrought Mg alloys, poses significant challenges to comprehensively understand the deformation mechanisms of wrought Mg alloys in different scenarios.

Although Mg alloys present 5 independent slip systems, including <a> basal slip, <a> prismatic slip, <a> I pyramidal slip, <c + a> I pyramidal slip and <c + a> II pyramidal slip, the dominant active slip system at room temperature is <a> basal slip due to its lowest CRSS. The accommodation of plastic strain along the $\vec{c}$ axis is commonly carried out by $\{10\bar{1}2\}$ $<10\bar{1}1>$ ET while <c + a> pyramidal slip, $\{10\bar{1}1\}$ $<10\bar{1}2>$ CT, and $\{10\bar{1}1\}$-$\{10\bar{1}2\}$ DT play a minor role.

Twinning is a polar mechanism that only occurs when the shear deformation is applied in the appropriate direction. This contributes to the anisotropy in mechanical properties, such as the tension-compression yield asymmetry, for strong-textured wrought Mg alloys. To improve the mechanical properties of wrought Mg alloys, various strategies, including but not limited to alloying, weakening texture, introducing precipitates and refining grains, were utilized [179]. Moreover, the influence of microstructure on the wrought Mg alloys was extensively explored using various experimental techniques and numerical simulations [55,153,180]. Despite that, the pursuit of high-performance, low-cost wrought Mg alloys is still ongoing and the correlation between microstructure and dominant deformation mechanisms in wrought Mg alloys is not fully understood [181].

One of the obstacles hampering a comprehensive understanding of the deformation mechanisms of Mg alloys is the lack of advanced characterization techniques to monitor the development and interactions among them. The analysis of the deformation mechanism using TEM is very powerful at the nanoscale but fails to provide statistical information in large areas. High resolution digital image correlation (HRDIC), synchrotron X-ray diffraction (XRD) and neutron diffraction, can also be used to identify the active deformation mechanisms during plastic deformation [182–186]. However, these techniques are time-consuming, expensive and have limited accessibility, which significantly restricts their widespread application. Although EBSD could provide orientation information in a large area, most of EBSD observations in previous works are extracted from ex-situ experiments after deformation [66,187,188]. The lack of orientation before deformation makes it hard to track the orientation evolution as well as identify the interactions among deformation mechanisms during deformation.

Slip trace analysis in combination with EBSD information is the most common approach to identify the active slip system(s) insofar [189]. This approach works well when there is only one possible slip direction (slip system) in a given slip plane, e.g. $\{1\bar{1}00\}$ of HCP lattice. However, the active slip system cannot be identified with this strategy when there are 2 or more possible slip directions (slip

systems) in a slip plane, e.g. {0001} of HCP lattice, because all slip directions in the same slip plane generate identical slip traces [190]. These limitations highlight the need for a new and feasible technique to obtain a more comprehensive understanding of deformation mechanisms of Mg alloys during deformation and this was the main objective of this doctoral thesis.

In particular, the first goal of this thesis was to develop experimental techniques, based on the combination of in-situ characterization during mechanical deformation and post-mortem analytical tools to provide accurate information on the active deformation mechanisms of wrought Mg alloys. The second objective was to apply these techniques to establish the correlation between the microstructure and the active deformation mechanisms in wrought Mg alloys of interest. To this end, novel analysis strategies based on machine learning (ML) were used to unveil these correlations from the large data sets obtained experimentally.

Following these goals, the thesis is structured as follows:

Chapter 1 briefly summarized the deformation mechanisms of wrought Mg alloys, as well as the main factors influencing them. Some controversies on the deformation mechanisms of wrought Mg alloys in previous studies were also indicated and the motivation and objectives of this thesis were presented.

Chapter 2 introduced the processing routes of the various wrought alloys used in the thesis as well as the mechanical characterization techniques. Particular attention is paid to the techniques used to study the dominant deformation mechanisms of wrought Mg alloys. They include conventional EBSD, TEM, in-situ EBSD, slip trace analysis, slip trace - modified lattice rotation analysis (ST-MLRA), grain reference orientation deviation (GROD), as well as ML tools. The advantages and disadvantages of each technique were also discussed. It should be noted that some of these techniques contain novel contributions that go beyond the state-of-the-art and that were developed for this investigation.

Chapter 3 explored the deformation mechanisms of an as-extruded Mg-6.5Zn alloy with the dual texture and the limited yield asymmetry under tension and

compression. The influence of <a> non-basal slips on the DT behavior was also explored in this chapter. The information in this chapter has led to two publications:

- B. Yang, J. Wang, Y. Li, M. Barnett, J. LLorca - Deformation mechanisms of dual-textured Mg-6.5Zn alloy with limited tension-compression yield asymmetry. Acta Materialia, 248, 118766, 2023.
- B. Yang, J. Wang, Y. Li, M. Barnett, J. LLorca - Suppressed transformation of compression twins to double twins in Mg by activation of non-basal slip. Scripta Materialia, 235, 115620, 2023.

Chapter 4 studied the influence of prismatic rod-shaped precipitates on the deformation mechanisms (in particular on the dominant slip systems) of Mg-4.5Zn alloys with a strong prismatic texture during tension. The information in this chapter has led to the following publication:

- B. Yang, J. Wang, M. R. Ghandehari Ferdowsi, Q. Chao, X. Gao, Y. Li, Y. Zhu, M. Barnett, J. LLorca - Effect of precipitates on the dominant active slip systems in Mg-4.5Zn (wt.%) alloy. Acta Materialia, 278, 120231, 2024.

Chapter 5 examined the deformation of Mg-1Al alloy with a strong prismatic texture, focusing on the nucleation and growth of anomalous ETs during tension. These results led to the following publication:

- B. Yang, J. LLorca - Origin of nucleation and growth of ETs in grains unsuitably oriented for twinning during deformation of Mg-1%Al. Journal of Magnesium and Alloys, 12, 1186-1203, 2024.

Chapter 6 studied the influence of microstructure on the nucleation of ET using a large dataset (>3000 grains × 28 features) and ML (supervised Bayesian networks). The key microstructural features associated with ET behavior and 3 different twinning scenarios are revealed. This information led to the following publication:

- B. Yang, V. Vassilev-Galindo, J. LLorca - Application of machine learning to assess the influence of microstructure on twin nucleation in Mg alloys. npj Computational Materials, 10, 26, 2024.

Finally, the results regarding the relationship between microstructure and deformation mechanisms as well as mechanical properties in the previous chapters are discussed in Chapter 7, that also includes the main conclusions of the thesis and the avenues for future work.

2. Methodology

2.1. Materials processing

Various wrought Mg alloys with different microstructures were obtained using different processing strategies. They can be roughly categorized into two groups: extruded Mg alloys and rolled Mg alloys. In particular, their materials processing histories are the following:

The Mg-6.5Zn (wt.%) alloy used in this thesis was prepared by casting (raw materials: pure Mg (99.8 wt.%) and pure Zn (99.7 wt.%); resistance heating furnace at 750°C), solid solution treatment (335°C for 72 h), first extrusion (extrusion temperature: 370°C, ram speed: 0.1 $mm \cdot s^{-1}$, reduction ratio: 4), short time annealing (340°C for 1 h), and second extrusion (extrusion temperature: 350°C, ram speed: 0.1 $mm \cdot s^{-1}$, reduction ratio: 28).

The Mg-4.5Zn (wt.%) alloy ingot was prepared by casting using a resistance heating furnace under Ar protective gas. The alloy ingot was homogenized at 330°C for 24 h and then at 370°C for 120 h. Afterwards, the ingot was hot extruded at 350°C with a reduction ratio of ~ 36 and a ram speed of 0.1 $mm \cdot s^{-1}$, followed by water quenching to avoid the formation of precipitates during cooling. The as-extruded Mg-4.5Zn rod will be designated as 'AE' throughout the thesis. AE samples were peak aged at 150°C for 84 h to introduce precipitates. They will be referred to as 'PA' throughout the thesis.

Both Mg-1Al and Mg-0.3Zn (at.%) alloy ingots were prepared by vacuum melting, followed by a homogenization treatment at 400°C for 2 h and furnace cooling. Then, the cast billets were extruded (temperature: 300°C, extrusion ratio: 16:1, ram speed: ≈ 2 $mm \cdot s^{-1}$) and subjected to another homogenization heat treatment at 400°C for 2 h and furnace cooling.

Slabs of 80 × 65 × 500 mm^3 of a rolled AZ31B-O Mg alloy were purchased from Magnesium Elektron Ltd. (Manchester, UK). The nominal chemical composition of the alloy is 2.89 wt.% Al, 1.05 wt.% Zn, and 0.42 wt.% Mn.

2.2. Mechanical tests

The macroscopic tensile mechanical properties of Mg alloys were carried out at room temperature using an Instron 8501 servo-hydraulic dynamic testing machine equipped with a dynamic extensometer (Instron 2620-602 series, gauge length: 12.5 mm, maximum travel: 2.5 mm) at an initial tensile strain rate of 10^{-3} s^{-1}. Due to the smaller size of the Mg-6.5Zn samples, their macroscopic tensile properties were tested at room temperature using a micro-mechanical testing instrument (MZ.Sb module) provided by Kammrath & Weiss at an initial strain rate of 10^{-4} s^{-1}. The macroscopic compressive properties of the Mg-6.5Zn samples were obtained at room temperature using an Instron 5567 electro-mechanical testing machine equipped with a high-precision video extensometer at an initial strain rate of 10^{-3} s^{-1}. Additionally, Teflon tape was applied to both the top and bottom surfaces of the cylindrical compression samples to reduce friction between the compression plate and the sample surface. The variations in strain rates from 10^{-3} s^{-1} to 10^{-4} s^{-1} between tension and compression had a negligible influence on the stress-strain curves and deformation mechanisms [191].

To gain a deeper understanding of the microstructural evolution of Mg alloy samples at different strains, interrupted plastic deformation experiments were conducted on the wrought Mg alloys. The experiments were performed at room temperature using a micro-mechanical testing machine (MZ.Sb module) from Kammrath & Weiss at an initial strain rate of 10^{-4} s^{-1}.

2.3. Microstructural characterization

2.3.1.X-ray diffraction (XRD)

XRD is a rapid analytical technique primarily used for phase identification of a crystalline material. In this thesis, the only phase in the Mg-1Al (at.%) alloy was identified as HCP Mg using a diffractometer (Bruker-AXS D8, Bruker, Germany) equipped with Cu-Kα radiation source, which excludes the influence of precipitates on the anomalous twinning behavior. The scanning rate was 0.02° s^{-1}, the 2theta range was 20° - 80°, and the step size was 0.01°.

2.3.2. Scanning electron microscopy (SEM)

Scanning electron microscopy (SEM) is a surface-imaging technique that produces images of a sample by scanning it with a focused beam of electrons. In this thesis, an Apreo 2S LoVac SEM was utilized to characterize the surface slip traces after deformation under the secondary electron (SE) mode, a working distance of 10 mm, accelerating voltages from 10 kV to 20 kV, and beam currents from 0.1 nA to 2.7 nA.

2.3.3. Electron backscatter diffraction (EBSD)

EBSD is a SEM-based technique used to study the crystallographic structure of materials [192]. In the microscope, an incident beam of electrons hits the sample, at an angle of 70°. The electrons interact with the atoms in the sample and rebound elastically at various scattering angles. Some of these electrons are incident on atomic lattice planes at angles which satisfy the Bragg equation, $n\lambda_w = 2d_s \cdot \sin\delta$, where n is an integer (1, 2, 3, …), λ_w is the wavelength of the electrons, d_s is the spacing of the diffracting plane, and δ the angle of incidence of the electrons on the diffracting plane. These electrons are diffracted to form a set of paired large-angle cones that correspond to each diffracting plane. The image produced on the EBSD detector (usually using a phosphor screen to convert the electrons to photons) contains characteristic Kikuchi bands. The centerline of each Kikuchi band is equivalent to the intersection line between the corresponding diffracting plane satisfying Bragg equation at the scattering point of electrons on the sample surface and the EBSD detector. The following indexing requires each Kikuchi pattern to be compared with the dictionary to find the best match, and then to determine the crystal orientation at the scattering point.

Four field emission SEMs equipped with EBSD were used in the study: the Helios NanoLab 600i SEM (for the AZ31 Mg and Mg-4.5Zn alloys), the Apreo 2S LoVac SEM (for the Mg-1Al and Mg-6.5Zn Mg alloys), the LEO 1530 SEM (primarily for the Mg-6.5Zn alloy), and the FEI XL30S SEM (for the Mg-0.3Zn alloy). The acceleration voltage and beam current were set at 20 kV and 2.7 nA, respectively, with a working distance of approximately 10 mm in all cases. The

initial EBSD scan areas and step sizes for the AZ31, Mg-1Al, Mg-4.5Zn and Mg-6.5Zn alloys were 560 × 900 μm² and 0.7 μm, 1130 × 1645 μm² and 1 μm, 550 × 1130 μm² and 1 μm, and 810 × 1073 μm² and 0.7 μm, respectively. After deformation, the EBSD step sizes for the AZ31, Mg-1Al, Mg-4.5Zn and Mg-6.5Zn alloys were approximately 0.4 μm, 0.5 μm, 0.5 μm, and 0.3 μm, respectively. In-situ EBSD tracking of the microstructural evolution of the Mg-1Al alloy during tension was also conducted, with an observation area of 374.0 × 493.5 μm². In addition, EBSD were performed on Mg-0.3Zn alloy at a small region to evaluate the feasibility of proposed ST-MLRA technique with a step size of 0.5 μm.

2.3.4. Transmission electron microscopy (TEM)

TEM is a technique that is very useful for ascertaining the nature of defects, such as dislocations and precipitates, in crystalline materials. In this thesis, TEM was utilized to analyze the morphology and distribution of precipitates in Mg-4.5Zn alloy after ageing as well as the interaction between precipitates and dislocations after deformation.

Both the distribution of precipitates in the PA specimen and the interaction between dislocations and precipitates in the PA specimen after 10% of tensile deformation were analyzed by TEM. The TEM foils in the PA specimen before deformation were prepared by GATAN PIPS (precision ion polishing system), and the TEM observations were performed using a JEOL 2100 FEG TEM. More details about the preparation of specimen before deformation can be found in Ref. [149]. For deformed sample, sheets with a thickness of ~ 0.4 mm were sliced from the PA tensile samples. Discs of 3 mm in diameter were punched from the sheets and then ground to a thickness of ~ 0.1 mm. TEM samples were electro-polished by Struers Tenupol-5 using a solution of 15.9 g LiCl + 33.48 g $Mg(ClO_4)_2$ + 1500 ml methanol + 300 ml 2 butoxy ethanol at -50°C and 100 V. The determination of Burgers vectors of slip dislocations was achieved using FEI Tecnai G2 T20 TWIN TEM (200 kV) under two-beam diffraction conditions with various diffraction $\vec{g}$ vectors. Table 2.1 shows the three selected $\vec{g}$ vectors of $[0002]_{Mg}$, $<10\bar{1}0>_{Mg}$ and $<11\bar{2}0>_{Mg}$. The active slip dislocation Burgers vector was identified according to the $\vec{g} \cdot \vec{b}$

invisibility criterion, where $\vec{b}$ is the Burgers vector. Based on the $\vec{g} \cdot \vec{b}$ analysis for dislocations, three types of Burgers vectors $\vec{b}$ in the Mg matrix, i.e., <a>, <c + a> and <c>, can be determined. <a> dislocation is invisible under the diffraction $\vec{g}$ vector of $[0002]_{Mg}$. <c> dislocation is invisible under both the diffraction $\vec{g}$ vectors of $<10\bar{1}0>_{Mg}$ and $<11\bar{2}0>_{Mg}$. Partial <a> and <c + a> dislocations are invisible under the diffraction $\vec{g}$ vector of $<10\bar{1}0>_{Mg}$. The comparison of the same region under various diffraction $\vec{g}$ vectors allows us to identify the active slip systems.

Table 2.1: Values of $\vec{g} \cdot \vec{b}$ at various diffraction $\vec{g}$ vectors used to analyze active slip dislocation types. ± 1, ± 3 and ± 6 represent the dislocation visibility, while 0 represents the dislocation invisibility.

$\vec{g}$	$\pm \vec{b}$									
	<a>			<c + a>						<c>
	$[11\bar{2}0]$	$[\bar{2}110]$	$[\bar{1}2\bar{1}0]$	$[11\bar{2}3]$	$[\bar{2}113]$	$[\bar{1}2\bar{1}3]$	$[11\bar{2}\bar{3}]$	$[\bar{2}11\bar{3}]$	$[\bar{1}2\bar{1}\bar{3}]$	[0003]
[0002]	0	0	0	6	6	6	- 6	- 6	- 6	6
$<10\bar{1}0>$	3	- 3	0	3	- 3	0	3	- 3	0	0
$<11\bar{2}0>$	6	- 3	3	6	- 3	3	6	- 3	3	0

2.4. In-situ EBSD

In-situ EBSD has become a vital tool for studying the deformation mechanisms of Mg alloys, providing information about the evolution of crystallographic information during mechanical testing [193]. Its application is particularly valuable for investigating dislocation slip and twinning as well as texture in Mg alloys, which exhibit an obvious anisotropic deformation due to their HCP crystal structure.

To be specific, in-situ EBSD allows the direct observation of $\{10\bar{1}2\}$ ET, $\{10\bar{1}1\}$ CT, and their interaction with dislocations. This information is crucial to understand how these mechanisms accommodate strain under different loading conditions. By tracking changes in grain orientation during deformation, in-situ EBSD reveals how crystallographic texture evolves, which is critical for tailoring the mechanical properties of Mg alloys.

Despite that in-situ EBSD provides valuable insights of the deformation mechanisms, it is limited by its reliance on surface observations, sensitivity to

sample preparation artifacts, and reduced spatial resolution compared to TEM. Enhancements in detector technology in combination with other techniques such as TEM and HRDIC can provide a very detailed picture of the deformation processes that control the mechanical behavior of Mg alloys.

In this thesis, in-situ EBSD was utilized to track the progression of twinning in a Mg-1Al alloy during the tensile tests at room temperature. The in-situ EBSD tensile tests were carried out within an SEM (Apreo 2S LoVac, FEI Company, Portland, OR, USA) using a micromechanical testing machine (Kammrath and Weiss Technologies, Inc., Model MZ.Sb) under displacement control at 1 $\mu m \cdot s^{-1}$, which led to an approximate strain rate of 10^{-4} s^{-1}. The samples for the in-situ EBSD tests were mechanically polished using SiC paper, 0.5, 0.05 µm diamond slurries, and 40 nm oxide suspensions. Slight etching using 5% Nital solution (a mixture of nitric acid and ethanol) was applied for ~ 5 seconds on the surface. The specimen was positioned in the micromechanical testing machine, fixed, and introduced into the microscope. The machine was initially titled by 50° (cf. Figure 2.1), and the stage of microscope was further tilted by 20° to guarantee that the signal could be captured by the EBSD detector.

The in-situ EBSD tensile tests were interrupted at different engineering strains of 1.5%, 4.5%, 10.0%, and 15.3% and the sample was analyzed by EBSD (Oxford HKL Channel 5, Oxford Instruments, Abingdon, UK; step size: 0.5 µm, working distance: 10 mm) in a region of 374.0 × 493.5 μm^2 near the center of the gauge. Note that the specimen was not unloaded during the analysis by in-situ EBSD.

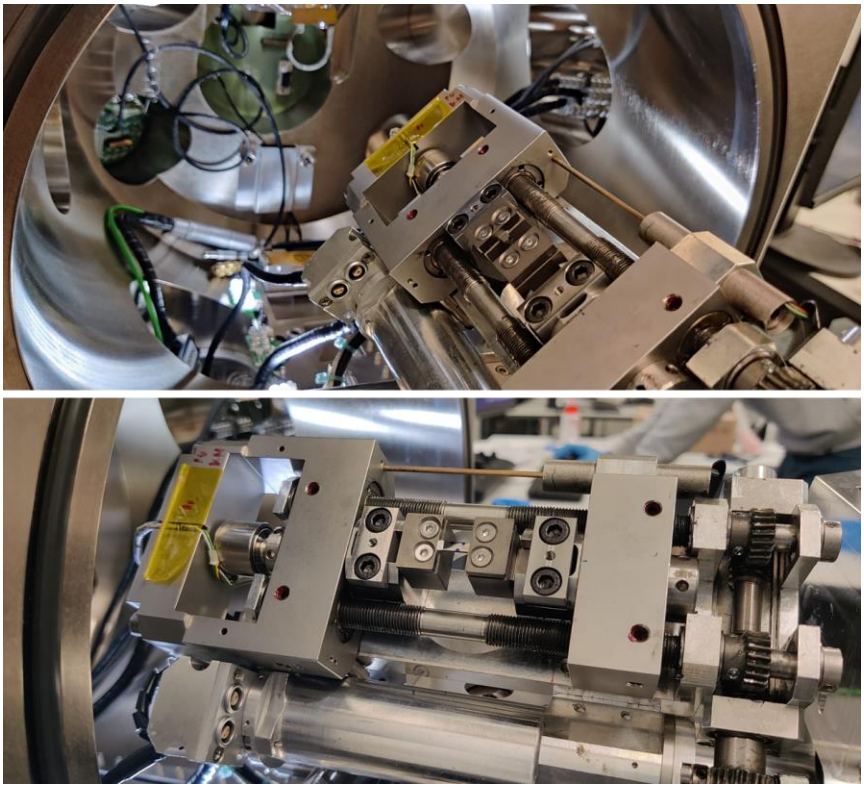

Figure 2.1: Images of in-situ EBSD set-up inside the SEM.

2.5. EBSD-based analysis

2.5.1. Slip trace analysis

Mg alloys have a variety of slip systems, and it is crucial to identify the active slip systems in each grain to assess the deformation mechanisms (such as slip localization, forest hardening, and interactions between dislocations and GBs or twin boundaries) that arise during plastic deformation.

So far, slip trace analysis combined with EBSD information has been the most common method to identify the activate slip systems [189,194,195]. The key to this method is the comparison between the orientation of slip traces observed on the surface of one grain via SEM with the orientation predicted for the different slip planes based on grain orientation provided by EBSD. This comparison helps to identify the most likely slip planes, but it does not indicate the actual active slip system if several slip systems can be active on the same plane (as it is the case for <a> basal slip in Mg).

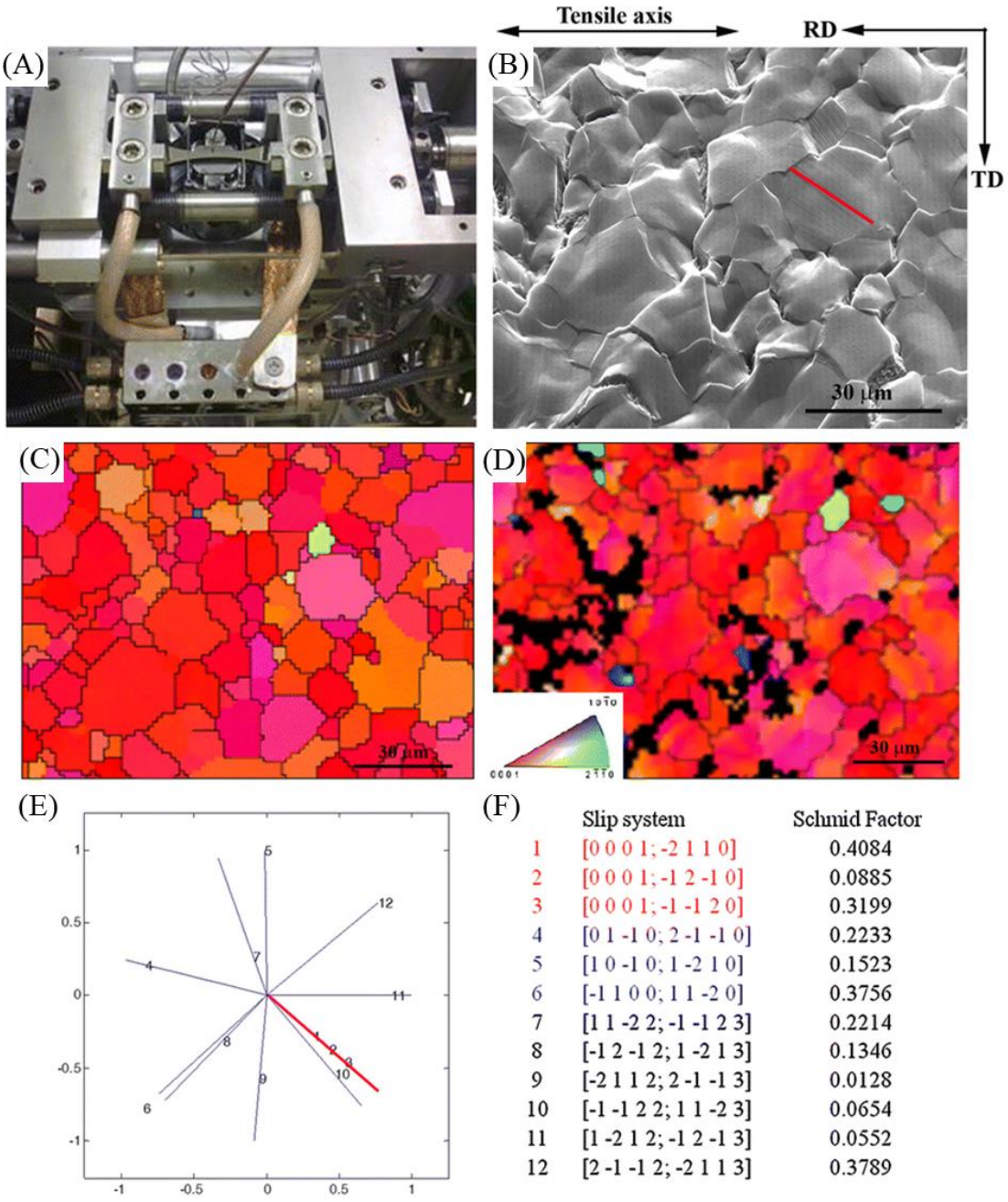

Figure 2.2: Methodology of slip trace analysis. (A) Screw-driven micromechanical testing machine inside a SEM. (B) SEM micrograph showing the slip traces (red lines). (C) and (D) EBSD IPF maps in the normal direction corresponding to the SEM micrograph before and after deformation, respectively. (E) Orientation of the 12 possible traces and determination of the potential active slip systems (in red) and (F) SFs for the different slip systems in the grain [196].

An example of the slip trace analysis is shown in Figure 2.2 [196]. Using in-situ EBSD, Cepeda-Jiménez et al. [196] characterized the deformation mechanisms in polycrystalline pure Mg. They identified that the surface slip traces belong to the (0001) basal plane by comparing the slip traces observed on the

deformed sample surface (Figure 2.2(B)) with the ideal slip traces calculated based on the grain orientation (Figure 2.2(E)), After checking the SFs of the three different slip systems on this basal plane (Figure 2.2(F)), they concluded that the active slip system in this grain was (0001) [$\bar{2}$110], since it had the highest global SF of 0.4084.

Slip trace analysis can accurately identify the slip system when there is only one possible slip direction (slip system) on a given slip plane, such as the [01$\bar{1}$0] in the prismatic plane and the [$\bar{2}$112] in the II pyramidal plane of HCP crystals. However, the active slip system cannot be determined when there are two or more possible slip directions (slip systems) on a slip plane because all slip directions on the same slip plane led to the same slip trace. Thus, other criteria, such as the maximum global SF, the minimum CRSS, or the highest Luster-Morris geometric compatibility factor [95,190,197,198] can be used to determine the active slip system within the slip plane in this case. But the results based on these criteria may lead to incorrect conclusions.

2.5.2. Slip trace - modified lattice rotation analysis (ST-MLRA)

A modified lattice rotation analysis -that enables precise identification of the RA for the active slip system- was proposed [187]. This analysis relies on the EBSD results after deformation and is based on the comparison between the experimental and calculated evolution of the grain orientation due to deformation, as indicated by the projection on the pole figure. However, one RA can be shared by 2 or 3 different slip systems and the active slip system cannot be discriminated solely using the modified lattice rotation analysis. This is the case, for instance, of <a> basal slip in the {0001} plane and <c + a> II pyramidal slip in {11$\bar{2}$2} plane, that share the same <1$\bar{1}$00> RA family in the HCP lattice, leading to identical evolution of the grain orientation due to plastic deformation.

In this thesis, a new and efficient strategy, denominated ST-MLRA, is presented to identify the dominant active slip system in each grain during plastic deformation of polycrystalline metallic alloys. The input information are the Bunge Euler angles (**g** and **g'** matrices) from the region near the observed slip traces before

and after deformation, respectively, and the orientation of the slip trace (given by the slip trace vector $\vec{T}$) in the sample surface. The first step in the analysis is to determine the SP. The vector normal to any slip plane ($\overrightarrow{SP}_{sc}$) in the sample coordinate system can be calculated as [199]:

$$\overrightarrow{SP}_{sc} = \overrightarrow{SP}_{cc} \cdot \mathbf{g} \tag{2.1}$$

where $\overrightarrow{SP}_{cc}$ stands for the vector normal to the slip plane in the crystal coordinate system. Note that the scalar and cross products of $\vec{A}$ and $\vec{B}$ are expressed by $\vec{A} \cdot \vec{B}$ and $\vec{A} \times \vec{B}$, respectively. The slip trace vector ($\vec{T}$) on the sample surface can be computed from the cross product of $\overrightarrow{SP}_{sc}$ and the vector normal to sample surface ($\vec{N}$) as:

$$\vec{T} = \overrightarrow{SP}_{sc} \times \vec{N} \tag{2.2}$$

and the comparison of $\vec{T}$, computed from eq. (2.2), with the experimental $\vec{T}$ determined from the SEM images indicates the actual SP.

The second step is to determine the slip direction within the SP. To this end, the Bunge Euler angles of the crystal after rotation (**g′** matrix) can be determined as the scalar product of the **g** matrix and rotation matrix **rot** as:

$$\mathbf{g'} = \mathbf{g} \cdot \mathbf{rot} \tag{2.3}$$

where **rot** matrix is calculated with MATLAB using the function of rotation.byAxisAngle(axis, angle) in MTEX [200] that takes into account the RA vector $\overrightarrow{RA}_{sc}$ in the sample coordinate system and the rotation angle θ according to:

$$\mathbf{rot} = \text{rotation.byAxisAngle}(\overrightarrow{RA}_{sc}, \theta) \tag{2.4}$$

The RA vector depends on the slip plane and slip direction [201] and can be computed as:

$$\overrightarrow{RA}_{sc} = \overrightarrow{RA}_{cc} \cdot \mathbf{g} \tag{2.5}$$

$$\overrightarrow{RA}_{cc} = \overrightarrow{SP}_{cc} \times \overrightarrow{SD}_{cc} \tag{2.6}$$

where $\overrightarrow{RA}_{cc}$ and $\overrightarrow{SD}_{cc}$ stands for the RA and slip direction vectors in crystal coordinate system respectively of various slip systems, as summarized in the Table 2.2. The initial orientation of the crystal in the pole figure before deformation (given by **g**) and after deformation (given by **g'**) should be connected by a line that

is given by eq. (2.3) and that indicates which one is the actual slip direction within the slip plane. The rotation angle θ is normally $\leq 5^{o}$ based on slip-induced local lattice rotations [187,202]. Note that error source may derive from the misalignment of sample before and after deformation by quasi-in situ SEM/EBSD measurements. In this case, the utilization of mean orientation of the grain after deformation to calculate theoretical deflection by various slip modes will be more accurate after avoiding the influence of sample misalignment.

Table 2.2: Summary of all considered slip planes, slip systems and RAs as well as corresponding nominations for ST-MLRA.

	SP	Slip system	RA (nomination)
Basal plane	(0001)	(0001) [$2\bar{1}\,\bar{1}0$]	[$01\bar{1}0$] (A)
		(0001) [$\bar{1}2\bar{1}0$]	[$10\bar{1}0$] (B)
		(0001) [$\bar{1}\,\bar{1}20$]	[$1\bar{1}00$] (C)
Prismatic plane	($01\bar{1}0$)	($01\bar{1}0$) [$2\bar{1}\,\bar{1}0$]	[0001] (D)
	($\bar{1}100$)	($\bar{1}100$) [$\bar{1}\,\bar{1}20$]	
	($\bar{1}010$)	($\bar{1}010$) [$\bar{1}2\bar{1}0$]	
I pyramidal plane	($01\bar{1}1$)	($01\bar{1}1$) [$2\bar{1}\,\bar{1}0$]	[$0\bar{1}12$] (E)
		($01\bar{1}1$) [$11\bar{2}\,\bar{3}$]	[$\bar{3}21\bar{1}$] (F)
		($01\bar{1}1$) [$1\bar{2}13$]	[$\bar{3}121$] (G)
	($\bar{1}101$)	($\bar{1}101$) [$\bar{1}\,\bar{1}20$]	[$1\bar{1}02$] (H)
		($\bar{1}101$) [$\bar{2}11\bar{3}$]	[$\bar{1}\,\bar{2}31$] (I)
		($\bar{1}101$) [$1\bar{2}13$]	[$\bar{2}\,\bar{1}3\bar{1}$] (J)
	($\bar{1}01\bar{1}$)	($\bar{1}01\bar{1}$) [$\bar{1}2\bar{1}0$]	[$\bar{1}012$] (K)
		($\bar{1}01\bar{1}$) [$\bar{2}113$]	[$\bar{1}3\bar{2}\,\bar{1}$] (L)
		($\bar{1}01\bar{1}$) [$11\bar{2}\,\bar{3}$]	[$\bar{2}3\bar{1}1$] (M)
	($\bar{1}011$)	($\bar{1}011$) [$\bar{1}2\bar{1}0$]	[$10\bar{1}2$] (N)
		($\bar{1}011$) [$\bar{2}11\bar{3}$]	[$1\bar{3}2\bar{1}$] (O)
		($\bar{1}011$) [$11\bar{2}3$]	[$2\bar{3}11$] (P)
	($\bar{1}10\bar{1}$)	($\bar{1}10\bar{1}$) [$\bar{1}\,\bar{1}20$]	[$\bar{1}102$] (Q)
		($\bar{1}10\bar{1}$) [$\bar{2}113$]	[$12\bar{3}1$] (R)
		($\bar{1}10\bar{1}$) [$1\bar{2}1\bar{3}$]	[$21\bar{3}\,\bar{1}$] (S)
	($0\bar{1}11$)	($0\bar{1}11$) [$2\bar{1}\,\bar{1}0$]	[$01\bar{1}2$] (T)
		($0\bar{1}11$) [$11\bar{2}3$]	[$3\bar{2}\,\bar{1}\,\bar{1}$] (U)
		($0\bar{1}11$) [$1\bar{2}1\bar{3}$]	[$3\bar{1}\,\bar{2}1$] (V)
II pyramidal plane	($\bar{2}112$)	($\bar{2}112$) [$\bar{2}11\bar{3}$]	[$01\bar{1}0$] (A)
	($\bar{2}11\bar{2}$)	($\bar{2}11\bar{2}$) [$\bar{2}113$]	
	($1\bar{2}1\bar{2}$)	($1\bar{2}1\bar{2}$) [$1\bar{2}13$]	[$10\bar{1}0$] (B)
	($\bar{1}2\bar{1}\,\bar{2}$)	($\bar{1}2\bar{1}\,\bar{2}$) [$1\bar{2}1\bar{3}$]	
	($11\bar{2}2$)	($11\bar{2}2$) [$11\bar{2}\,\bar{3}$]	[$1\bar{1}00$] (C)
	($\bar{1}\,\bar{1}22$)	($\bar{1}\,\bar{1}22$) [$11\bar{2}3$]	

The feasibility of the ST-MLRA strategy to identify the actual slip system is demonstrated below for a HCP Mg alloy, a good example because of the large number of slip systems. A dog-bone-shaped tensile sample with the gauge dimensions of 10 × 2 × 2 mm^3 (length × width × thickness) was manufactured from the extruded Mg-0.3Zn (at.%) bar by electron discharge machining with the tensile direction parallel to ED. The sample preparation and mechanical tests of this Mg-0.3Zn alloy can be found in Ref. [203]. In addition, during ST-MLRA analysis, it was assumed that plastic slip in HCP Mg could take place along 16 slip planes (numbered from 1 to 16) and the corresponding RAs for all the slip directions in all slip planes (denominated from A to V). This detailed information can be found in Table 2.2.

The application of ST-MLRA to identify the active slip system in grain G1 with Euler angles of (165.4°, 64.7°, 48.8°) is depicted in Figure 2.3. The observed slip traces in G1 (Figure 2.3(A)) are in good agreement with the calculated one for the (0001) basal plane (number 1, Figure 2.3(B)). However, there are 3 slip directions in this plane: $[2\bar{1}\bar{1}0]$ (SF, m = 0.20, RA: $[01\bar{1}0]$ (A)), $[\bar{1}2\bar{1}0]$ (m = 0.15, RA: $[10\bar{1}0]$ (B)), and $[\bar{1}\bar{1}20]$ (m = 0.05, RA: $[1\bar{1}00]$ (C)), and the active one cannot be discriminated by conventional slip trace analysis. The SF (m) for slip system is calculated by eq. (1.1). Obviously, the SF is calculated neglecting local effects associated with the deformation of neighbor grains that may change the actual stress state in the grain. These effects are particularly significant at large applied strains (10%) but can also be important at smaller strains and, thus, the SF is not always an accurate criterion to predict the most active slip system within a slip plane.

The experimental projection of the orientation of grain G1 in the pole figure before and after deformation is plotted in Figure 2.3(C). Plastic deformation stretches the projection in the horizontal direction which is in good agreement with the predictions corresponding to the RA $[01\bar{1}0]$ (A) and far away from those predicted for RAs $[10\bar{1}0]$ (B) or $[1\bar{1}00]$ (C), as shown in Figure 2.3(D). Therefore, it can be concluded that the only active slip system in G1 is the <a> basal (0001)

[$2\bar{1}\bar{1}0$] which, in this case, is consistent with the result predicted by the maximum SF criterion.

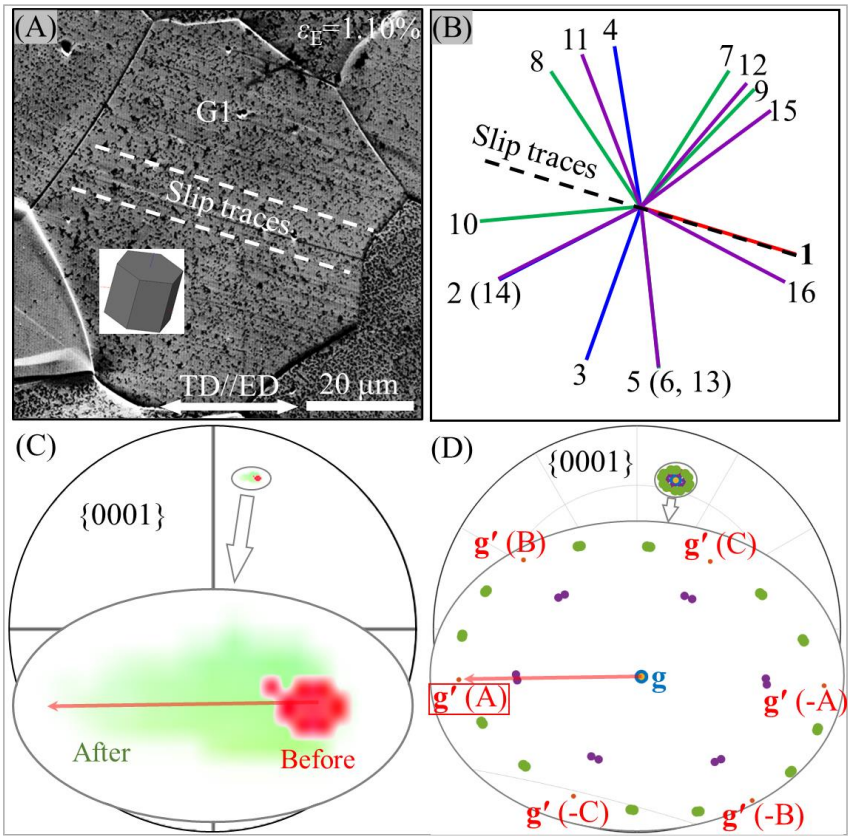

Figure 2.3: (A) Experimental slip traces observed by SEM on grain G1 of the Mg alloy surface (applied tensile strain 1.10%). (B) Calculated slip traces of different slip planes according to the EBSD information from G1. (C) Experimental {0001} pole figure of grain G1 before (red) and after (green) deformation. The main stretching direction of the trace of the grain is shown with a red arrow. (D) Simulated projections of grain G1before (**g**) and after (**g′**) a rotation of 5° around various possible RAs. The projection points of the **g′** matrix are shown in different colors corresponding to different RAs: red (RA: ± [$01\bar{1}0$] / A), blue (RA: ± [$10\bar{1}0$] / B), yellow (RA: ± [$1\bar{1}00$] / C).

A more complex scenario is found in grain G2 with Euler angles (167.6°, 90.4°, 13.7°) (Figure 2.4). As shown in Figure 2.4(A) and (B), the experimental slip traces are compatible with two possible active slip planes: ($0\bar{1}11$) I pyramidal (number 10) and ($1\bar{2}1\bar{2}$) II pyramidal (number 13). There are 3 possible slip directions in the ($0\bar{1}11$) I pyramidal plane: [$2\bar{1}\bar{1}0$] (<a> dislocation, m = 0.13) with RA [$01\bar{1}2$] (T), [$11\bar{2}3$] (<c + a> dislocation, m = 0.08) with RA [$3\bar{2}\bar{1}\bar{1}$] (U), and [$1\bar{2}1\bar{3}$] (<c + a> dislocation, m = 0.01) with RA [$3\bar{1}21$] (V). However, there is one slip system in the ($1\bar{2}1\bar{2}$) II pyramidal plane: ($1\bar{2}1\bar{2}$) [$1\bar{2}13$] (<c + a> dislocation, m = 0.02) with RA

[10 $\bar{1}$ 0] (B). These four possible slip systems cannot be discriminated using conventional slip trace analysis. In fact, the normal procedure to determine the active slip plane using standard slip trace analysis is to adopt an arbitrary "tolerance" angle to discard the potential slip planes that are not within this tolerance [182,183]. However, the deviation between the experimental and the predicted slip traces for both slip planes are very similar in this case: α = 10.7° for (0$\bar{1}$11) I pyramidal (number 10) and β = 10.8° for (1$\bar{2}$1$\bar{2}$) II pyramidal (number 13) (Figure 2.4(B)).

The experimental projection of the orientation of grain G2 in the pole figure before and after deformation is plotted in Figure 2.4(C) while the predictions for the stretching of the projections corresponding to the four possible RAs are plotted in Figure 2.4(D), (E) and (F). It is evident that the best match between experiments and simulations is found for the RA [10$\bar{1}$0] (B) and, thus, plastic deformation in grain G2 took place along the <c + a> (1$\bar{2}$1$\bar{2}$) [1$\bar{2}$13] pyramidal slip system. The large deviation angle between the orientation of the experimental and calculated slip trace (10.85°) in Figure 2.4(B) should be related to the rotation of grain during the tensile tests [204]. Thus, ST-MLRA allows to find out the correct slip system when the slip traces are slightly misoriented with respect to the theoretical ones due to strain gradients associated with the polycrystalline deformation.

Planar slip in a single slip system was dominant in the examples in Figure 2.3 and Figure 2.4 but double or multiple slip is also a possibility that should be accounted for. For instance, the experimental slip traces in grain G3 (Euler angles = (170.9°, 73°, 0.9°)) are not parallel to one another (Figure 2.5(A)). They are compatible with three possible active slip planes: (0001) basal (number 1), (1$\bar{2}$1$\bar{2}$) II pyramidal (number 13) and ($\bar{1}$2$\bar{1}\bar{2}$) II pyramidal (number 14) (Figure 2.5(B)). There are 3 possible slip directions in the (0001) basal plane: [2$\bar{1}\bar{1}$0] (m = 0.13 with RA [01$\bar{1}$0] (A)), [$\bar{1}$2$\bar{1}$0] (m = 0.01 with RA [10$\bar{1}$0] (B)), and [$\bar{1}\bar{1}$20] (m = 0.13, with RA [1$\bar{1}$00] (C)). However, there is only one slip direction in the (1$\bar{2}$1$\bar{2}$) II pyramidal and ($\bar{1}$2$\bar{1}\bar{2}$) II pyramidal planes: [1$\bar{2}$13] (<c + a>) (m = 0.01, with RA [10$\bar{1}$0] (B)) and [1$\bar{2}\bar{1}\bar{3}$] (<c + a>) (m = 0.01, with RA [10$\bar{1}$0] (B)), respectively. The active slip systems

cannot be discriminated among these 5 possibilities using standard slip trace analysis.

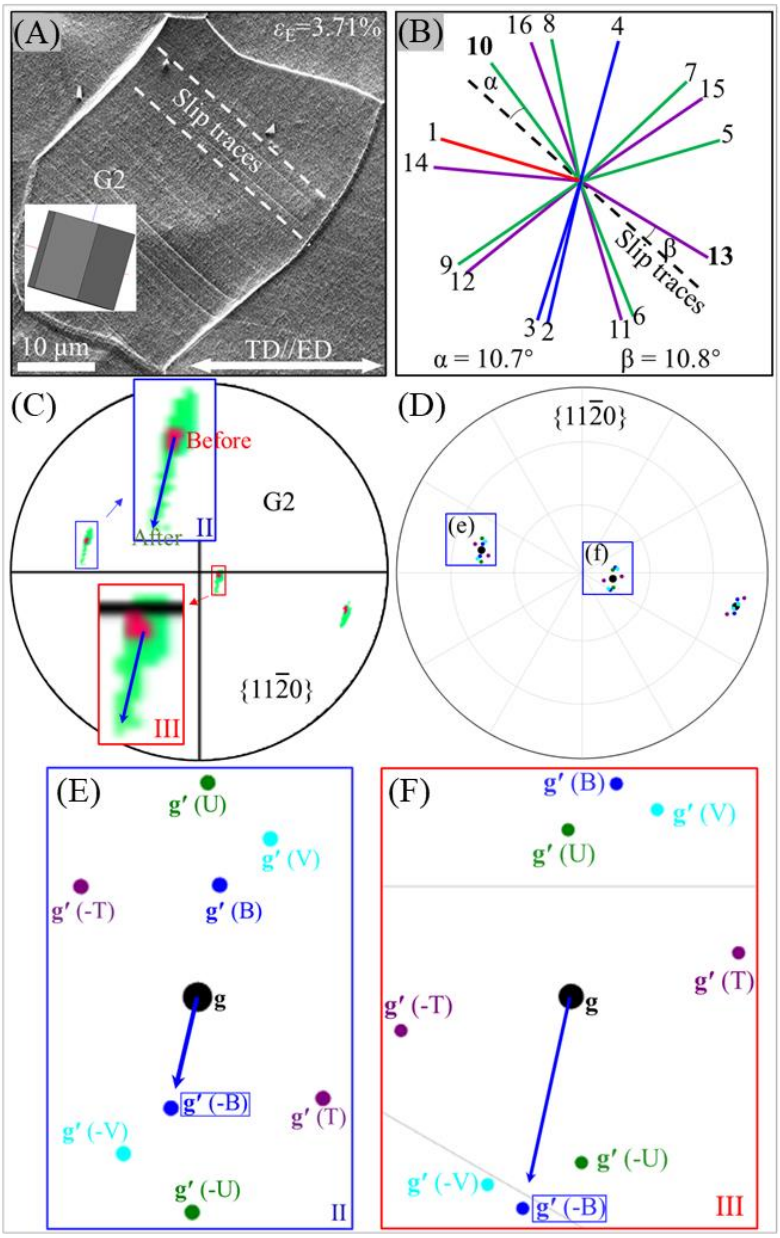

Figure 2.4: (A) Experimental slip traces observed by SEM in G2 of the Mg alloy surface (applied tensile strain 3.7%). (B) Calculated slip traces of different slip planes according to the EBSD information from G2. (C) Experimental {11$\bar{2}$0} pole figure of grain G2 before (red) and after (green) deformation. Note that the {11$\bar{2}$0} rather than the {0001} pole figure was selected because the projection of grain G2 in the {0001} pole figure was too close to the edge. The main stretching directions of the traces of the grain are shown with blue arrows. (D) Simulated projections of grain G2 before (**g**) and after (**g′**) 5° rotation around various axes based on the Euler angles. Enlarged views of regions I and II in Figure 2.4(D) are shown in (E) and (F), respectively. The projection points of the **g′** matrix are shown in different colors corresponding to the different RAs: blue (RA: ± [10$\bar{1}$0] / B), purple (RA: ± [01$\bar{1}$2] / T), green (RA: ± [3$\bar{2}\bar{1}$1] / U), cyan (RA: ± [3$\bar{1}$2$\bar{1}$] / V).

The experimental projection of the orientation of grain G3 in the pole figure before and after deformation is plotted in Figure 2.5(C) while the predictions for the stretching of the projections corresponding to the three possible RAs are plotted in Figure 2.5(D). The best match between the experimental stretching of projections and the simulations is found for the RA $[1\bar{1}00]$ (C) and, thus the main active slip system in G3 is <a> basal (0001) $[\bar{1}\bar{1}20]$ slip system. However, the experimental projection of grain G3 was also stretched in two other directions, which were compatible with the activation of the other two <a> basal slip systems (with RA $[01\bar{1}0]$ (A) or RA $[10\bar{1}0]$ (B)), and/or <c + a> $(1\bar{2}1\bar{2})$ $[1\bar{2}13]$ and $(\bar{1}2\bar{1}\bar{2})$ $[1\bar{2}1\bar{3}]$ II pyramidal slip systems with RA $[10\bar{1}0]$ (B). The intensity of the slip activity in each slip system can be estimated by the rotation angle necessary to move the initial orientation of grain G3 to the final one in the experimental pole figure in each of the three orientations. They lead to 9.2° for the rotation around $[1\bar{1}00]$ (C), 3.8° around $[01\bar{1}0]$ (A) and 5.7° along $[10\bar{1}0]$ (B), which provides an estimation of the relative activity of each slip system.

The precise identification of slip system is very important, for instance, in order to assess the geometrical factors that determine whether slip transfer or blocking occurs at GBs. This information can be used within the framework of crystal plasticity to develop microstructure-based models for polycrystalline deformation [205,206]. Among the different criteria to assess slip transfer at GBs, the geometric compatibility factor or Luster-Morris parameter (m') is one of the most relevant ones [112,207–210]. It is based upon the angles between the slip plane normal directions ψ and the Burgers vector directions κ according to:

$$m' = (\overrightarrow{SP_{in}} \cdot \overrightarrow{SP_{out}}) \cdot (\overrightarrow{SD_{in}} \cdot \overrightarrow{SD_{out}}) = \cos(\psi) \cdot \cos(\kappa) \quad (2.7)$$

where $\overrightarrow{SP_{in}}$, $\overrightarrow{SP_{out}}$, $\overrightarrow{SD_{in}}$, and $\overrightarrow{SD_{out}}$ represents the slip planes normal vectors and slip directions of incoming and outgoing slip systems, respectively (Figure 2.6).

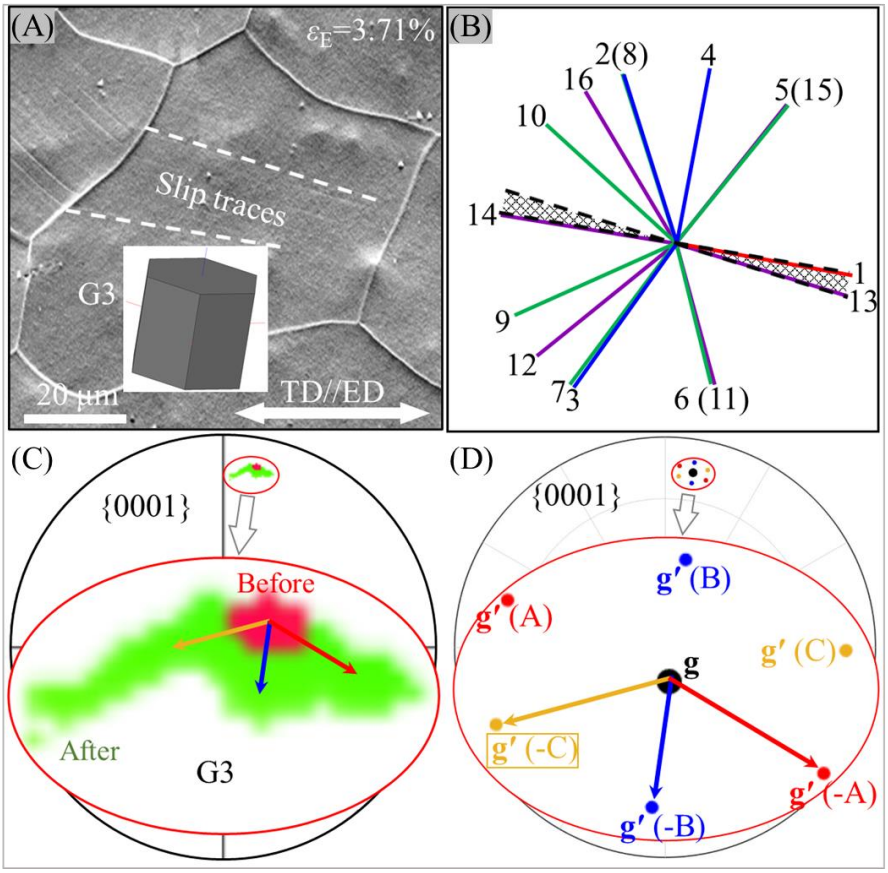

Figure 2.5: (A) Experimental slip traces observed by SEM in grain G3 of the Mg alloys surface (applied tensile strain 3.7%). (B) Calculated slip traces of different slip planes according to the EBSD information from G3. (C) Experimental {0001} pole figure of grain G3 before (red) and after (green) deformation. (D) Simulated projections of grain G3 before (**g**) and after (**g′**) 5° rotation around various axes based on the Euler angles. The projection points of the **g′** matrix are shown in different colors corresponding to the different RAs: red (RA: ± [01$\bar{1}$0] / A), blue (RA: ± [10$\bar{1}$0] / B), yellow (RA: ± [1$\bar{1}$00] / C).

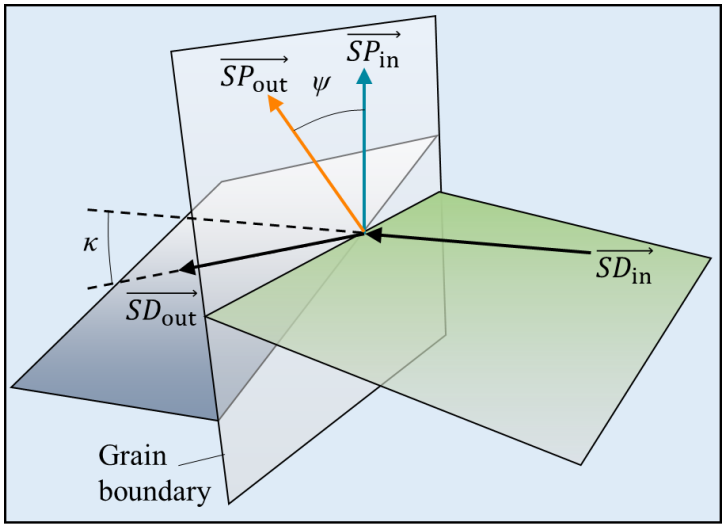

Figure 2.6: Geometrical factors to define the Luster-Morris parameter (m') at a GB.

The SEM micrograph in Figure 2.7 shows slip traces in neighbor grains G2 and G3. The presence of a ledge at the boundary and the lack of correlation between most of the slip traces in both grains indicate that slip transfer did not take place and that both two grains deformed heterogeneously. The active slip system in grain G2 was identified as $(1\bar{2}1\bar{2})$ $[1\bar{2}13]$ with a SF of 0.02 (Figure 2.4). The main active slip system in G3 was identified as (0001) $[\bar{1}\bar{1}20]$ with a SF of 0.13 (Figure 2.5) and the m' parameter corresponding to both slip systems is 0.25 (highlighted in bold in Table 2.3). This low m' value is consistent with the lack of slip transfer at the GB, as indicated by the SEM observations. It should be noted, however, that if all the possible active slip systems -according to standard slip trace analysis- are included in Table 2.3, high values of m' (> 0.80) can be found for several pairs of slip systems (m' = 0.887 for $(1\bar{2}1\bar{2})$ $[1\bar{2}13]$ in grain G2 and $(1\bar{2}1\bar{2})$ $[1\bar{2}13]$ in grain G3 and m' = 0.836 for $(0\bar{1}11)$ $[1\bar{2}1\bar{3}]$ in grain G2 and $(\bar{1}2\bar{1}2)$ $[1\bar{2}1\bar{3}]$ in grain G3) (Table 2.3). Note these pyramidal slip systems are hard to be activated because of the large CRSS and, in addition, their SF is very low (m < 0.02). Thus, it is very likely that pyramidal slip in G2 was activated as a result of the stress concentration at the GB induced by the pile-up of the basal dislocations in G3.

Table 2.3: SFs, m, for slip systems in grains G2 (G2ss) and G3 (G3ss), and geometric compatibility factor m' across the boundary for the different possible active slip systems identified by ST-MLRA. The highlighted slip systems are expected to be dominant in G2 and G3 according to ST-MLRA. The m' value corresponding to the main active slip systems in each grain is highlighted.

m'	G2ss	$(0\bar{1}11)$ $[2\bar{1}\bar{1}0]$ / 10T	$(0\bar{1}11)$ $[11\bar{2}3]$ / 10U	**$(1\bar{2}1\bar{2})$ $[1\bar{2}13]$ / 13B**	$(0\bar{1}11)$ $[1\bar{2}1\bar{3}]$ / 10V
G3ss	m	0.13	0.08	**0.02**	0.01
(0001) $[2\bar{1}\bar{1}0]$ / 1A	0.13	0.177	0.054	0.404	0.076
(0001) $[\bar{1}\bar{1}20]$ / 1C	**0.13**	0.123	0.102	**0.250**	0.012
(0001) $[\bar{1}2\bar{1}0]$ / 1B	0.01	0.054	0.048	0.654	0.088
$(1\bar{2}1\bar{2})$ $[1\bar{2}13]$ / 13B	0.01	0.233	0.259	0.887	0.156
$(\bar{1}2\bar{1}2)$ $[1\bar{2}1\bar{3}]$ / 14B	0.01	0.216	0.677	0.056	0.836

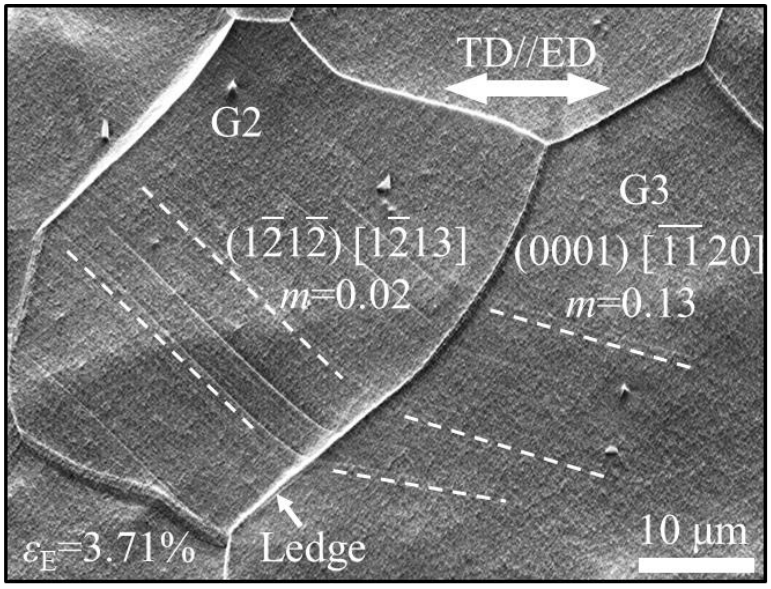

Figure 2.7: Example of slip system identification using ST-MLRA strategy for neighbor grains G2 and G3 in the Mg alloy to determine the geometric computability factor for slip transfer (applied tensile strain 3.7%). The main active slip systems are shown in each grain.

Thus, this strategy allows us to determine the active slip system in each grain during plastic deformation of polycrystalline samples from slip trace analysis and EBSD information. The ST-MLRA strategy is based on the determination of the orientation of the slip traces on the grain surface in combination with the changes in the grain orientation given by the EBSD maps before and after deformation. The slip traces indicate the potential active slip planes while the stretching of the trace of the grain orientation in the pole figure confirms the actual RAs in the potential slip planes. The strategy has been demonstrated in grains of Mg polycrystals subjected to relatively low tensile strains (< 5%) which show single slip or multiple slips but with one dominant slip system. The accuracy may be reduced at high strains because more slip systems are active and more slip traces emerge to surface, e.g. leading to diffuse and/or wavy slip traces. Thus, identification of the actual active slip planes becomes more difficult, and the combinations of the rotations associated with the different slip systems make less obvious the stretching of the trace in the pole figure along well-defined directions.

The strategy can be very easily implemented and provides the precise identification of the active slip system(s) in many cases from simple surface

observations and EBSD inside the SEM. Thus, large data sets with the precise active slip system in each grain can be obtained and this strategy has been used in the Mg alloys studied in this thesis.

It should be noted that ST-MLRA still has certain limitations to distinguish accurately the active slip system, as it is influenced by some factors such as the degree of deformation, sample surface quality, and the number of active slip systems. At higher levels of deformation, the results based on the average orientation of the deformed grain may deviate significantly from those based on the initial grain orientation. Additionally, ST-MLRA only considers cases where a single slip system dominates within a single grain, and it cannot precisely distinguish active slip systems when multiple slip systems are active within the same grain. However, compared to traditional slip trace analysis, ST-MLRA can still provide a more accurate identification of active slip systems by incorporating the grain orientation information.

2.5.3. Grain reference orientation deviation (GROD)

GROD is an EBSD-based characterization technique that uses the orientation deviation of any point within a grain relative to a reference orientation (e.g., the average grain orientation) [211]. The orientation deviation is expressed in terms of a RA and a rotation angle. The EBSD projection of the RA can be dividedly expressed with respect to the sample coordinate system or to the crystal coordinate system. In the crystal coordinate system, the comparison between the experimental RA, calculated based on the intragranular grain orientation, and the theoretical RA corresponding to various slip systems (Table 2.2) allows the identification of active slip systems.

Similar to the modified lattice rotation analysis, any method that infers the active slip system from the rotation of the crystal inevitably has to account for the possibility of different slip systems with the same RA. For Mg alloys, this issue primarily concerns the <a> basal slip and the <c + a> II pyramidal slip, both of which share the same RA (i.e., $<01\bar{1}0>$). Thus, a specific analysis is required for all HCP metals to assess the activity of <c + a> II pyramidal slip using the CRSS.

For the GROD analysis, the rotation matrix of $\boldsymbol{GROD_{x,y}}$ between the $\boldsymbol{o_{x,y}}$ orientation at position (x,y) and $\boldsymbol{o_g}$ (reference orientation) can be calculated as:

$$\boldsymbol{GROD_{x,y}} = \mathrm{inv}(\boldsymbol{o_g}) \bullet \boldsymbol{o_{x,y}} \tag{2.8}$$

where inv($\boldsymbol{o_g}$) stands for the inverse of $\boldsymbol{o_g}$ [50,211]. Note that both $\boldsymbol{o_g}$ and $\boldsymbol{o_{x,y}}$ are the rotation matrices expressed in the sample coordinate system, which could be calculated from the Euler angles [212].

Using the rotm2axang function in MATLAB, the rotation matrix ($\boldsymbol{GROD_{x,y}}$) can be transformed into a combination of the RA and rotation angle, i.e., GROD axis ($\overrightarrow{GROD\_axis}$, unit vector) and GROD angle (*GROD_angle*, scalar). $\overrightarrow{GROD\_axis}$ can be projected simultaneously in both the crystal and sample coordinate systems. The former allows for the experimental intragranular grain RA to be linked to the theoretical slip system RA, while the latter helps compare lattice rotation behavior among multiple grains.

The initial orientation of the grain before deformation is used as the reference orientation, and the $\overrightarrow{GROD\_axis}$ and *GROD_angle* are combined (the rotation angle multiplied by the projection of the RA onto the axes in sample coordinate system) to provide the grain rotation evolution around the sample coordinate axes. The in-plane lattice rotation (ϑ_i, angle, around the sample coordinate axis i (either X, Y or Z)) derived from EBSD can be calculated from:

$$\vartheta_i = GROD\_angle * (\overrightarrow{GROD\_axis} \cdot \overrightarrow{A_i}) \tag{2.9}$$

where $\overrightarrow{A_i}$ (i can be unit vectors in the X, Y, Z directions) represents the main axes in sample coordinate system.

Compared to ST-MLRA, GROD allows for a quick and rough evaluation of active slip systems in many grains, reducing significantly the experimental effort. Therefore, GROD is used in this thesis as an additional technique to ST-MLRA to analyze the active slip systems in wrought Mg alloys.

2.6. Machine learning (ML)

ML strategies (and, in particular, Bayesian inference) have been used in this thesis to establish the relationship between microstructural features and twin nucleation in two different textured Mg alloys. To this end, the microstructural

features and the nucleation of twins were ascertained by means of 2D EBSD in more than 3000 grains, including 28 relevant parameters for each grain, categorized in four different groups (loading condition, grain shape, global SFs, and GB features). The information provided by 2D EBSD does not take into account the nucleation of twins nor the microstructure beneath the surface layer and this may induce some errors. However, the construction of a large dataset of 3D EBSD (as the one necessary for ML) [213] is an extremely challenging task and, thus, only 2D EBSD was used in this thesis. The information was used to train supervised ML classification models to analyze twinning. The combination of a large experimental dataset and the potential of ML tools allowed us to determine the most important microstructural features promoting twin nucleation. This thesis, therefore, provides results on the influence of the microstructural features on the nucleation of ETs in Mg alloys. This information can help to design polycrystal microstructures with controlled twinning during deformation.

2.6.1. ML Methods

The performance of several ML classification methods was tested in order to select the best method to predict twin nucleation, including nearest neighbors, logistic regression, support vector machines, decision trees, Gaussian processes, neural networks, random forests, extremely randomized trees, Adaboost, gradient boosting (GDB), naïve Bayes, local discriminant analysis, and Bayesian networks (BNs). All of them were used as implemented in the scikit-learn Python package [214], except from the BN models that were constructed as implemented in the pyAgrum Python package [215]. However, only those methods that performed the best are described here. Such methods are Adaboost [216], GDB [217], random forest [218], naïve Bayes [219], and BNs [220].

The first three methods (Adaboost, GDB, and random forest) are part of a family of methods known as ensemble methods. Ensemble methods combine the predictions of different base estimators built with a given algorithm (e.g., a decision tree) with the goal of providing a more robust / more general model over the one provided by a single estimator. The difference between different ensemble

methods relies on the strategy followed in order to combine the predictions of all base estimators. In general, these methods either take the average of the predictions of all estimators (averaging methods) or build the base estimators sequentially in order to reduce the bias of the combined estimator, for instance, by applying weights depending on how difficult is to correctly predict a given sample (boosting methods). The remaining two methods (Gaussian naïve Bayes and BNs) are based on Bayesian statistics. The main pillar of Bayesian statistics is Bayes' theorem:

$$P(y|x_1, \dots, x_n) = \frac{P(y)P(x_1, \dots, x_n|y)}{P(x_1, \dots, x_n)} \tag{2.10}$$

where y is the class (target) variable and vector x_1 through x_n correspond to the vector of features. $P(y)$ is known as the prior probability of the target variable y, which expresses the probability of having a given value of y before evidence is considered. $P(x_1, \dots, x_n\,|y)$ is the likelihood function that contains the probability of having $x_1, \dots, x_n$ given that y is true. $P(y|x_1, \dots, x_n)$ is the posterior probability, the probability of having y after taking the evidence $x_1, \dots, x_n$ into account. Finally, $P(x_1, \dots, x_n)$ is the probability of the evidence. The objective of Bayes-based classifiers is to find the class that has the maximum posterior probability:

$$\hat{y} = \arg\max_{y} P(y|x_1, \dots, x_n) \tag{2.11}$$

The difference between different Bayes-based models depends on the adopted assumptions on probability distributions. For instance, naïve Bayes methods assume a 'naïve' conditional independence between every pair of features given the value of the class variable:

$$P(x_1, \dots, x_n|\, y) = \prod_{i=1}^{n} P(x_i|y) \tag{2.12}$$

In the case of the Gaussian naïve Bayes method used in this thesis, the likelihood of the features is assumed to be Gaussian:

$$P(x_i|\, y) = \frac{1}{\sqrt{2\pi\sigma_y^2}} e^{-\frac{(x_i-\mu_y)^2}{2\sigma_y^2}} \tag{2.13}$$

where σ_y^2 and μ_y are the variance and mean of the continuous variable x_i computed by a maximum likelihood estimation for a given class y.

On the other hand, BNs assume conditional independence in the joint distribution following the Markov condition (i.e., every node in a BN is conditionally independent of its non-descendants, given its parents):

$$P(y,x_1, \ldots, x_n) = P\left(y\middle|\text{Parents}(y)\right) \prod_i^n P\left(x_i\middle|\text{Parents}(x_i)\right) \quad (2.14)$$

where the class (target) variable y also forms part of the BN.

2.6.2. Preprocessing of ML Models

Before constructing any ML model, two preprocessing steps were carried out: i) feature scaling and ii) removal of highly correlated features. Feature scaling is important to avoid biases towards features having values with big magnitudes. For instance, an ML model could consider angles to be more important than twinning SFs solely because the former can be as large as 90º, while the latter cannot exceed a value of 0.5. The feature scaling procedure that we followed was a *MinMax* scaling setting all features in a range between 0 and 1. For a given feature vector $\vec{\boldsymbol{X}}$ and a sample i, the scaled value was obtained by:

$$X_i^{scaled} = \frac{X_i - min(\vec{\boldsymbol{X}})}{max(\vec{\boldsymbol{X}}) - min(\vec{\boldsymbol{X}})} \quad (2.15)$$

To assess the correlation between features we computed Pearson coefficients (r) for every pair of features in our dataset. Such coefficients were calculated with:

$$r = \frac{\sum(\vec{\boldsymbol{x}} - m_x)(\vec{\boldsymbol{y}} - m_y)}{\sqrt{\sum(\vec{\boldsymbol{x}} - m_x)^2 \sum(\vec{\boldsymbol{y}} - m_y)^2}} \quad (2.16)$$

in which $\vec{\boldsymbol{x}}$ and $\vec{\boldsymbol{y}}$ are the feature vectors whose correlation is being calculated, and m_x and m_y are the mean of vectors $\vec{\boldsymbol{x}}$ and $\vec{\boldsymbol{y}}$, respectively. We removed one feature of all pairs whose absolute value of Pearson coefficient was above 0.95. Specifically, the features that we removed with this procedure were *Neighbor_grain_n* (neighbor grain numbers), *T_SF2*, *T_SF4*, and *T_SF6* (correlated with *Triple_points* (triple point numbers), *T_SF1*, *T_SF3*, and *T_SF5*, respectively).

2.6.3. Performance of ML Models

The accuracy of our ML models was assessed by the Area Under the Receiver Operating Characteristic Curve (ROC AUC) score [221–223]. The ROC curve is created by plotting the rate of true positive predictions against the false positive ones at various threshold settings (i.e., the threshold used to decide whether a prediction is positive or negative in a binary classification task). It has advantages over other evaluation measures since it decouples classifier performance from class skew and error costs. However, a ROC curve is a two-dimensional depiction of classifier performance and, as such, it does not provide a single scalar value to compare easily the expected performance of different classifiers. Hence, a common method to solve this issue is to calculate the AUC of the ROC curve. Since the AUC is always a portion within the area of the unit square defined by the rate of true positive and false positive predictions, its value will always be between 0 and 1. However, no realistic classifier will present a ROC AUC below 0.5 because this is a result random guessing would produce. The AUC performs very well and is often used when a general measure of predictiveness is desired [223].

2.6.4. Model selection

The final step in the ML model pipeline was the model selection. The objective at this step was to select the best performing model out of several models trained using both different hyperparameters as well as different training/test sets. The procedure to achieve this is cross-validation (CV). In general terms, CV is a resampling method that uses different portions of the data to train and test a model on different iterations. Among the different CV approaches, the stratified 10-fold CV was used because it ensures that each portion of the dataset approximately contains the same percentage of samples of each target class in the complete dataset. Here, 10-fold means that the dataset was split into 10 subsets and repeated the training and testing 10 times. At each of these iterations, 9 subsets were used for training and the remaining one for testing. Formally, the stratified 10-fold CV was not used directly to select a model, but for assessing the

performance of different models as the average of all CV tasks. This allowed to avoid overfitting.

In addition to stratified CV, the robustness of our BN models was ensured by implementing a grid search CV procedure for selecting the best hyperparameters. The main idea behind grid search techniques is to find the optimal parameters that are not learnt from data by training models with different combinations taken from a grid of parameter values. The best model was the one that achieved the highest CV score (we used again as CV procedure a stratified 10-fold CV). Specifically, we optimized the number of discretization bins ('discretizationNbBins'), the discretization strategy ('discretizationStrategy'), the learning method ('learningMethod'), and whether to use or not the threshold of precision-recall curves to make predictions ('UsePR'). All other hyperparameters were kept with default values since initial tests showed that they remain unchanged after the grid search. The reader is referred to PyAgrum's documentation for an explanation of all hyperparameters for training a BN model [215].

3. Deformation mechanisms of an as-extruded Mg-6.5Zn alloy with a dual-texture

3.1. Introduction

Mg alloys have emerged as competitive alternatives for structural components because of the growing demand for materials with high strength-to-weight ratio in transportation. Nonetheless, one important limitation to manufacture Mg components is the large tension-compression yield asymmetry of textured Mg alloys, which leads to early fracture during deformation [224]. This behavior can be fundamentally ascribed to the different deformation mechanisms activated during tension and compression due to the strong texture that appears as a result of thermomechanical processing and to the polar nature of $\{10\bar{1}2\}$ ET [225,226].

Thus, strategies to reduce the yield asymmetry of wrought Mg alloys are relevant and they have received significant attention in recent decades. They can be summarized in (i) suppression of nucleation and growth of ETs by increasing the ratio of the CRSS for ET with respect to <c + a> pyramidal slip and/or <a> prismatic slip through the presence of solute atoms [132,158,227–230], and introducing precipitates [147,158,231–234], and reduction of the grain size [15,16]; (ii) weakening the texture through the addition of RE elements or adopting multi-step thermomechanical processes [4,13,17–21]. A typical case of the former is the study of Stanford et al. [145], who reported that the CYS to the TYS ratio of AZ91 Mg alloy increased from 0.75 in the solid solution condition to 0.91 in the aged one. The reduction in yield asymmetry was attributed to the strong interaction of precipitates with ETs -that limited the amount of twining- while it did not affect <a> prismatic slip. It should be noted, however, that the effect of precipitates on the yield asymmetry depends on the shape and habit plane of precipitates. For instance, Robson et al. [241] reported an increase in the yield asymmetry of a Mg-Zn binary alloy as a result of precipitation. Alloying, especially with RE, is also a common and feasible avenue to attenuate the yield asymmetry of Mg alloys [132,227–230,233,242]. The underlying mechanism is associated with a weakened

basal texture and a reduction in the ratio of the CRSS for non-basal slip with respect to the CRSS for ET [187,227,228,243–246]. For instance, 1 wt.% addition of Nd to extruded Mg-1Mn (wt.%) alloy can lead to near equivalent CRSS values for all deformation modes, thus bringing an isotropic yielding behavior [227]. Nevertheless, the high cost and environmental toxicity of RE have limited to some extent their use as alloying elements in Mg alloys [247]. In addition, thermomechanical processes that lead to a bimodal microstructure are also recognized as a promising strategy to weaken the yield asymmetry of Mg alloys [248–252]. For example, a Mg-Gd-Y-Zr alloy including fine grains due to dynamic recrystallization and coarse grains exhibits a limited yield asymmetry (CYS / TYS ratio: ~1.0) because the same deformation mechanisms (<a> prismatic and <a> basal slips) governed tensile and compressive yielding [249].

The strategies to reduce the yield asymmetry enumerated above were focused on the inhibition of the nucleation and growth of ETs. However, they did not consider another possibility based on the activation of the same amount of ET in both tension and compression. Recently, a novel Mg-6.5Zn (wt.%) alloy with a bimodal texture was prepared and reported by Wang et al. [253], who analyzed the origin of the apparition of the unusual texture with the crystallographic $\vec{c}$ axis parallel to the ED. This $\vec{c}$ axis texture was associated with high extrusion ratio and large applied force. Note that similar texture was also found in extruded Mg alloys containing RE, especially after two-stage extrusion [254–257]. In addition, the effect of precipitation on the CRSS for ET and CT was investigated [258].

It is reported in this chapter that the yield asymmetry of the dual-textured Mg-6.5Zn alloy is only 0.90. The deformation mechanisms in tension and compression are analyzed in detail by means of EBSD on samples of this Mg-6.5Zn (wt.%) alloy with a dual texture deformed up to different strains. Both GROD [211] and ST-MLRA [203] were used to quantify the contributions to deformation of $\{10\bar{1}2\}$ $<10\bar{1}1>$ ET, $\{10\bar{1}1\}$ $<10\bar{1}2>$ CT, <a> basal slip, <a> prismatic slip, <a> pyramidal slip, <c + a> I pyramidal slip and <c + a> II pyramidal slip. GROD provides full-field statistics about slip-induced lattice rotation of all grains from the EBSD maps, while ST-MLRA - in combination with the slip trace orientation

on the sample surface - provides an unambiguous determination of the actual active slip system [203]. These results provide guidance to design dual-textured Mg alloys with limited yield asymmetry.

3.2. Experimental methods

Mg-6.5Zn (wt.%) alloy samples for compressive and tensile tests were first cut into cylindrical (height: 8.5 mm, diameter: 5.5 mm) and dog-bone (gage length: 6 mm, width: 2 mm, thickness: 1 mm) shapes, respectively, by electro-discharge machining. The surface of samples was mechanically ground using SiC paper (up to 2000 grit), followed by polishing with 1 μm and 0.05 μm diamond slurries, and a suspension containing oxide particles of 40 nm. It was finally slightly etched using 5% Nital solution (a mixture of nitric acid and ethanol) for ≈10 seconds.

The tensile sample surface was analyzed before and after deformation using a SEM (Apreo 2S LoVac, FEI Company, Portland, OR, USA; beam current: 2.7 nA, accelerating voltage: 20 kV, mode: SEs) equipped with EBSD (Oxford HKL Channel 5, Oxford Instruments, Abingdon, UK; step size: ~0.3 μm, working distance: 10 mm). A flat surface was introduced in the lateral section of the compression sample, near the center cylindrical specimen, to analyze the microstructure by EBSD in a field-emission LEO 1530 SEM (equipped with HKL Technology Flamenco data collection software; accelerating voltage: 20 kV, step size: ~0.3 μm, working distance: 10-12 mm). The step size of EBSD observation of initial microstructure is 0.7 μm.

The mechanical tests in compression were performed in an Instron 5567 universal testing machine equipped with a high-resolution video extensometer at a strain rate of 1×10^{-3} s^{-1}. The tests were interrupted at -1.5% and -7.3% plastic strains to analyze the microstructure by EBSD. The tensile tests were carried out in micromechanical testing machine (Kammrath and Weiss Technologies, Inc., Model MZ.Sb) under displacement control at 1 μm / s, which leads to an approximate strain rate of 0.2×10^{-3} s^{-1}. The tensile tests were interrupted at different plastic strains of +1.0%, +2.5%, +7.3%, and +13.3% and the deformation mechanisms were analyzed by EBSD in a region of 162×188 μm^2 in the gage

length. All the plastic strains were measured by subtracting the elastic strains from the total true strains, based on the true stress-true strain curves. The nomenclature of the samples herein is the following: T and C denote tension and compression deformation, respectively, and they are followed by the plastic strain level (e.g., "T+13.3" stands for "tensile specimen deformed up to 13.3%"). Additional EBSD data were obtained from an area of 803 × 806 um^2 in the sample T+13.3 and from an area of 604 × 817 um^2 in sample T+18.6 (fracture point in tension). The EBSD areas of samples C-1.5 and C-7.3 were 647 × 506 and 540 × 420 μm^2, respectively. The area selected for EBSD observation in sample T+18.6 was 0.5 mm below the fractured surface, while the remaining EBSD observations were carried out at the center of the sample.

The EBSD data were analyzed and plotted using in-house codes based on MTEX (version 5.7.0), an open-source MATLAB toolbox [200,259]. Some DTs were detected after tension and compression. DTs are formed by the nucleation of a secondary ET within the primary CT, suggesting that the activation of DTs is accompanied by CT. Therefore, after identifying the DT variants, the corresponding CTs were collected into CT dataset. Taking into account that the most prevalent twin variant of DTs exhibits a rotation angle of 37.55° and a RA of $<11\bar{2}0>$ [260], only DTs of this type were analyzed. Furthermore, the initial CTs of these DTs were included in the statistics of CT. Moreover, some CTs and DTs could not be identified by EBSD due to their small thickness in comparison with the step size. They were accurately identified using the point-counting method based on the band contrast (BC) EBSD maps [261].

The GROD calculation equation was presented in eq. (2.8), and the GROD misorientation axes were displayed with respect to the crystal coordinates to associate the slip RAs with the GROD maps. The slip behavior of the sample T+7.3 was also analyzed using ST-MLRA from both the slip traces (that indicate the SP) and the major RA in that grain. The detailed procedure of ST-MLRA is described in chapter 2.

3.3. Results and discussion

3.3.1. Initial microstructure

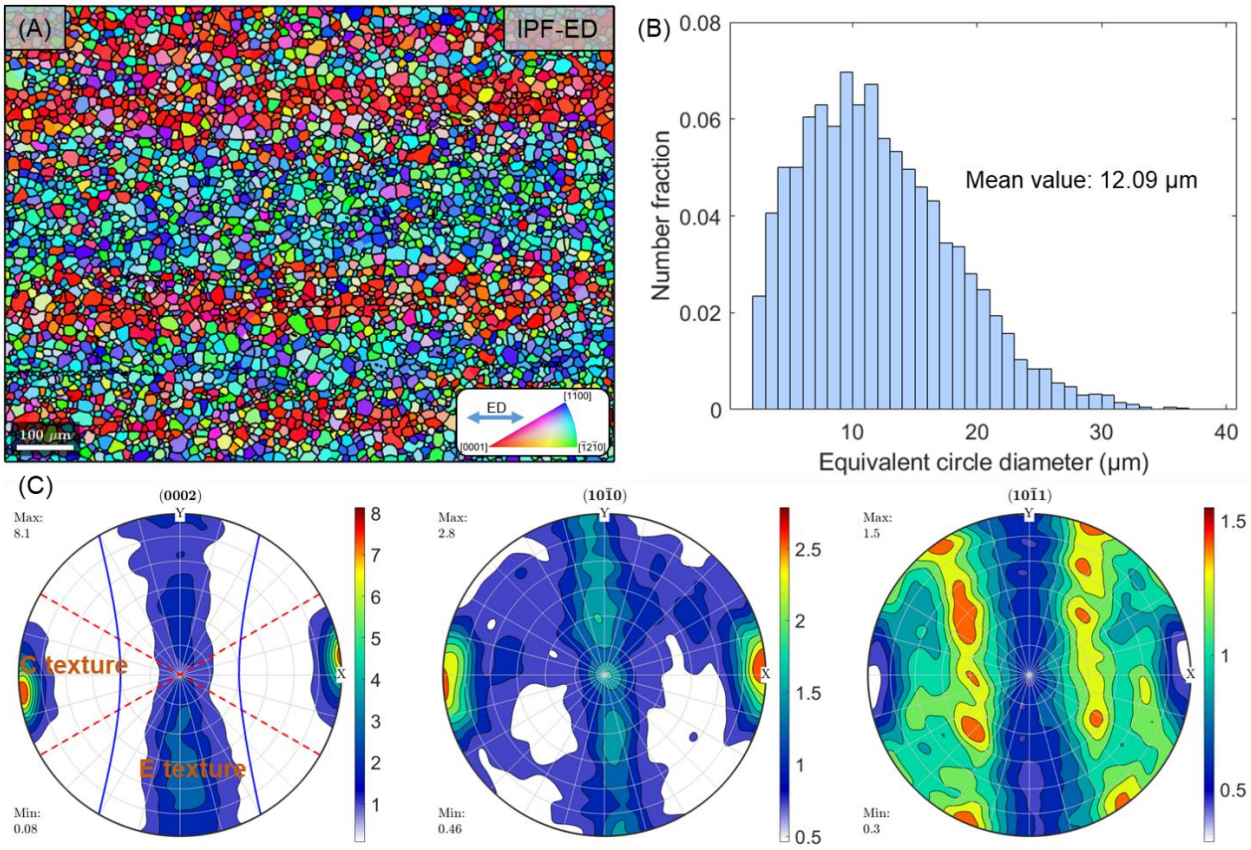

Figure 3.1: Microstructure of Mg-6.5Zn alloy before deformation. (A) EBSD orientation map colored according to IPF with respect to the ED. All GBs were overlaid in black. (B) Grain size distribution histogram and (C) {0002}, {10$\bar{1}$0}, and {10$\bar{1}$1} pole figures.

The initial microstructure of Mg-6.5Zn alloy before deformation is depicted in Figure 3.1 along the ED. The grains in red (Figure 3.1(A)) have the C texture with the $\vec{c}$ axis parallel to the ED according to the IPF. On the contrary, E-textured grains appear in blue and green (Figure 3.1(A)) and their $\vec{c}$ axis is perpendicular to the ED. Grains with different orientations are clustered along bands parallel to the ED. Accordingly, the {0001} pole figure is split into two regions corresponding to the C texture (~20%) and E texture (~80%), respectively, which exhibit a maximum deviation angle of 30° (red dashed and blue curved lines in Figure 3.1(C)). The maximum intensity of {10$\bar{1}$0} and {10$\bar{1}$1} pole figures is only 2.8 and 1.5, respectively, while the maximum intensity of {0001} pole figure is 8.1,

revealing the dual texture of the Mg-6.5Zn alloy. The grain size distribution is plotted in Figure 3.1(B) and the average grain size was 12.1 ± 6.1 μm. The average grain sizes of the grains belonging to the C texture and to the E texture were 12.9 ± 6.6 μm and 12.0 ± 5.9 μm, respectively.

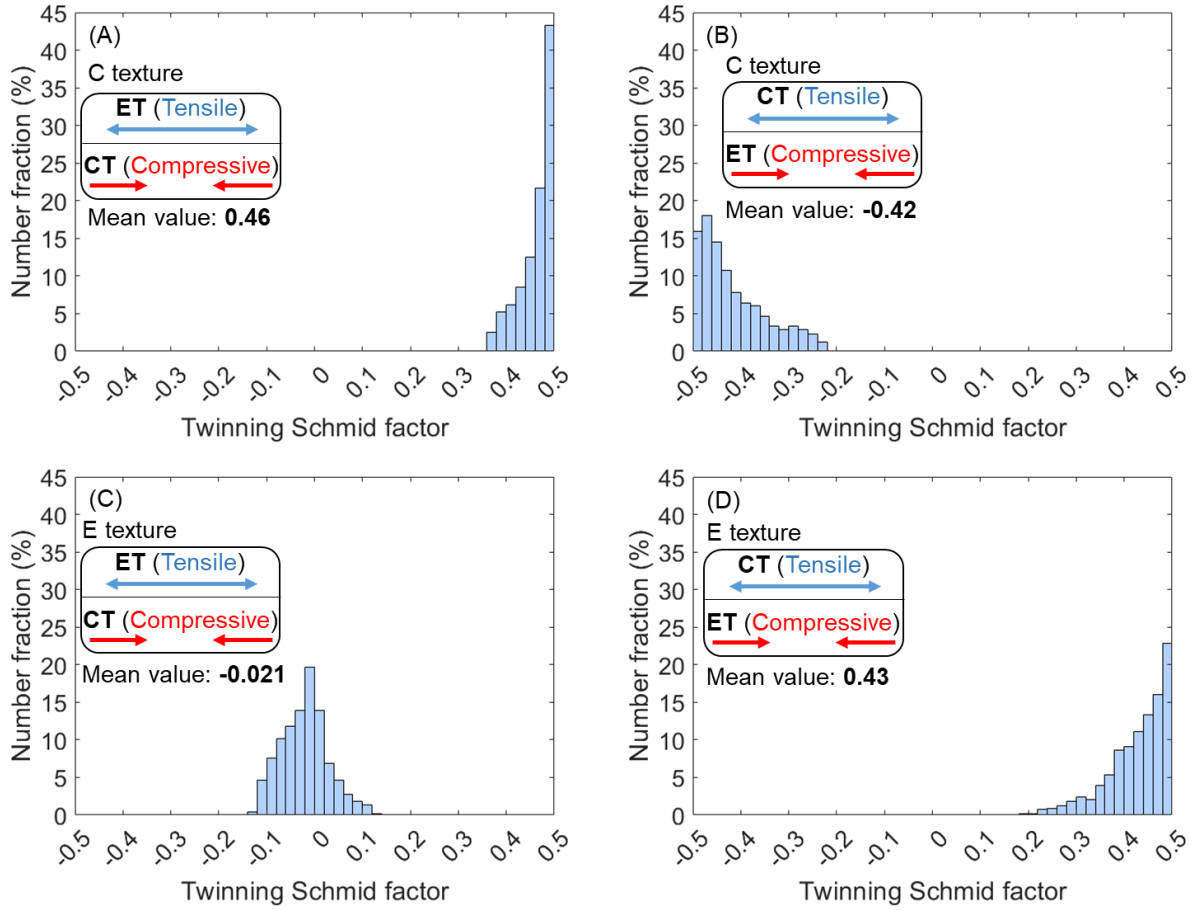

Figure 3.2: Frequency histograms of SFs for (A) ET under tension and CT under compression in C-textured grains, (B) CT under tension and ET under compression in C-textured grains, (C) ET under tension and CT under compression in E-textured grains, and (D) in E-textured grains, CT under tension and ET under compression along the ED.

Based on the average orientations of grains before deformation, the SFs of CTs and ETs for both C-textured and E-textured grains were calculated under tensile and compressive deformation along the ED and are plotted in Figure 3.2 [123]. Under tension, the C-textured grains will undergo tensile deformation along the $\vec{c}$ axis, facilitating the activation of ETs. Conversely, the E-textured grains will be subjected to compressive deformation along the $\vec{c}$ axis and the SFs for CT will be high and positive. Obviously, the SF of ET under tensile deformation is identical to that of CT under compression along the same orientation. Therefore, under

compression, C-textured grains exhibit high SFs for CT and E-textured grains are suitably oriented to nucleate ETs. These results indicate that whether tension or compression is applied along ED, there is always one population of grains with a high probability to activate ETs and another with a high probability to activate CTs according to the SF distribution.

3.3.2. Mechanical behavior

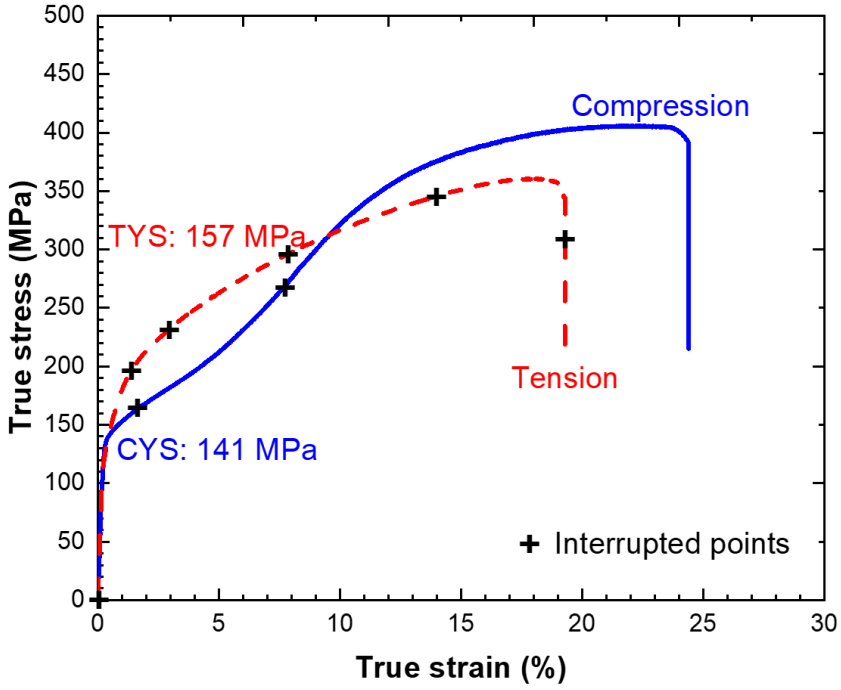

Figure 3.3: True stress-true strain curves of Mg-6.5Zn alloy in tension and compression along the ED.

The true stress-true strain curves in tension and compression of the dual-textured Mg-6.5Zn alloy are plotted in Figure 3.3 along the ED. The sigmoidal shape during compression reveals that twinning may dominate the deformation [10] while the tensile stress-strain curve exhibits a parabolic shape, suggesting that other deformation mechanisms are dominant [10,262]. Despite these differences, the 0.2% offset yield strengths in tension (TYS = 141 MPa) and compression (CYS = 157 MPa) are very close. Compared to other Mg-Zn binary alloys (Table 3.1), the Mg-6.5Zn alloy with dual texture presents the highest TCA = CYS / TYS = 0.90. It should be noted that some cast Mg-Zn alloys also show high CYS / TYS ratios owing to their random texture. However, their CYS, TYS, and

ultimate strength (< 180 MPa) are very low in comparison with wrought alloys [242,263].

Table 3.1: Composition, condition, average grain size (d), CYS, TYS, and the TCA = CYS / TYS of different Mg-Zn binary alloys [155,242,263,264] as well as from this investigation. The atomic fractions in [263] were converted into mass fractions based on the relative atomic masses of Mg and Zn, 24.31 and 65.38, respectively. Moreover, the CYS and TYS in [263] were determined as 0.2% offset yield strength from the true stress-true strain curves.

Alloy (wt.%)	Condition	d (μm)	CYS (MPa)	TYS (MPa)	TCA
Mg-6.5Zn (This thesis)	As-extruded	12	141	157	0.90
Mg-1.9Zn [264]	As-extruded	~20	80	125	0.64
Mg-4.5Zn [264]	As-extruded	~20	88	131	0.67
	Extrusion + Peak-aged		146	232	0.63
Mg-5Zn [155]	As-extruded	~30	88	153	0.58
	Extrusion + Aged (10 h × 250°C)		98	154	0.64
	Extrusion + Aged (18 h × 200°C)		116	230	0.50
	Extrusion + Aged (8 days × 150°C)		176	282	0.62
	Extrusion + Aged (32 days × 110°C)		150	305	0.49
Mg-2.15Zn [242]	Cast in sand mold	300	30	37	0.81
Mg-1.07Zn [263]	Cast in sand mold	60	55	69	0.80
Mg-2.12Zn [263]	Cast in sand mold	65	69	78	0.88
Mg-5.95Zn [263]	Cast in sand mold	500	31	38	0.82
		344	31	43	0.72
		81	74	88	0.84
	Cast in permanent mold	48	99	116	0.85

3.3.3. Deformation mechanisms

The evolution of twins as well as grain orientation gradients associated with dislocation slip were characterized by EBSD at different strains indicated in Figure 3.3. The EBSD maps, showing the grain orientation according to the IPF-ED and the BC maps of the sample after compression along ED up to -1.5% and -7.3%, are plotted in Figure 3.4. Many grains with E texture (green and blue in Figure 3.1) changed to red in the C-1.5 condition (Figure 3.4(A)), suggesting that ET makes a major contribution to the onset of plastic deformation in compression, in agreement with the sigmoidal shape of the stress-strain curve. As compressive

strain increases to ~7.3%, most grains of the IPF map are colored in red (Figure 3.4(C)), owing to the re-orientation associated with ET (86.3°) of the grains with E texture [112]. Moreover, secondary twin and DT boundaries are clearly distinguished in Figure 3.4(D). The appearance of distinctive DTs implies that CTs have been activated after yielding in compression.

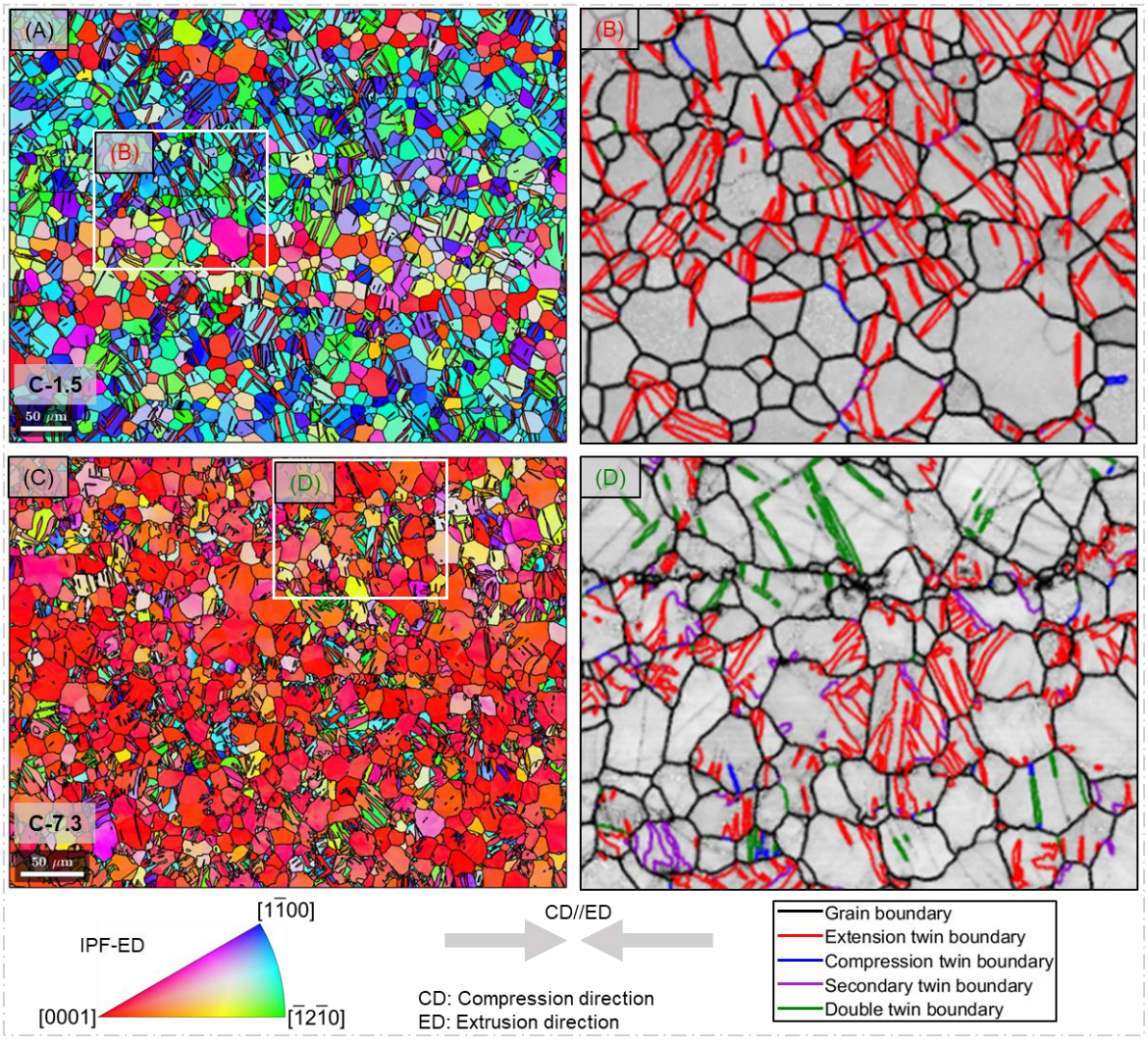

Figure 3.4: (A, C) IPF maps and (B, D) BC maps of the Mg-6.5Zn alloy after compression up to (A, B) 1.5% and (C, D) 7.3%. The reference direction of IPF was ED, and all GBs were overlaid in black. ET, CT, secondary, and DT boundaries were highlighted in red, blue, purple, and green, respectively, in the BC maps. Note that their identification was performed by measuring the RA - misorientation angle of every boundary. The RA & angle pairs for ET, CT, secondary twin and DT are <2$\bar{1}\bar{1}$0> & 86.3°, <2$\bar{1}\bar{1}$0> & 56.15°, <1$\bar{1}$00> & 60°, and <2$\bar{1}\bar{1}$0> & 37.5°, respectively. The threshold misorientation angle was 5°. Other GBs were overlaid in black in the BC maps.

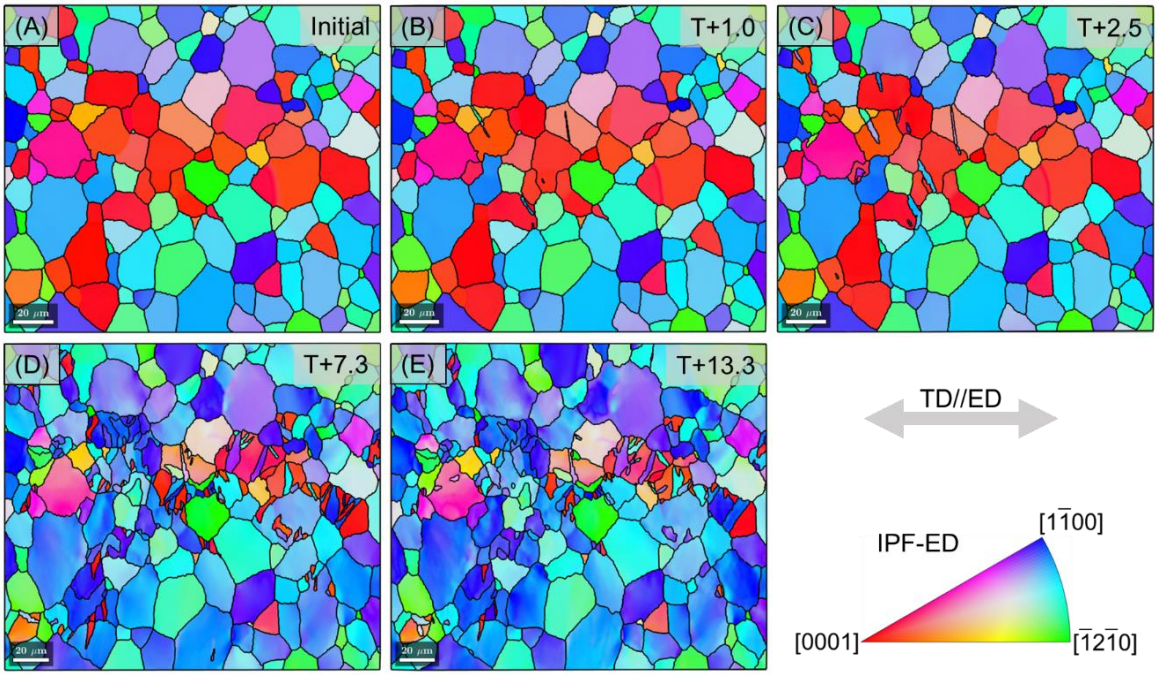

Figure 3.5: EBSD maps showing the grain orientation according to the IPF for the Mg-6.5Zn alloy deformed in tension along the ED up to (A) 0, (B) 1.0%, (C) 2.5%, (D) 7.3%, and (E) 13.3%.

The EBSD maps showing the grain orientation according to the IPF-ED and the BC maps of the sample deformed in tension along ED up to 1.0%, 2.5%, 7.3%, and 13.3% are plotted in Figure 3.5 and Figure 3.6, respectively, together with the initial microstructure. As the tensile strain increases, the grains colored in red of Figure 3.5(A), belonging to the C texture, are gradually occupied with ETs colored in green and blue, as shown by the ET boundaries in Figure 3.6. Thus, ET dominates the deformation in C-textured grains in tension and only one CT and one DT are distinguished by EBSD in Figure 3.6(D) and Figure 3.6(E). To provide more accurate statistical information, a larger area of the T+13.3 sample was analyzed by EBSD. 251 CT and DT were found in 3196 E-textured grains (7.85%), which is significantly lower than that reported in the sample deformed in compression up to 7.3, 633 CT and DT in 244 C-textured grains (259%) [258]. Although the strain applied to the sample T+13.3 is nearly twofold than that of sample C-7.3 and both samples display high SFs for CT, activation of CT is very limited during tension. This negligible activity of CT and DT in the sample deformed in tension is surprising taking into account that these mechanisms were found in the C-7.3 sample. The reasons for this behavior are analyzed below.

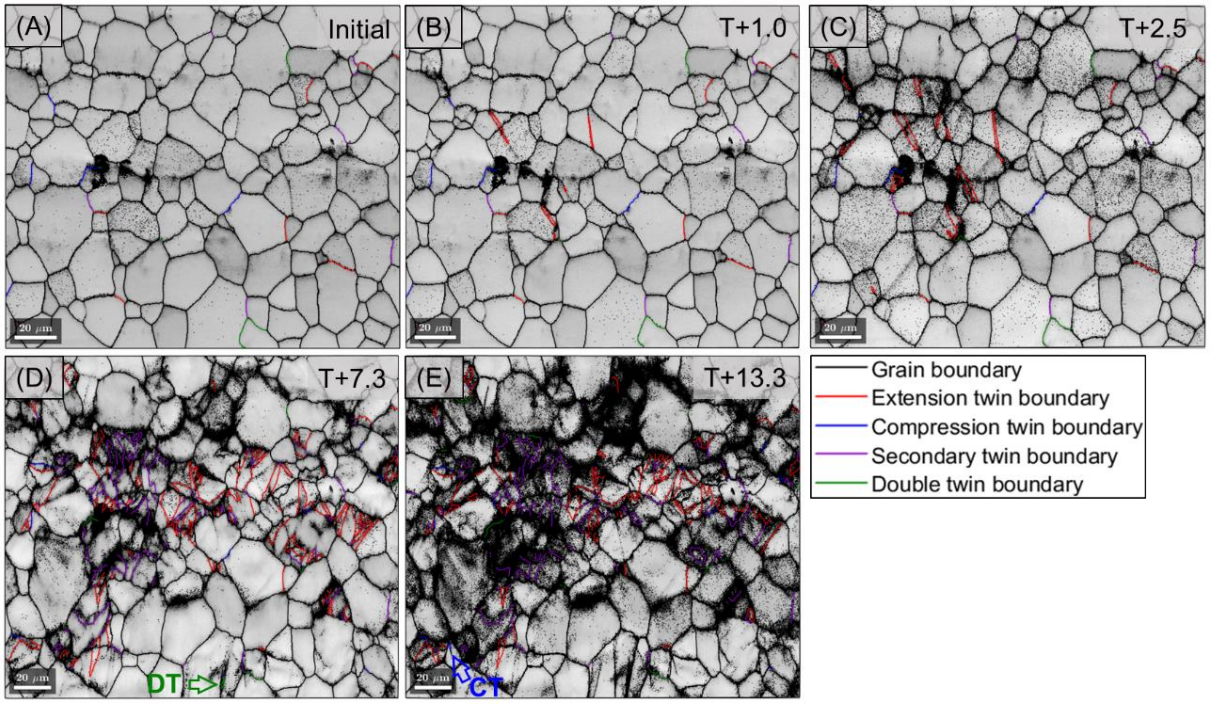

Figure 3.6: BC maps for the Mg-6.5Zn alloy deformed in tension along the ED up to (A) 0, (B) 1.0%, (C) 2.5%, (D) 7.3%, and (E) 13.3%. The overlaid grain and twin boundaries are the same as the BC maps in Figure 3.4. Only one CT and one DT are found in this figure, suggesting that their contribution to plastic deformation is negligible in this case.

The limited CT activity during tensile deformation is in conflict with the high SF for CT in E-textured grains. This discrepancy seems to indicate that the activation of CT during tensile deformation does not follow the SF criteria. In order to assess this hypothesis, the SFs of CT and ET of the grains that underwent twinning during deformation were calculated from the initial EBSD map and are plotted in Figure 3.7. Most of the ETs and CTs found experimentally were located in grains with a high SF, apparently following SF criteria. A few twins are also observed in grains with a SF that is low or even negative, presumably associated with a stress concentration [265]. The only difference among the data in Figure 3.7 is that the average SF of the active CTs during tensile deformation is 0.31 and 0.40-0.41 in the other three cases. It should also be noted that the average SF for CT under tension of all the E-textured grains was 0.43 (Figure 3.2(D)), slightly higher than the experimental value of 0.31 (Figure 3.7(B)). Thus, the activation of CTs and ETs seems to follow the SF criteria, except for a slight deviation of CT during tensile deformation. However, the contribution of CT to plastic deformation during tension is much less pronounced than predicted from the distribution of SF

in Figure 3.2(D). These results indicate that most of the grains, that nucleate CT under tensile deformation, have a high SF for CT but are grains with high SF for CT in which CTs do not develop. Thus, the contribution of CT to the macroscopic plastic deformation in tension is limited and other deformation mechanisms should be active to accommodate the tensile strain.

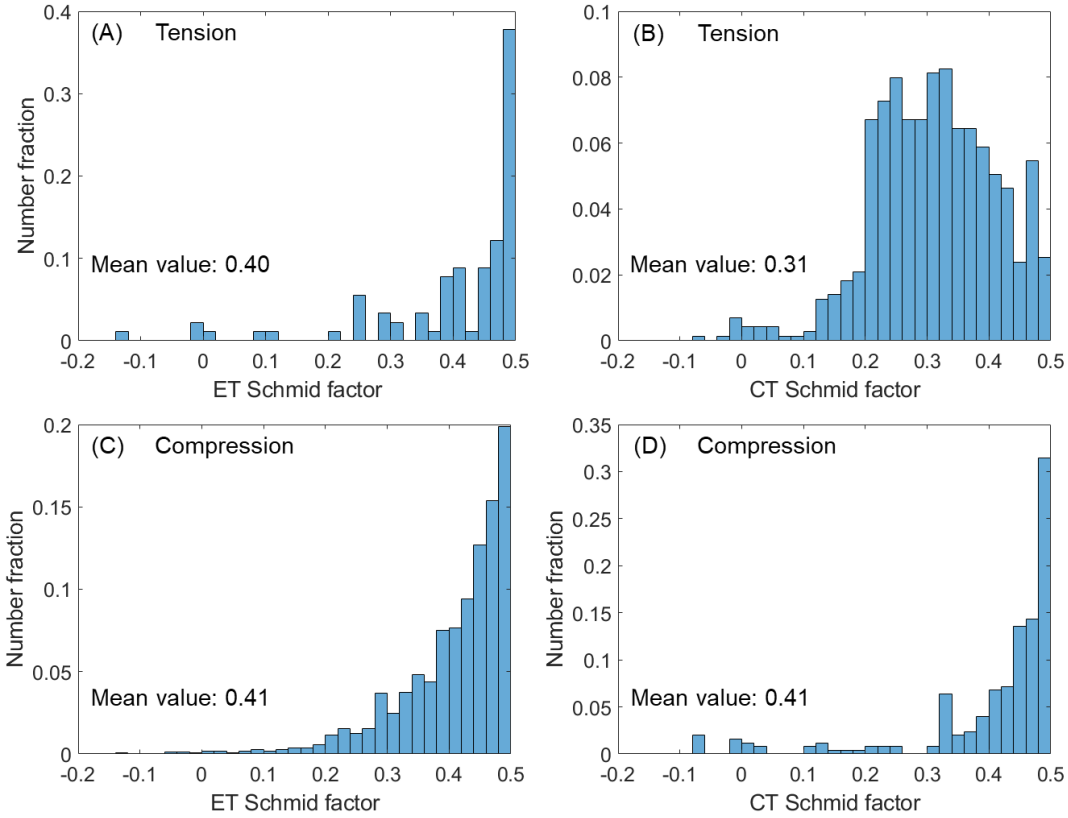

Figure 3.7: SFs of CT and ET in the grains that underwent twinning during deformation. (A) ET during tensile deformation (dataset number: 90), (B) CT during tensile deformation (dataset number: 714), (C) ET during compressive deformation (dataset number: 1791), (D) CT during compressive deformation (dataset number: 251).

The average SFs of the different slip and twin deformation modes in each grain were calculated from the initial EBSD map in the E-textured and C-textured grains. The average values are indicated in Table 3.2 for both tensile and compressive deformation along the ED. Although the SFs for basal slip are low for both E-textured and C-textured grains, this deformation mode is always expected to be active due to its low CRSS (around 11 - 25 MPa has been reported for various Mg-xZn alloys with x in the range 3.9 - 6.5 wt.%), according to experimental micropillar compression and Visco-Plastic Self-Consistent (VPSC) simulation

[92,155,266,267]). However, accommodation of plastic deformation in the polycrystals can only be achieved if other deformation modes are active and the most likely ones are those with high SFs (> 0.40), that are highlighted in bold in Table 3.2. Thus, CT or ET as well as <c + a> pyramidal slip should be the dominant deformation modes during compressive or tensile deformation, respectively, of C-textured grains. However, the CRSS for <c + a> pyramidal slip (200 - 246 MPa for reported Mg-xZn alloys, according to experimental micropillar compression and VPSC simulation [152,155,266,267]) is much higher than that for ET (18 - 39 MPa for reported different Mg-xZn alloys, according to experimental micropillar compression and VPSC simulation [152,155,266–268]) or CT (114 - 185 MPa for pure Mg [11,12], based on single crystal compression and VPSC simulation, and higher values are expected for Mg-xZn alloys although there are no data in the literature). Therefore, ET or CT are likely active during tensile or compressive deformation, respectively, of C-textured grains, in agreement with the experimental observations. In the case of E-textured grains, ET and CT have to compete with <c + a> pyramidal slip but also with <a> prismatic and <a> pyramidal slip. As the CRSS for these latter slip modes (<a> prismatic slip: 54 - 113 MPa for reported Mg-xZn alloys, based on VPSC simulation [155,267]) is lower than that for <c + a> pyramidal slip as well as CT, it is possible that non-<a> basal slip (either prismatic or pyramidal or both) replaces CT as of the dominant deformation mechanisms during tensile deformation of E-textured grains. This is not the case for compressive deformation because the CRSS for ET in Mg is much lower than that for <a> non-basal slip.

To experimentally validate the above assumption, the dislocation slip mechanisms during tensile deformation were analyzed using GROD [211] and ST-MLRA [203]. GROD can provide statistical information about the active slip systems from the lattice rotations induced by dislocation slip while ST-MLRA facilitates the precise identification of actual active slip system from slip trace analysis and grain rotation when several slip systems share the same SP. Their combination provides comprehensive and accurate information about the active slip systems during deformation.

Table 3.2: SFs for slip and twinning in E-textured and C-textured grains during tensile or compressive deformation along ED. For each grain, the average grain orientation obtained for the initial EBSD map was used to calculate the SFs. In the case of slip and twin, the highest SF among all the variants in each grain was chosen. The data are the average of 3891 E-textured and 1241 and C-textured grains, respectively. The SFs > 0.40 are highlighted in bold to emphasize the deformation mode that is more likely active.

SF	Compression		Tension	
	E texture	C texture	E texture	C texture
<a> basal slip	0.15	0.22	0.15	0.22
<a> prismatic slip	**0.46**	0.03	**0.46**	0.03
<a> pyramidal slip	**0.46**	0.12	**0.46**	0.12
<c + a> I pyramidal slip	**0.46**	**0.48**	**0.46**	**0.48**
<c + a> II pyramidal slip	**0.44**	**0.48**	**0.44**	**0.48**
ET	**0.43**	-0.42	-0.02	**0.46**
CT	-0.02	**0.46**	**0.43**	-0.42

GROD provides information about the orientation of the axes that define the intragranular misorientation in each grain, which can be associated with the active slip systems in the corresponding grain. <a> basal and <c + a> II pyramidal slip lead to a rotation of the crystal around the $<\bar{1}100>$ axis, while <a> prismatic slip is associated with rotation around <0001>, <a> pyramidal slip around $<01\bar{1}2>$ and <c + a> I pyramidal slip around $<1\bar{3}21>$ (Figure 3.8(A)) [269,270]. The distribution of the intragranular misorientation axes (expressed in multiples of a random distribution, mrd) in the crystal coordinate system of the Mg-6.5Zn alloy is depicted in Figure 3.8(B) before tensile deformation. The distribution of the misorientation axes has peaks near the center and also around [0001] of the IPF, which is representative of residual grain orientation gradients caused by <a> non-basal and <c + a> pyramidal slip during extrusion [253]. As the applied strain increases, the RAs move towards $[\bar{1}100]$ (and towards the curved line joining $[\bar{1}100]$ to $[\bar{1}2\bar{1}0]$) as well as towards [0001] (Figure 3.8(C) to Figure 3.8(D)). Due to the high CRSS of <c + a> II pyramidal slip in comparison to that of <a> basal slip, the $<\bar{1}100>$ RA has to be associated with the activation of <a> basal slip at the beginning of deformation. The translation of this RA along the curved line joining $[\bar{1}100]$ to $[\bar{1}2\bar{1}0]$ at larger strains is associated with the simultaneous operation of two basal slip systems [271,272]. Moreover, another peak in the distribution of RAs is found in between the orientations corresponding to <a> prismatic and <a> pyramidal slip

(Figure 3.8(E)), indicating that <a> non-basal slip plays a significant role to accommodate plastic deformation.

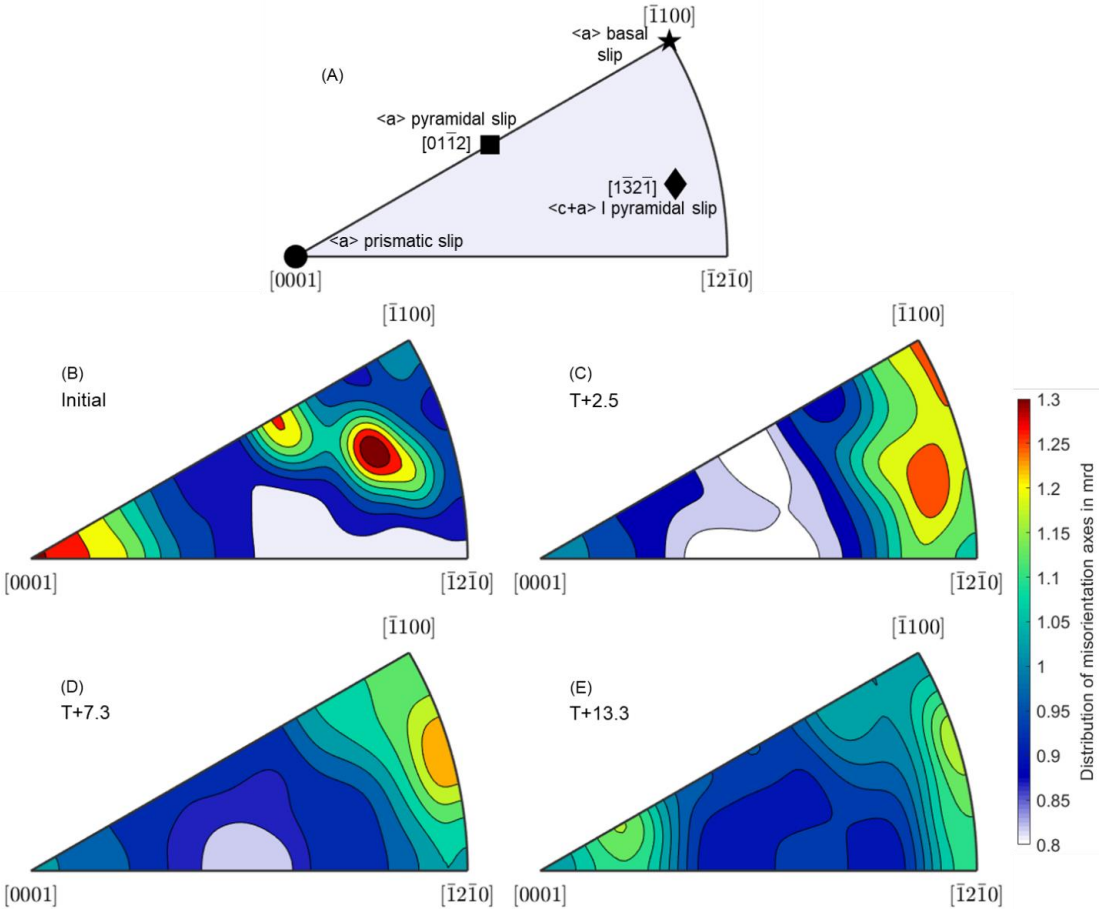

Figure 3.8: (A) RAs associated with dislocation slip along different systems in HCP Mg. Evolution of the distribution of intragranular misorientation axes in the crystal coordinate system (expressed in mrd) of Mg-6.5Zn alloy during tensile deformation along ED. (B) Before deformation, (C) T+2.5, (D) T+7.3, and (E) T+13.3.

The sample deformed in compression along the ED was also analyzed using GROD and the corresponding results are plotted in Figure 3.9. Compression is associated with intragranular misorientation axes concentrated around <2$\bar{1}\bar{1}$0>. This RA does not match with isolated slip system of HCP of Mg but Wang et al. [271] and Yamasaki et al. [272] demonstrated that a RA close to [2$\bar{1}\bar{1}$0] was due to the simultaneous operation of (0001) [1$\bar{2}$10] and (0001) [11$\bar{2}$0] basal slip systems with the same intensity. Thus, plastic deformation of dual-textured Mg-6.5Zn alloy compressed along the ED is dominated by CT and ET as well as <a> basal slip.

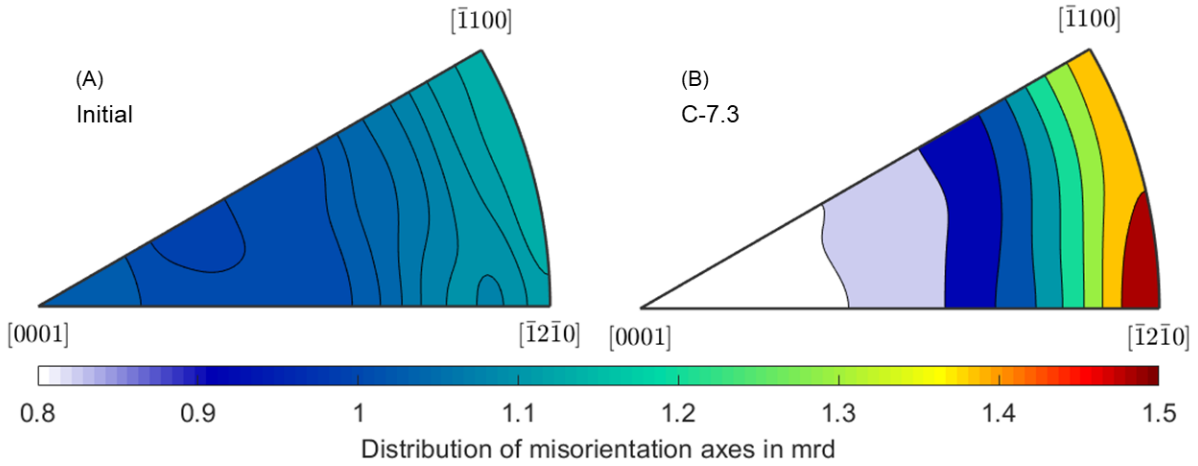

Figure 3.9: Evolution of the distribution of intragranular misorientation axes in the crystal coordinate system (expressed in mrd) of Mg-6.5Zn alloy during compressive deformation along ED. (A) before deformation, and (B) C-7.3.

ST-MLRA was also used to support the results obtained by GROD on the sample T+7.3. ST-MLRA combines the information of slip planes (obtained from conventional slip trace analysis) and slip directions (obtained from the translation of the projection of the grain orientation in the pole figure) to identify the actual slip system(s) that are active in a grain [203,273]. Obviously, ST-MLRA provides more accurate information than GROD (that only gives statistical information about the most active slip systems during deformation of the polycrystal) but it requires a large experimental effort and, thus, it can only be performed in a limited number of grains.

A typical example of the application of ST-MLRA to identify the actual active slip system in grain G46 with Euler angles of (4.05°, 117.76°, 9.36°) in the sample T+7.3 is depicted in Figure 3.10. The orientation of the slip traces in G46 (Figure 3.10(A)) are in good agreement with the calculated ones for the ($\bar{1}$101) I pyramidal plane (Figure 3.10(B)). However, there are possible three slip directions in this plane: [$\bar{1}\bar{1}$20] (SF = 0.45, RA: [1$\bar{1}$02] (A)), [$\bar{2}$11$\bar{3}$] (SF = 0.27, RA: [$\bar{1}\bar{2}$31] (B)), and [1$\bar{2}$13] (SF = 0.06, RA: [$\bar{2}\bar{1}$3$\bar{1}$] (C)), and the active one cannot be discriminated by conventional slip trace analysis. The projection of the orientation of grain G46 in the {0001} pole figure before and after deformation (obtained from EBSD) is plotted in Figure 3.10(C). Plastic deformation stretches the projection of the undeformed grain towards a direction that coincides with that indicated by the rotation around

[1$\bar{1}$02] (A) (Figure 3.10(D)). Thus, the main active slip system in G46 is <a> pyramidal ($\bar{1}$101) [11$\bar{2}$0].

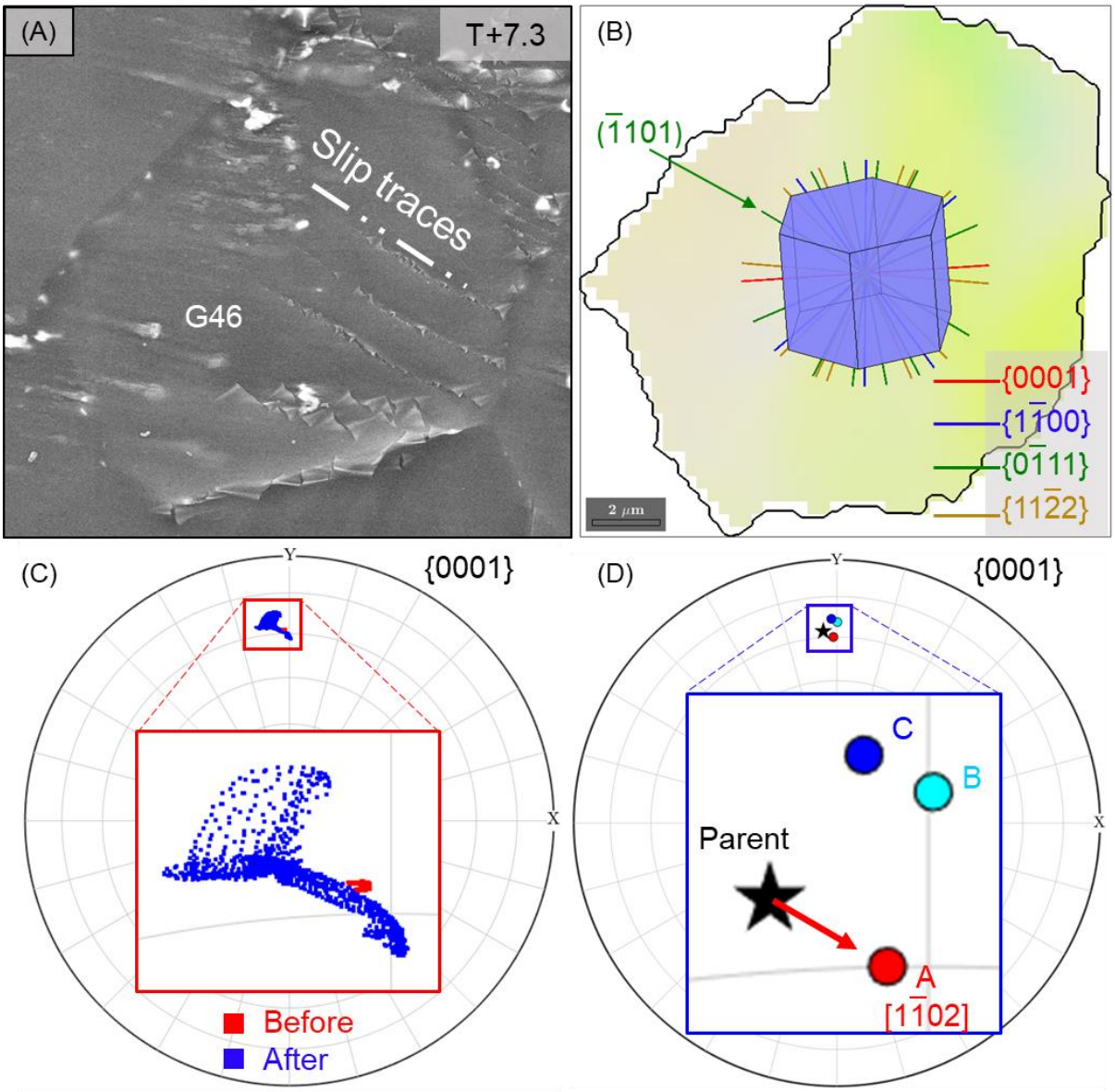

Figure 3.10: Example of application of ST-MLRA in grain G46 of the sample T+7.3. (A) SE micrograph of grain G46. The slip traces corresponding to the ($\bar{1}$101) [11$\bar{2}$0] slip system are clearly visible on the grain surface. (B) Orientation of the slip traces of different slip planes from the EBSD map before deformation. (C) Trace of the orientation of grain G46 on the {0001} pole figure before (red) and after (blue) deformation. (D) Simulated change in the trace of the orientation of grain G46 on {0001} pole figure as a result of rotation around the three axes corresponding to the three possible slip directions in the ($\bar{1}$101) plane.

Over 200 grains of the T+7.3 sample were analyzed, and the main active slip system could be determined by means of ST-MLRA in 36 grains. The results are

depicted in Table 3.3 split into three different groups: E-textured grains, C-textured grains and 'Other' grains. The category 'Other' stands for residual grains that do not belong to either C-textured or E-textured groups. The basal plane of the 'Other' grains forms an angle of ~45º with the loading direction, leading to a high SF of <a> basal slip. <a> basal slip is found in grains that belong to the three categories as a result of the low CRSS to activate this mechanism and is the only one active in the grains of the 'Other' category. Similarly, <a> basal slip is the main active system in C-textured grains although a minor contribution of <c + a> I and II pyramidal slip was also found, in agreement with their high SF (Table 3.2). Finally, dislocation slip in E-textured grains was concentrated in <a> basal, <a> prismatic and <a> pyramidal slip systems which had the highest SFs (Table 3.2). The contribution of <c + a> I and II pyramidal slip was minor for grains with this orientation.

Table 3.3: Active slip systems identified by ST-MLRA in C-textured, E-textured and other grains in sample T+7.3. The category 'Other' stands for residual grains that do not belong to either C-textured or E-textured groups.

	Grains analyzed	Grains with slip traces	Non-basal slip				
			<a> basal slip	<a> prismatic	<a> pyramidal	<c + a> I pyramidal	<c + a> II pyramidal
C-textured	46	9	7	0	0	1	1
E-textured	154	23	13	2	5	1	2
Other	15	4	4	0	0	0	0

The previous results indicate that similar yield strength in tension and in compression could be obtained by increasing slightly (up to 25 - 30%) the fraction of C-textured grains in the microstructure but we cannot guarantee that reduction in the TCA is proportional to the volume fraction of E-textured and C-textured grains. For example, the yield strength in tension of extruded AZ31 rods, whose microstructure was formed by a mixture of <0002> // ED (soft orientation) and <0002> ⊥ ED (hard orientation) grains, did not decrease linearly with the volume fraction of soft orientations [252]. Thus, the interaction between grains with different texture (that will depend on the texture and on the spatial distribution of grains with different texture) has to be carefully considered to predict the mechanical properties of dual-textured Mg alloys [252]. Despite this, the present

chapter provides physical insights into the deformation mechanism of dual-textured Mg alloy in order to design cost-effective Mg alloys with negligible TCA.

3.3.4. Sensitivity of double twinning to slip behavior

The EBSD maps showing the grain orientation according to the IPF in the ED and the BC maps after compression up to 7.3% and after tension up to 18.6% along the ED are plotted in Figure 3.11. ET and secondary twin boundaries are found after deformation in compression and tension. In addition, CTs develop in the C-textured regions during compression and in the E-textured regions during tension. Many DT boundaries (colored in green) yet few CT boundaries (colored in blue) are found in Figure 3.11(B), suggesting that most CTs have transformed to DT by the activation of ET after compression up to 7.3% plastic strain. Conversely, many CT boundaries but few DT boundaries are found in Figure 3.11(D) when the specimen was deformed in tension up to 18.6% plastic strain. Thus, activation of ET within the CT is not favored by tensile deformation along the ED even though the tensile plastic strain was almost three times higher than the plastic strain applied in compression, where DT readily developed. Quantitatively, the ratio of DT with respect to the sum of DT + CT for C-7.3, T+13.3 and T+18.6 specimens is 85%, 22%, and 36%, respectively (Table 3.4). These data show that the transformation from CT to DT is significantly more difficult in tension than in compression.

The standard strategy to explain whether or not twinning will develop in a grain is based on the global SF for different twinning variants that can be easily obtained from the grain orientation and the macroscopic loading axis [48]. The SFs of the experimentally active primary CT and secondary ET in DT are plotted in Figure 3.12. The SFs of the active primary CTs in C-textured grains during compression are high and positive (Figure 3.12(A)) and those of the active primary CTs in E-textured grains under tension are also positive although slightly lower (Figure 3.12(C)). Nevertheless, the activation of secondary ET within primary CT for both C-textured grains under compression and E-textured grains under tension takes place in most cases for very low or even negative SFs (Figure 3.12(B) and Figure 3.12(D)). Thus, SF cannot explain the formation of DT and cannot shed light

about the differences in the prevalence of DT during tensile and compressive deformation.

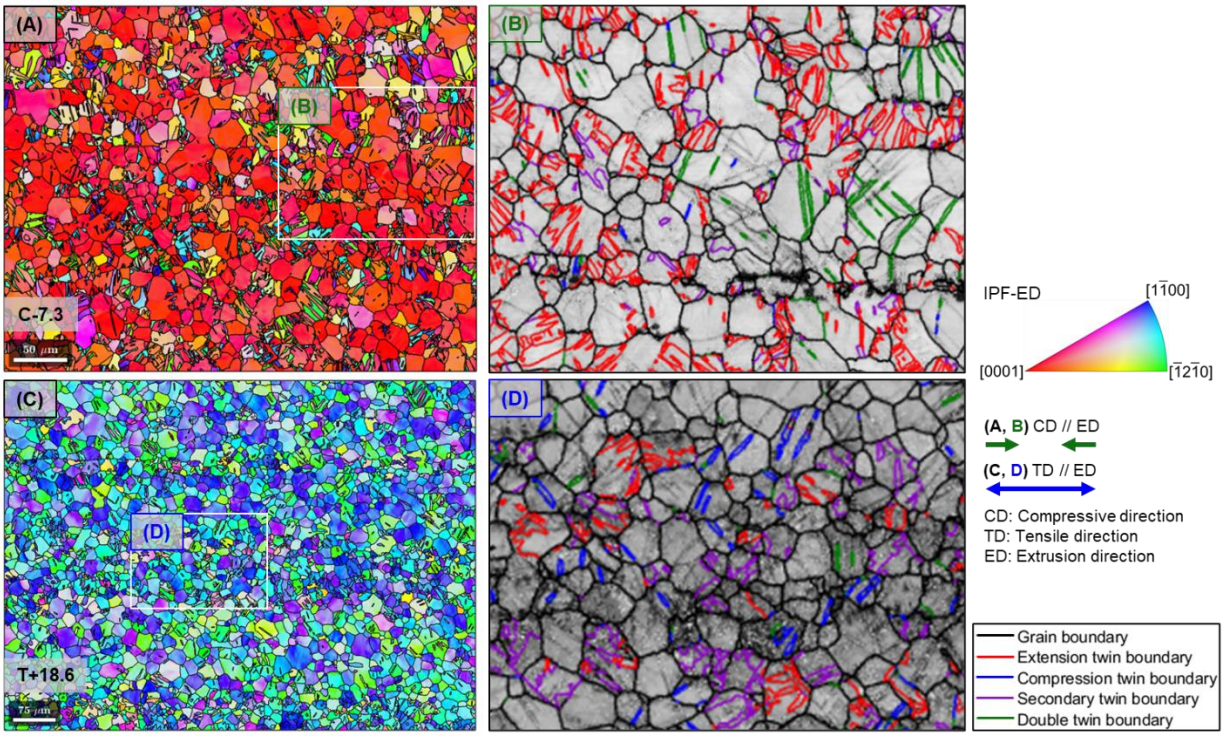

Figure 3.11: (A) IPF and (B) BC map after compression up to 7.3% along the ED. (C) IPF and (D) BC map after tension up to 18.6% along the ED. The reference direction of IPF was ED, and all GBs were overlaid in black. ET, CT, secondary twin, and DT boundaries were highlighted in red, blue, purple, and green, respectively, in the BC maps. They were identified from the boundary's RA - misorientation angle pairs, i.e., <2$\bar{1}\bar{1}$0> & 86.3°, <2$\bar{1}\bar{1}$0> & 56.2°, <1$\bar{1}$00> & 60.0° and <2$\bar{1}\bar{1}$0> & 37.5° for ET, CT, secondary and DT, respectively. The threshold misorientation angle was set to 5°. Other GBs were overlaid in black on BC maps. Note that the secondary twin boundaries are the product of interaction between the multiple primary ETs.

Table 3.4: Number of CTs and DTs found in C-7.3, T+13.3, and T+18.6 specimens. The ratios DT / (CT + DT) were also included.

Specimen	Applied stress (MPa)	CTs	DTs	DT / (CT + DT), %
C-7.3	267	29	158	85
T+13.3	346	277	78	22
T+18.6	361	231	128	36

GROD can provide information about the active slip systems from the lattice rotations induced by dislocation slip [211]. GROD was used to analyze the grains in which DT and CT develop during compressive and tensile deformation,

respectively, and the corresponding results are plotted in Figure 3.13. 7 DTs are distinguished by EBSD in grain G1 with Euler angles (87.3°, 84.0°, 25.4°) (Figure 3.13(A1) and Figure 3.13(A2)) and the slip-induced RA in (Figure 3.13(A3)) are located around the curved line joining $[\bar{1}100]$ (in blue, corresponding to single <a> basal slip according to Figure 3.13(C) [273]) to $[\bar{1}2\bar{1}0]$ (in green, corresponding to the simultaneous activation of two <a> basal slip systems [271,272]). However, only one CT is observed in grain G2 with Euler angles (359.7°, 89.5°, 48.6°) (Figure 3.13(B1) and Figure 3.13(B2)), and the slip induced RA concentrates around [0001] (in red, Figure 3.13(B3)), indicating that <a> prismatic slip is the main active slip system in G2 (Figure 3.13(C)) [187,203]. Similar results were found for other grains with similar orientations containing CT and DT.

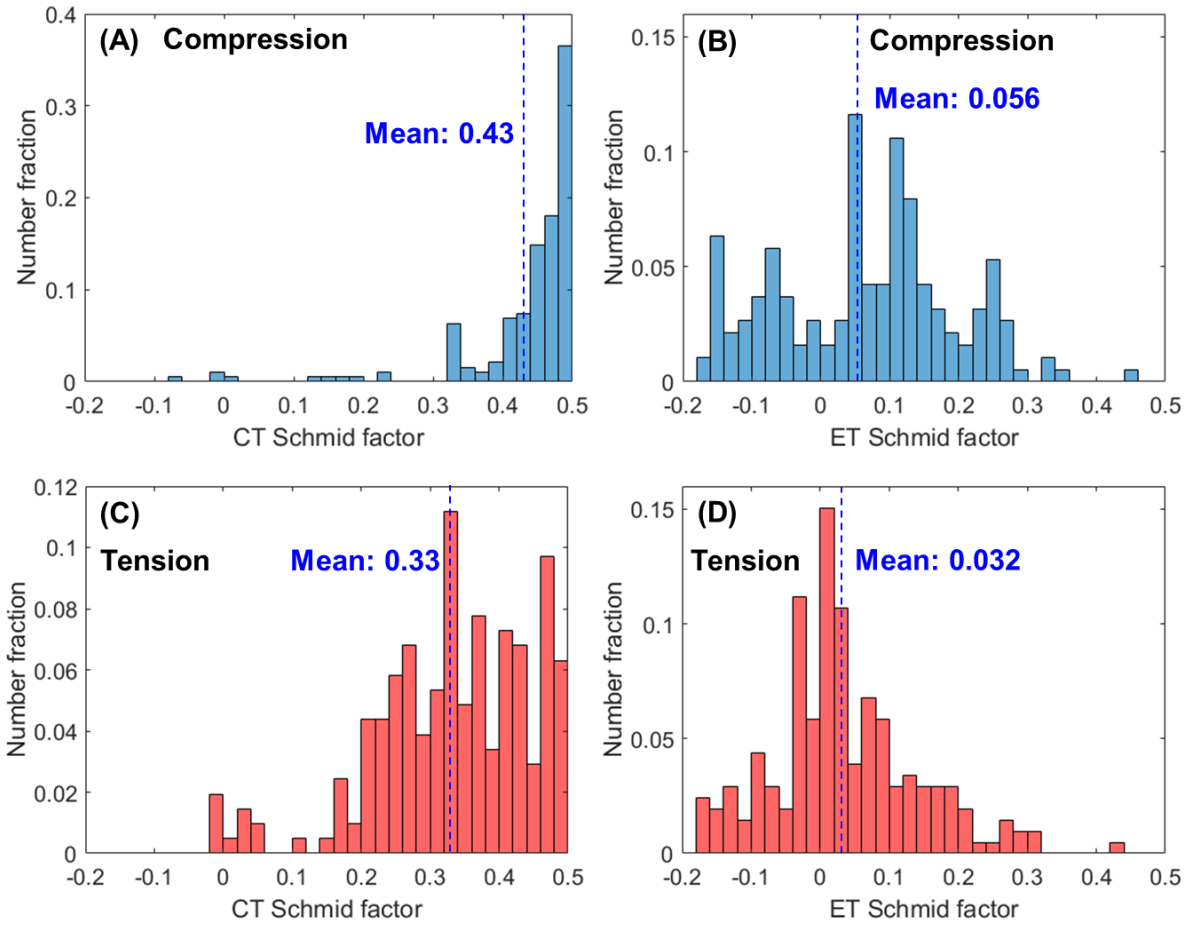

Figure 3.12: (A) SFs of primary CTs under compressive deformation in the C-textured grains. (B) SFs of secondary ETs within primary CTs under compressive deformation in the C-textured grains. (C) SF of primary CTs under tensile deformation in E-textured grains. (D) SFs of secondary ETs within primary CTs under tensile deformation in E-textured grains.

Further examination of the SFs of various deformation modes in grains G1 and G2 reveals that the most suitable slip system in G1 is <c + a> pyramidal slip and in G2 is <a> prismatic slip (Table 3.5). The GROD results in Figure 3.13(B3) confirm that <a> prismatic slip is active in G2, but they do not provide evidence that <c + a> pyramidal slip is active in G1 (Figure 3.13(A3)). This is very likely because the CRSS of <c + a> pyramidal slip in Mg-6.5% Zn is very high (200 - 246 MPa, [152,155,266,267]), and <a> basal slip -whose CRSS is one order of magnitude lower (11 - 25 MPa, [92,155,266,267])- is the main slip mechanism. Taking into account that the SF to nucleate secondary ET within primary CT is comparable for grains G1 and G2 (i.e., 0.30 and 0.22, respectively, in Table 3.5), the differences in CT → DT transformation between tension and compression could be attributed to the dominance of <a> basal slip during compression and of <a> non-basal slip during tension.

Table 3.5: SFs for slip and twinning in grains G1 during compressive deformation and G2 during tensile deformation, respectively. The average grain orientation was used to calculate the SFs. In the case of slip and twinning, the highest SF among all the variants in each grain was chosen. The highest SF to nucleate a secondary ET was chosen in the most likely primary CT.

Deformation modes	SF	
	G1	G2
<a> basal slip	0.055	0.0039
<a> prismatic slip	0.0055	0.50
<a> pyramidal slip	0.054	0.44
<c + a> I pyramidal slip	0.45	0.34
<c + a> II pyramidal slip	0.49	0.40
ET	-0.48	-0.051
CT	0.49	0.48
ET in primary CT	0.30	0.22

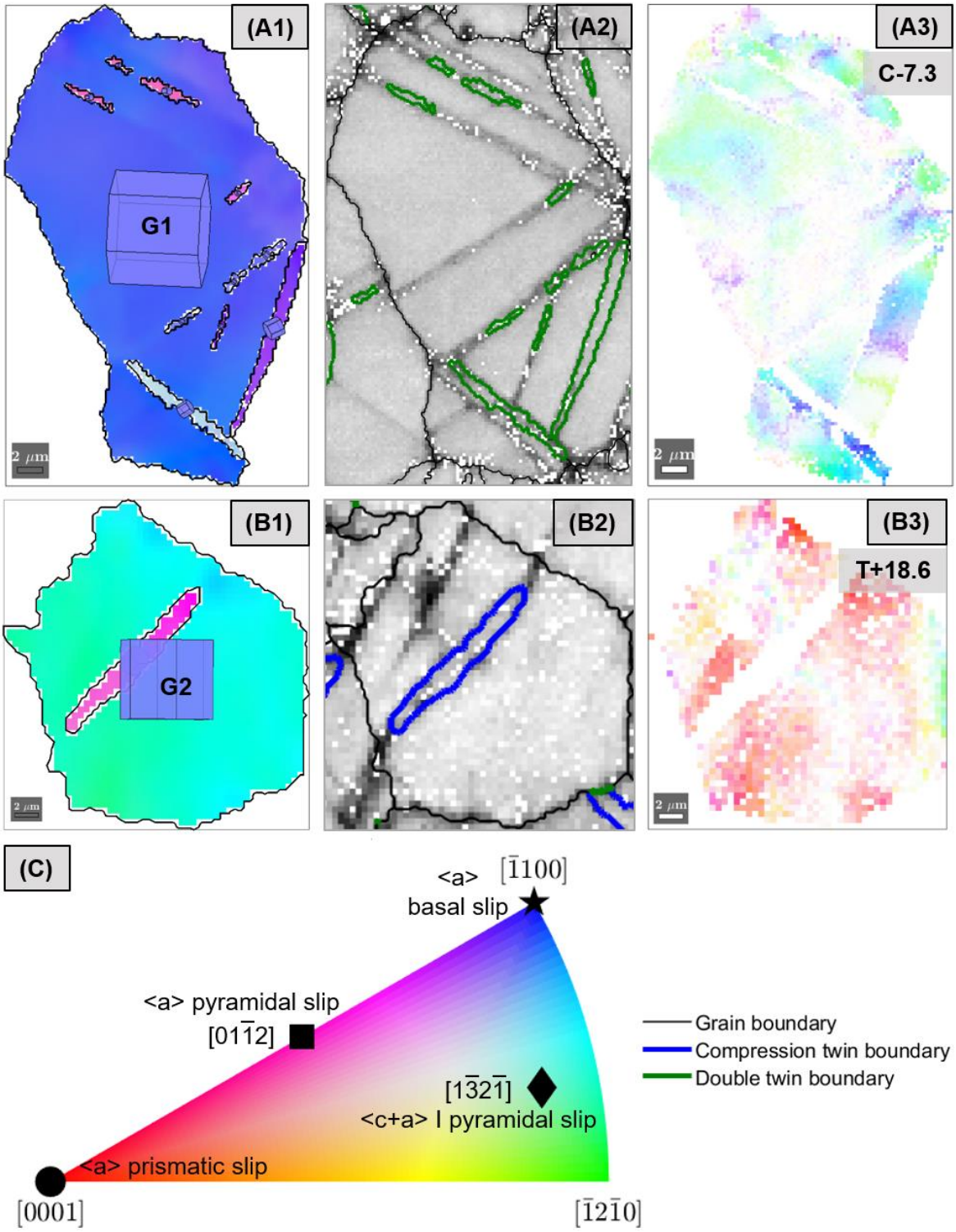

Figure 3.13: (A1) IPF, (A2) BC, and (A3) GROD maps of grain G1 after compression up to 7.3%. (B1) IPF, (B2) BC, and (B3) GROD maps of G2 after tension up to 18.6%. The reference direction of the IPF was perpendicular to the image. (C) RAs associated with dislocation slip along different systems in HCP Mg.

3.4. Conclusions

The mechanical properties in tension and compression along the ED were measured in a dual-textured Mg-6.5Zn alloy. The 80% of the grains in the alloy presented the typical extrusion texture (denominated E texture) in which the basal planes were oriented (± 30º) parallel to the extrusion axis. However, the other 20% of the grains presented an unconventional texture (denominated C texture) in which the $\vec{c}$ axis was oriented (± 30º) along the ED. The presence of this population of grains with C texture led to a ratio of 0.9 between the yield strength in compression and tension, leading to a TCA in the yield strength much lower than that found in any extruded Mg alloy without REs.

The origin of the limited TCA was analyzed by means of EBSD, GROD and ST-MLRA in samples deformed up to different strains in tension and compression to ascertain the dominant deformation mechanisms. The behavior of the E-textured grains was typical of wrought Mg alloys. Compressive deformation was accommodated by <a> basal slip and ET while tensile deformation promoted <a> basal slip and <a> non-basal (prismatic and pyramidal) slip. These mechanisms are associated with a large TCA because the CRSS for ET in Mg is much lower than that for <a> prismatic or <a> pyramidal slip. However, the C-textured grains presented the opposite (and much stronger) TCA. Tensile deformation in the C-textured grains was absorbed by <a> basal slip and ET while compression deformation required <a> basal slip and CT. As the CRSS for CT is much higher than that of ET (and also of <a> prismatic and <a> pyramidal slip), the contribution of the 20% grains with C texture to the overall mechanical behavior led to (almost) similar values of the yield strength in tension and compression. Thus, introduction of dual texture appears as a cost-effective route to manufacture wrought Mg alloys with similar yield strength in tension and compression.

This study also shows that the transformation of CT to DT can be significantly hampered by the activation of <a> non-basal slip, which could explain the lower activation of DT in dual-textured Mg-6.5Zn alloy deformed in tension as compared with in compression. The present finding not only advances the understanding of the DT mechanism but also provides an effective strategy to hinder the

transformation of CT to DT. Moreover, given the strong correlation between DT and the fracture behavior of Mg alloys [15,274–276], understanding how to suppress CT → DT may help to design Mg alloys with improved ductility.

4. Effect of precipitates on the deformation mechanisms in an as-extruded Mg-4.5Zn alloy

4.1. Introduction

Mg alloys have promising applications in transportation due to their low density and high specific stiffness. They also have potential applications in the biomedical field because they are bioresorbable and biocompatible [1,277,278]. However, their mechanical properties at room temperature are limited due to the insufficient number of slip systems [18] and the low CRSS of the easiest slip mode (i.e., <a> basal slip, ~ 0.5 MPa for pure Mg [5,6]). Therefore, a variety of strategies have been developed to improve the mechanical performance (strength and ductility) of Mg and its alloys, including -but not limited to- the addition of alloying elements [279–281], in particular RE [282–286], ageing treatments [148,248,287,288], grain refinements [169,235,289–291], texture optimizations [48,50,292,293], and others [120,294–297].

Alloying is one of the most effective and simple strategies to improve the ductility of Mg [298–302]. Sandlöbes et al. [244] have reported that the addition of 3 wt.% Y led to ~ 4-fold increment in ductility, as compared with pure Mg with a similar grain size, owing to the activation of pyramidal <c + a> slip and secondary twinning. Other RE elements, like Gd, Ce, Tb, Dy, Ho, etc., have also been shown to improve the ductility of Mg [187,303,304]. The addition of other more cost-effective solutes (such as Li, Ca, Zn, etc.) has also led to noticeable improvements in ductility [186,195,305–310]. For example, the presence of 2 wt.% Zn in Mg improved the ductility by ~ 3-fold, enhanced the work hardening and promoted higher activity of <c + a> II pyramidal slip at room temperature, in comparison with pure Mg [262].

Apart from a minimum ductility, high strength is another critical requisite for the application of Mg alloys in structural components [289,311]. Therefore, precipitation hardening via ageing treatments is commonly used, and the

corresponding mechanisms have been studied for several decades from the experimental and theoretical viewpoints [99,107,241,312,313]. Mg-Zn alloys stand for one of the most widely known age-hardenable Mg alloys. Its precipitation sequence follows the path: supersaturated solid solution → Guinier-Preston zones → rod-shaped β_1' (monoclinic Mg_4Zn_7 and/or hexagonal $MgZn_2$) parallel to the $\vec{c}$ axis → coarse basal plate β_2' (hexagonal $MgZn_2$) → equilibrium phase β (monoclinic MgZn) [148–151]. The rod-shaped β_1' precipitates provide most of the strengthening because of their smaller diameter and higher number density than others [148].

The rod-shaped β_1' precipitates grow along the $\vec{c}$ axis and stand as strong obstacles to the movement of <a> basal slip dislocations, leading to a large increase in the corresponding CRSS [153,155,314,315]. An increment in the CRSS of basal slip from 26-29 MPa to 34-38 MPa was attributed to the presence of β_1' precipitates through in-situ synchrotron experiments of polycrystalline Mg-4.5Zn (wt.%) bulk samples after ageing at 150°C for 84 h [153]. Using the room temperature micropillar compression tests, the CRSS of basal slip was determined to be ~ 11 MPa [92] and 55.1 MPa [156] for the Mg-4Zn (wt.%) after solution treatment and after ageing at 149°C for 100 h, respectively. However, less attention has been paid in the literature to the effect of β_1' precipitates on twinning and pyramidal <c + a> slip as well as on <a> non-basal slip [152,156,258,266,316], i.e., <a> prismatic slip and <a> pyramidal slip, despite that they may also contribute considerably to the deformation of Mg-Zn alloys containing precipitates [153,310]. Therefore, a comprehensive and quantitative evaluation of the influence of β_1' precipitates on the different deformation modes of Mg-Zn alloys is lacking, and this information is relevant to assess the effect of precipitation on the strength and ductility of Mg and other hexagonal metals.

In this investigation, the influence of β_1' precipitates on the deformation mechanisms of polycrystalline Mg-4.5Zn (wt.%) alloy was studied by means of EBSD and TEM. The same alloy without precipitates was also analyzed. Conventional EBSD-assisted slip trace analysis as well as ST-MLRA were used to identify the dominant plastic deformation mechanisms (and to distinguish <a>

pyramidal slip from <c + a> I pyramidal slip) in the grains with planar slip traces. GROD was utilized to explore possible deformation mechanisms in the grains with non-planar slip traces. Furthermore, the deformation mechanisms responsible for non-planar slip traces were explored by TEM. The results explain why non-planar slip traces were stimulated by β_1' precipitates and the interaction mechanisms between <a> non-basal slip dislocations and β_1' precipitates. Overall, they provide a comprehensive picture of the effect of precipitates on the deformation mechanisms of hexagonal metals.

4.2. Materials and experimental techniques

Dog-bone tensile specimens of Mg-4.5Zn (wt.%) alloy were cut from the rod by electrical discharge machining. The dimensions of the gauge section were 2 × 2 × 7.9 mm^3 (thickness × width × length). Note that when tension is applied along ED for Mg alloy with a strong prismatic texture, the SFs for various slip systems will be varied greatly, i.e., from 0 for <a> basal slip to 0.50 for <c + a> pyramidal slip [317]. The longitudinal axis was 15° away from the ED to reduce the difference of SF between <a> basal slip and other deformation modes and to better compare the activity among various slip systems. Note that 15° is near the maximum angle to cut the tensile bar from the extruded rod with a diameter of 10 mm. The gauge section of the specimens was mechanically polished using SiC paper, 0.5 μm and 0.05 μm diamond slurries, and 40 nm oxide suspensions, successively. Light etching using 5% Nital solution (a mixture of nitric acid and ethanol) was applied for ~ 5 seconds on the surface after polishing. The initial microstructure of both PA and AE specimens was studied by EBSD with a step size of 1 μm in a region of 550 × 1130 μm^2 (Oxford HKL Channel 5, Oxford Instruments, Abingdon, UK; working distance: 10 mm, accelerating voltage: 20 kV, probe current: 2.7 nA).

The tensile stress-strain curve until failure was measured in a universal mechanical testing machine (Instron 5567) with a 30 kN load cell and a high-resolution video extensometer at a strain rate of 10^{-3} s^{-1}. In addition, both AE and PA samples were deformed in a micromechanical testing machine (Kammrath and Weiss Technologies, Inc., Model MZ.Sb) under displacement control at 1 $\mu m \cdot s^{-1}$,

which led to an approximate strain rate of 10^{-4} s^{-1}. These tests allow the in-situ tracking of the same region for surface imaging and EBSD before and after deformation inside the SEM. The true plastic strain of AE and PA specimens at the end of the test was 5.7% and 7.2%, respectively. A region of 350 × 500 μm^2 near the center of the gauge was analyzed before and after deformation by EBSD in each material with a step size of 0.5 µm. Additional EBSD analysis was performed on the deformed AE and PA samples in a larger region to increase the number of twins in the datasets. The deformed surfaces were also observed in the SEM (Apreo 2S LoVac, FEI Company, Portland, OR, USA) under the SE mode.

The EBSD data were analyzed and plotted using in-house codes based on MTEX (version 5.7.0), an open-source MATLAB toolbox [200,259]. The identification of active twins is based on the orientation or Euler angles of active twins and those of theoretical possible twins according to the parent grain orientation. A detailed description of twin identification procedure can be found in [317].

The active slip system was analyzed using conventional EBSD-assisted slip trace analysis, ST-MLRA and GROD. While conventional EBSD-assisted slip trace analysis only provides information about the active SP, ST-MLRA also incorporates lattice rotation information based on the stretched projection of the grain on the pole figure (that reveals the major RA) [203]. Thus, ST-MLRA can help distinguish the active slip system when different slip systems co-exist in one given SP, i.e., <a> and <c + a> slips in I pyramidal plane [50]. The analysis based on surface slip traces may be influenced by the slip trace observability and surface quality [199]. If both the slip plane and the slip direction are nearly parallel to the surface, their activity may not lead to observable slip traces, as it was reported in pure Al using [199]. However, clear basal slip traces after deformation were found in strong basal textured Mg (basal plane // observation plane) using slip trace analysis [169,318]. The observation plane was nearly perpendicular to the ED (with a deviation of 15^{o}) in the Mg alloys (with and without precipitates) with prismatic texture in this chapter. Thus, both alloys (with and without precipitates) exhibited a nearly similar slip trace observability and, therefore, the statistical

results from the slip trace analysis in hundreds of grains can be considered representative of the actual active slip systems in each material. It should be noted that both conventional EBSD-assisted slip trace analysis and ST-MLRA require the presence of planar slip traces on the grain surface after deformation. However, non-planar slip traces were also found in some grains after deformation and GROD (that does not require any slip trace information) was used to explore the active slip systems of grains with non-planar slip traces.

The GROD analysis of all the grains in the whole EBSD map can provide statistical information about the active slip systems from the lattice rotations induced by dislocation slip. For the grains having non-planar slip traces after deformation, the GROD analysis of that individual grain can reveal the main active slip systems, when the value of the maximum distribution intensity is higher than 2.0 [270]. Note that the analysis using EBSD data is sensitive to the step size. Humphreys [319] and Randle [320] reported that the step size should be approximately one tenth of the grain size for reliable EBSD data acquisition and processing. The step size in this investigation was 0.5 μm, which can be compared to the average grain size of 20.6 ± 10.8 μm and is small enough for the interpretation of grain orientation gradients after ~6% tensile deformation. About 1000 pixels were captured for each grain, large enough to guarantee the accurate identification of projection stretching.

4.3. Results

4.3.1. Microstructure

The texture and grain size distributions of the PA Mg-4.5Zn alloy before deformation are depicted in Figure 4.1. Note that the temperature of the ageing treatment was too low to change the grain size and texture. Thus, nearly the same EBSD results were obtained for the initial microstructures of both AE and PA samples. Due to the 15° deviation of the loading axis from the ED, some grains in the IPF of Figure 4.1(A) are colored in pink (rather than in blue and green for the typical prismatic texture), in agreement with the (0002) pole figure. The maximum

intensity of $(10\bar{1}0)$ and $(10\bar{1}1)$ pole figures is 2.8 and 1.8, respectively, both slightly lower than that of (0002) pole figure (4.3; Figure 4.1(C)). The grain size distribution is plotted in Figure 4.1(B) and the average grain size is 20.6 ± 10.8 μm.

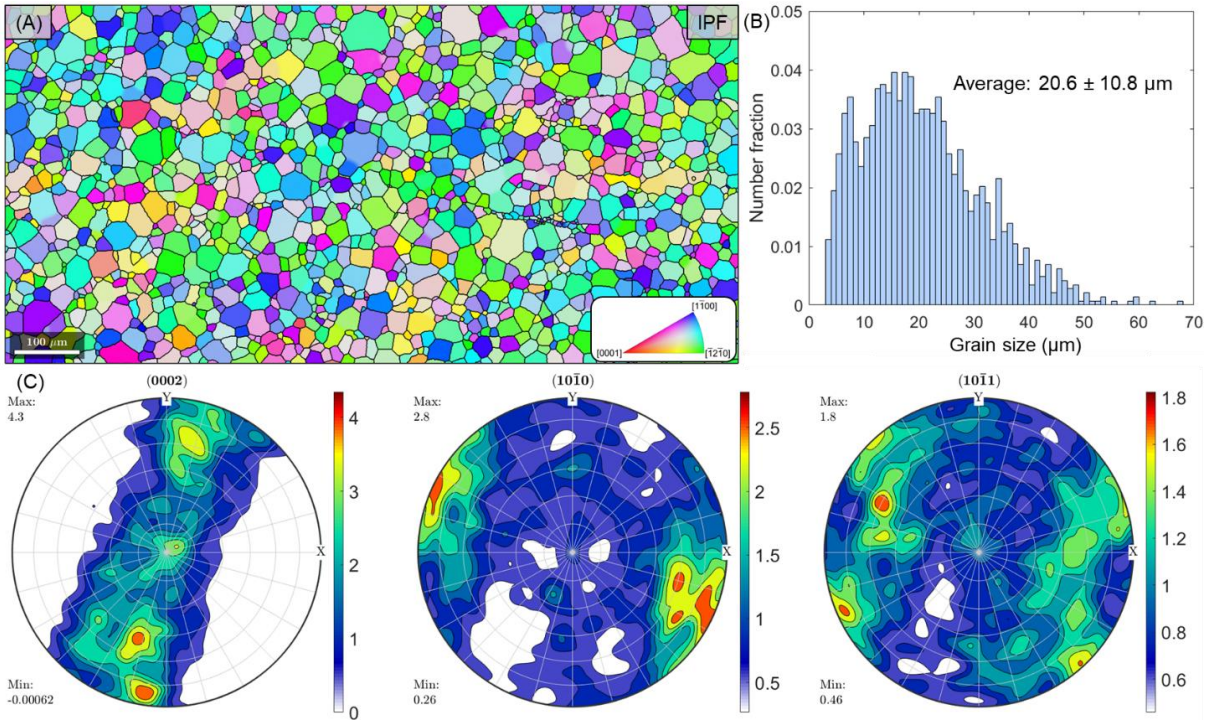

Figure 4.1: Microstructure of PA sample before deformation. (A) EBSD orientation map according to IPF. The reference orientation of the IPF is the horizontal direction. All GBs were overlaid in black. (B) Grain size distribution histogram. (C) (0002), $(10\bar{1}0)$, and $(10\bar{1}1)$ pole figures. The observed direction of EBSD is perpendicular to the ED and the loading direction is parallel to the horizontal direction throughout this chapter.

Based on the average orientations of the grains before deformation, the SFs in tension of various deformation modes were calculated and plotted in Figure 4.2 [123]. Due to the 15° deviation of loading direction from the ED, the SFs of <a> basal slip are evenly distributed, ranging from 0 to 0.5 (Figure 4.2(A)). High SFs of <a> prismatic slip, <a> pyramidal slip, <c + a> II pyramidal slip and CT are found. Lower SFs are observed for ET; thus, this mechanism should not be active during deformation based on the SF criterion. Note that owing to the similar texture and the same loading condition for PA and AE samples, the SF cannot be responsible for the differences in the slip behavior between them.

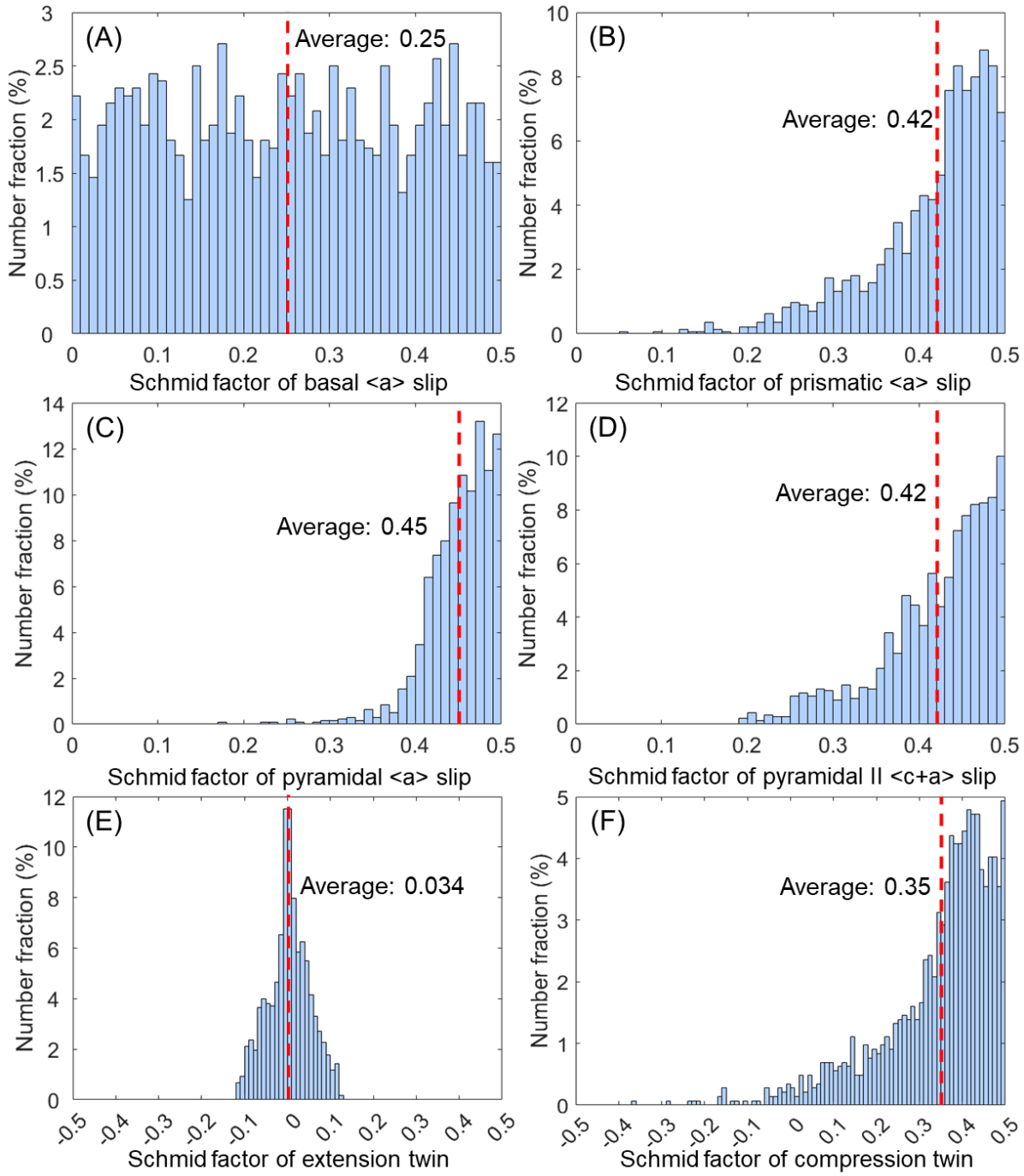

Figure 4.2: Histograms of the SFs for various deformation modes during tension of PA sample. (A) <a> basal slip, (B) <a> prismatic slip, (C) <a> pyramidal slip, (D) <c + a> II pyramidal slip, (E) ET and (F) CT. The average grain orientation obtained from the initial EBSD map was used to calculate the SFs for each grain. For each deformation mode of one grain, the highest SF among all slip systems or twin variants was chosen. 1440 grains were collected for the statistics.

TEM micrographs of PA as well as the length and diameter statistics of the rod-like precipitates are plotted in Figure 4.3. Most precipitates grew parallel to the $\vec{c}$ axis of the grain (Figure 4.3(A)), consistent with previous works [151,314].

The rod-like precipitates have a length of 262 ± 170 nm and a diameter of 10.6 ± 3.2 nm (Figure 4.3(B)).

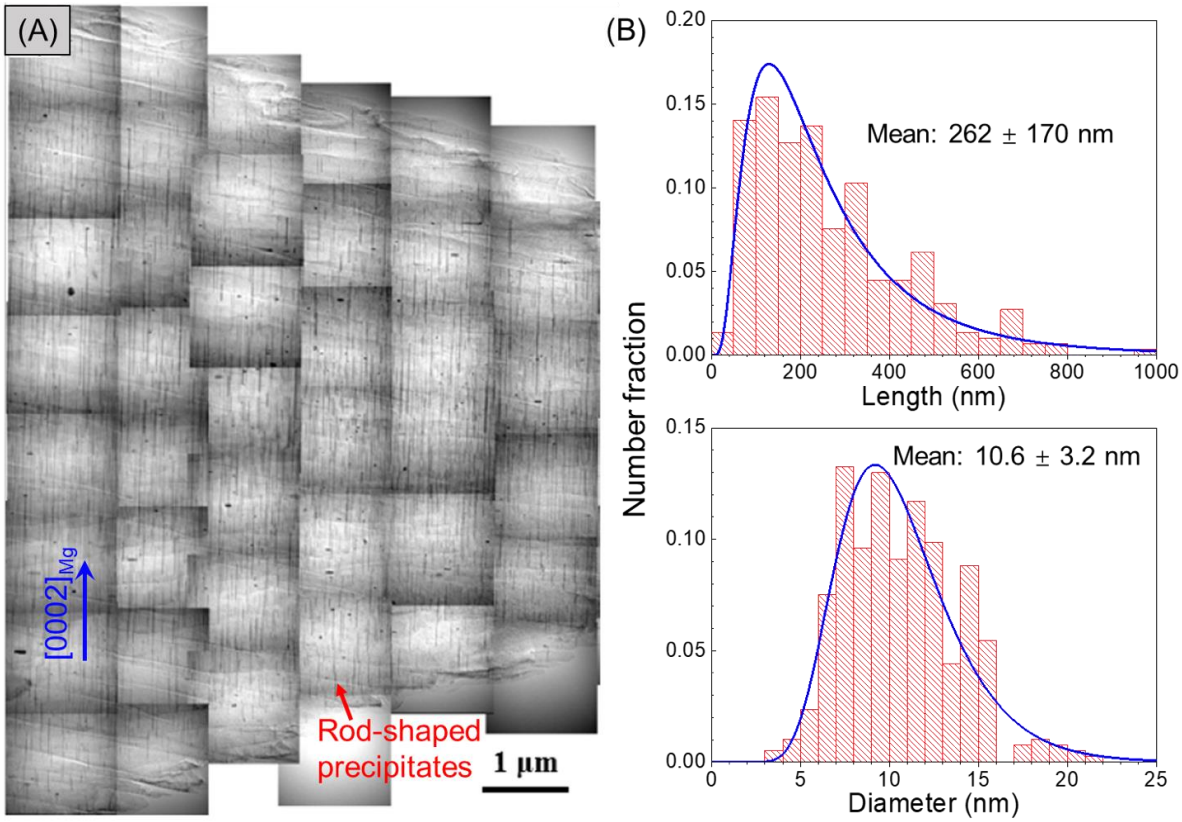

Figure 4.3: β_1' precipitates in the PA sample. (A) TEM micrograph showing the rod-shaped β_1' precipitates parallel to the $[0002]_{Mg}$ and the prismatic plane. (B) Histograms of the precipitate length and precipitate diameter. Around 400 precipitates were considered for the statistics.

4.3.2. Mechanical behavior

True stress-true strain and strain hardening rate-true strain curves in tension of the Mg-4.5Zn alloy with and without precipitates are plotted in Figure 4.4. The parabolic shape of the tensile stress-strain curve in Figure 4.4(A) suggests that the deformation of both PA and AE samples is dominated by dislocation slips [10]. The presence of precipitates increased the yield strength from 122.7 to 183.7 MPa, but also decreased the work hardening rate (Figure 4.4(B)).

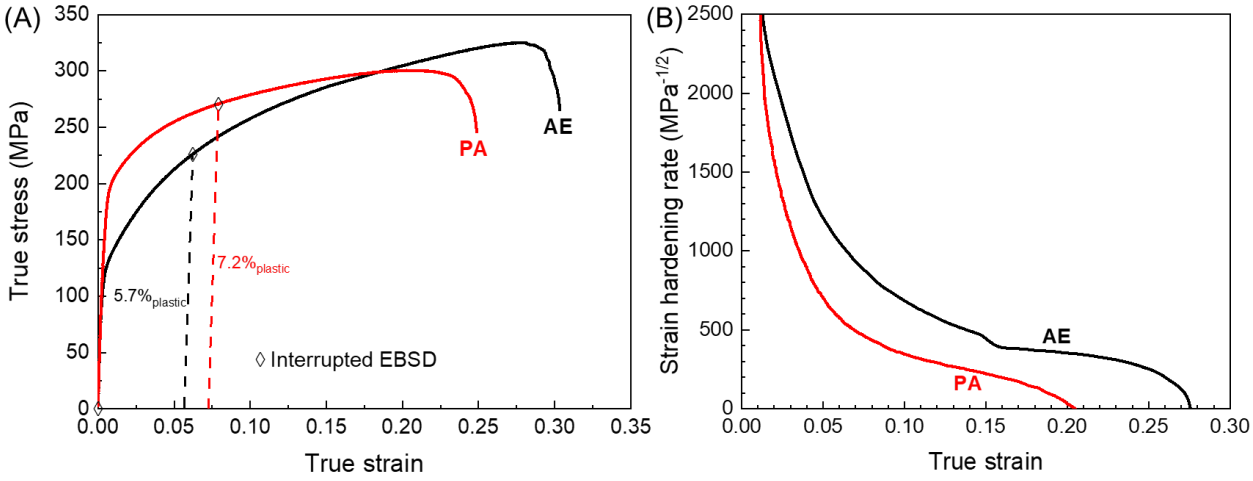

Figure 4.4: Tensile deformation results. (A) true stress and (B) strain hardening rate curves of PA and AE samples with respect to the true strain.

4.3.3. Deformation behavior

EBSD maps in Figure 4.5 show the grain orientations according to the IPF and the BC maps of the Mg-4.5Zn alloy with and without precipitates before and after deformation. A few new lamella grains appeared after tension in both samples. They were identified as twins, including ETs, CTs and DTs. Note that DTs are formed by the nucleation of a secondary ET within a primary CT, and its presence follows the formation of a CT [69,70].

Table 4.1 tabulates the twinned grains and twinning SFs from the results of Figure 4.5 and the larger EBSD maps shown as Annex Figure A.1. It reveals that the fraction of grains twinned in the PA condition is double that in the AE condition, irrespective of twinning mode. However, it should be noted that this difference may arise from the slightly higher stress/strain applied during the tensile deformation of the PA sample, as compared with the AE sample. Anomalous ETs with low and even negative SFs for twinning were observed, and their nucleation mechanisms were analyzed in next chapter [317]. The activation of CTs was also observed, agreeing well with the SF criteria (Figure 4.2(F)).

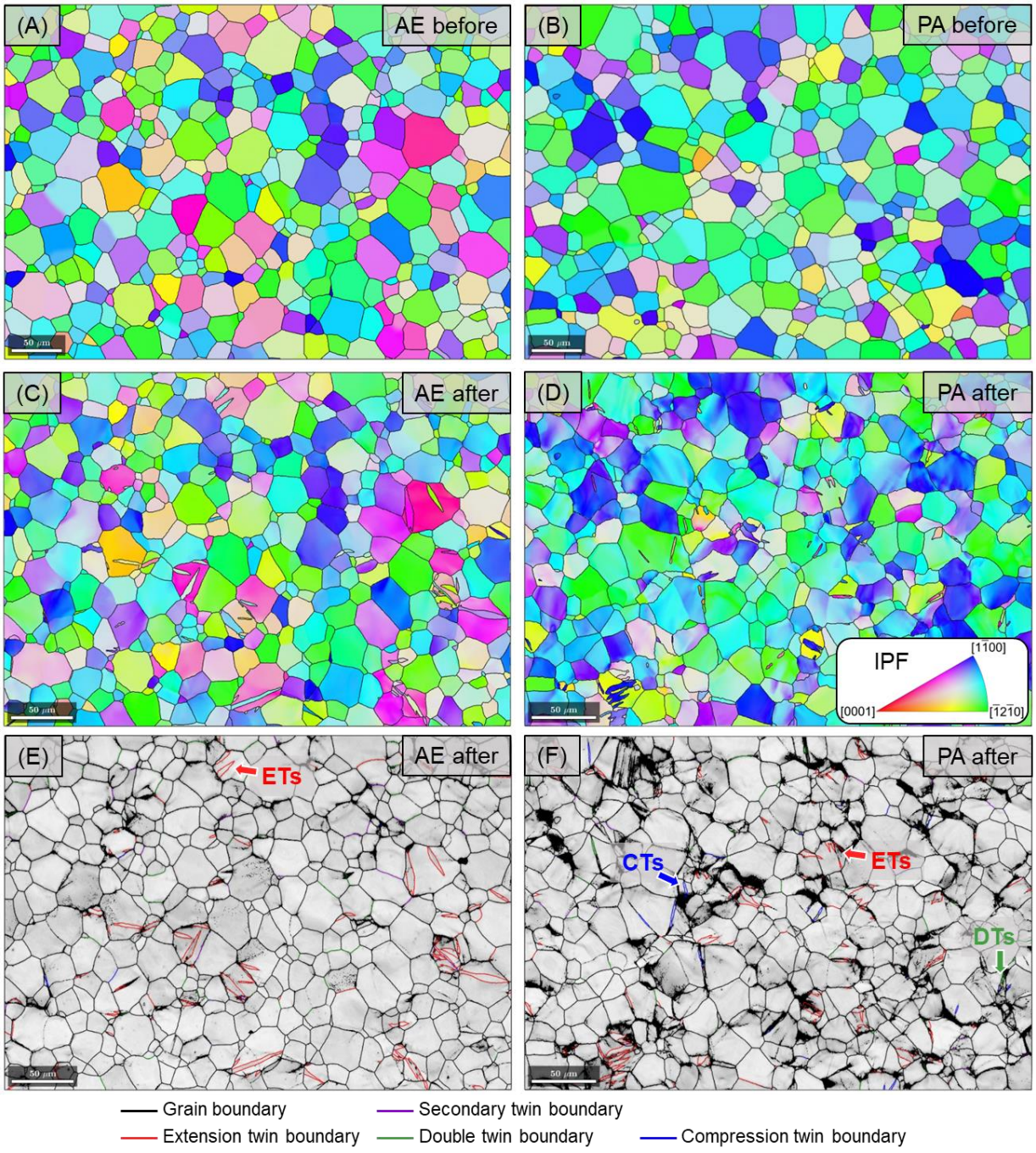

Figure 4.5: Microstructures of (A, C, E) AE and (B, D, F) PA samples (A-B) before and (C-F) after deformation. (A-D) EBSD orientation maps in terms of IPF and (E-F) BC maps. The reference direction of IPF is the horizontal direction, and all GBs were overlaid in black. ET, CT, secondary twin, and DT boundaries were highlighted in red, blue, purple, and green, respectively, in the BC maps. Note that their identification was performed by measuring the RA - misorientation angle of every boundary. The RA & angle pairs of ET, CT, secondary twin, and DT are $<2\bar{1}\bar{1}0>$ & 86.30°, $<2\bar{1}\bar{1}0>$ & 56.15°, $<1\bar{1}00>$ & 60.00°, and $<2\bar{1}\bar{1}0>$ & 37.50°, respectively. The threshold misorientation angle was set to 5°.

Table 4.1: Statistics of twinning features in AE and PA samples. Note that some CTs and DTs could not be identified by EBSD due to their small thickness in comparison with the step size. They were accurately identified using the point-counting method based on the BC maps [261]. Moreover, only 1 CT was identified in AE specimen after deformation with a twinning SF of 0.50.

	Grains analyzed	Grains twinned by ET	Grains twinned by CT	ET Schmid factors	CT Schmid factors
AE	973	67 (6.9%)	25 (2.6%)	0.099 ± 0.13	0.50 (1)
PA	1214	158 (13%)	63 (5.2%)	-0.022 ± 0.14	0.32 ± 0.13

GROD was used to analyze dislocation slip of both AE and PA samples. The distribution of the intragranular misorientation axes (expressed in mrd) in the crystal coordinate system of the Mg-4.5Zn alloy before deformation is depicted in Figure 4.6(B) for the AE specimen (that of the PA is very similar and it is not plotted for the sake of brevity). The distribution is very homogeneous, and no clear maximum is found. After tensile deformation, the misorientation axes moved towards the curved line joining $[\bar{1}100]$ to $[\bar{1}2\bar{1}0]$ for the AE and PA samples (Figure 4.6(C) and Figure 4.6(D)), but also towards [0001] for the PA sample (Figure 4.6(D)). The $[\bar{1}100]$ RA corresponds to the activation of <a> basal slip and/or <c + a> II pyramidal slip while $[\bar{1}2\bar{1}0]$ stands for the simultaneous activation of two <a> basal and/or <c + a> II pyramidal slip. Finally, the RA [0001] indicates the activation of <a> prismatic slip [270–272]. In addition, the low values of the maximum intensities below 2.0 mrd in Figure 4.6(C) and Figure 4.6(D) suggest that several slip deformation modes contribute simultaneously to the deformation and no one can be considered dominant [270].

The surface slip traces after deformation were observed by SEM and first analyzed using conventional EBSD-assisted slip trace analysis. The typical results are depicted in Figure 4.7. Distinct planar slip traces are observed in grain G1 of the AE sample (Figure 4.7(A)), that are nearly parallel to the calculated one for the (0001) basal plane (Figure 4.7(G)), indicating that <a> basal slip the main plastic deformation mechanism in grain G1. The activation of <c + a> II pyramidal slip in grain G2 of the AE sample was shown by the good match between the planar slip traces and the calculated ones for the $\{11\bar{2}2\}$ II pyramidal planes (Figure 4.7(B) and Figure 4.7(H)). Note that this conventional EBSD-assisted slip trace analysis

cannot distinguish between <a> pyramidal slip and <c + a> I pyramidal slip because both occur in the same SP. Moreover, most grains that show slip traces in the PA sample display non-planar (wavy or diffuse) characteristics (Figure 4.7(C)), which cannot be analyzed using conventional EBSD-assisted slip trace analysis.

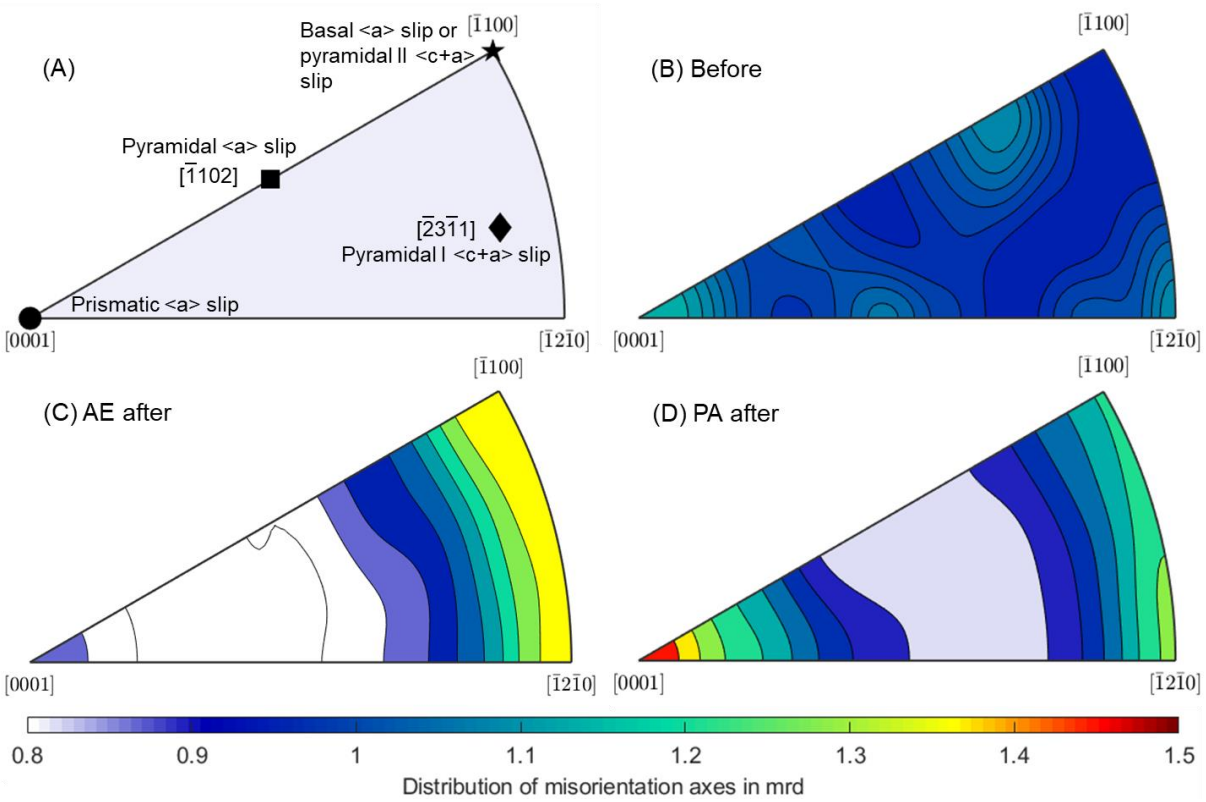

Figure 4.6: GROD results after analyzing all the grains in the whole EBSD map. (A) RAs associated with dislocation slip along different systems in Mg. Evolution of the distribution of intragranular misorientation axes in the crystal coordinate system (expressed in mrd) of AE and PA samples during tension: (B) before deformation for both AE and PA specimens (here showed for the AE specimen), (C) AE specimen after deformation, and (D) PA specimen after deformation.

ST-MLRA was used to elucidate the activation of <a> pyramidal slip and <c + a> I pyramidal slip. ST-MLRA combines the information of slip plane (obtained from conventional EBSD-assisted slip trace analysis) and slip direction (obtained from the translation of the projection of the grain orientation in the pole figure) to identify the actual slip system(s) that are active in one grain [203,273]. Therefore, ST-MLRA provides more accurate information than GROD and conventional EBSD-assisted slip trace analysis but requires a much larger experimental effort.

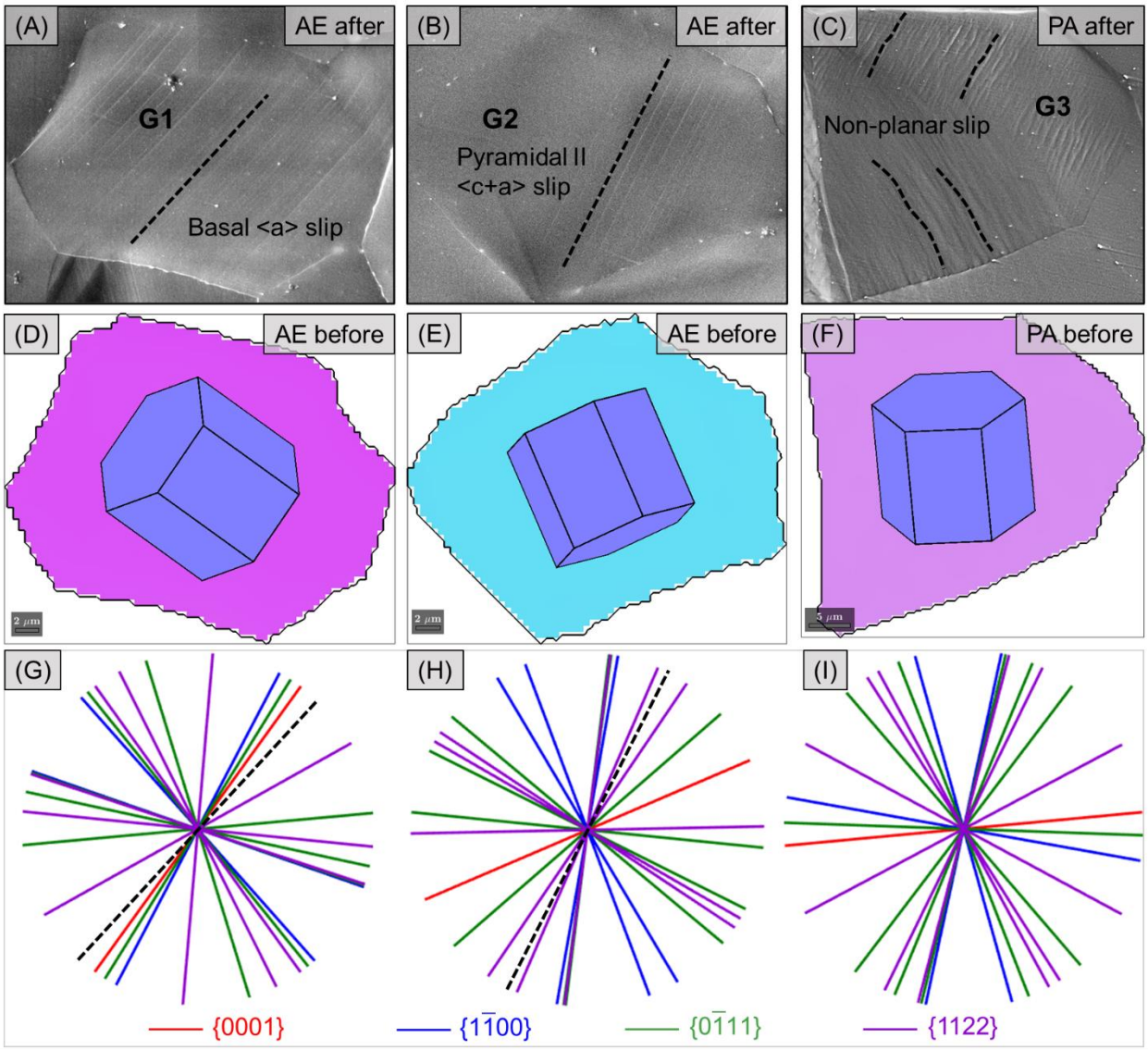

Figure 4.7: Typical slip traces on the surface after deformation. Planar slip traces in (A, D, G) Grain G1 showing <a> basal slip and (B, E, H) grain G2 showing <c + a> II pyramidal slip; non-planar slip traces in (C, F, I) grain G3, which cannot match with any theoretical slip traces. The reference direction of (D-F) IPF maps is the out-of-plane (Z) direction.

A typical example of the application of ST-MLRA to identify the active slip system (either <a> pyramidal slip or <c + a> I pyramidal slip) is depicted in Figure 4.8 in grain G4 with Euler angles of (48.1°, 51.3°, 5.4°). The orientation of the slip traces in the deformed grain G4 (Figure 4.8(A)) is in good agreement with the calculated one for the $(10\bar{1}1)$ pyramidal plane (Figure 4.8(B)). However, there are three possible slip directions in the I pyramidal plane: $[\bar{1}2\bar{1}0]$ (<a> dislocation; SF = 0.40, RA = $[\bar{1}012]$ (I)), $[\bar{2}113]$ (<c + a> dislocation; SF = 0.087, RA = $[1\bar{3}21]$ (II)), and $[11\bar{2}\bar{3}]$ (<c + a> dislocation; SF = 0.30, RA = $[2\bar{3}1\bar{1}]$ (III)). The experimental

projections of the orientation of grain G4 on the (0002) pole figure before and after deformation are plotted in Figure 4.8(C), which were compared with the predictions for the stretching of the projections corresponding to the three possible RAs in Figure 4.8(D). It is evident that the RAs of $[1\bar{3}21]$ (II) and/or $[2\bar{3}1\bar{1}]$ (III) lead to better predictions of the stretching of the pole figure than that of $[\bar{1}012]$ (I). It is concluded that the dominant slip system in grain G4 is the <c + a> I pyramidal slip.

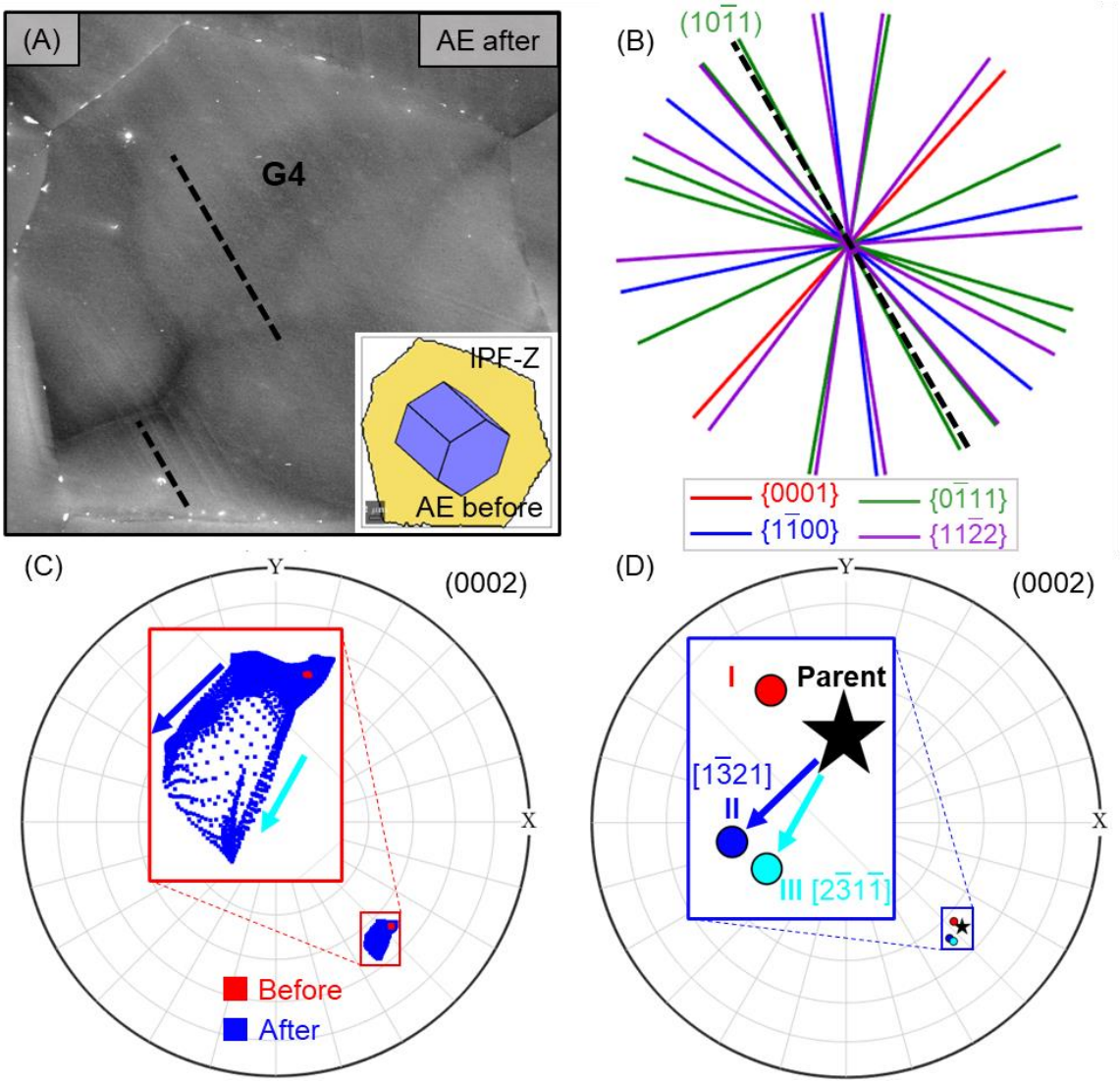

Figure 4.8: Application of ST-MLRA to identify the active slip system in the I pyramidal slip plane in grain G4. (A) SEM micrograph showing planar slip traces corresponding to (10$\bar{1}$1) plane. The EBSD map of grain G4 before deformation is also included in the lower right corner of (A). (B) Orientation of the slip traces of different slip planes from the EBSD map of grain G4 before deformation. (C) Experimental orientation projections on (0002) pole figure of grain G4 before (red) and after (blue) deformation. (D) Simulated change in the trace of the orientation of grain G4 on (0002) pole figure because of rotation around the three axes corresponding to three possible slip directions in the (10$\bar{1}$1) plane.

Table 4.2: Statistics of slip behavior in AE and PA samples using both conventional EBSD-assisted slip trace analysis and ST-MLRA at grain-level.

	Grains analyzed	Grains with slip traces	Planar slip traces					Non-planar slip traces
			<a> basal	<a> prismatic	<a> pyramidal	<c + a> pyramidal I	<c + a> pyramidal II	
AE	437	128	33 (25.8%)	11 (8.6%)	14 (10.9%)	14 (10.9%)	46 (36.0%)	10 (7.8%)
PA	437	144	2	4 (2.8%)	4 (2.8%)	4 (2.8%)	21 (14.5%)	109 (75.7%)

The dominant deformation mechanisms in the grains with planar slip traces were analyzed in both AE and PA samples through the combination of conventional EBSD-assisted slip trace analysis and ST-MLRA. The results are summarized in Table 4.2. In the AE sample, the most active slip system is <c + a> II pyramidal slip, followed by <a> basal slip, and the other three slip systems share a similar low activity. In comparison, pyramidal <c + a> slip only contributed by 5% to the total slip activity when compression was applied along the ND up to 5% strain in pure Mg with an average grain size of 45 µm and a strong basal texture [321]. Thus, the activity of <c + a> II pyramidal slip in Mg-Zn alloy without precipitates is enhanced by ~ 7-fold in comparison with pure Mg and this effect was also experimentally reported in [262,310]. For instance, Shi et al. [262] ascribed the enhanced non-basal slip activation in Mg-2Zn (wt.%) to the strong hardening effect of solid-solution Zn on <a> basal slip. In addition, atomistic simulations performed by Jang and Lee [322] claimed that Zn can activate pyramidal <c + a> slip by reducing the CRSS anisotropy among various slip systems. The hardening of <a> basal slip and softening of <a> prismatic slip by alloying Zn was also reported in the earlier works [323–325]. However, solid solution strengthening of alloying Zn was found to contribute to the hardening of all deformation modes in recent experimental single crystal micropillar compression tests on Mg-2Zn (at.%) alloy and the pyramidal to basal CRSS ratios remained still above 10 [266,316]. Indeed, there is not a consensus on the influence of Zn alloying to enhance non-basal slip activity.

More interestingly, the presence of β_1' precipitates led to a dramatic reduction in the proportion of planar slip traces and, accordingly, the activity of non-planar

slip traces increased dramatically by ~ 10-fold. In addition, the decline of planar slip trace activity depends on the specific slip system. It is maximum in the case of grains dominated by <a> basal slip traces (reduction by a factor of ~ 20), while this factor is ~ 3 for the other 4 non-basal slip systems. This agrees well with the reduced pyramidal to basal CRSS ratio (< 5) in the precipitation strengthened Mg-2Zn (at.%) alloys, mostly because the hardening of basal slip is considerably higher than that found for pyramidal slip by rod-like β_1' precipitates parallel to the $\vec{c}$ axis [266,316].

Another key issue is to figure out the underlying slip mechanisms in the grains that show non-planar slip traces, which cannot be analyzed using either conventional EBSD-assisted slip trace analysis or ST-MLRA. GROD, that is not influenced by the surface slip traces information, was used for this task. A typical example of the application of GROD to distinguish the active slip systems in grain G5 with distinct non-planar slip traces is presented in Fig. 4.9. It is obvious that the wavy slip traces in grain G5 (Fig. 4.9(A)) cannot be matched with any of the calculated ones for the different slip planes (Fig. 4.9(C)). However, the intragranular misorientation axes distribution of grain G5 in the crystal coordinate system shows a conspicuous maximum near the middle between [0001] and $[\bar{1}102]$ (Fig. 4.9(D)), that corresponds to the activation of <a> prismatic slip and pyramidal <a> slip (Fig. 4.6(A)), respectively. Therefore, the most likely active slip system in grain G5 is the simultaneous activation of <a> prismatic slip and <a> pyramidal slip.

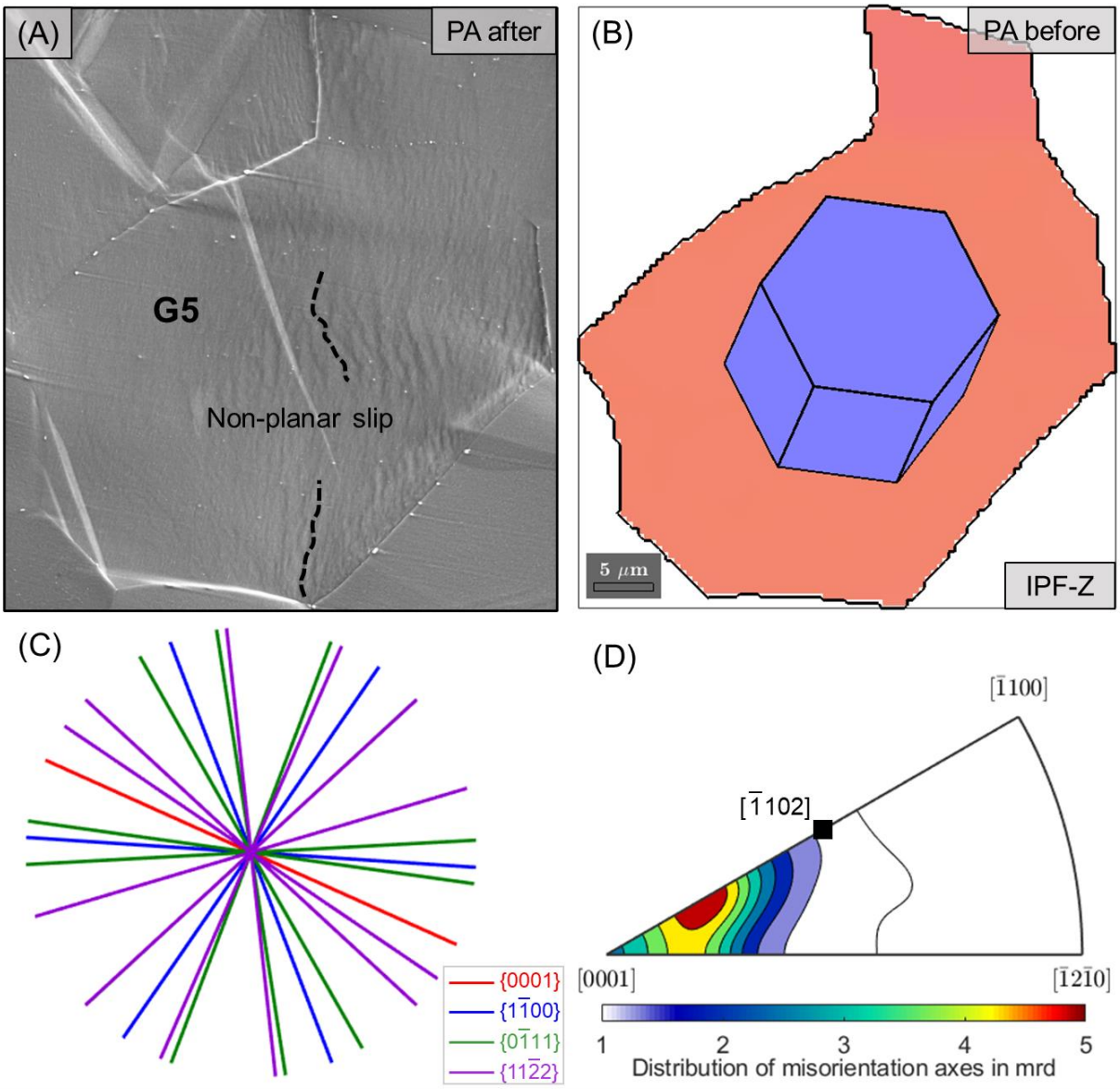

Figure 4.9: Application of GROD to distinguish the main active slip system(s) at the individual grain level (grain G5 with non-planar slip traces in PA sample). (A) SEM micrograph showing non-planar slip traces. (B) EBSD map of grain G5 before deformation. (C) Orientation of the slip traces of different slip planes from the EBSD map before deformation. (D) Distribution of intragranular misorientation axes of grain G5 after tensile deformation in the crystal coordinate system. The microstructure of bright contrast in the middle of Figure 4.9(A) may be a thin twin.

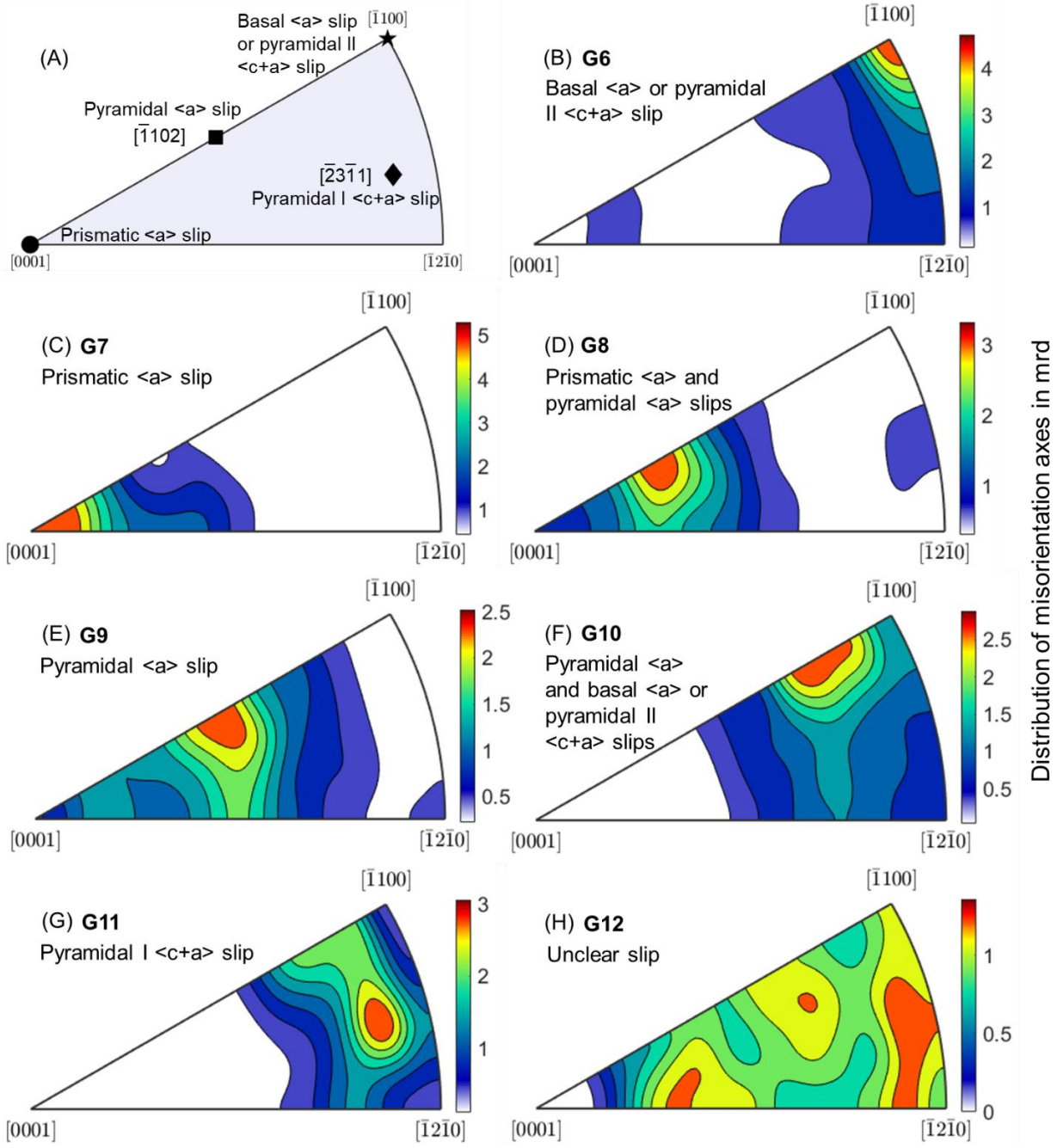

Figure 4.10: Intragranular misorientation axes distribution in the crystal coordinate system (expressed in mrd) in individual grains in the PA sample. (A) RAs associated with dislocation slip along different systems in Mg. (B) Maximum of intragranular misorientation axes distribution around [$\bar{1}$100] in grain 6. (C) *Idem* around [0001] in grain G7. (D) i*dem* between [0001] and [$\bar{1}$102] in grain G8. (E) *Idem* around [$\bar{1}$102] in grain G9. (F) *Idem* between [$\bar{1}$102] and [$\bar{1}$100] in grain G10. (G) *Idem* around [$\bar{2}\bar{3}$11] in grain 11. (H) The maximum intensity was low in grain G12, and no apparent maximum could be found. It was thus classified as 'unclear slip'. In other cases, the maximum in the intragranular misorientation axes distribution was found along the line between [$\bar{1}$100] and [$\bar{1}$2$\bar{1}$0], but their GROD maps were not presented here because they stand for the same active slip system(s) shown in Figure 4.10(B).

Table 4.3: Statistics of slip behavior of grains with non-planar slip traces in AE and PA samples using GROD at grain-level.

	AE	PA
Grains analyzed	10	109
<a> basal or <c + a> pyramidal II	2	11 (10.1%)
<a> prismatic	2	34 (31.2%)
<a> prismatic and pyramidal<a>	1	10 (9.2%)
<a> pyramidal	0	8 (7.3%)
<a> pyramidal and <a> basal or <c + a> pyramidal II	0	7 (6.4%)
<c + a> pyramidal I	1	2
Unclear	4	37 (34.0%)

A quantitative evaluation of active slip systems by GROD was also performed in grains with non-planar slip traces in both AE and PA samples. Representative results of this analysis in several grains are presented in Figure 4.10. The maximum of the intragranular misorientation axes distribution were found around [$\bar{1}$100] (grain G6 in Figure 4.10(B)), [0001] (grain G7 in Figure 4.10(C)), [$\bar{1}$102] (grain G9 in Figure 4.10(E)), and [$\bar{2}3\bar{1}1$] (grain G11 in Figure 4.10(G)), that correspond to the activation of <a> basal slip or <c + a> II pyramidal slip, <a> prismatic slip, <a> pyramidal slip, and <c + a> I pyramidal slip, respectively [270–272]. Moreover, the maximum of the distribution in the GROD maps corresponding to grains G8 and G10 (Figure 4.10(D) and Figure 4.10(F) cannot match with any RAs from single slip system, but it is distinctly located near the middle between two already-known RAs corresponding to two different slip systems. In particular, the maximum of the distribution is found near the middle between [0001] and [$\bar{1}$102] (grain G5 in Figure 4.9 and grain G8 in Figure 4.10(D)). Thus, the most likely active slip systems in these grains are <a> prismatic and <a> pyramidal (Figure 4.9 and Figure 4.10(D)). Similarly, the maximum of the distribution locating near the middle between [0001] and [$\bar{1}$102] stands for the activation of <a> pyramidal and <a> basal or <c + a> II pyramidal s (grain G10 in Figure 4.10(F)). Besides, no obvious maximum of the distribution is observed in some grains, e.g., grain G12 in Figure 4.10(H), thus they were classified as 'unclear slip'.

The results of the GROD analysis in grains with non-planar slip traces are depicted in Table 4.3 for the AE and PA sample. After 'unclear slip', <a> prismatic slip is dominant in the grains with non-planar slip traces in the PA sample. The

other cases are distributed evenly except for a relatively low intensity of <c + a> I pyramidal slip. If the 'unclear slip' cases are not considered, ~ 76% of grains with non-planar slip traces in the PA sample were associated with the activation of <a> non-basal slip, mostly <a> prismatic slip, in line with the maximum of the intragranular misorientation axes locating around [0001] in Figure 4.6(D). Only 10 grains with non-planar slip traces were found in the AE sample and, thus, the information is not relevant for the statistical viewpoint.

In addition, the dominant slip systems were also analyzed by GROD in grains with planar slip traces in both AE and PA samples. The results are presented in Table 4.4. In these grains, the most active slip system(s) are <a> basal and/or <c + a> II pyramidal slip, and the other three slip systems exhibit a relatively lower activity in both AE and PA conditions. These results are in good agreement with the statistical data of Table 4.2, obtained using both conventional EBSD-assisted slip trace analysis and ST-MLRA. Besides, the nearly similar results of Table 4.2 and Table 4.4 using different techniques demonstrate that these techniques can provide comparable and credible information on the active slip systems at the grain level.

Table 4.4: Statistics of slip behavior in grains with planar slip traces in AE and PA samples using GROD at grain-level.

	AE	PA
Grains analyzed	118	35
<a> basal or <c + a> pyramidal II	53 (44.9%)	16 (45.7%)
<a> prismatic	7 (5.9%)	5 (14.3%)
<a> prismatic and pyramidal<a>	1	2
<a> pyramidal	1	1
<a> pyramidal and <a> basal or <c + a> pyramidal II	9 (7.6%)	0
<c + a> pyramidal I	4 (3.4%)	3
Unclear	43 (36.4%)	8 (22.9%)

4.3.4. Analysis of the interaction between dislocations and precipitates by TEM

TEM analysis was performed on the PA sample deformed to ~ 10% engineering strain to further understand the effect of β_1' precipitates on the plastic deformation mechanisms. The weak beam dark field images of the same grain and/or near the

same area are depicted in Figure 4.11 under three different two-beam diffraction conditions, i.e., $\vec{g}$ = $[0002]_{Mg}$, $\vec{g}$ = $<10\bar{1}0>_{Mg}$, and $\vec{g}$ = $<11\bar{2}0>_{Mg}$, respectively. The $\vec{g}\cdot\vec{b}$ analysis was used to determine the active Burgers vector type, based on Table 2.1. From the invisible contrast of Figure 4.11(A), both <c> type and <c + a> type dislocations can be easily excluded. The dislocations are visible in Figure 4.11(B) and Figure 4.11(C), indicating that the values of $\vec{g}\cdot\vec{b}$ are not zero. Their combination reveals that the dominant slip dislocation in the PA sample is of <a> type, which is in good agreement with the results of Table 4.3.

Detailed analysis was also conducted on the line defects. Based on the diffraction patterns, the theoretical dislocation traces of various slip systems were simulated for both pure edge and pure screw dislocation conditions, as shown in Figure 4.11(E) and Figure 4.11(F). It is clear that the angle between some short dislocation lines (in white) and the precipitate axis ($[0002]_{Mg}$) is ~ 90°. Under the assumption of a pure edge dislocation, -whose line segments are parallel to the SP-, the most likely slip system for these dislocations should be <a> basal slip. However, under the assumption of pure screw dislocation, -whose line segments are perpendicular to the SP-, they belong to the <a> prismatic slip system. Besides, some kinked or curved dislocation lines (in red) were also observed, and their angles with respect to $[0002]_{Mg}$ are not 90° or 0°, indicating that these line segments may lie in pyramidal planes and/or exist as mixed dislocations. Typical curved dislocation lines and one curved dislocation line across $\vec{c}$ axis rod-shaped precipitates are shown in Figure 4.11(D). Thus, it's mostly likely that <a> basal screw dislocations can cross-slip to the prismatic plane when they are stopped by the precipitates and slip in the prismatic plane, parallel to the precipitates. In addition, those spots with bright contrast in Figure 4.11(C) could be related to the other dislocation lines with <a> components, and these dislocation lines are on the prismatic plane parallel to the zone axis of $[10\bar{1}0]_{Mg}$.

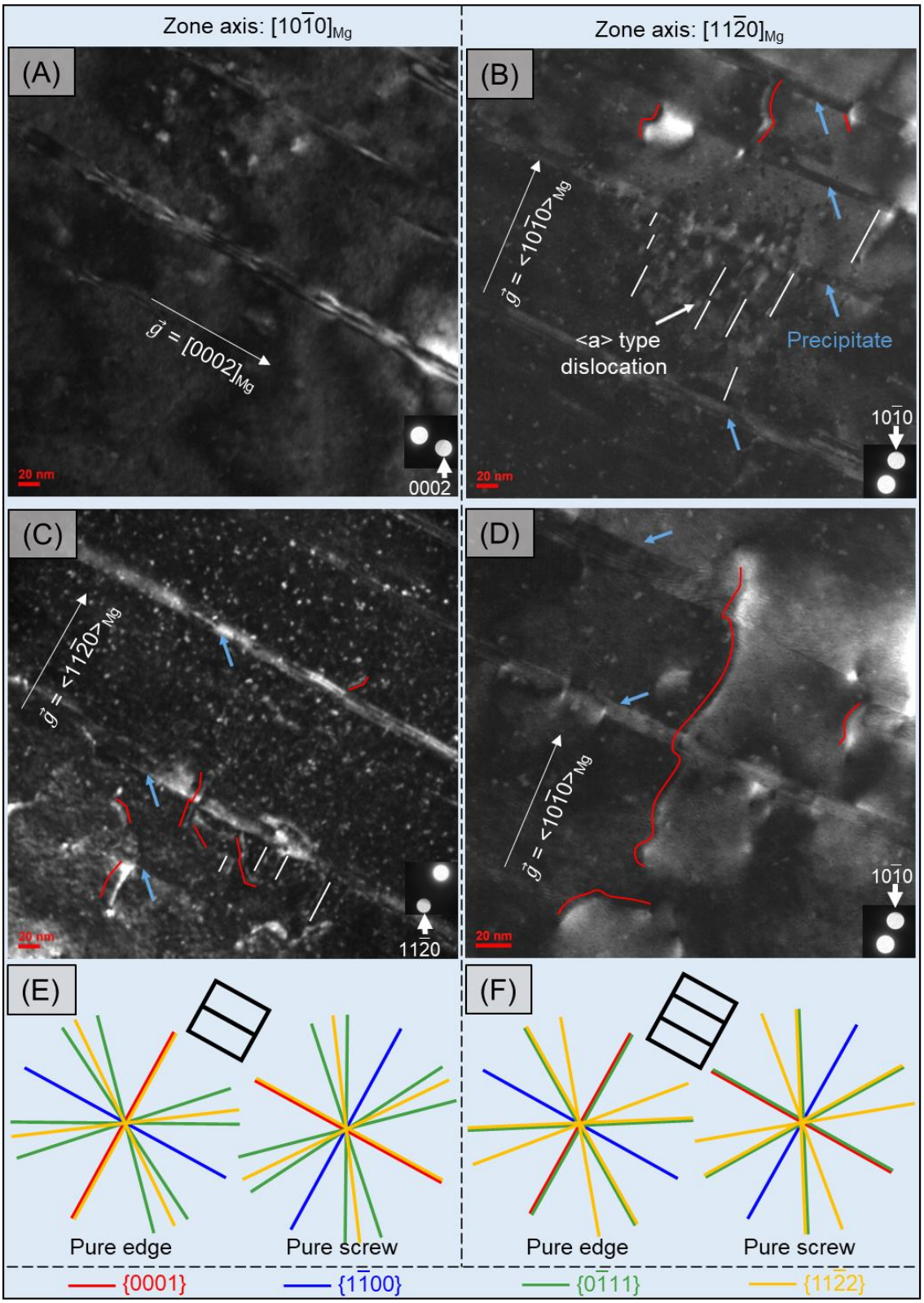

Figure 4.11: Analysis of the dislocation structure in the deformed PA sample. (A) $\vec{g}$ = $[0002]_{Mg}$, and (C) $\vec{g}$ = $<11\bar{2}0>_{Mg}$ with the zone axis of $[10\bar{1}0]_{Mg}$. (B, D) $\vec{g}$ = $<10\bar{1}0>_{Mg}$ with the zone axis of $[11\bar{2}0]_{Mg}$. Theoretical traces corresponding to various slip dislocation planes under the zone axes of (E) $[10\bar{1}0]_{Mg}$ and (F) $[11\bar{2}0]_{Mg}$, for pure edge and pure screw dislocations.

4.4. Conclusions

The dominant plastic deformation mechanisms were studied in an extruded Mg-4.5Zn (wt.%) alloy with and without $\vec{c}$ axis rod-shaped β_1' precipitates. The analysis was carried out by a combination of EBSD, conventional slip trace analysis, GROD, ST-MLRA, and weak beam dark field - TEM. The main conclusions are summarized as follows:

(1) The dominant plastic deformation mechanisms of Mg-Zn alloy without precipitates were <c + a> II pyramidal slip, followed by <a> basal slip. They led to planar slip traces on the specimen surface. The dominance of <c + a> II pyramidal slip with respect to <a> basal slip in the sample without precipitates could be attributed to the texture (that favors pyramidal slip) and to solution hardening induced by Zn atoms on basal slip.

(2) The dominant plastic deformation mechanisms in Mg-Zn alloy containing β_1' rod-shaped precipitates were <a> prismatic slip, followed by <c + a> II pyramidal slip. <a> I pyramidal, <c + a> pyramidal I, and <a> basal slips were also present, but they were not very relevant. Moreover, non-planar slip traces were dominant, particularly in the grains showing <a> non-basal slip.

(3) The β_1' rod-shaped precipitates hindered the glide of <a> basal slip dislocations and increased the CRSS for basal slip. Under these circumstances, plastic deformation progressed by cross-slip of basal dislocations to the prismatic plane followed by the glide of <a> prismatic slip dislocations parallel to the precipitates.

(4) Future investigations may take advantage of advanced in-situ diffraction techniques combined with crystal plasticity / phase field simulations to provide a more comprehensive understanding of the <a> dislocation cross-slip mechanism and a quantitative estimation of the contribution of the active slip systems to the overall plastic deformation.

5. Deformation mechanisms of an as-extruded Mg-1Al alloy studied by in-situ EBSD

5.1. Introduction

Mg and its alloys have high specific stiffness and strength, and thus, have a large potential for structural components in transport [141,326,327]. Nevertheless, one critical issue that hinders their broad application is the low room temperature ductility and formability because of the limited number of available slip systems in the HCP crystal structure. The dominant deformation mode in Mg at room temperature is {0001} <11$\bar{2}$0> basal slip that has the lowest CRSS (≈ 0.5 MPa for pure Mg [5,6]). However, <a> basal slip can only provide 2 independent slip systems in the basal plane and other deformation systems have to be active to accommodate the deformation along the $\vec{c}$ axis of the HCP lattice [13]. They include {10$\bar{1}$1} <11$\bar{2}\bar{3}$> I pyramidal slip, {11$\bar{2}$2} <11$\bar{2}\bar{3}$> II pyramidal slip, as well as {10$\bar{1}$2} <10$\bar{1}$1> ET, and {10$\bar{1}$1} <10$\bar{1}$2> CT [328]. It should be noted that twinning is a polar mechanism that only occurs when the shear deformation is applied in the appropriate direction so the twinned region has a mirror symmetry with the parent region along the twin plane [16]. Six different ET variants are available and all of them are associated with an 86.30° rotation of the $\vec{c}$ axis around the <11$\bar{2}$0> axis. ET has the lowest value of the CRSS among the deformation systems accommodating the deformation along the $\vec{c}$ axis, and becomes the second dominant plastic deformation in HCP grains that are deformed in the tension along the crystallographic $\vec{c}$ axis or in the compression perpendicular to the crystallographic $\vec{c}$ axis [329,330,50].

Owing to the importance of ET in Mg alloys, many investigations have been devoted to analyze the mechanisms of twin nucleation, twin variant selection and twin growth [22,26,46,59,97,331–337]. Insofar, the most common criterion to assess the occurrence of ET and to predict the active twin variant comes from the SF. For instance, Hong et al. analyzed the active ET variants using EBSD in a hot-

rolled AZ31 Mg alloy that was deformed either in compression perpendicular to the $\vec{c}$ axis or in tension parallel to the $\vec{c}$ axis [338]. The most of the active twin variants in each grain had the highest SF along both strain paths. Similar results can be found in other investigations [48,49,51], although it should be noted that the Mg alloys analyzed in these papers presented a very sharp texture and the soft orientations for ET were particularly well defined.

However, the SF criteria cannot explain the development of ET in grains with SFs close to 0, or even negative, observed in Mg alloys with a strong texture unsuitable for ET or even in particular grains of Mg alloys with random texture [61,67,202,339,340]. For example, Koike et al. reported the nucleation of ETs in grains with negative SFs in an AZ31 Mg alloy deformed in tension along the RD at room temperature [61]. Similarly, activation of ET variant in which the SF was low in the rank (4^{th} out of 6 variants) was reported by Zhou et al. via in-situ SEM / EBSD in a Mg-5Y (wt.%) alloy with a weak texture [202]. Both investigations attributed the formation of ET or the one particular ET variant to the stress concentration caused by localized <a> basal slip. Koike et al. [61] argued that <a> basal slip in twinned grains was responsible, while Zhou et al. [202] claimed the cause could be found in the basal slip activities in the neighbor grains. In addition to slip-assisted ET [59,67], the activation of the anomalous ETs was also reported to be associated with the twins in neighbor grains near the GBs [66,332] and to local stress fluctuations near GBs [265,318]. More recently, twin nucleation was studied by EBSD in > 3000 grains in a hot-rolled AZ31B Mg alloy deformed in different orientations with respect to the RD [341]. Up to 28 different relevant parameters, categorized in four different groups (loading condition, grain shape, global SF, and GB features) were also recorded for each grain. This information was used to train supervised ML classification models to analyze the influence of the microstructural features on the nucleation of ETs. It was concluded that twin nucleation is favored in larger grains and in grains with high SFs for twinning, but also that ET may form in the grains with very low or even negative SFs for twinning if they have at least one smaller neighbor grain and another one (or the same) that is more rigid. Moreover, ET of small grains with high SFs is favored if

they have low <a> basal slip SFs and have at least one neighbor grain with a high <a> basal slip SF that will deform easily.

Thus, prior investigations concluded that the nucleation of anomalous ETs was triggered by inhomogeneous localized deformation but there is not a consensus on the underlying nucleation mechanism of abnormal ETs. Furthermore, most of these investigations were focused on the nucleation of the anomalous ETs, whilst their evolution with strain level was not analyzed although this point is relevant to understand the role of these anomalous ETs on the plastic deformation and fracture of Mg alloys. To fill these gaps, the nucleation and growth of anomalous ETs were analyzed in detail by means of in-situ EBSD as a function of the applied tensile strain in an extruded Mg-1Al (at.%) alloy with prismatic texture. The correlation between the microstructural features and the SFs of anomalous ETs was statistically established. Moreover, GROD [50,211] and ST-MLRA [187,203] were used to obtain a detailed information of active deformation mechanisms in and around each grain. This information provides a detailed picture of the mechanisms responsible for the activation and growth of anomalous ETs with low or negative global twinning SFs in Mg alloys.

5.2. Materials and experimental techniques

Dog-bone Mg-1Al (at.%) alloy samples with dimensions of 15 × 5 × 2.5 mm^3 and 10 × 3 × 1.5 mm^3 (length × width × thickness) were cut by electro-discharge machining to perform *ex-situ* and in-situ EBSD tensile tests along the ED. The samples for the in-situ EBSD tests were mechanically polished using SiC paper, 0.5, 0.05 µm diamond slurries, and 40 nm oxide suspensions. Slight etching using 5% Nital solution (a mixture of nitric acid and ethanol) was applied for ~ 5 seconds on the surface.

The tensile stress-strain curve was obtained from the *ex-situ* tensile tests in an Instron 8501 universal testing machine. Load was measured with a 5.0 kN load cell and deformation with an extensometer of 12.5 mm gauge length (Instron model 2620-602) at an approximate strain rate of 10^{-3} s^{-1}. The in-situ EBSD tensile tests were carried out within the SEM (Apreo 2S LoVac, FEI Company, Portland, OR,

USA) using a micromechanical testing machine (Kammrath and Weiss Technologies, Inc., Model MZ.Sb) under displacement control at 1 μm·s^{-1}, which led to an approximate strain rate of 10^{-4} s^{-1}. The in-situ EBSD tensile tests were interrupted at different engineering strains of 1.5%, 4.5%, 10.0%, and 15.3% and the sample was analyzed by EBSD (Oxford HKL Channel 5, Oxford Instruments, Abingdon, UK; step size: 0.5 μm, working distance: 10 mm) in a region of 374.0 × 493.5 μm^2 near the center of the gauge. Besides, the initial microstructure of Mg-1Al alloy before deformation was also studied by EBSD with a step size of 1 μm in a region of 1130 × 1645 μm^2.

The EBSD data were analyzed and plotted using in-house codes based on MTEX (version 5.7.0), an open-source MATLAB toolbox [200,259]. The detailed twin systems of all ET (ET1-ET6) and CT (CT1-CT6) variants are tabulated into Table 5.1. For the active twin variant identification, the first step is to calculate the theoretical orientation ($\boldsymbol{o}_{t\_the}$) of a twinned grain, based on the twin variant information and the mean orientation of the grain ($\boldsymbol{o}_g$) before deformation according to:

$$\boldsymbol{o}_{t\_the} = \boldsymbol{o}_g * \boldsymbol{rot} \tag{5.1}$$

where $\boldsymbol{rot}$ matrix is calculated with MATLAB using the function of *rotation.byAxisAngle (axis, angle)* in MTEX [200,259]. It takes into account the RA vector ($\overrightarrow{RA}_{sc}$) in the sample coordinate system and the rotation angles θ of 86.30° and 56.15° for ET and CT, respectively. $\overrightarrow{RA}_{sc}$ was calculated by eq. (2.5), with the critical twin systems shown in Table 5.1. The second step is to compute the misorientation angle between ($\boldsymbol{o}_{t\_the}$) and the orientation of the active twin. Among 6 CTs and 6 ETs, the twin variant exhibiting the lowest misorientation (i.e., disorientation) angle is the active one.

Additional GROD analysis was conducted in several grains, -in which anomalous twins with low and negative SFs nucleated and grew-, using the mean orientation of the grain before deformation as the reference orientation. The EBSD-derived in-plane lattice rotation, ϑ_i, around the sample coordinate axis i (either X, Y or Z) can be calculated according to the eq. (2.9).

For the individual grains, the longitudinal strain (ε_1) along the loading direction was calculated as:

$$\varepsilon_1 = \frac{L_g - L_g^0}{L_g^0} \tag{5.2}$$

where L_g^0 and L_g represents the grain length along the loading direction before and after deformation, respectively.

The active slip systems of one grain at the deformation up to 15.3% were analyzed by ST-MLRA from both the slip traces (that indicate the SP) and the stretched projection of the grain on the pole figure (that reveals the major RA) in the grain [203]. Note that ST-MLRA can only be used to analyze the active slip system in grains with discernible slip traces. This information was useful to correlate the localized lattice rotation (obtained by GROD) with the active slip behavior at grain level.

Table 5.1: Denominations and twin systems of all possible ET and CT variants.

	Nomination	Rotation axis	Twinning plane	Twinning direction
ETs	ET1	$[\bar{1}2\bar{1}0]$	$(\bar{1}012)$	$[10\bar{1}1]$
	ET2	$[1\bar{2}10]$	$(10\bar{1}2)$	$[\bar{1}011]$
	ET3	$[\bar{1}\bar{1}20]$	$(1\bar{1}02)$	$[\bar{1}101]$
	ET4	$[11\bar{2}0]$	$(\bar{1}102)$	$[1\bar{1}01]$
	ET5	$[2\bar{1}\bar{1}0]$	$(01\bar{1}2)$	$[0\bar{1}11]$
	ET6	$[\bar{2}110]$	$(0\bar{1}12)$	$[01\bar{1}1]$
CTs	CT1	$[1\bar{2}10]$	$(10\bar{1}1)$	$[10\bar{1}\bar{2}]$
	CT2	$[\bar{1}2\bar{1}0]$	$(\bar{1}011)$	$[\bar{1}01\bar{2}]$
	CT3	$[11\bar{2}0]$	$(\bar{1}101)$	$[\bar{1}10\bar{2}]$
	CT4	$[\bar{1}\bar{1}20]$	$(1\bar{1}01)$	$[1\bar{1}0\bar{2}]$
	CT5	$[\bar{2}110]$	$(0\bar{1}11)$	$[0\bar{1}\bar{1}2]$
	CT6	$[2\bar{1}\bar{1}0]$	$(01\bar{1}1)$	$[01\bar{1}\bar{2}]$

5.3. Results and discussion

5.3.1. Microstructure

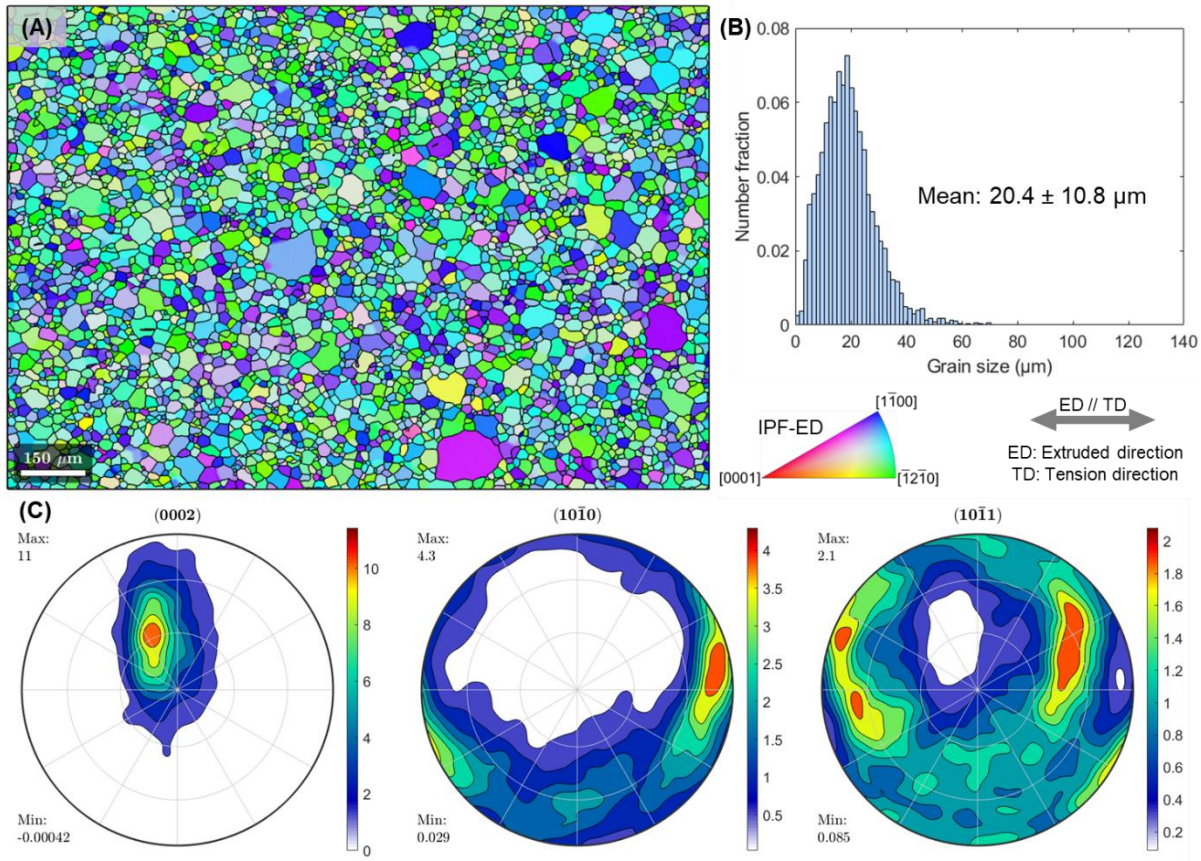

Figure 5.1: Microstructure of Mg-1Al alloy before deformation. (A) EBSD orientation map colored with respect to the ED according to IPF. All GBs were overlaid in black. (B) Grain size distribution histogram. (C) (0002), (10$\bar{1}$0), and (10$\bar{1}$1) pole figures. The normal direction of observed EBSD is perpendicular to the ED and the loading direction is parallel to the horizontal direction throughout this chapter.

The microstructure of Mg-1Al alloy along the ED before deformation is depicted in Figure 5.1. Most of the grains in the IPF of Figure 5.1(A) are colored in blue and green and their $\vec{c}$ axis is perpendicular to the ED, following with the (0002) pole figure. The maximum intensity of (10$\bar{1}$0) and (10$\bar{1}$1) pole figures is only 4.3 and 2.1, respectively, while that of (0002) pole figure is 11 (Figure 5.1(C)). The grain size distribution is plotted in Figure 5.1(B) and the average grain size is 20.4 ± 10.8 μm.

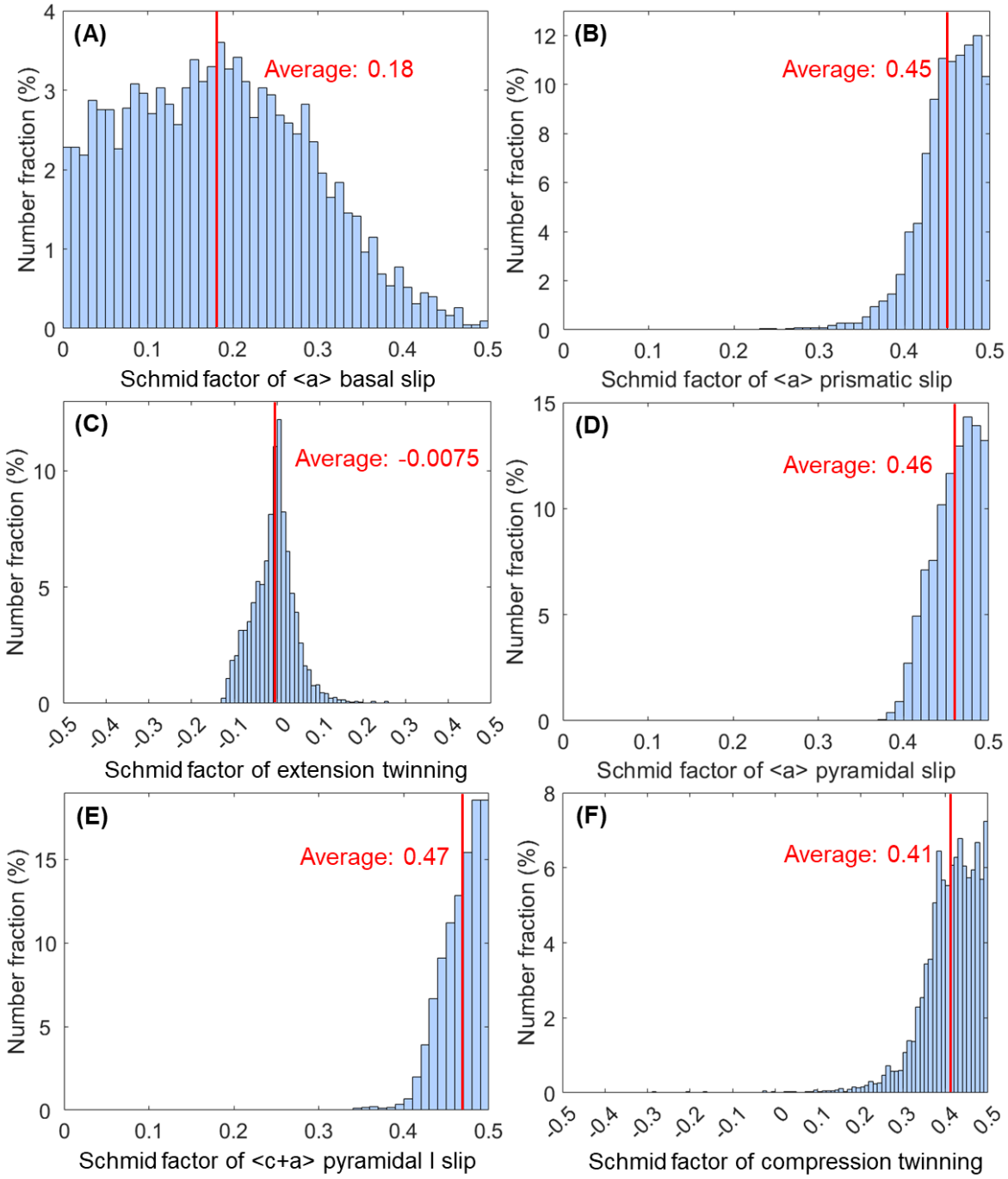

Figure 5.2: Histograms of the SFs for various deformation modes during tensile deformation along the ED. (A) <a> basal slip, (B) <a> prismatic slip, (C) ET, (D) <a> pyramidal slip, (E) <c + a> I pyramidal slip, and (F) CT. The average grain orientation obtained from the initial EBSD map was used to calculate the SFs for each grain. For each deformation mode of one grain, the highest SF among all slip systems or twin variants was chosen. 4251 grains were considered for the statistics.

Based on the average orientations of the grains before deformation, the SFs of various deformation modes were calculated in tension along the ED and are plotted

in Figure 5.2 [123]. The SFs for <a> basal slip were low but this deformation mode is always expected to be active due to its low CRSS [5,6]. Compared to <a> basal slip, lower SFs are found for ET and 55% of them are negative. Thus, this mechanism should not be active during deformation based on the SF criterion. High SFs are observed for <a> prismatic slip, <a> pyramidal slip, <c + a> I pyramidal slip, and CT but their activities are hindered by their relatively high CRSS [11,12,245,299,342].

5.3.2. Mechanical behavior

The engineering stress-engineering strain and strain hardening rate-true strain curves in tension of the Mg-1Al alloy are plotted in Figure 5.3(A) and Figure 5.3(B), respectively. The near parabolic shape of the tensile stress-strain curve in Figure 5.3(A) suggests that the deformation of Mg-1Al alloy is dominated by dislocation slip [10] but oscillations in the stress-strain curve are clearly observed after yielding. Accordingly, serrations in strain hardening rate curve that correspond to abrupt stress drops followed by sudden stress increments, particularly between 1% and 3% strain (Figure 5.3(B), indicate that twinning may have also been active [343].

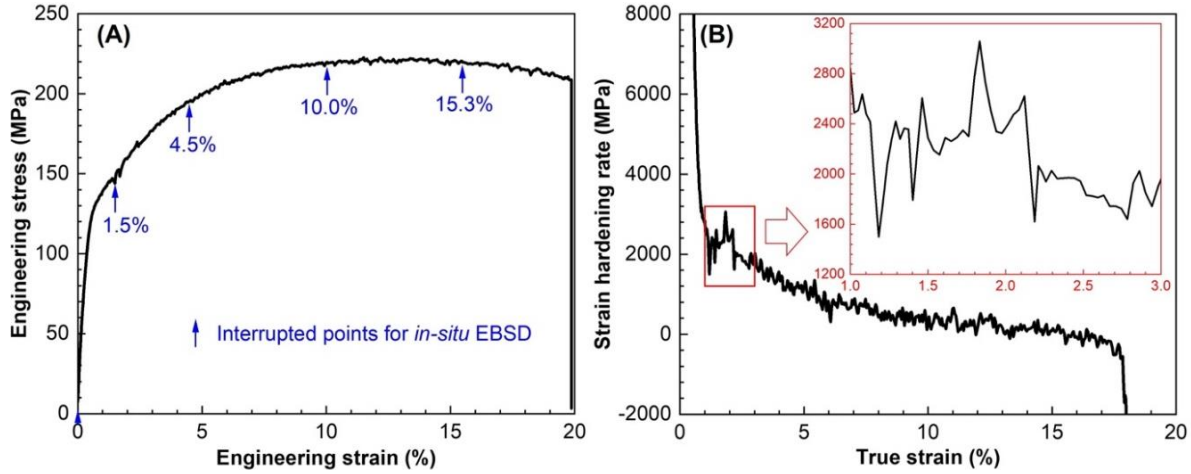

Figure 5.3: Tensile behavior of Mg-1Al alloy. (A) Engineering stress-engineering strain and (B) strain hardening rate-true strain curves in tension along the ED.

5.3.3. Deformation mechanisms

The in-situ EBSD maps showing the grain orientations according to the IPF-ED and the BC maps of the Mg-1Al alloy deformed in tension along the ED up to 1.5%, 4.5%, 10.0%, and 15.3% are plotted in Figure 5.4, together with the initial microstructure. A few new lamellar grains appeared after 1.5% strain (Figure 5.4(B)) and they were identified as ETs from the GB misorientation axis and angle in Figure 5.4(G). More ETs were activated as the tensile strain increased to 4.5% (Figure 5.4(C) and Figure 5.4(H)) and this behavior conflicts with the low and even negative SFs of ETs in Figure 5.2(B). Besides, 3 CTs were also found in the samples deformed up to 4.5%. As the tensile strain further increased up to 15.3%, the number of ETs did not change, whilst more CTs and few DTs were observed. Note that DTs are formed by nucleating of a secondary ET within a CT, indicating that its presence follows the formation of a CT [69,70].

The evolution of various ET features is plotted in Figure 5.5 as a function of the applied strain. The number of active ETs increased from 23 at 1.5% to 106 at 4.5%, and remained practically constant afterwards (Figure 5.5(A)), in agreement with the serrations observed in the strain hardening rate curve (Figure 5.3(B)). This result indicates that nucleation of ETs is associated with the onset of plastic deformation of the Mg-1Al alloy. The number of grains twinned by CT increased gradually from 1.5% to 15.3% (Figure 5.5(A)) although the fraction of grains twinned by ET and CT was ~16% and ~3%, respectively, at 15.3% strain, indicating the smaller contribution of CT to plastic deformation in comparison with ET. Besides, two grains were observed in which CT and ET were simultaneously activated. This is interesting because the stress orientations to activate CT and ET are opposite, e.g., compression and tension along the crystallographic $\vec{c}$ axis of HCP lattice will favor the nucleation of CT and ET, respectively. That means severe stress / strain gradients should be present within these two grains.

Most active ETs exhibit negative SFs, with an average of ~ -0.15, regardless of the applied strain (Figure 5.5(B)) and, thus, they should not have been nucleated according to the SF criterion. It should be noted that the twinned area fraction for each parent grain increased (Figure 5.5(C)), and the aspect ratio of ETs decreased

(Figure 5.5(D)) with the applied strain. These metrics indicate these anomalous ETs grew with the applied strain even though they were not suitably oriented according to the SF criterion.

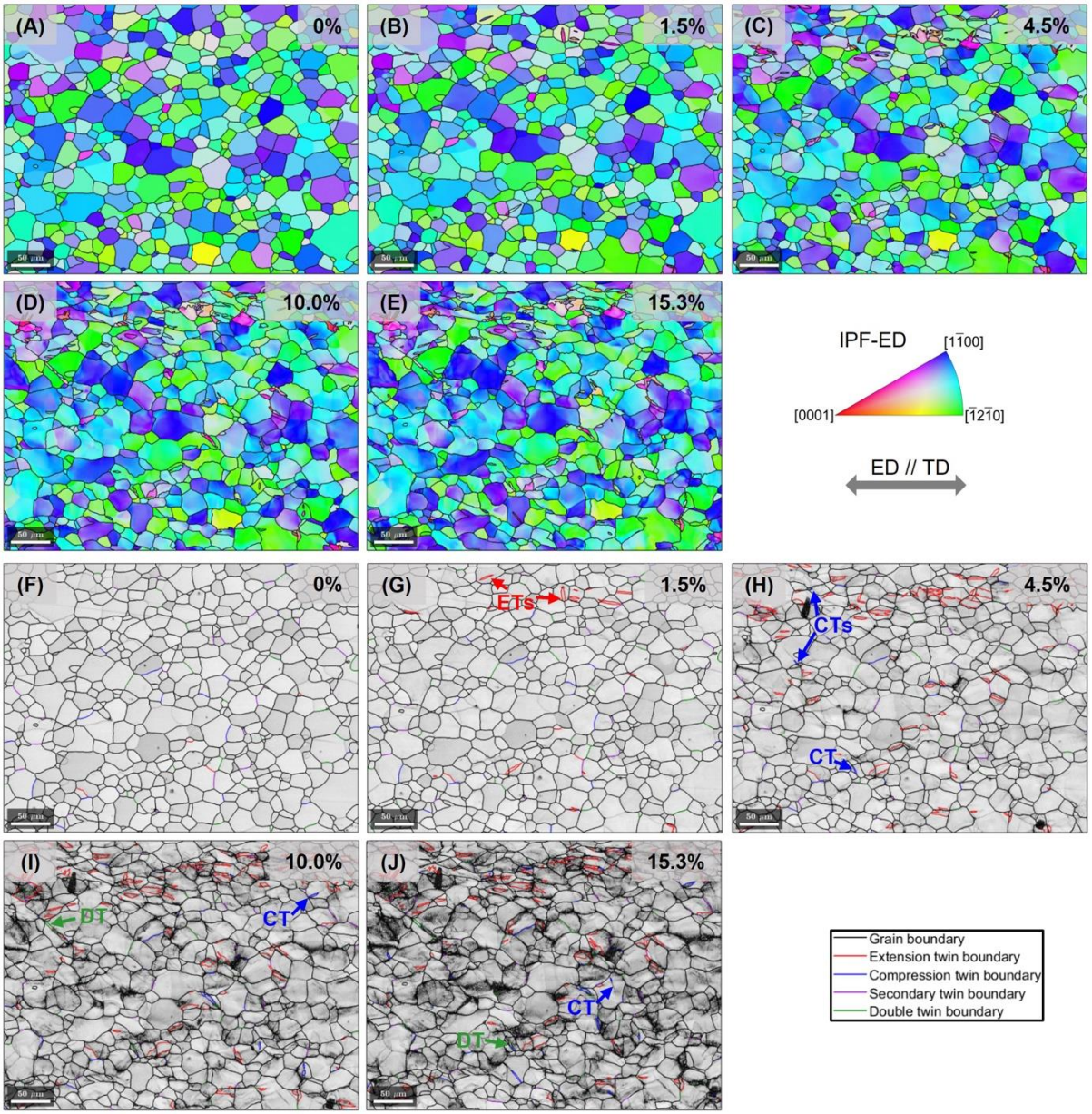

Figure 5.4: Microstructural evolution of Mg-1Al alloy during tension as characterized by the in-situ EBSD. EBSD (A-E) IPF maps and (F-J) BC maps of the Mg-1Al alloy (A, F) before deformation, and after tension up to (B, G) 1.5%, (C, H) 4.5%, (D, I) 10.0%, (E, J) 15.3%. The reference direction of IPF was the ED, and all GBs were overlaid in black. ET, CT, secondary twin, and DT boundaries were highlighted in red, blue, purple, and green, respectively, in the BC maps. Note that their identification was performed by measuring the RA - misorientation angle of every boundary. The RA & angle pairs for ET, CT, secondary twin and DT are <2$\bar{1}\bar{1}$0> & 86.30°, <2$\bar{1}\bar{1}$0> & 56.15°, <1$\bar{1}$00> & 60.00°, and <2$\bar{1}\bar{1}$0> & 37.50°, respectively.

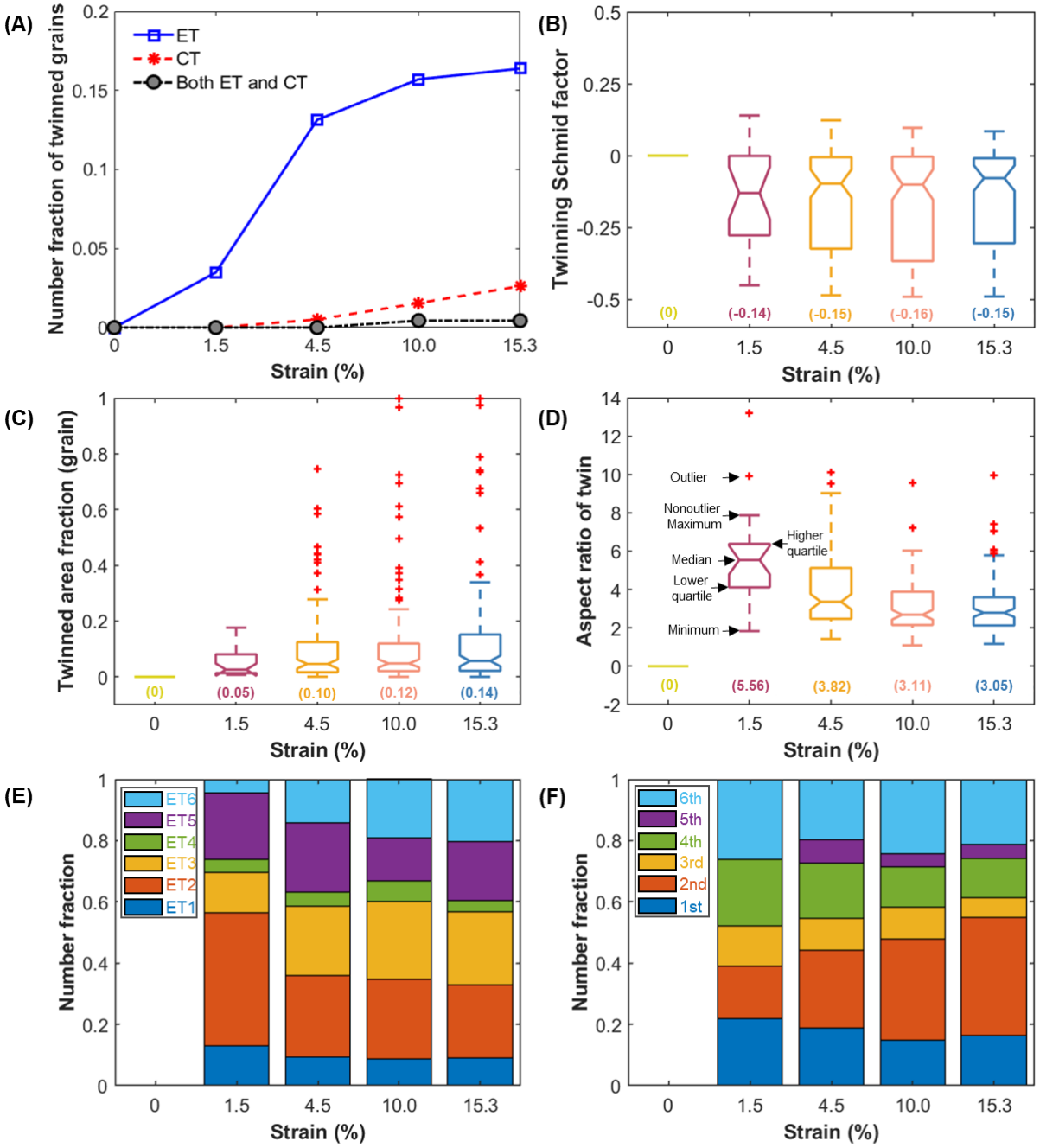

Figure 5.5: Evolution of ET features in the Mg-1Al alloy as a function of the applied tensile strain along the ED. (A) Number fraction of grains twinned by ET, CT, or both. (B) SFs of active ETs. (C) ET area fraction in the parent grain. (D) Aspect ratio of ET. The aspect ratio is the twin length to width ratio, and was calculated with MATLAB using the function of *aspectRatio (grains)* in MTEX [200,259]. Note that minimum, 25th, median and 75th percentile, as well as maximum or nonoutlier maximum feature values at given for each box chart in (B-D). The red '+' represents the outliers of data. The numbers between parenthesis in (B-D) stand for the average of the corresponding feature. Number fractions of (E) ET variants and (F) ET variant SF rankings.

All 6 ET variants, i.e., ET1-ET6, were observed during deformation but the distribution of active ET variants did not follow the SF criteria (Figure 5.5(E)). For

instance, nearly half of the active ETs belong to ET2, and ET3 after 15.3% strain, and their average SF is -0.21, and -0.30, respectively. Moreover, only ~ 20% of active ETs were associated with the highest global SFs at any strain and the SFs of ~ 25% of them were the 5th or the 6th SF among all the possible twin variants (Figure 5.5(F)), again in opposition to the SF criterion.

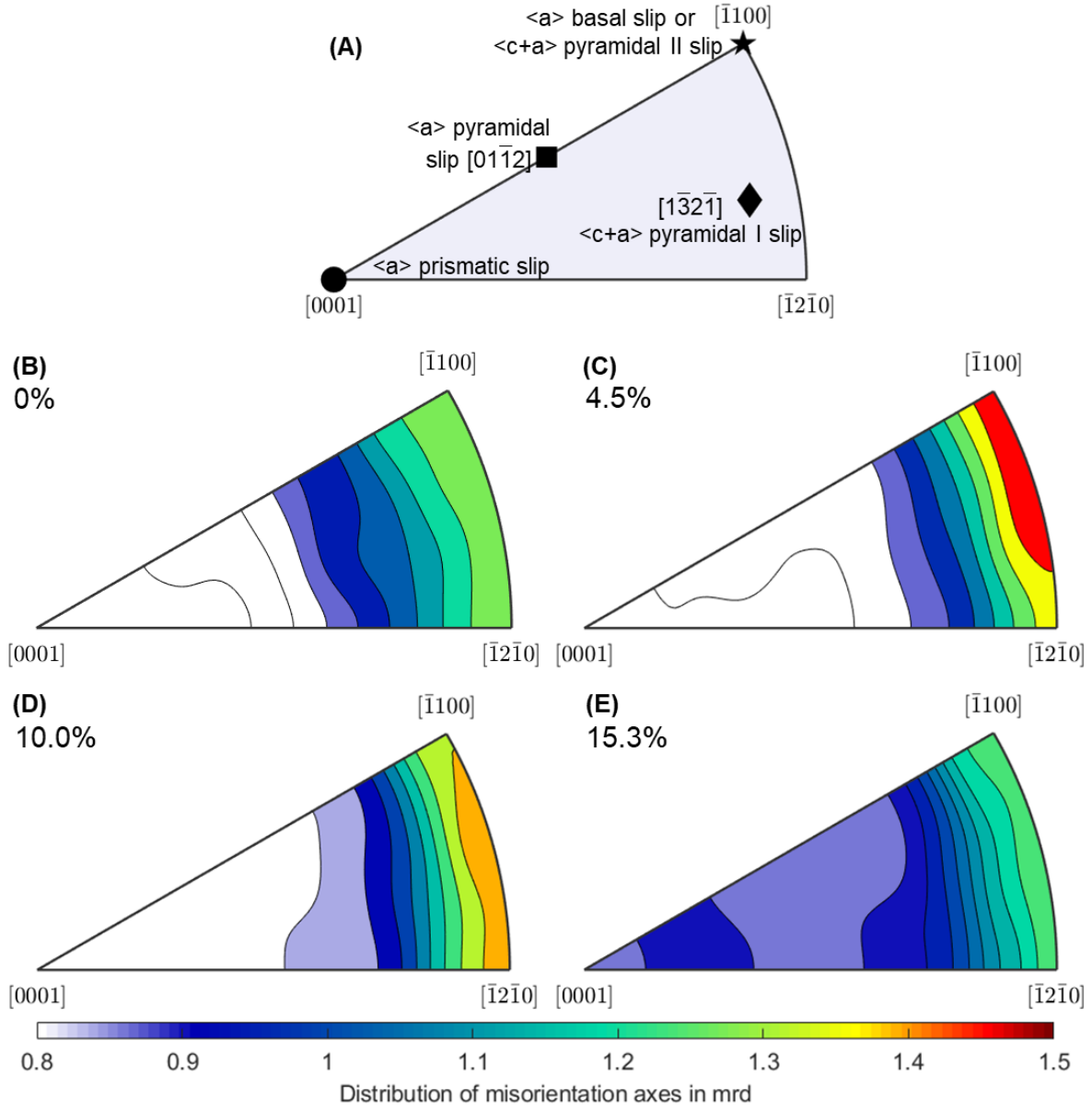

Figure 5.6: Slip behavior analysis using GROD. (A) RAs associated with dislocation slip along different systems in HCP Mg. Evolution of the distribution of intragranular misorientation axes in the crystal coordinate system (expressed in mrd) of Mg-1Al alloy during tensile deformation along the ED: (B) before deformation, (C) 4.5%, (D) 10.0%, and (E) 15.3% strains. The GROD analysis was carried out in all the grains in the whole EBSD map.

The distribution of the intragranular misorientation axes (expressed in mrd) in the crystal coordinate system of the Mg-1Al alloy before tensile deformation is depicted in Figure 5.6(B). The maximum of this distribution is found around the curved line joining $[\bar{1}100]$ to $[\bar{1}2\bar{1}0]$, which is representative of residual grain orientation gradients during extrusion. The misorientation axes moved towards $[\bar{1}100]$ with the applied tensile strain, then towards $[\bar{1}2\bar{1}0]$, and finally towards the curved line joining $[\bar{1}100]$ to $[\bar{1}2\bar{1}0]$) (Figure 5.6(C-E)).

Although <a> basal and <c + a> II pyramidal slip lead to a similar rotation of the crystal around the $<\bar{1}100>$ axis, the CRSS of <c + a> II pyramidal slip is much higher than that of <a> basal slip [344]. Moreover, the RA of $[\bar{1}2\bar{1}0]$ was generally associated with the simultaneous activation of two <a> basal slip systems [271,272]. These results reveal that <a> basal slip is the most likely active slip system during tensile deformation of Mg-1Al alloy, although the maximum intensity in Figure 5.6(C-E) is still low.

ST-MLRA was also used to support the results obtained by GROD on the sample deformed up to 15.3%. ST-MLRA combines the information of slip plane (obtained from conventional slip trace analysis) and slip direction (obtained from the translation of the projection of the grain orientation in the pole figure) to identify the actual slip system(s) that are active in a grain [203,273]. Therefore, ST-MLRA provides more accurate information than GROD but requires a much larger experimental effort.

A typical example of the application of ST-MLRA to identify the actual active slip system in grain G231 with Euler angles of (30.8°, 50.1°, 32.5°) is depicted in Figure 5.7. The orientation of the slip traces in G231 (Figure 5.7(B)) are in good agreement with the calculated one for the (0001) basal plane (Figure 5.7(A)). However, there are possible three slip directions in the basal plane: $[2\bar{1}\bar{1}0]$ (SF = 0.33, RA = $[01\bar{1}0]$), $[1\bar{2}10]$ (SF = 0.29, RA = $[10\bar{1}0]$), and $[11\bar{2}0]$ (SF = 0.042, RA = $[1\,\bar{1}\,00]$). The actual active slip system(s) cannot be distinguished using the conventional slip trace analysis. The experimental projections of the orientation of grain G231 on the (0002) pole figure before and after deformation are plotted in

Figure 5.7(C) together with the predictions for the stretching of the projections corresponding to the three possible RAs. It is evident that the best match between the experiments and the prediction for the lattice rotation is found for the RA of $[01\bar{1}0]$. Thus, the dominant slip system in grain G231 is (0001) $[2\bar{1}\bar{1}0]$. Besides, using ST-MLRA, the main slip system of Twin1 with Euler angles of (146.1°, 68.4°, 12.8°), -that appeared inside grain G231 after tension-, is also identified to be (0001) $[2\bar{1}\bar{1}0]$ with a global SF of 0.38.

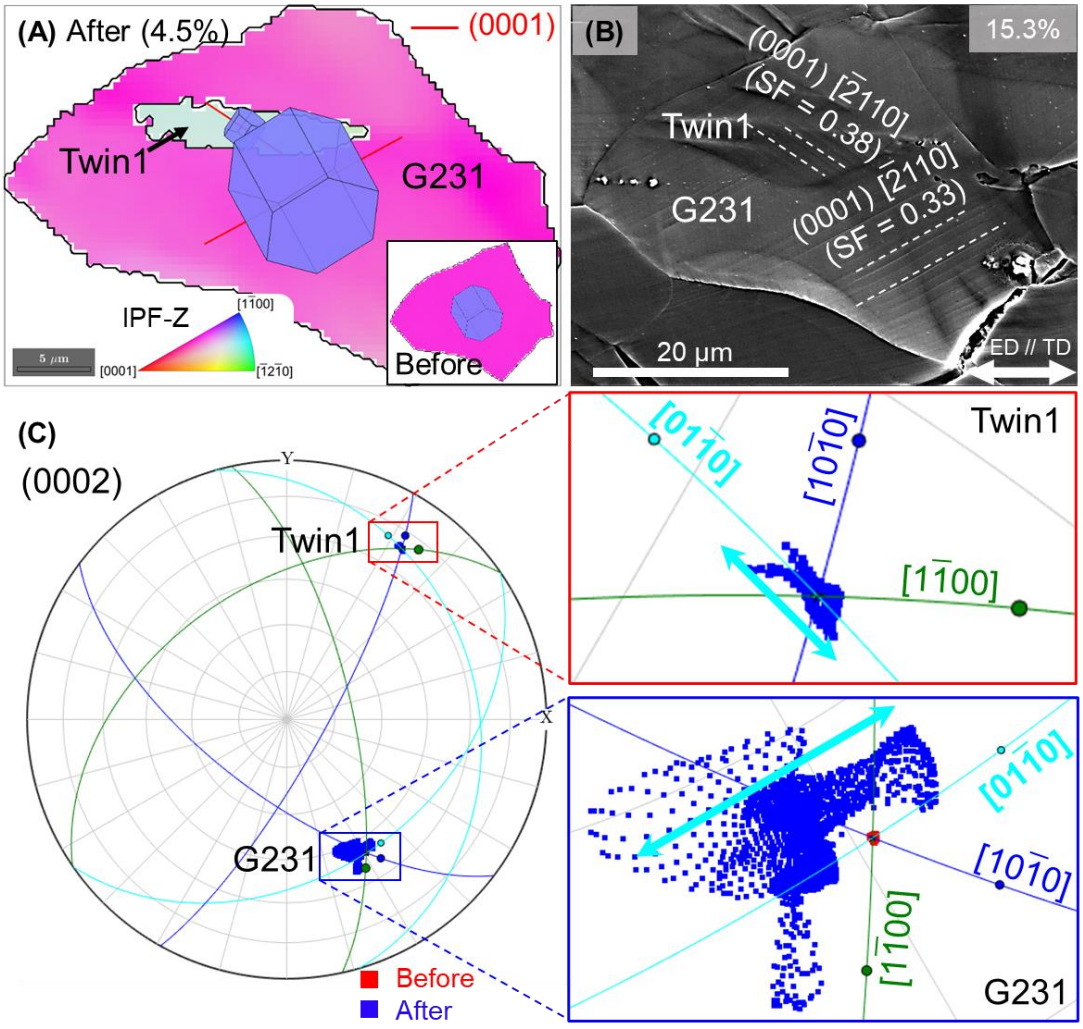

Figure 5.7: Typical example of ST-MLRA. (A) EBSD IPF map of the parent grain G231 and Twin1 after tensile deformation up to 4.5%. The crystal lattice orientations as well as slip traces of basal plane in both the parent grain G231 and the Twin1 were overlaid. The EBSD IPF map before deformation of grain G231 was also included. (B) SE image of grain G231 and Twin1 after tensile deformation up to 15.3%. The slip traces, corresponding to the basal slip system, were clearly visible on the surface of both G231 and Twin1. (C) Projections of the orientations of grain G231 and Twin1 on the (0002) pole figure before (red) and after (blue) deformation. The circular lines stand for the theoretical variation in orientation due to the rotation along the RA of each basal slip system. The dots on the circular lines correspond to a rotation of ± 5° aligned to each basal slip system.

Near 500 grains of the sample deformed up to 15.3% were analyzed, and the main active slip system could be determined by means of ST-MLRA in 154 grains, which have discernible slip traces on the surface after deformation. The results are tabulated in Table 5.2. <a> basal slip is the main active slip system in Mg-1Al alloy during tensile deformation, in line with the results of GROD (Figure 5.6).

Table 5.2: Active slip systems identified by ST-MLRA in the sample deformed up to 15.3%.

Slip system	Number
<a> basal	147
<a> prismatic	3
<a> pyramidal	1
<c + a> pyramidal I	1
<c + a> pyramidal II	2

5.3.4. Local deformation mechanisms at the grain level

The nucleation of anomalous ETs with negative SFs is commonly associated with particular features of the deformation at the grain level that result in stress concentrations near GBs. They may be caused by intragranular dislocation slip and / or slip or twin behaviors in neighbor grains [59,61,345,346]. Therefore, the likelihood of twin-twin transfer and slip-twin transfer across GB, as well as the influence of the grain size and of the basal slip on the activation of anomalous ETs were analyzed and the results are plotted in Figure 5.8.

The geometric compatibility factor, aka Luster-Morris parameter (m'), was selected to assess the probability of twin-twin transfer and slip-twin transfer across GB. m' is calculated based upon the angles between the slip / twin plane normal directions (ψ) and the Burgers vector / shear direction (κ) according to eq. (2.7). 17 twin-twin transfer cases were found in 115 ETs at 10.0%, and only 10 of them presented the highest or near the highest m' among 6 possible twin variants (Figure 5.8(A)). Thus, twin-twin transfer across GB only accounts for the nucleation of 9% ETs while many twins were found for low values of m'. Meanwhile, the formation of 23 active twins (27%) can be explained by the slip-twin transfer across the GB with the highest or near the highest m' among 6

possible twin variants (Figure 5.8(B)), after excluding 10 twins induced by twin transfer -that can be explained by m'- and 20 unclear cases where nucleated twins do not connect with any known GBs from EBSD [202,203]. Thus, the Luster-Morris parameter fails to predict the nucleation of the majority of anomalous ETs, in agreement with the results reported in a strongly basal-textured Mg sheet that was deformed in tension along the ED [347].

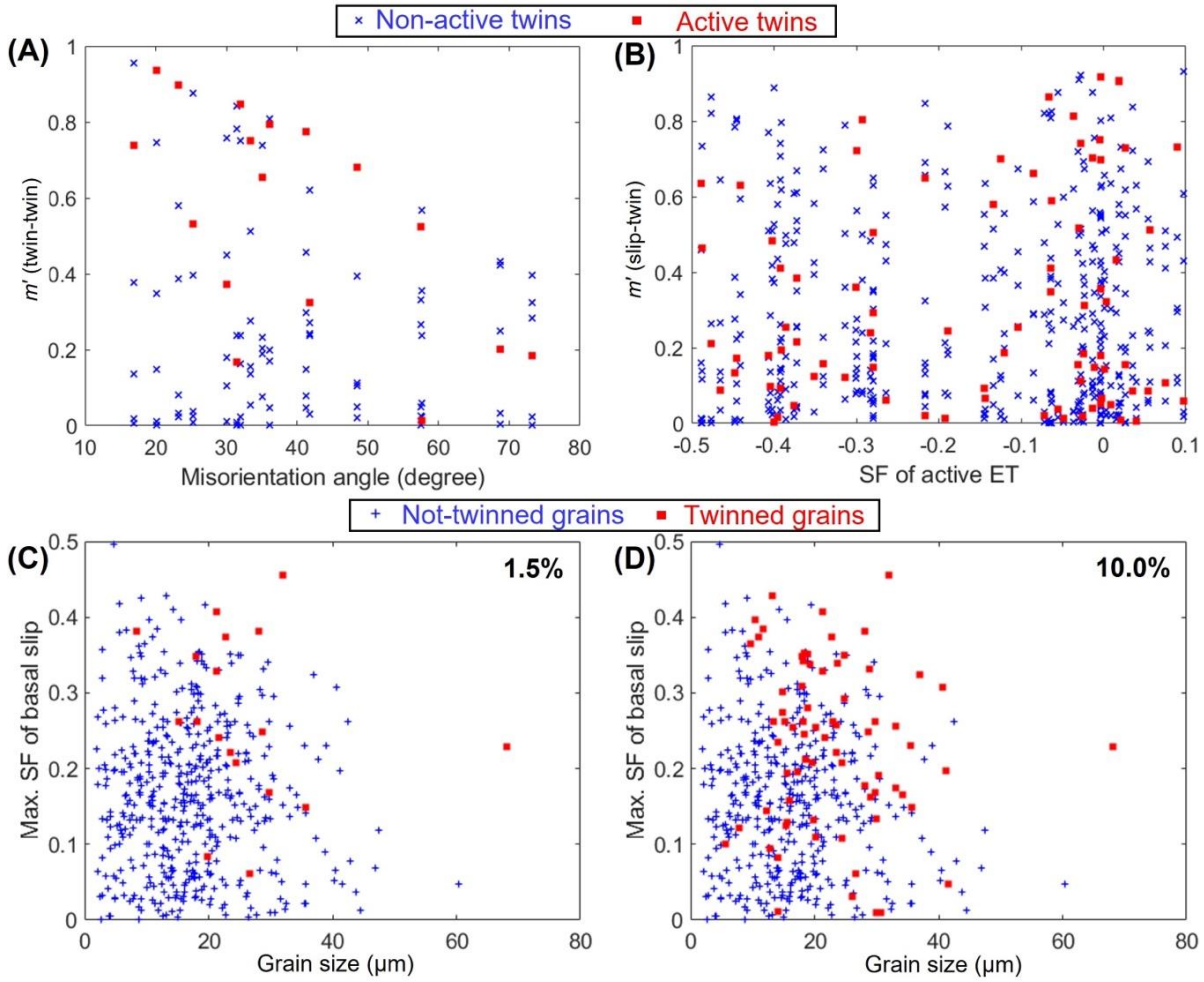

Figure 5.8: Influence of microstructural features on twin nucleation. (A) Luster-Morris parameter (m') associated with twin-twin transfer at the GB with respect to the misorientation angle between the neighbor twinned grains, when twin-twin connection emerged at 10.0% strain. (B) m' associated with <a> basal slip-twin transfer at the GB with respect to the SF of active ET at 10.0% strain. Note that the active slip systems to calculate m' in (B) were identified by ST-MLRA. 'Non-active twins' are defined as the ET variants which were not activated in the twinned grain during deformation. Their m' were calculated as that of 'active twins' based on eq. (2.7). Besides, the neighbor grain with a longer boundary with the ET was selected to calculate the m' in (B) in the case of ET near GB triple junctions. (C) Maximum SF of <a> basal slip with respect to the grain size at 1.5% strain for twinned and not-twinned grains. (D) *Idem* at 10.0% strain.

Finally, the effect of grain size and of the intragranular basal slip activity on the activation of anomalous ET is presented in Figure 5.8(C) and Figure 5.8(D), respectively. The twinning probability increased with the grain size as well as with the SF of <a> basal slip, in accordance with previous investigations [47,51,64,65,348–350]. But it should be noted that neither of them was the dominant factor for twin nucleation according to Figure 5.8(C) and Figure 5.8(D). Further evidence was provided in Annex Figure B.1 using quasi-in situ EBSD before and after deformation, including one large grain with a grain size of 110.5 µm and its neighbor grains. Note that out of the 6 large grains in Annex Figure B.1, only grain G2 with the highest <a> basal slip SF of 0.38 and a grain size of 65.4 µm was twinned. Thus, this analysis reveals that twin-twin and slip-twin transfer across the GB, <a> basal slip SF as well as grain size may be responsible for the nucleation of some anomalous twins but cannot explain the majority of them in the Mg-1Al alloy.

5.3.5. Lattice rotation behavior at the sub-grain level

The limitations of the Luster-Morris parameter to predict the nucleation of anomalous ETs may be related to the fact that only one neighbor grain is considered but ~ 51% anomalous ETs emerged around the GB triple junctions rather than from regular GBs. It should be noted that nucleation of normal ETs in grain with high SF for twinning has not been associated with GB triple junctions. Chaudry et al. [351] have reviewed patterns and morphologies of normal ETs and found two types: parallel morphology and cross twin morphology, but both weakly correlated with GB triple junctions. Quantitatively, we analyzed the EBSD data from Park et al. [352] and only found that ~ 12% (19 / 163) of normal ETs emerged from GB triple junctions. This information indicates that the nucleation of anomalous ETs is more complicated than that of normal ETs, and all the grains around the GB triple junction should be included to ascertain the critical condition for twin nucleation.

A typical example of the nucleation of several anomalous twins is depicted in Figure 5.9. The corresponding evolution of EBSD map for the grains in Figure 5.9

with applied tensile strain is shown in Annex Figure B.2. One CT (Twin2) and eight ETs (Twin3-Twin10) were found in 3 grains G92, G121, and G146. One crack between grains G87 and G121 and several ledges are distinctly observed near the GBs (Figure 5.9(B)). The SF and the rank of the active twin variants are depicted in Table 5.3. Only Twin2 exhibits a positive SF and the SF of this CT variant ranks 4th, whilst all ETs in Figure 5.9 exhibit negative SFs around -0.5, and accordingly, the SFs of their twin variants rank the 5th or the 6th.

The distribution of intragranular misorientation angles of the parent grains in Figure 5.9 are plotted in Figure 5.10 as a function of the applied tensile strain, while the average value for each grain is presented in Figure 5.11(A). The average misorientation angle increases with strain in all grains (Figure 5.11(A)), indicating a sustained contribution of <a> basal slip to deformation. Moreover, grains G87 and G121 are elongated along the loading direction with strain, while the length of grain G92 along the loading direction decreases with the applied tensile strain (Figure 5.11(B)). Quantitatively, the elongation of grains G87 and G121 along the loading direction is 8.1% and 7.0% respectively after the application of global strain of 15.3%, whilst the reduction in the length of G92 is 18.8% (cf. Annex Table B.1). These results indicate that grain G92 is likely subjected to localized compression rather than to tensile deformation along the ED. Based on the localized compression, the local SFs of Twin6, Twin8, Twin9 and Twin10 in grain G92 should be positive and high.

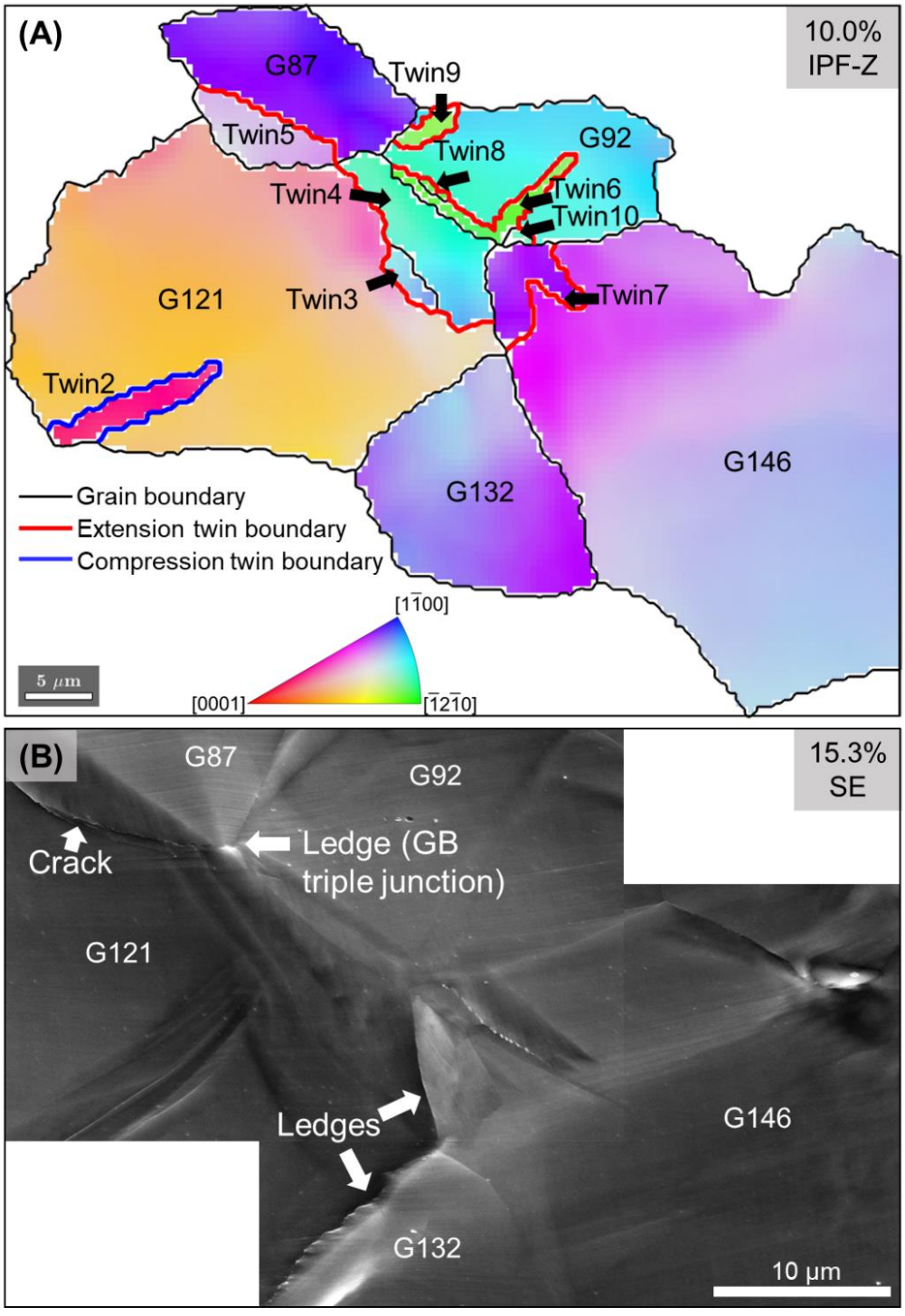

Figure 5.9: Local microstructure in region which presented the nucleation of multiple twins. (A) EBSD IPF map and (B) SEM micrograph.

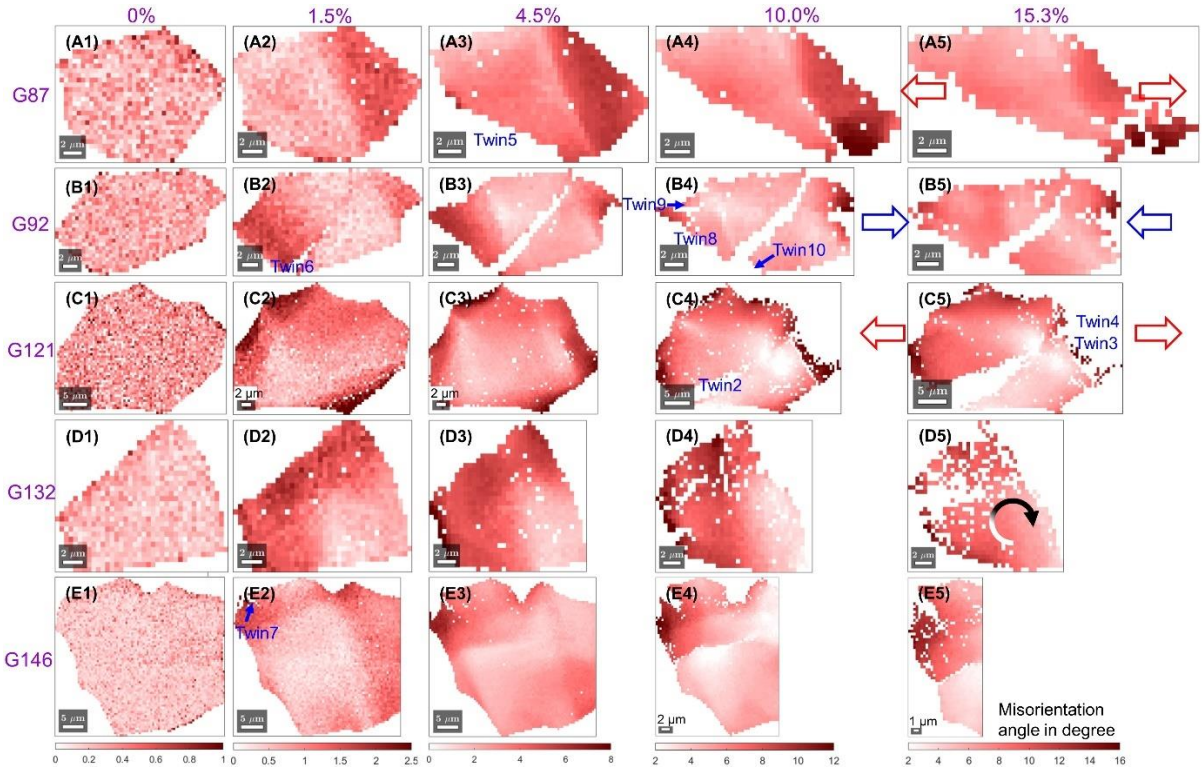

Figure 5.10: Evolution of the intragranular misorientation angle. Grains (A1-A5) G87, (B1-B5) G92, (C1-C5) G121, (D1-D5) G132, and (E1-E5) G146 (A1-E1) before deformation, and after (A2-E2) 1.5%, (A3-E3) 4.5%, (A4-E4) 10.0%, and (A5-E5) 15.3% strains. The average orientation of grain before deformation was used as the reference orientation during the analysis.

Table 5.3: Active twin type, twin variant, SF, and rank of the SF for the twins in Figure 5.9.

Active twin	Parent grain	Twin variant	Twin variant SF	Rank of the twin variant SF
Twin2	G121	C1	0.19	4
Twin3	G121	T4	-0.49	6
Twin4	G121	T3	-0.49	5
Twin5	G87	T2	-0.38	6
Twin6	G92	T3	-0.46	6
Twin7	G146	T2	-0.38	6
Twin8	G92	T3	-0.46	6
Twin9	G92	T3	-0.46	6
Twin10	G92	T3	-0.46	6

Besides, the distribution of misorientation angle within the grains is not uniform in many cases, as shown by the components of the lattice rotation around the principal directions (Figure 5.12). For instance, lattice rotations in opposite

directions can be observed in the upper and lower regions of the grain G146 (Figure 5.12(E1) and Figure 5.12(E2)). In addition, the major lattice rotation orientation varies significantly among these grains, even though they are in the same region. A typical example can be found in grains G92 (Figure 5.12(B3)) and G132 (Figure 5.12(D3)), that present lattice rotations in opposite directions.

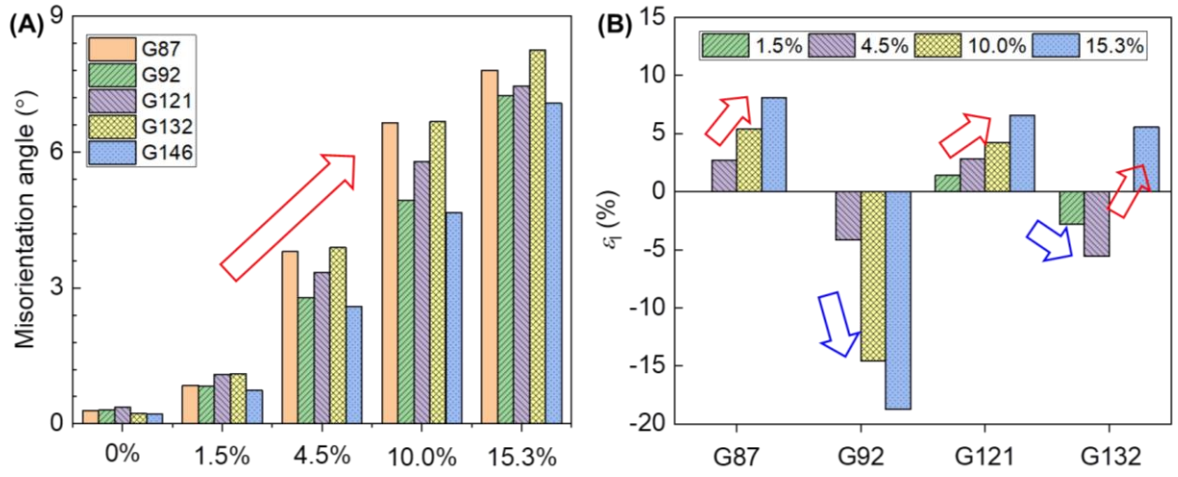

Figure 5.11: (A) Evolution of the average misorientation angle with the applied strain for the grains in Figure 5.9. (B) Evolution of the longitudinal strain (ε_l) (see eq. (5.2)) with the applied strain for the grains in Figure 5.9.

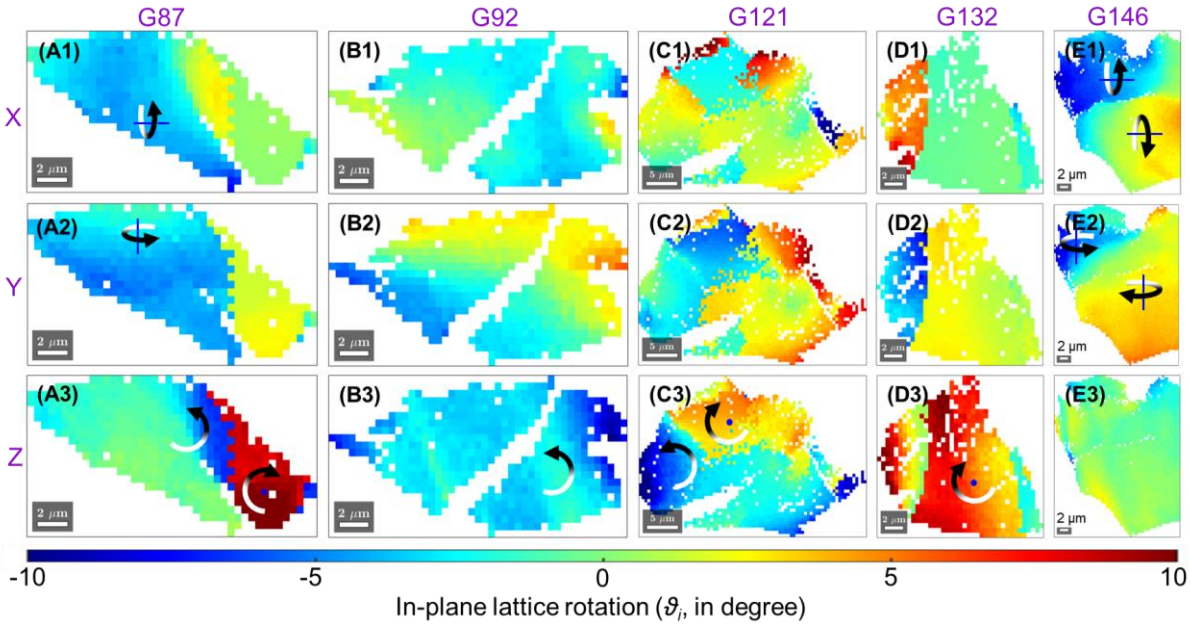

Figure 5.12: Components of lattice rotation (ϑ_i) around the principal directions (see eq. (2.9)). (A1-E1) X, (A2-E2) Y, and (A3-E3) Z for grains (A1-A3) G87, (B1-B3) G92, (C1-C3) G121, (D1-D3) G132, (E1-E3) G146 after 10.0% strain. Positive values indicate rotation in the clockwise direction.

To better understand the underlying deformation mechanism that led to the differences in the lattice rotation, the active slip systems in the grains of Figure 5.9 were identified by ST-MLRA. All the active slip systems in these grains correspond to <a> basal slip (Figure 5.13), in agreement with Figure 5.6 and Table 5.2. However, the active basal slip systems have different SFs (in the range from 0.01 (grain G121) to 0.20 (grain G92)) as well as different RAs (Figure 5.13). Besides, in comparison with other grains with discernible slip traces, only limited slip traces were observed around the corner of grain G121, in line with its low SF of active <a> basal slip (0.01).

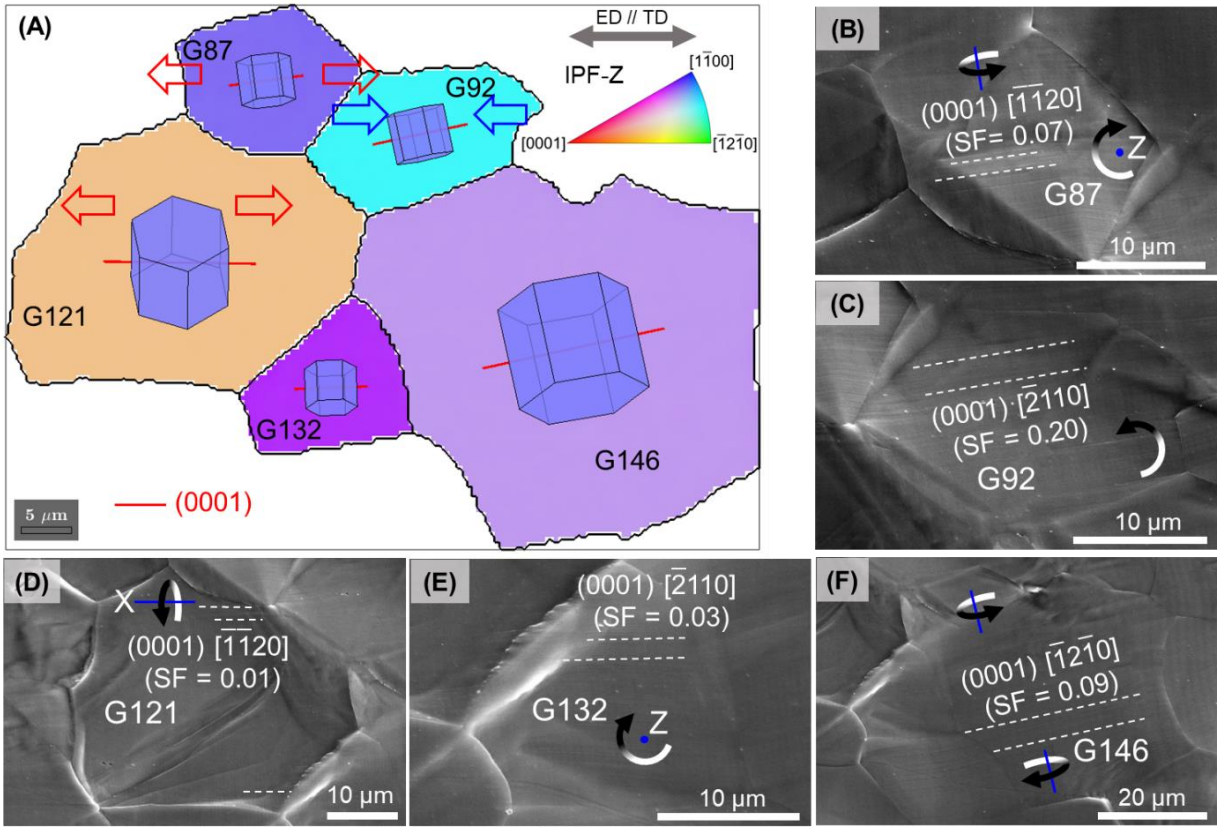

Figure 5.13: Slip analysis by ST-MLRA of the grains in Figure 5.9. (A) EBSD IPF map of the grains before deformation overlaid with the (0001) slip traces and the crystal lattice orientations. SEM micrographs of grains (B) G87, (C) G92, (D) G121, (E) G132, and (F) G146 after 15.3% strain. The dominant active slip system and its SF were identified in each grain via ST-MLRA and included in the corresponding SEM micrograph.

To ascertain whether the local compression of grain G92 was a general phenomenon, the longitudinal strain along the loading direction of the twinned grains was measured at different applied strains and the results are plotted in

Figure 5.14. The longitudinal strain of the twinned grains was similar to applied strain at 4.5% and the scatter between grains was limited. However, as the applied deformation increased to 10.0% and 15.3%, the longitudinal strain of the twinned grains showed more scatter, and the average value was also smaller than the applied tensile strain. This means that the deformation of the twinned grains was constrained by the neighbor grains, leading to lower local tensile strains (or even compressive strains along the loading axis) that facilitated the nucleation of anomalous ETs.

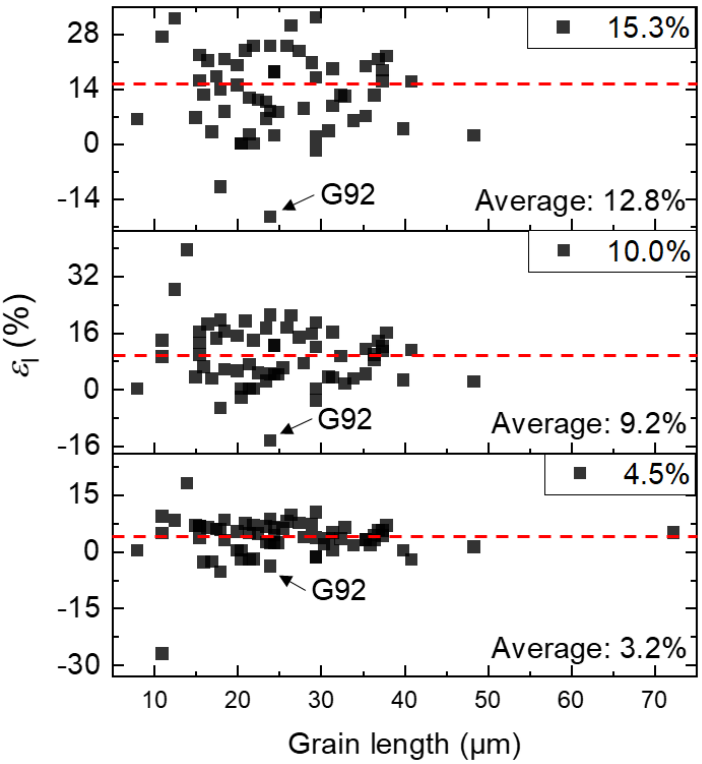

Figure 5.14: Evolution of the longitudinal strain (ε) along the loading direction during deformation (following eq. (5.2)) for the twinned grains as a function of the applied strain. The horizontal red dashed lines stand for the applied strain. The average longitudinal strain from all twinned grains under is also included for each value of the applied strain.

5.3.6. Limitations and outlooks

In the end, 2D EBSD measurements neglect the microstructural information beneath the surface and do not provide information about local stresses and local SFs. Besides, 2D -or even 3D- EBSD still cannot reveal quantitatively the

contributions from various deformation modes (including all kinds of dislocation slip, twinning and detwinning) to abnormal twin nucleation. The use of advanced diffraction techniques, including the in-situ neutron diffraction [353] or in-situ high energy X-rays [354], is necessary to provide quantitative information about the role and the magnitude of each deformation mode. Thus, in-situ EBSD should be combined with 3D microstructural characterization using diffraction contrast tomography and in-situ synchrotron diffraction [353,355], crystal plasticity / phase field simulations [55,180,356] as well as ML techniques [341,357] to provide a comprehensive understanding of the physics behind twin nucleation mechanisms.

5.4. Conclusions

Many anomalous ETs, with low even negative twinning SFs, were found to nucleate and grow in a strongly textured Mg-1Al alloy during tensile deformation along the ED. The deformation mechanisms responsible for this behavior were thoroughly investigated via in-situ EBSD, GROD, and ST-MLRA. The main conclusions are the following:

(1) Plastic deformation during tension was mainly accommodated by <a> basal slip but the nucleation of anomalous ETs -with negative SFs- was important at the onset of plastic deformation. A few anomalous ETs were nucleated at larger plastic strains, but the ones nucleated at the beginning were able to grow.

(2) The probability of nucleation of anomalous ETs only increased slightly with the grain size and the SF of <a> basal slip. Similarly, neither twin-twin transfer nor slip-twin transfer (as indicated by the Luster-Morris parameter) were able to predict most nucleated twins because half of them occurred near GB triple junctions and not at regular GBs.

(3) Nucleation of anomalous extensions twins was experimentally proven to be associated with the severe strain incompatibility between neighbor grains, particularly at GB triple junctions, that is promoted by the different <a> basal slip-induced lattice rotations in the grains. Due to the strain incompatibility between neighbor grains, lattice rotations in opposite directions were observed within the same grain, and localized compression was also found in several grains along the

direction of the applied tensile strain.

(4) The anomalous ETs that were nucleated at the beginning of plastic deformation were able to grow with the applied strain due to the continuous activation of <a> basal slip in different grains, which enhances the strain incompatibility.

(5) Future investigation may utilize the advanced in-situ diffraction techniques combining with crystal plasticity / phase field simulations to provide a more comprehensive understanding of the physics behind twin nucleation mechanisms.

6. Influence of microstructure on twinning in wrought Mg alloys studied by machine learning

6.1. Introduction

Mg and its alloys have emerged as promising candidates for structural components in transport, owing to their light weight, high strength-to-weight ratio, and good recyclability [1,299], as well as in biomedical applications due to their biodegradable and biocompatible behavior and have been recently used in scaffolds for bone tissue engineering [358,359]. Mg has a HCP crystal lattice and its plastic deformation is dominated by <a> basal slip, which presents a very low CRSS (< 1 MPa in pure Mg [344]). However, <a> basal slip can only accommodate deformation in the basal plane, and plastic strains along the <c> axis have to be accommodated through different mechanisms. The CRSS for <c + a> pyramidal slip on Mg is very high (98 MPa in pure Mg [9]) and, thus, plastic deformation along the <c> in Mg is often accommodated by twinning. The twinning systems are defined by the twin plane and the twin direction as well as by the shear deformation that is accommodated in the twin direction [16]. In the case of Mg HCP lattice, the $\{01\bar{1}2\}\langle 0\bar{1}11\rangle$ ETs are often nucleated during plastic deformation because of their low CRSS, as compared with $\{01\bar{1}1\}\langle 0\bar{1}12\rangle$ CT [14,15,328]. It should be noted, however, that twinning is a polar mechanism that only occurs when the shear deformation is applied in the appropriate direction, so the twinned region has a mirror symmetry with the parent region across the twin plane. Thus, ET in Mg only occurs under stress states that lead to an extension of the <c> axis of the HCP Mg lattice. As a result, twinning deformation leads to a large difference between the TYS and CYS and work hardening of textured Mg alloys, and this marked plastic anisotropy has negative effects on the ductility and formability of wrought Mg alloys [225,226].

However, it is still unclear of the critical microstructural feature responsible for the nucleation of ETs. In this chapter, ML strategies (and, in particular,

Bayesian inference) are used to establish the relationship between microstructural features and twin nucleation in two different Mg alloys. This chapter provides results on the influence of the microstructural features on the nucleation of ETs in Mg alloys. This information can help to design polycrystal microstructures with controlled twinning during deformation.

6.2. Methods

6.2.1. Sample preparation

Mg-1Al (at.%) and AZ31 alloy samples for microstructural and mechanical characterization were cut into dog-bone shape via electro-discharge machining. The dimensions (length × width × thickness) of the central gauge of the specimens were 15 × 5 × 2.5 mm^3 (to obtain whole tensile stress-strain curves) and 10 × 3 × 1.5 mm^3 (to perform interrupted EBSD measurements), for both Mg-1Al and AZ31 Mg alloys. The longest dimensions of the AZ31 samples were parallel to the ND (denominated S0), at 45° between TD and ND (denominated S45), and to the TD (denominated S90). The sample surface was always perpendicular to the RD. In the case of Mg-1Al alloy, the longest dimension of the sample was parallel to the ED. For EBSD measurement, the surfaces of all samples were manually ground on an abrasive SiC paper, followed by four polishing steps with 3 μm, 1 μm, 0.25 μm diamond paste and with a suspension containing oxide particles of 40 nm.

6.2.2. Mechanical tests

Tensile tests along the longest direction of each sample were conducted in an Instron model 8501 universal testing machine under displacement control at room temperature. Deformation was measured with an extensometer (Instron model 2620-602, gauge length: 12.5 mm) at an average strain rate of 10^{-3} s^{-1} while the applied load was monitored with a load cell. The tension for EBSD measurement before and after deformation was carried out in the micromechanical testing machine (Kammrath and Weiss Technologies, Inc., Model MZ.Sb) under the displacement control at 1 $\mu m \cdot s^{-1}$.

6.2.3. EBSD observations

The sample surface was analyzed within the gage length before and after deformation using a SEM (Apreo 2S LoVac, FEI Company, Portland, OR, USA; beam current: 2.7 nA, accelerating voltage: 20 kV) equipped with EBSD (Oxford HKL Channel 5, Oxford Instruments, Abingdon, UK; step size: 0.4 µm for AZ31 Mg alloy and 0.5 µm for Mg-1Al alloy, working distance: ~10 mm). The area of EBSD observation for the initial microstructure of AZ31 Mg and Mg-1Al alloys was 560 × 900 μm^2 and 1130 × 1645 μm^2, respectively. The step size of EBSD observation for the initial microstructure of both alloys was 1 µm. The microstructures in terms of IPF of samples S0, S45, S90 and Mg-1Al before and after deformation are shown Annex Figure C.1 and Annex Figure C.2.

6.3. Results

6.3.1. Microstructures

The development of deformation twins in Mg alloys is very sensitive to the microstructure [187,213,360]. The microstructures of extruded AZ31 Mg and rolled Mg-1Al alloys before deformation are depicted in Figure 6.1. Most grains in the IPF of AZ31 alloy were colored in red because their <c> axis is parallel to the ND (Figure 6.1(A)). This agrees well with the strong intensity of the (0002) pole figure around the ND in Figure 6.1(B), which is a 2D graphical representation of orientation showing the orientation of (0002) plane normal with respect to the sample reference frame. In contrast, most grains in the Mg-1Al alloy (Figure 6.1(E)) were colored in green and blue, indicating that their <c> axis is perpendicular to the ED. Accordingly, the (0002) pole diagram of the Mg-1Al alloy is near 90° away from the ED (Figure 6.1(F)). This means that hot extrusion results in a strong prismatic texture where most of the grains have the <c> axis perpendicular to the ED, whereas hot rolling generates a strong basal texture where the <c> axis are oriented parallel to the ND of the rolled sheet.

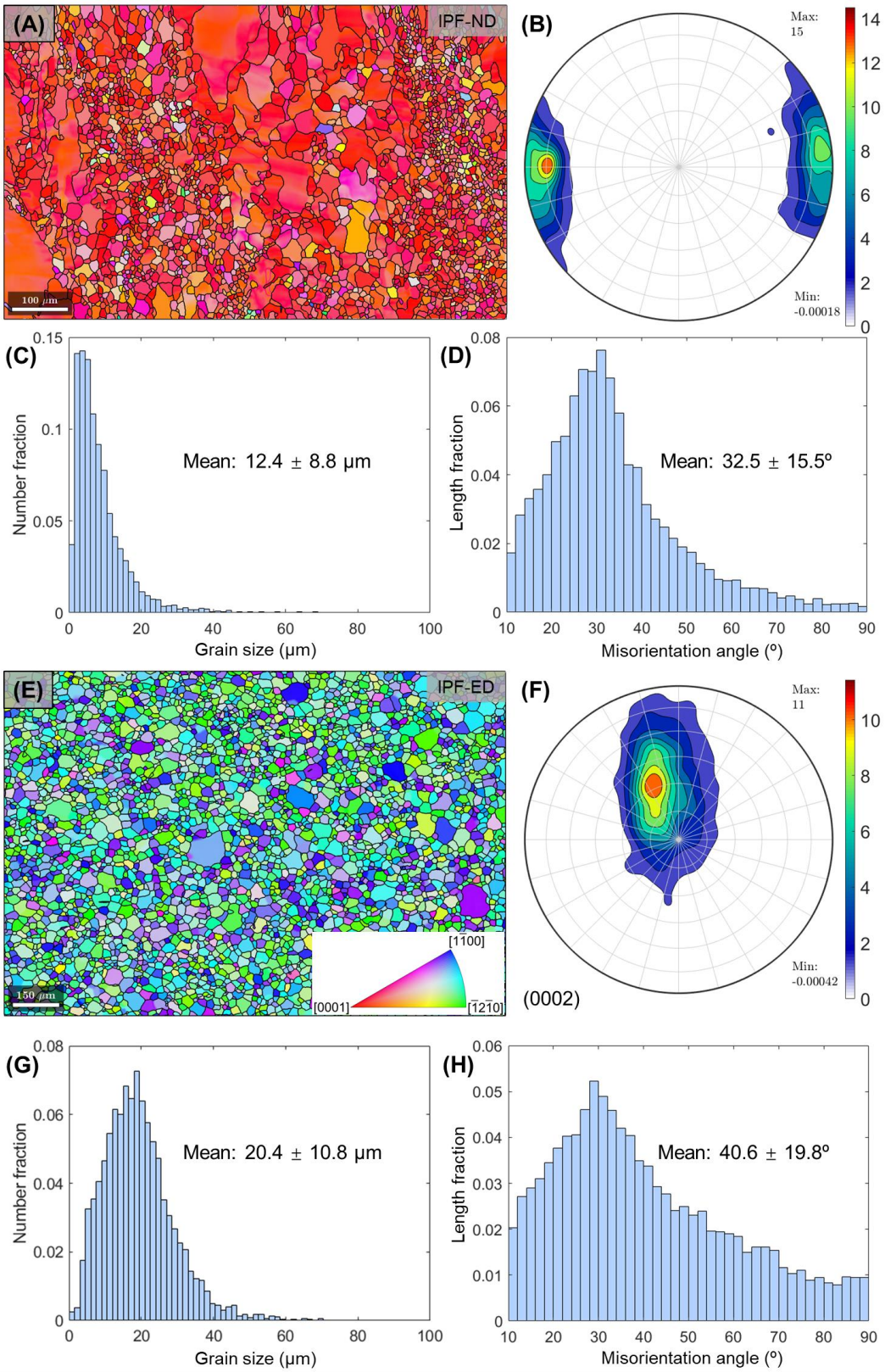

Figure 6.1: Microstructures of AZ31 Mg and Mg-1Al alloys before deformation. EBSD IPF maps in the (A) ND of AZ31 Mg alloy and (E) ED of Mg-1Al alloy. (0002) pole figures of (B) AZ31 Mg alloy and (F) Mg-1Al alloy. Distributions of (C, G) Grain size and (D, H) GB misorientation angle of (C, D) AZ31 Mg alloy and (G, H) Mg-1Al alloy.

The average grain size of AZ31 Mg and Mg-1Al alloys are 12.4 ± 8.8 µm and 20.4 ± 10.8 µm, respectively (Figure 6.1(C) and Figure 6.1(G)) but both alloys present a wide size distribution that also includes a few large grains (> 40 µm). Besides, the Mg-1Al alloy with a prismatic texture (mean: 40.6 ± 19.8°) exhibits a higher GB misorientation angle than the AZ31 alloy with a basal texture (mean: 32.5 ± 15.5°) (Figure 6.1(D) and Figure 6.1(H)). This is because the strong basal texture (with the <c> axis of many grains parallel to the ND) leads to misorientation angles in the range 0° to 30°. However, the GB misorientation angle varies from 0° to 90° for strong prismatic texture (with <c> axis of many grains perpendicular to the ED). The schematic illustration of the difference between two textures is shown in Annex Figure C.3. Such a difference of GB misorientation angle can influence the localized twinning behavior [58]. Overall, the different textures as well as the wide grain size distributions allowed us to collect a comprehensive dataset for twin nucleation.

6.3.2. Mechanical behavior

The tensile stress-strain curves of the AZ31 alloy in three different orientations (S0, parallel to the ND; S90, parallel to the TD; and S45 at 45° between the TD and ND) and of the Mg-1Al along the ED are plotted in Figure 6.2. The sigmoidal shape and the parabolic shape of the curves are generally associated with twin-dominated and slip-dominated deformation, respectively [10,262]. Thus, the nucleation and growth of ETs controls the deformation of sample S0, while slip should be the dominant deformation mode for samples S90 and Mg-1Al. The stress-strain curve of sample S45 is neither sigmoidal nor parabolic, suggesting that both slip and twinning may simultaneously contribute to the deformation. These hypotheses were corroborated by the experimental EBSD maps of AZ31 Mg and Mg-1Al alloys before and after deformation (shown in Annex Figure C.1 and Annex Figure C.2). In fact, after tensile deformation up to ~6%, the percentage of grains containing ETs is 57%, 25%, 2.4%, and 15%, for samples S0, S45, S90, and Mg-1Al, respectively (Table 6.1). Note that most active ETs exhibit low, or even negative SFs, in samples S90 and Mg-1Al (Table 6.1). This behavior is conventionally (and

ambiguously) related to stress concentrations at GBs [265,318] but its linkage with the microstructure has not been analyzed.

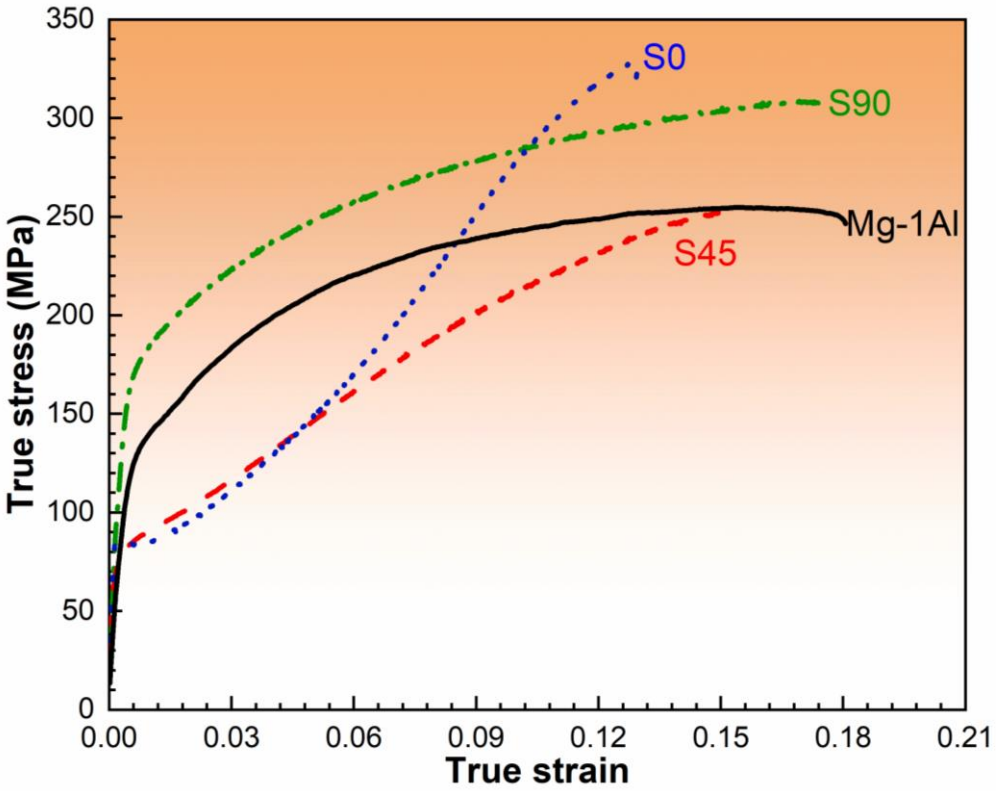

Figure 6.2: True stress-true strain curves of samples S0, S45, S90 and Mg-1Al under tension.

Table 6.1: Summary of the twinning features for various samples. Note that the number of grains in Table 6.1 is slightly larger than the number of grains in database used for ML because the grains on the edge of the EBSD region were not included in the ML database. The theoretical twinning SF was determined as the average for all grains of the highest SFs of all twin variants in each grain. For each grain, the average grain orientation obtained from the initial EBSD map was used to calculate the twinning SF.

	Tensile strain (true)	All grains	Twinned grains	Twinned fraction	Theoretical twinning SF	Active twinning SF
S0	~6%	369	210	57%	0.40	0.40
S45		693	171	25%	0.22	0.23
S90		1578	38	2.4%	0.036	0.083
Mg-1Al		941	138	15%	-0.0096	-0.062
	9.5%	555	78	14%	-0.014	-0.16

6.3.3. Database of microstructural features

The EBSD data of all our samples before deformation were exported using in-house codes based on MTEX (version 5.7.0), an open-source MATLAB toolbox [200,259], to collect the information of all microstructural features. Given that the microstructural features of the grains at the edge of the EBSD map were not fully captured, these grains were removed from the dataset. A total of 28 features were selected for each grain, which can be categorized into loading condition, grain shape parameters, apparent SFs, and GB parameters.

The loading condition is given by the *Orientation* feature, with values of 0, 45, and 90 for S0, S45, and S90, respectively, while all grains have a loading condition of 90 for the Mg-1Al alloy, as shown in Figure 6.3(A). The shape parameters of the grains include the diameter of a circle with the same area of the grain (*Grain_size*; in μm), the number of triple points (*Triple_points*), and the number of neighbor grains (*Neighbor_grain_n*) (Figure 6.3(B)). The apparent SFs for the 6 possible ET variants and for the 3 <a> basal slip systems were considered for each grain, which are the dominant plastic deformation mechanisms during tensile deformation, as shown in GROD maps of Annex Figure C.4. The values of the SFs were ordered from the highest to the lowest and named *T_SFn* (n = [1,6]) and *S_SFn* (n = [1,3]) for the ET variants and the <a> basal slip systems, respectively (Figure 6.3(C)). It should be noted that the local SFs (that account for the local stress state) may play more decisive roles than the apparent SFs on the activation of slip and twinning in polycrystalline Mg alloys [208,213]. However, the determination of local SFs for a large dataset (as the one necessary for ML) is extremely challenging and would require either costly diffraction experiments or 3D computational polycrystalline simulations based on the actual 3D grain structure [213,345,346,361]. Considering that the main aim of this investigation is to assess the microstructural features that lead to the formation of ETs, the apparent SF, which is a geometrical factor that takes into account interaction between the macroscopic stress and the grain orientation, is a good descriptor for ML.

Finally, the GB parameters were subdivided into i) the Luster-Morris geometric compatibility factor (m'), ii) the GB misorientation (i.e., disorientation)

angle (*GB_misang*; in °), iii) the difference of grain size (*deltaGs*; in µm), and iv) the difference between the <a> basal slip SF of a given grain and its neighbors (*deltaBSF*). The maximum (*max*), the mean (*mean*), and the minimum (*min*) values of all GB features for each grain were included in the dataset.

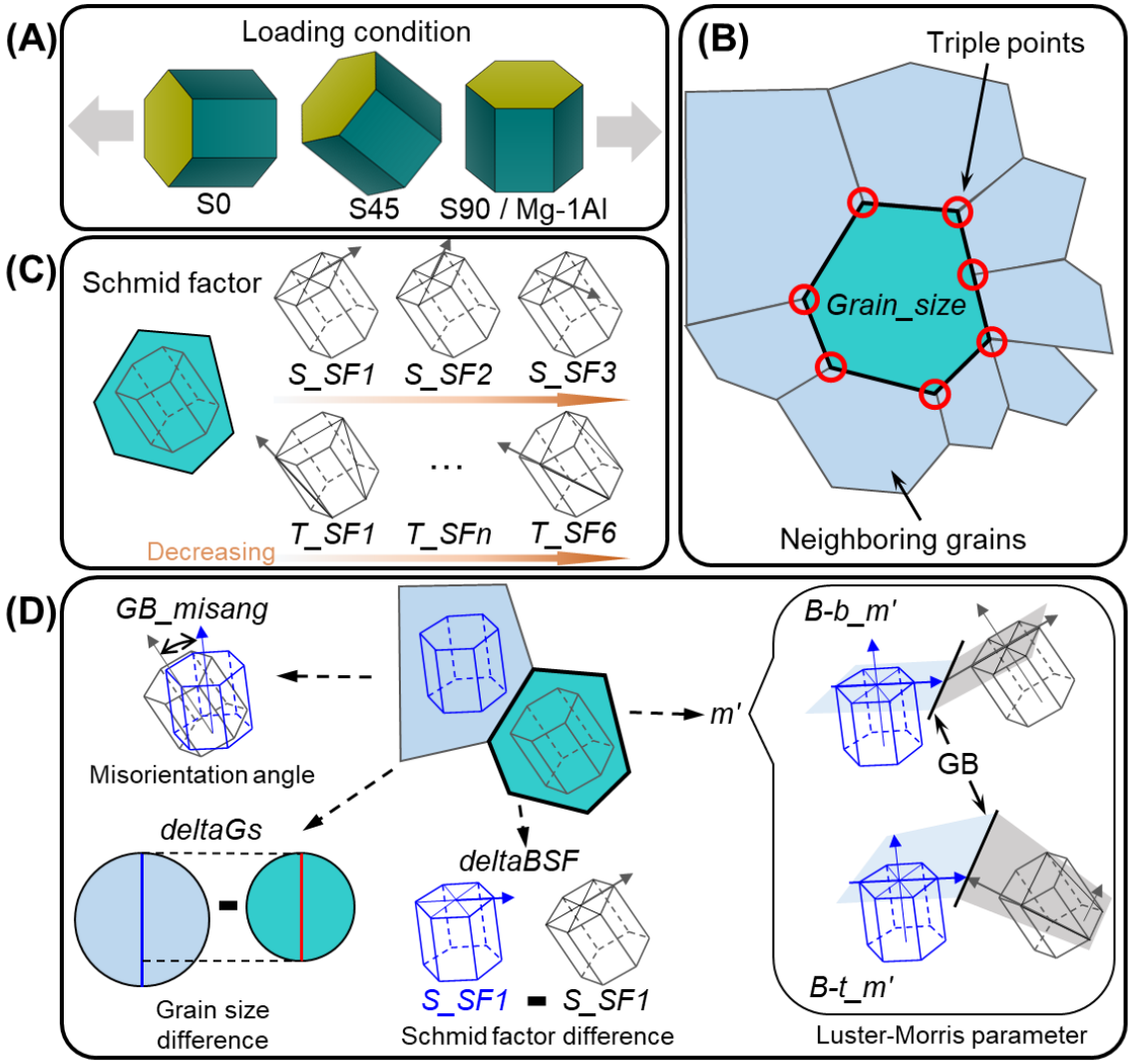

Figure 6.3: Schematic of the microstructural features considered in the ML models. (A) Loading conditions for various samples, (B) grain shape parameters, (C) apparent SFs, and (D) GB parameters.

The Luster-Morris geometric compatibility factor (m') is one of the most relevant criteria to assess slip / twin transfer as well as slip-induced twinning events at GB [59,60,199]. It is based upon the angles between the active slip / twin plane normal directions ψ and the Burgers vector / twin shear directions κ according to eq. (2.7) [208]. The m' between <a> basal slip systems of a given grain

and its neighbors (*B-b_m*) and the *m'* between the 6 ET variants of a given grain and the <a> basal slip systems of its neighbors (*B-t_ m*) were chosen as features, as schematically depicted in Figure 6.3(D). Hence, transmission of <a> basal slip across the GB and nucleation of ETs at the GB induced by <a> basal slip in the neighbor grain are considered. It is worth noting that, although there are 3 possible <a> basal slip systems, only the one with the highest SF was considered to compute *m'*. However, all 6 ET variants were considered since the nucleation of ETs induced by <a> basal slip in the neighbor grain is triggered by the stress concentration at the GB and all ET variants are possible. Even though ETs in neighbor grains have also been reported to induce nucleation of ETs [48,345,346], this feature was not considered because it is strongly correlated with the GB misorientation angle (*GB_misang*) [58,361].

The differences of grain size (*deltaGs*; in μm) and <a> basal slip SF (*deltaBSF*) were calculated by subtracting the value of the feature of a given grain to the value of the feature for each of its neighbors. For *deltaBSF*, only the highest SF for the <a> basal slip systems (*S_SF1*) in the given grain and its neighbors was considered.

The mean grain orientations were used to calculate the geometric compatibility factors and the theoretical SFs for twinning and slip. The slight deviations in the grain orientation, indicated by the intragranular grain orientation (mostly < 5°), may lead to small errors in the calculation of the GB characters.

The dataset of AZ31 Mg alloy includes 2301 entries, corresponding to 338 twinned grains and 1963 not twinned grains. The dataset of Mg-1Al alloy includes 811 entries, corresponding to 115 twinned grains and 696 not twinned grains. The variable *Twinned* in the dataset indicates whether a grain is twinned (1) or not twinned (0).

6.3.4. Presentation of some microstructural features

The distributions of some of the microstructural features used for descriptors in the data set are plotted in Figure 6.4. The distributions of the maximum SF for <a> basal slip (*S_SF1*) and ET (*T_SF1*) in Figure 6.4(A) confirm that the three

loading orientations in AZ31 lead to the activation of different dominant deformation mechanisms. For instance, the S45 sample exhibits the highest SF for <a> basal slip, while the highest SF is found for ET in the S0 sample. Hard-oriented samples (S90 and Mg-1Al) show the lowest SFs for both <a> basal slip (although there are grains with high SFs) and ET (Figure 6.4(A)).

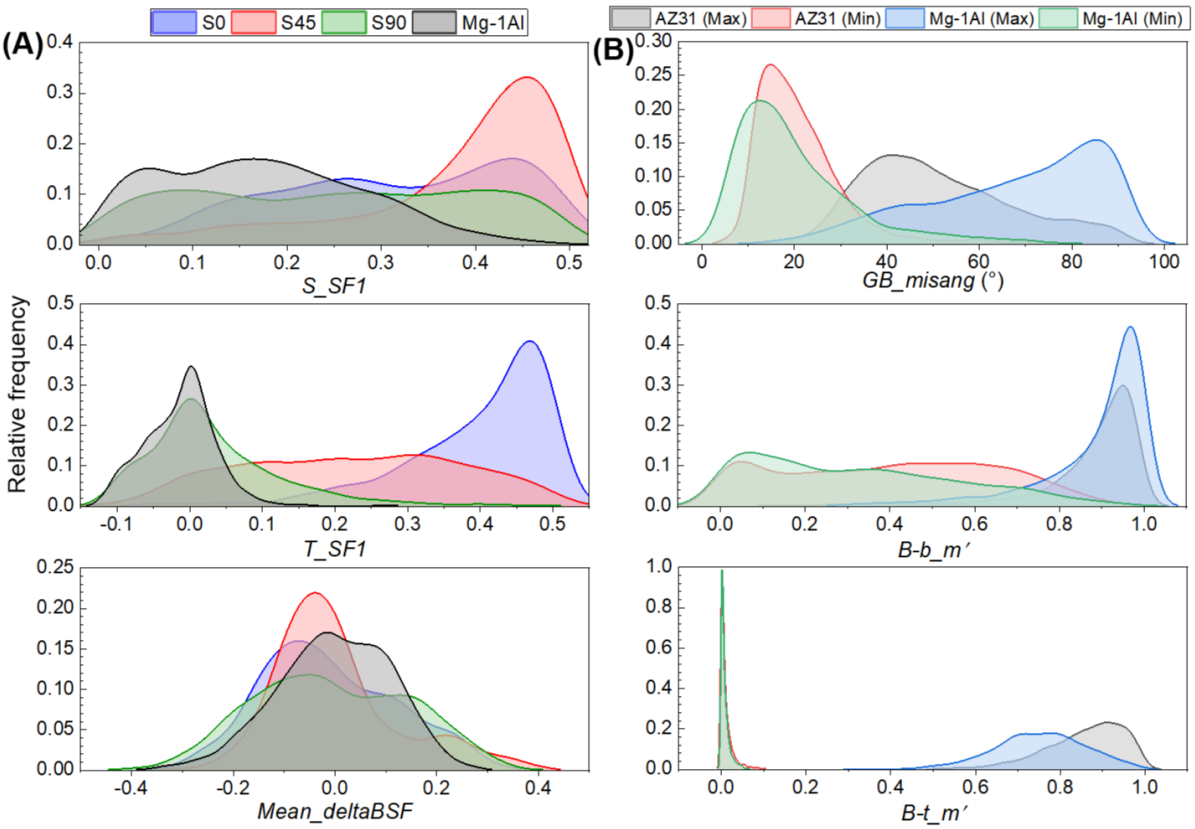

Figure 6.4: Distributions of some microstructural features. (A) *S_SF1* (upper), *T_SF1* (middle), and *Mean_deltaBSF* (bottom) values for different loading conditions of the AZ31 alloy and for the Mg-1Al alloy, and (B) *Min*/*Max* values of *GB_misang* (upper), *B-b_m′* (middle) and *B-t_m′* (bottom) for both alloys.

Other features, such as *Mean_deltaBSF* (Figure 6.4(A) **Bottom**), are, however, independent of the orientation, and are distributed symmetrically around 0 within a wide range from -0.3 to 0.2. Other GB parameters, such as *GB_misang*, *B-b_m′*, and *B-t_m′* are also independent of the loading orientations and the distributions for the full AZ31 data set (including the three orientations) are provided in Figure 6.4(B). The *GB_misang* feature for the Mg-1Al alloy is considerably higher than that of the AZ31 alloy (Figure 6.4(B) **upper**), which could be ascribed to the different textures of both alloys (Figure 6.1). Despite that, the distributions of *B-*

b_m', and *B-t_m'* are independent of the alloy. These distributions demonstrate the comprehensive sampling of different features in the database.

6.3.5. Machine learning for twin nucleation

With the goal of finding the apparent causal relations of twinning, the datasets were used to train ML models that can predict if a given grain will twin or not. This can be achieved through ML classification methods, a type of supervised ML approaches whose objective is the prediction of labels (in our case, 'twinned' or 'not twinned'). Several ML models (e.g., support vector machines, decision trees, random forests, AdaBoost, GDB, BNs, etc.) were initially trained on the AZ31 dataset to select the most suitable method for predicting twinning. As a preprocessing step before training, '*MinMax*' scaling procedure was used to scale all features in the dataset to values in a range between 0 and 1 and removed all highly correlated features (absolute values of Pearson coefficient ≥ 0.95) that led us to a final dataset containing 24 features. A stratified 10-fold cross validation procedure was used for training to avoid possible biases (and overfitting). The ROC AUC score [221–223] was used to evaluate the performance of our ML models since it is a good metric to select optimal models independently from the cost context or the class distribution.

The accuracy in terms of the ROC AUC score for the 6 best performing ML models as well as the individual accuracy on predicting if the grain twins or not is shown in Table 6.2. All models present a rather good overall prediction accuracy (over 0.8) that indicates that the dataset contains enough information to differentiate the grains that will twin from those that will not. However, there are differences in the accuracy when predicting twinned (or not twinned) grains between the ensemble methods (GDB [217], AdaBoost [216], and random forests [218]) and the 'Bayes-based' methods (naïve Bayes [219] and the BNs [220]). While the former show a contrast in accuracy between twinned (0.663 in average) and not twinned (0.964 in average) grains, the latter have a more balanced prediction accuracy of 0.850 and 0.866 in average for twinned and not twinned grains, respectively. This means that ensemble methods are prone to bias towards more

populated classes in the datasets, compromising their potential to learn from the less populated classes. In our case, both datasets are significantly unbalanced, with twinned grains accounting only for ~15% of the total grains. Hence, the ensemble methods are not considered suitable to achieve our goal of predicting twinning and ascertain the microstructural factors responsible for it.

Table 6.2: Overall accuracy in terms of the ROC AUC score and individual (twinned and not twinned) accuracy for the five best performing ML methods for the AZ31 dataset. The scores presented here are the mean over the 10 CV tasks. The 'individual' scores were obtained by calculating the ratio between correct predictions and total samples (i.e., a value of 0 would mean that all predictions were incorrect and a value of 1 that all predictions were correct). The default settings were used as implemented in the pyAgrum [215] and scikit-learn [214] Python packages for the BN and for all other methods, respectively. The highest accuracies are highlighted in bold.

Method	ROC AUC	Twinned accuracy	Not twinned accuracy
Bayesian network	**0.871**	**0.879**	0.863
Gaussian naïve Bayes	0.851	0.834	0.868
GDB	0.825	0.683	0.966
Random forests	0.812	0.660	0.954
AdaBoost	0.807	0.645	**0.972**

Regarding the Bayes-based models, the BNs outperforms naïve Bayes (Table 6.2). Compared to naïve Bayes, BNs provide both a higher overall accuracy (ROC AUC of 0.871) and a more reliable prediction of twinned grains (0.879), while keeping a similar accuracy when predicting not twinned grains (0.863). Moreover, BN models, as their names indicate, are constructed by building a network (a directed acyclic graph) from data, where nodes represent all features available in the dataset (including the target variable) and the edges connecting the nodes indicate dependences between features (see Figure 6.5(A), for an example of a BN for the AZ31 dataset). For instance, the BN in Figure 6.5(A) shows that the model is able to learn the connection between features belonging to the same category (size, SF, or angle features) directly from data, without any prior bias. In addition to a remarkable prediction accuracy, BNs can 'explain' what the model is learning. Hence, they offer the appropriate framework to obtain insights into the most relevant features defining twin nucleation. Henceforward, we will only focus on training BN models.

The next step to find the best possible model to describe twinning is to optimize the hyperparameters (i.e., those parameters that need to be fixed before training) of the BN model. A grid search CV procedure was used to this end. The description of the optimized hyperparameters and their optimal values for each model are provided in the methods section and in the Annex Methods C.1, respectively. The prediction accuracy in terms of the ROC AUC score and the individual accuracy on predicting twinned and not twinned grains for different optimized BN models is shown in Table 6.3. The BN model for the AZ31 dataset (BN1 in Table 6.3) shows a slight improvement in accuracy with respect to the non-optimized one (ROC AUC score increased from 0.871 to 0.877). Figure 6.5(A) shows the BN obtained from model BN1. Focusing on the target variable (*Twinned*), there are only three nodes directly connected to it: *Grain_size*, *T_SF1*, and *S_SF1*. Such a group of directly connected nodes is the Markov blanket (MB) of the variable *Twinned*. A MB is a subset of all the available features in the dataset that alone contains all the useful information to infer the random variable to which the MB belongs (*Twinned*, in this case). This is confirmed after building a model for the AZ31 dataset using for training only the MB (BN2 in Table 6.3). The overall accuracy is kept, and there are small differences in the accuracy on predicting (not) twinned grains (from 0.885 to 0.893 and from 0.869 to 0.862 for twin and not twins, respectively).

Table 6.3: Overall accuracy in terms of the ROC AUC score and individual (Twinned and Not twinned) accuracy for different BN models with optimized hyperparameters. The scores presented here are the mean over the 10 cross validation tasks. The 'individual' scores were obtained by calculating the ratio between correct predictions and total samples (i.e., a value of 0 would mean that all predictions were incorrect and a value of 1 that all predictions were correct). The models were trained with the BN implementation available in the pyAgrum Python package [215].

Model	Dataset	ROC AUC	Twinned accuracy	Not twinned accuracy
BN1	AZ31	0.877	0.885	0.869
BN2	AZ31 MB (*S_SF1*)	0.878	0.893	0.862
BN3	AZ31 MB (*Max_deltaBSF*)	0.878	0.894	0.862
BN4	AZ31 [*T_SF1* < 0.16]	0.639	0.417	0.862
BN5	Mg-1Al	0.626	0.629	0.622
BN6	AZ31 [*T_SF1* < 0.16] MB	0.735	0.767	0.703
BN7	Mg-1Al MB	0.685	0.664	0.705
BN8	AZ31 [*T_SF1* < 0.16] MB (*Min_deltaGs*)	0.686	0.667	0.704
BN9	Mg-1Al MB (*Grain_size*)	0.676	0.652	0.701

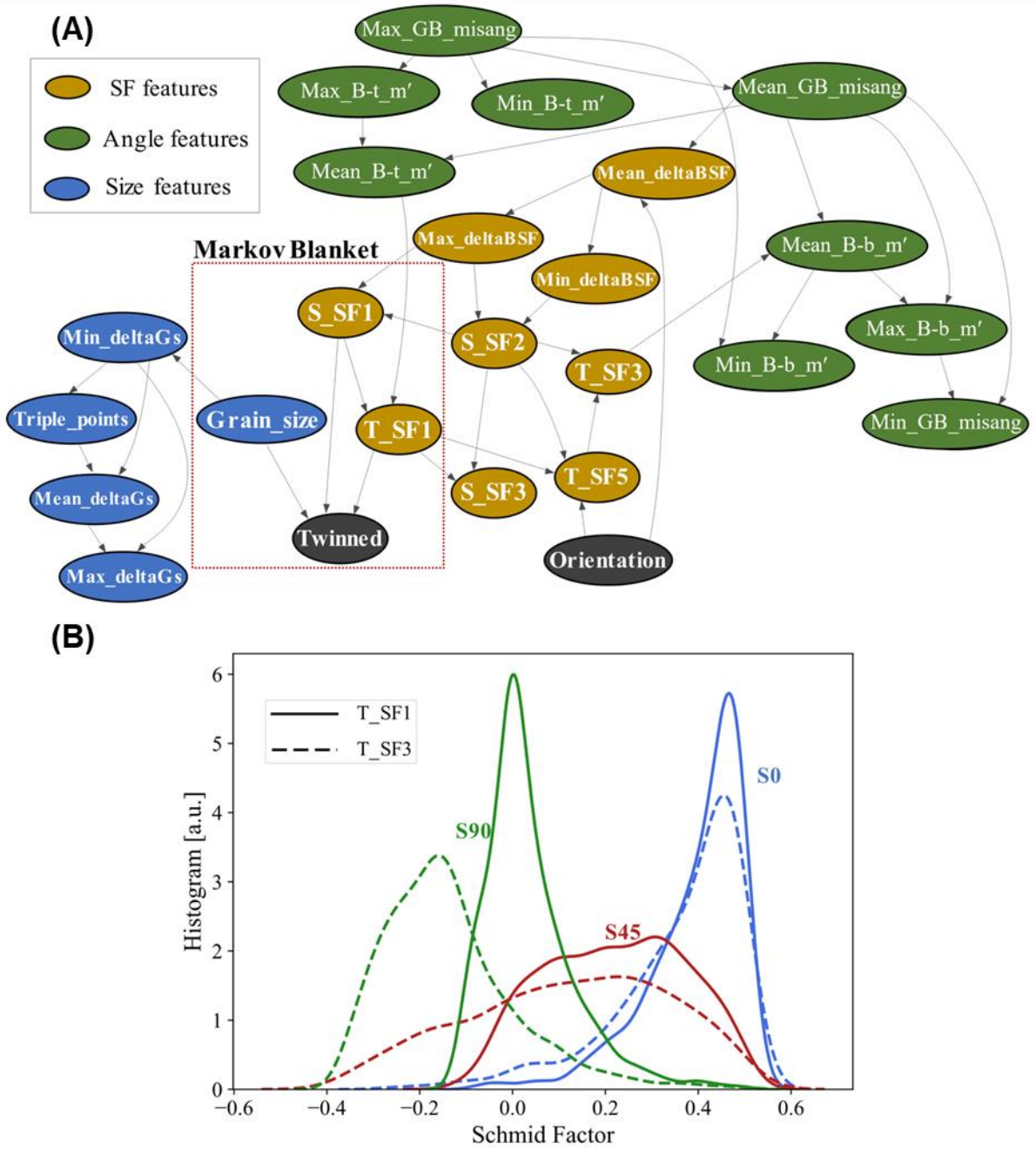

Figure 6.5: Selection of the members of the MB of twinning. (A) Example of a BN for the AZ31 dataset with the MB for the target variable 'Twinned' delimited with a dashed red square. Different colors for the nodes are used to indicate different types of features. (B) Distribution of values of the *T_SF1* and *T_SF3* features for the different loading conditions in the AZ31 dataset.

For the AZ31 dataset, the members of the MB of twinning can change depending on the training set. For example, *T_SF3* is sometimes selected instead of *T_SF1*. However, both features provide almost the same information since there is not much differences between the distribution of the former with respect to the one of the latter for the samples corresponding to S0 and S45 samples (see Figure

6.5(B)). Moreover, the highest twinning SF (represented by the *T_SF1* feature) endows a more relevant physical meaning because it corresponds to the twin variant with the highest resolved shear stress, under the macroscopic loading. Therefore, only *T_SF1* was used to train MB-based models for the AZ31 dataset. Another possible variation in the MB is the choice of *Max_deltaBSF* over *S_SF1*. For this case, training a BN including the former in the MB produces a model (BN3 in Table 6.3) with an accuracy equal to the BN2 model (ROC AUC score of 0.878 in the case of *S_SF1*).

So far, the accuracy of the models has been discussed. The next step is to analyze the insights they provide in describing twinning. Two features, *Grain_size* and *T_SF1*, can be highlighted from the MB of the AZ31 dataset (Figure 6.5(A)). They are also generally considered as the most important factors to predict twin nucleation from experimental observations [51–53,62–65]. The decision surface of a BN trained on the AZ31 dataset considering only the *Grain_size* and *T_SF1* features is shown in Figure 6.6(A). Remarkably, the BN is learning from our dataset a well-known causal relation: a grain has a high probability of twinning if its size is rather large (*Grain_size* > 7 μm) and its highest twinning SF has a high value (*T_SF1* > 0.16) [51–53,62–65]. This conclusion is true for all samples, regardless of the orientation of the sample.

However, the interplay between the size of the grains and their twinning SFs accounts only for 97% of the correct 'twinned' predictions of the BN2 (or BN3) model. In total, the BN2 (or BN3) model predicts correctly as 'twinned' 302 samples out of 338, meaning that the third member of the MB (either *S_SF1* or *Max_deltaBSF*) helps in correctly classifying 9 twinned grains more than when using only *Grain_size* and *T_SF1*. These additional correct predictions correspond to grains that have a grain size lower than 7 μm and a very large twinning SF (*T_SF1* > 0.46) identified in Figure 6.6(A) with an orange square. The scatter plots of all twinned samples of the AZ31 dataset considering all variables in the MBs are presented in Figure 6.6(B), one with *S_SF1* and another one with *Max_deltaBSF*. The analysis of the new correctly predicted samples (surrounded by an orange square like in Figure 6.6(A)) shows that these samples possess both

a high value of *Max_deltaBSF* (i.e., neighbor grains have higher basal slip SFs) and a very small value of *S_SF1*. Specifically, *Max_deltaBSF* > 0.22 and *S_SF1* < 0.22. These results indicate that small grains with a high twinning SF still have a high probability to twin if they do not have favorable conditions to deform (e.g., low basal slip SFs), but also have at least one neighbor grain with a high basal slip SFs that will deform easily because the CRSS for basal slip is very low.

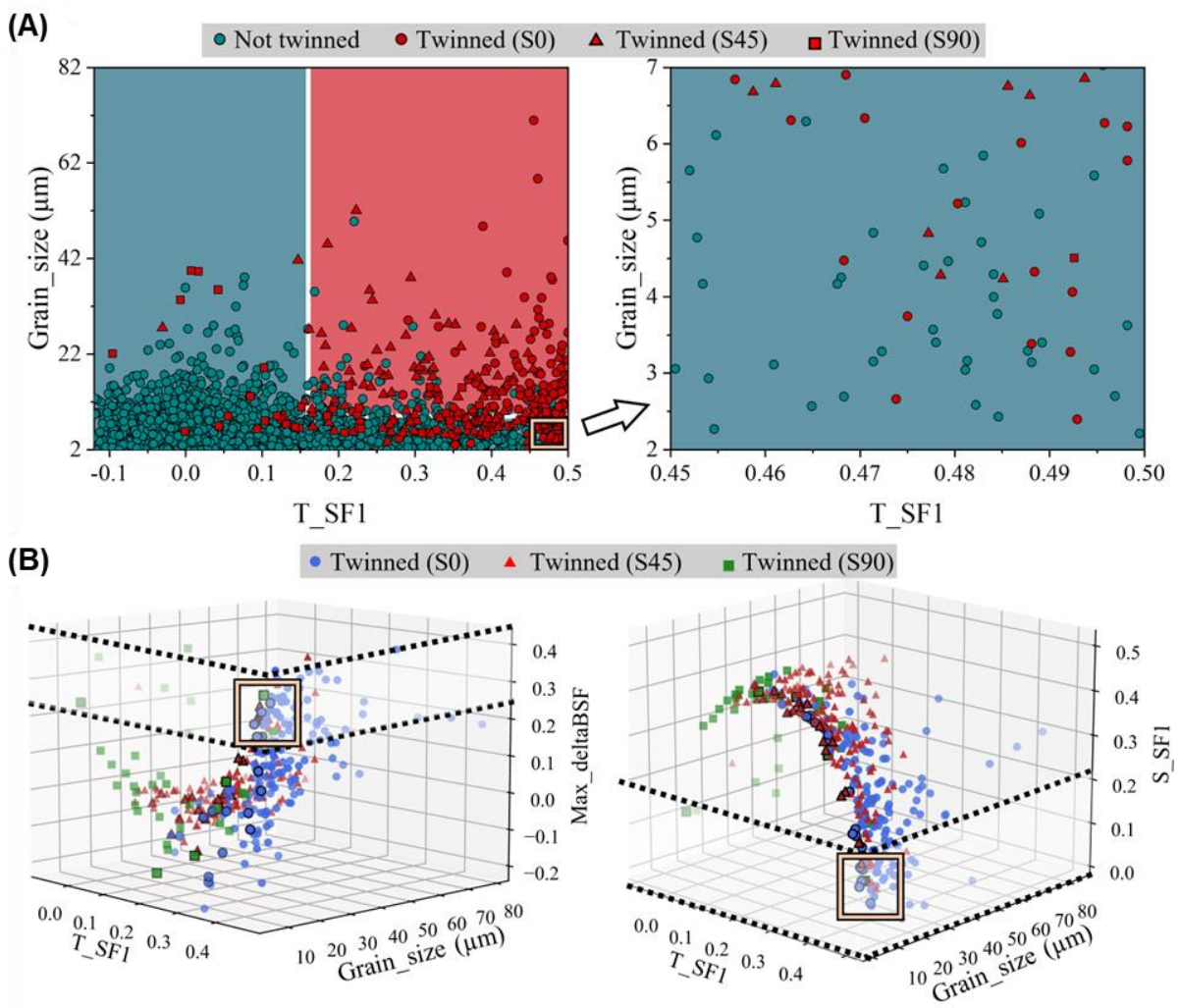

Figure 6.6: Feature analysis of small-sized grains that twin. (A) Decision surface of a BN model trained on the AZ31 dataset using only the *Grain_size* and *T_SF1* features. Blue and red colors identify the zones of the *xy* plane where the model will predict 'Not twinned' or 'Twinned', respectively. (B) Scatter plots of all twinned grains in the AZ31 dataset considering all variables in the MBs. The dashed lines delimit the range of values of the third member of the MB (*Max_deltaBSF* or *S_SF1*) within which the probability of twinning is high for small grains (*Grain_size* < 7 μm) with very high twinning SF (*T_SF1* > 0.46). The orange squares surround the small-sized grains that are correctly predicted as 'twinned' by the BN model when considering for training the three features in the MB.

Besides small-sized grains that twin, the decision surface in Figure 6.6(A) also shows that there are some grains in the S45 and S90 samples that twin despite having low, even negative, twinning SFs (*T_SF1* < 0.16). Given that the BN trained on the full AZ31 dataset does not provide any clue on why these grains twin, a BN model was trained using only the samples in the AZ31 dataset with values of *T_SF1* lower than 0.16 (the value at the boundary in the decision surface) and another model was trained on the Mg-1Al dataset (for which almost all twinned grains have very low, and negative twinning SFs). The performance of the 'reduced' AZ31 model (BN4 in Table 6.3) shows that, despite the number of twinned samples is very small (22) and the dataset is extremely unbalanced (1465 not twinned samples), the model is able to correctly predict almost half of the twinned grains (0.417) while achieving a good accuracy on the not twinned samples (0.862). As per the model trained on the Mg-1Al dataset (BN5 in Table 6.3), the overall accuracy is comparable to that of the BN4 model (0.626) but shows a more balanced prediction accuracy between twinned (0.629) and not twinned (0.622) samples than the BN4 model. Apart from the comparable performances of both models, their MBs share similar information. Their MBs indicate that *Min_deltaBSF* and a size-related feature (*Grain_size* for the AZ31 alloy and *Min_deltaGs* for the Mg-1Al alloy) are the most important features defining twinning in grains with low twinning SFs. Indeed, training BN models using only the features in the MBs leads to an increment of the prediction accuracy. For the AZ31 dataset (BN6 in Table 6.3), the ROC AUC score increases from 0.639 to 0.735, whereas the model for the Mg-1Al (BN7 in Table 6.3) presents an increment from 0.626 to 0.685.

The similarities in the MBs suggest that the information both models are learning is, if not the same, very similar. In view of this, it was decided to exchange between the datasets the non-shared member of the MB and retrain the models (i.e., *Grain_size* was used for the Mg-1Al dataset and *Min_deltaGs* for the AZ31 dataset). As expected, the accuracy of the models dropped (see BN8 and BN9 models in Table 6.3), but it was possible to compare the BN models of both datasets. The decision surfaces are plotted in Figure 6.7(A) and Figure 6.7(C) for the 'reduced' AZ31 models and in Figure 6.7(B) and Figure 6.7(D) for the Mg-1Al

models. Focusing on the shared feature in the MB, all models set almost the same upper limit for *Min_deltaBSF* (around -0.06) for large grains (larger than 24 μm in Figure 6.7(A) and Figure 6.7(B), or at least 16 μm larger than their smallest neighbor grain in Figure 6.7(C) and Figure 6.7(D)). This means that large grains that have at least one neighbor grain more rigid (i.e., lower slip SF) than them have a high probability to twin. Note that there is a difference in the limits learnt for the *Min_deltaBSF* feature between the AZ31 and the Mg-1Al models for smaller grains. Namely, the latter indicates that grains between 15 μm and 24 μm (or that are from 2 μm to 16 μm larger than their smallest neighbor grain) will be prone to twin only if at least one of their neighbors is far more rigid than them (*Min_deltaBSF* values lower than -0.16). Also, the Mg-1Al model suggests that grains smaller than 15 μm are very unlikely to twin regardless of the stiffness of their neighbors. Conversely, the 'reduced' AZ31 model trained with its MB shows that twin nucleation in a grain is favorable for almost all grain sizes (*Grain_size* > 2.4 μm) given that at least one neighbor is more rigid.

The differences between the AZ31 and Mg-1Al models are probably a consequence of the lack of data in the 'reduced' AZ31 dataset (there were only 22 twinned samples compared to the 115 available in the Mg-1Al) and not a difference in the causal relations of twinning between the alloys. To prove this, the Mg-1Al models of Figure 6.7(B) and Figure 6.7(D) were used to predict the labels of the samples in the 'reduced' AZ31 dataset. The boundary of the decision surface of the Mg-1Al models is also shown in Figure 6.7(A) and Figure 6.7(C) for an easy visual comparison between the models. While the models trained using *Grain_size* differ considerably in the region of very small grains (smaller than 15 μm), there is not much difference between the models trained with *Min_deltaGs* (the feature included in the MB of the Mg-1Al dataset). This is reflected in the accuracy of the Mg-1Al models in predicting the 'reduced' AZ31 dataset. The Mg-1Al model trained using *Grain_size* achieves a ROC AUC score of 0.639 with a very unbalanced accuracy between twinned (0.318) and not twinned (0.960) grains. On the other hand, the Mg-1Al model trained using *Min_deltaGs* has an overall accuracy of 0.782 with a good accuracy for both twinned (0.818) and not twinned (0.747) grains.

Such accuracies are even higher than the ones obtained by constructing any model from the 'reduced' AZ31 dataset directly (compared to models BN4, BN6, and BN8 in Table 6.3). This suggests that *Min_deltaGs* is more crucial than *Grain_size* to define twin nucleation for grains with low twinning SFs. Therefore, it can be concluded from our BN models that twin nucleation in grains with low (even negative) twinning SFs is the consequence of many-body relationships, where one needs to consider not only the grain itself but also its neighbors. Namely, these grains will have a high probability of twinning if they have at least one smaller neighbor grain and another one (or the same) that is more rigid because its basal SF is very low.

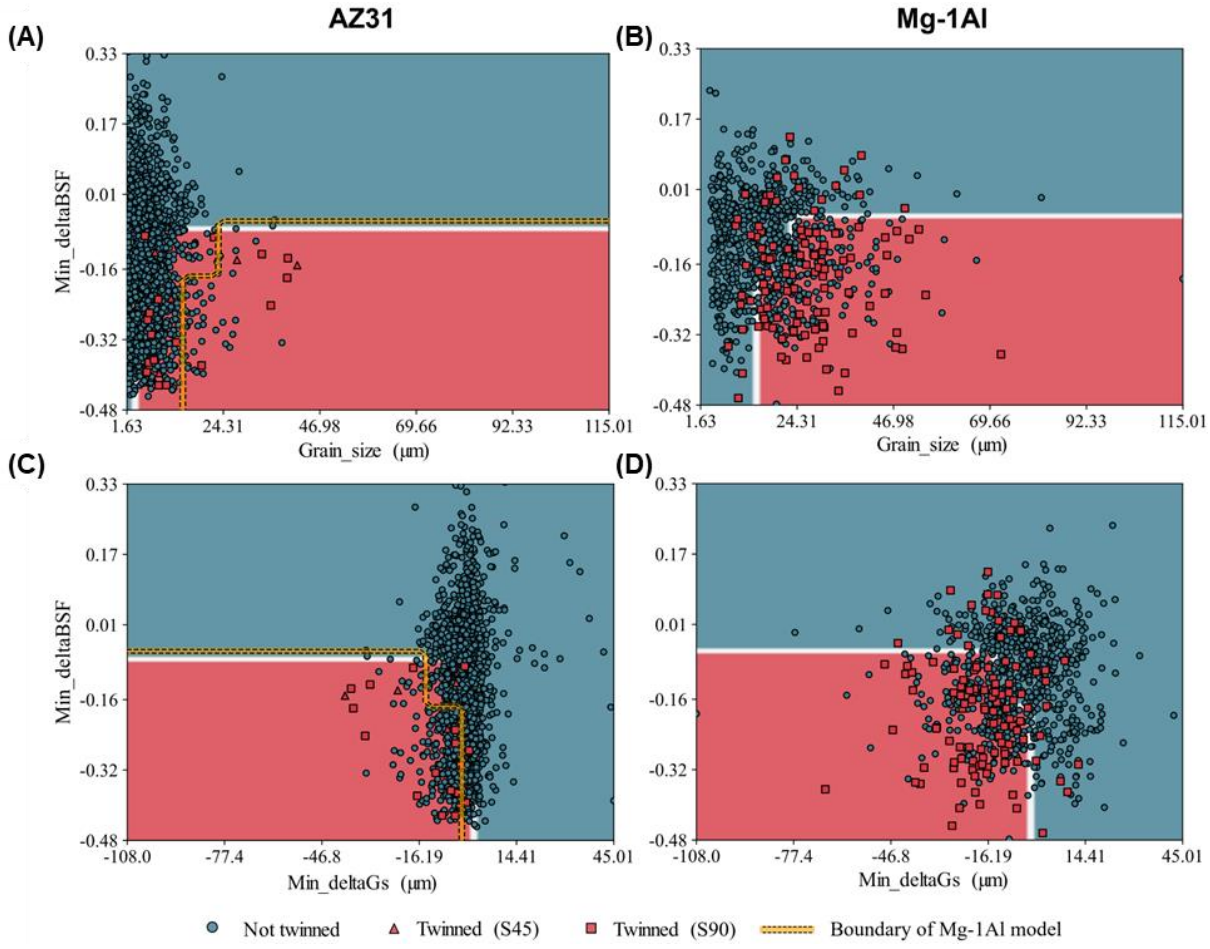

Figure 6.7: Decision surfaces of different BN models trained on the (A, C) 'reduced' AZ31 and (B, D) the Mg-1Al datasets. Models were trained using *Min_deltaBSF* and either (A, B) *Grain_size* or (C, D) *Min_deltaGs*. Blue and red colors identify the zones of the *xy* plane where the model will predict 'Not twinned' or 'Twinned', respectively. For comparison, the boundary of the Mg-1Al models is drawn with a yellow line on top the decision surfaces of the AZ31 models.

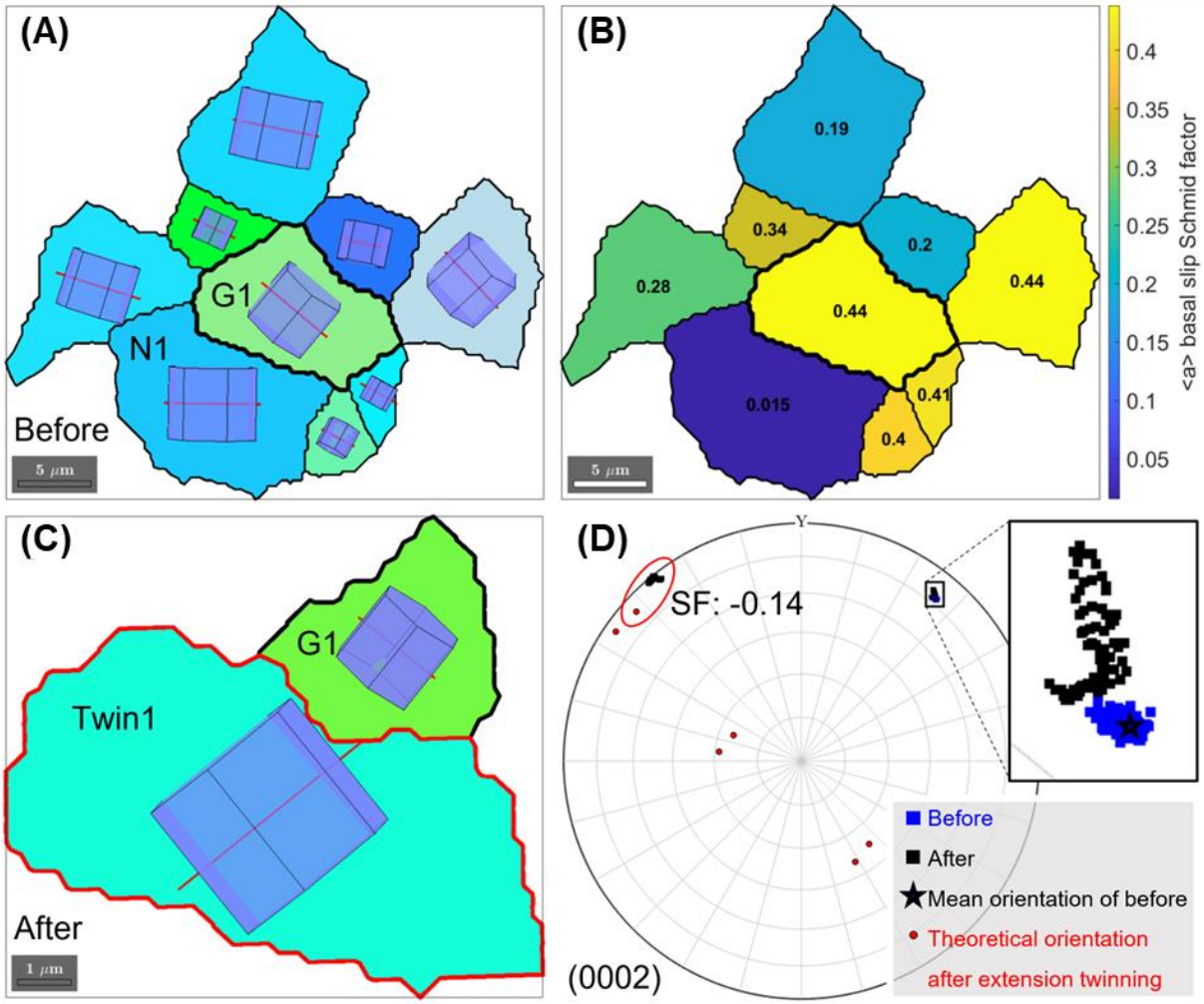

Figure 6.8: Experimental evidence of twinning nucleation in grain with a low twinning SF in sample S90. (A) IPF-Z map of grain G1 and its neighbor grains before deformation. Based on the mean orientation for each grain, the crystal lattice as well as the basal plane trace were determined and overlaid in this figure as a red line. (B) <a> basal slip SF map of the same grains under the tension along the horizontal direction. (C) IPF-Z map of grain G1 and formed Twin1 after deformation. The rotation of the crystal lattice and basal plane trace reveals a possible twinning behavior. (D) Projections of the orientation of grain G1 and Twin1 on the (0002) pole figure before (blue) and after (black) deformation. Based on the mean orientation of grain G1 before deformation, the orientations of all 6 possible ET variants were obtained, with their projections added in the pole figure.

The BN models suggested that the presence of a more rigid neighbor grain promotes twin nucleation in grains with unfavorable twinning SFs. To validate this conclusion, one of the grains that twinned with a low twinning SF was analyzed. The results of this analysis are presented in Figure 6.8. Grain G1 with a size of 11 μm and Euler angles of (140°, 77.4°, 6.5°) has 8 neighbors (Figure 6.8(A)). The SFs for <a> basal slip of the neighbor grains span a broad range from 0.015 to 0.44, while the maximum SF for <a> basal slip of G1 is equal to 0.44

(Figure 6.8(B)). After deformation, one twin (Twin1) with Euler angles of (38.8°, 91.7°, 11.5°) nucleates inside G1 (Figure 6.8(C)). According to the projection of Twin1 on the (0002) pole shown in Figure 6.8(D) -and taking the mean orientation of G1 as reference- Twin1 is located near the projection of an ET variant with a SF of -0.14. It is interesting to note that the deflection of G1 before and after deformation reveals that a slip deformation mode takes place at the same time that twinning (Figure 6.8(D)) [203]. More remarkable is, however, that Twin1 nucleates near the GB between G1 and the neighbor grain (N1), that has the lowest <a> basal slip SF (0.015) of all neighbors. This suggests that the nucleation of Twin1 tends to satisfy the strain compatibility between G1 and N1. Furthermore, the SFs for <a> basal slip of G1 and N1 lead to a *deltaBSF* = -0.425 (it is also the *Min_deltaBSF* value of G1), which is in full agreement with the criterion provided by the BN models.

6.4. Conclusions

Twin nucleation of Mg alloys was investigated by the combination of large database (over 3000 grains × 28 features) obtained from in-situ EBSD and state-of-the-art ML tools. The BN models reveal that twin nucleation is favored in larger grains and in grains with high twinning SFs, but also point out that twins may form in the grains with very low or even negative SFs for twinning (< 0.16) if they have at least one smaller neighbor grain and another one (or the same) that is more rigid. Moreover, twinning of small grains with high twinning SF is favored if they have low basal slip SFs and have at least one neighbor grain with a high basal slip SF that will deform easily. Very likely, twinning will be triggered in these small grains because it is the only way to maintain the deformation compatibility with soft neighbor grain. These results reveal that many-body relationships, such as differences in stiffness and size between a given grain and its neighbors, are crucial to assess ET nucleation in grains with characteristics commonly considered unfavorable for twinning (e.g., small grain size, low twinning SF).

Finally, the combination of the strategy presented in this chapter in combination with 3D microstructural characterization (to get information about

the microstructure and of twinning beneath the surface) and of crystal plasticity simulations (to obtain information about the local SFs) [180,357] is a promising path for future work to understand the physical mechanisms responsible for twin nucleation.

7. Discussion, conclusions, and outlook

7.1. Discussion

In this thesis, the influence of several parameters, including the global SF, precipitates, grain size and features of neighbor grains, on the deformation mechanisms were investigated in various wrought Mg alloys with different microstructures using in-situ EBSD, advanced EBSD-based analysis, TEM as well as ML. The overarching results of these analysis are discussed in the following sections.

7.1.1. Influence of the Schmid factor on the deformation mechanisms of wrought Mg alloys

The mechanical behavior and the deformation mechanisms in tension and in compression were analyzed in a Mg-6.5Zn alloy with a dual texture. Note that 80% of the grains in the alloy presented the typical E texture in which the basal planes were oriented parallel to the extrusion axis. However, 20% of the grains presented an unconventional C texture in which the $\vec{c}$ axis was oriented along the ED. This unusual C texture is closely associated with the high extrusion ratio and large applied force, especially during the second extrusion process [254–257].

The deformation mechanisms in tension and compression along the ED of a dual-textured Mg-6.5Zn alloy were analyzed. In the C-textured grains, the $\vec{c}$ axis is oriented ± 30° along the loading axis and ET are easily activated in tension along the ED, while the $\vec{c}$ axis in the E-textured grains is oriented ± 30° along the perpendicular to the loading axis and ET are easily activated in compression along the ED. Thus, <a> basal slip and ET are active during tension and compression along the ED (although ET appear in different regions of the microstructure as a function of the loading direction), leading to a minimum yield asymmetry ratio for a wrought Mg alloy without RE.

The different deformation mechanisms active in each region of the microstructure in tension and compression were analyzed as a function of the

applied strain by means of EBSD, GROD and ST-MLRA to find out why a limited volume fraction (20%) of C-textured grains leads to a minimum yield asymmetry ratio. It was found that the main deformation mechanisms during tensile deformation along the ED in the E-textured grains were <a> basal slip as well as <a> non-basal slips while <a> basal slip and ET were the main deformation mechanism in the E-textured grains subjected to compressive deformation along the ED. As the SFs for ET and <a> non-basal slip during compressive deformation were similar for E-textured grains and the CRSS for ET is lower than that of <a> non-basal slip, the yield strength of the E-textured grains in compression should be much lower than in tension, leading to the typical yield asymmetry of wrought Mg alloys (< 0.67). However, this large asymmetry is limited by the contribution of the C-textured grains in which <a> basal slip and CT (followed by DT) dominate the plastic deformation during compression along the ED and <a> basal slip and ET are main plastic deformation mechanisms during tension along the ED. The CRSS for CT is much higher than that for ET and, thus, the yield asymmetry of the C-textured grains is opposed (and more marked) than the one of E-textured grains. As a result, the presence of 20% of C-textured grains in the microstructure can reduce the yield asymmetry of the wrought alloy to a minimum.

Besides, the SFs of <a> basal slip and <a> non-basal slip can also influence the CT and DT activities in dual-textured Mg-6.5Zn alloy during tension and compression. Their relationships are depicted in Figure 7.1(A) and Figure 7.1(B), in which the presence of CT and DT in each grain is plotted as a function of the highest SF for <a> prismatic and <a> pyramidal slip, respectively, including also the influence of the SF for <a> basal slip and CT. The activity of both CT and DT decreases as the SF of <a> basal slip increases because the SF for CT also decreases. When the SF for <a> basal slip is < 0.4 and the SFs for <a> non-basal slip systems are low (< 0.12 for <a> prismatic slip or < 0.3 for <a> pyramidal slip), i.e., in region i, DT is dominant with respect to CT. In this region, the ratio of the number of grains with DT with respect to the sum of the number of grains containing CT and DT is 76%. However, this ratio drops to 23% if the SF for <a> basal slip is very low (< 0.1) and the SF for <a> non-basal slip is very high (> 0.36)

(region ii). Besides, this ratio increases slightly to 38% if the highest SF for <a> basal slip is in the range 0.1 - 0.4 and while the highest SF for <a> non-basal slip remains > 0.36 (region iii). These results suggest that the presence of <a> basal slip facilitates the transformation of CT to DT, while the activation of <a> non-basal slip suppresses the transformation of CT → DT.

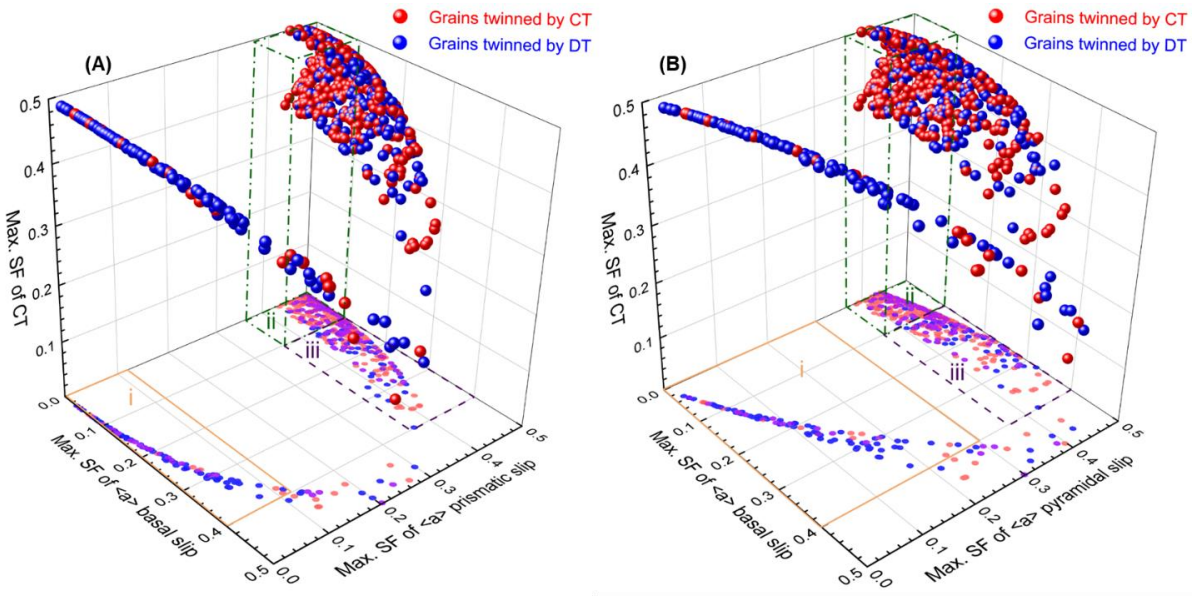

Figure 7.1: Experimental evidence of CT and DT as a function of (A) the maximum SFs for <a> basal slip, <a> prismatic slip and CT in each grain and (B) the maximum SFs for <a> basal slip, <a> pyramidal slip and CT in each grain. The average orientation was used to calculate the SF in each grain, and the highest SF among all the slip systems and CT variants was chosen.

Apart from the formation of ET within the CT (to form DT) in dual-textured Mg-6.5Zn alloy, ET in grains with low -or even negative- SFs were found in the Mg-4.5Zn alloy with and without precipitates, Mg-1Al alloy, as well as in the rolled AZ31 Mg alloy. Their nucleation and growth cannot be explained by the global SF, nor by the geometrical compatibility factor. Via the in-situ EBSD, the nucleation of anomalous ETs was associated with the severe strain incompatibility between neighbor grains as a result from the different <a> basal slip-induced lattice rotations. Moreover, the anomalous twins could grow with the applied strain due to the continuous activation of <a> basal slip in different neighbor grains. This abnormal behavior was also analyzed using ML. To be specific, twin nucleation is favored in larger grains and in grains with high twinning SFs, as shown in the

dual-textured Mg-6.5Zn alloys deformed in tension and compression. Nevertheless, twins also appear in grains with very low -or even negative- SF for twinning and in small grains with high twinning SFs. The influence of the neighbor grains on the formation of ETs will be thoroughly discussed in section 7.1.3.

7.1.2. Influence of the precipitates on the deformation mechanisms of wrought Mg alloys

The mechanical behavior and the associated dislocation slip mechanisms were analyzed in Mg-Zn alloys with and without β_1' precipitates. In the absence of precipitates (AE condition), slip traces were mostly planar, in accordance with previous investigations [50,262]. The dominant active slip systems in Mg-4.5Zn alloy without precipitates were <c + a> II pyramidal slip, followed by <a> basal slip. The other three slip systems, i.e., <a> prismatic, <a> pyramidal, and <c + a> I pyramidal slips, showed very low activities. The dominance of <c + a> II pyramidal slip could be attributed to two factors. Firstly, the theoretical SF of <c + a> II pyramidal slip (0.42) is higher than that of <a> basal slip (0.25) (Figure 4.2(A) and Figure 4.2(D)) because of the extrusion texture. The second factor is the high content of Zn atoms in solid solution, that induces a strong hardening for basal slip and promotes non-basal slip [262,362,363]. According to the single crystal micropillar compression tests, the CRSS of <a> basal slip in Mg-2Zn (at.%) alloy reached ~ 12.5 MPa [92]. Besides, the presence of Zn in solid solution reduces the axial ratio (c/a) value of the Mg hexagonal lattice, facilitating the activation of non-basal slip [323,324,364]. The activation of <c + a> II pyramidal slip together with basal slip can contribute to improve the room temperature ductility of the Mg-Zn alloy.

In the presence of precipitates (PA condition), most slip traces on the surface of the Mg-4.5Zn alloy changed from planar (Figure 4.7(A) and Figure 4.7(B)) to non-planar (Figure 4.7(C)). Moreover, <a> prismatic slip dominated the deformation of Mg-4.5Zn alloy with precipitates and TEM observations indicated that <a> prismatic dislocations glided parallel to the β_1' precipitates (Figure 4.11). The reason of why <a> prismatic dislocations are dominant in Mg-4.5Zn alloy with

precipitates will be discussed latter. The relative activity of <a> basal slip was reduced because glide of <a> basal slip dislocations was hindered by the precipitates, as evidenced in Figure 4.11. This phenomenon was also responsible for the elevated yield strength (Figure 4.4(A)). In addition, the Mg-4.5Zn alloy with precipitates has a lower strain hardening (Figure 4.4(B)) because latent hardening by dislocation-dislocation interactions is not favored by the presence of the precipitates [365]. The activation of <a> prismatic dislocations can accommodate the applied strain when easy basal slip is not available in the Mg-Zn alloy with rod-shaped precipitates. However, the strain provided by prismatic slip is still limited to the basal plane, thus hindering the ductility of Mg-Zn alloy with precipitates.

The interactions between dislocations and precipitates in Mg alloys have been studied through both computational simulations and experiments [106,366–368]. The dislocation-precipitate interactions can be generally categorized as precipitate shearing and precipitate bypassing. <a> basal slip dislocations were found to shear the β_1' precipitates in the single crystal micropillar compression tests at room temperature [152,156]. It should be noted here that strain tends to localize on a few crystallographic planes during micropillar compression of Mg single crystals, suitably oriented for basal slip, leading to dislocation avalanches which pile-up against the precipitates [369]. With the aid of the atomistic simulations, Esteban-Manzanares et al. [105] showed that <a> basal slip dislocations initially overcame the precipitate by the formation of an Orowan loop that penetrated in the precipitate. Precipitate shearing only took place after several Orowan loops were piled-up. The number of dislocations in the pile-up to shear the precipitate depended on the precipitate diameter and decreased with temperature, as experimentally observed in [156]. Thus, β_1' precipitates are expected to hinder the motion of basal dislocation in the case of polycrystals, which show smaller strain localization than single crystal micropillars. Overall, the reported CRSS for <a> basal slip in the peak-aged Mg-Zn alloys (with Zn contents in the range of 4 to 5.1 wt.%) were around 18 to 35 MPa [156,370], indicating the strong hardening effect of β_1' precipitates for <a> basal dislocations.

The interaction of pyramidal <c + a> slip dislocations with $\vec{c}$ axis rod-shaped β_1' precipitates was analyzed after micropillar compression tests along the ~ [0001] direction in Mg-Zn single crystals [316]. Dislocations overcame the precipitates by the formation of an Orowan loop, leading also to a strong hardening and the CRSS for pyramidal <c + a> slip reached 155 MPa. The interaction of <a> non-basal slip dislocations with $\vec{c}$ axis rod-shaped precipitates in Mg-Zn alloys has not been analyzed, to the best of the authors' knowledge. The weak beam dark field images in Figure 4.11 show that <a> basal slip screw dislocations can cross-slip to the prismatic plane in the presence of a precipitate that hinders its motion (Figure 7.2(A) to Figure 7.2(D)). The <a> basal slip screw dislocation will start to make an Orowan loop around the precipitate (Figure 7.2(C)), with the mixed dislocation character, but the screw segments far away from the precipitate will cross-slip to the prismatic plane (Figure 7.2(D)) and glide parallel to the precipitates (Figure 7.2(E)) while they are pinned by the mixed dislocations in contact with the precipitate that cannot cross-slip. Further slip of <a> prismatic dislocations parallel to the precipitates will be hindered by the pinning of the mixed <a> basal slip dislocations at the precipitates but <a> prismatic slip will become dominant with respect to <a> basal slip in Mg-Zn alloys containing β_1' precipitates.

It should be noted that this mechanism of dislocation/precipitate interaction is different from others reported in Mg alloys. For instance, Huang et al. found that <a> basal slip screw dislocations may overcome the β_1 precipitates (Mg_3Nd with a $D0_3$ ordered structure; prismatic plate) by multiple cross-slip steps (basal-to-prismatic-to-basal) via the Hirsch mechanism in Mg-Nd alloys [371], as confirmed by both in-situ TEM experiments and molecular dynamics simulations [372]. The Hirsch mechanism was also used to explain the dislocation cross-slip around the β-$Mg_{17}Al_{12}$ precipitate (basal plate) in Mg-Al alloys [373]. In our investigation, the interactions between <a> basal slip screw dislocations and $\vec{c}$ axis rod-shaped precipitates in Mg-Zn alloys leads to the formation of <a> prismatic slip screw dislocations, via basal-to-prismatic cross-slip mechanism and dislocation glide continues in the prismatic plane, parallel to the precipitates. The <a> basal slip screw dislocations could also possibly cross-slip to pyramidal plane.

However, the intersection angle of pyramidal plane and $\vec{c}$ axis is ~ 28.1° for Mg and the glide of the <a> pyramidal slip screw dislocations, formed by cross-slip of <a> basal slip screw dislocations, has to cross-slip again to the prismatic plane to avoid the $\vec{c}$ axis rod-shaped precipitates. This hypothesis agrees well with the experimental TEM image in Figure 4.11(D) as well as with the dominant role of the <a> prismatic slip on the deformation of polycrystalline Mg-4.5Zn bulk sample with $\vec{c}$ axis rod-shaped β_1' precipitates (Table 4.3).

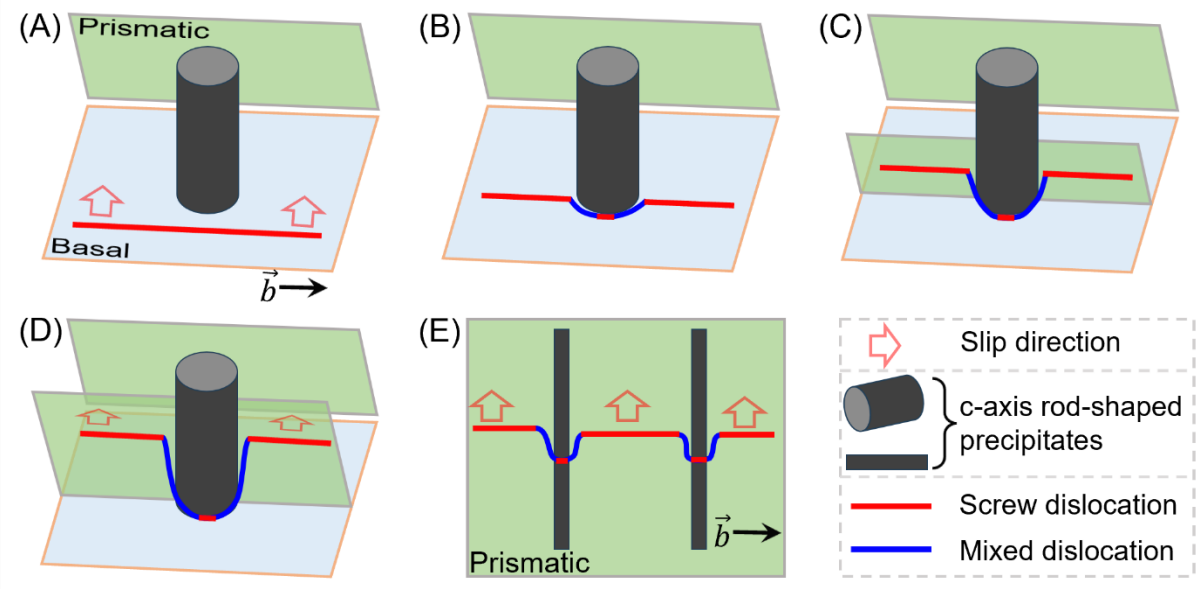

Figure 7.2: <a> screw dislocation cross-slip mechanisms in Mg alloys with the $\vec{c}$ axis rod-shaped precipitates. (A) Before the interaction of <a> basal slip screw dislocation and precipitate. (B) <a> basal slip dislocation starts to form an Orowan loop around the precipitate. (C) Basal-to-prismatic cross-slip of both ends of the dislocation line. (D-E) Dislocation slips along the prismatic plane after basal-to-prismatic cross-slip behavior, in agreement with the experimental observations in Figure 4.11(D). The observation direction in (E) is perpendicular to the $\vec{c}$ axis of lattice.

7.1.3. Influence of the neighbor grains on the twinning mechanisms of wrought Mg alloys

The nucleation and growth behavior of anomalous ETs with low -or even negative- SFs was tracked using in-situ EBSD technique on Mg-1Al alloy under various loading strains. The most likely explanation for the nucleation of anomalous ETs in Figure 5.9 can be found in the presence of the localized compressive deformation and in the severe strain incompatibility between

neighbor grains, as a result from the different <a> basal slip-induced lattice rotations. To be specific, grain G92 undergoes a localized compressive deformation along the ED (Figure 5.11(B)), which is favorable for the nucleation of Twin6, Twin8, Twin9 and Twin10. No twin is observed in Grain G132, but the slip-induced lattice rotation orientation of G132 is opposed to that of G92 (Figure 5.13(C) and Figure 5.13(E)). Their combination induces local compression on the GB between grains G121 and G146, leading to the nucleation of Twin3, Twin4, and Twin7 as well as the formation of ledges around the GB (Figure 5.9(B)), though G121 experiences a tensile deformation, as shown in Figure 5.11(B). The nucleation of Twin5 should be ascribed to the strain incompatibility near the GB between grains G87 and G121, as evidenced by the different slip activities and the near perpendicular lattice rotation orientations in these two grains (Figure 5.13(B) and Figure 5.13(D)). Besides, the anomalous ETs can grow gradually with the applied tensile strain, despite their nucleation is not favored by the macroscopic loading condition, due to the continuous activation of <a> basal slip in various grains, which enhances the strain incompatibility.

In addition, using the ML tools, it is also found that ETs may nucleate in grains with negative twinning SFs if the grain has at least one smaller neighbor grain and another one (or the same) that is more rigid. The condition that 'at least one smaller neighbor grain' indicates that the number of neighbor grains may be larger, providing more GBs with the optimum conditions to nucleate twins. As a result, *Min_deltaGs* is more important than *Grain_size* to define twin nucleation for grains with low twinning SFs (Figure 6.7). In addition, the condition that 'at least one more rigid neighbor grain' points out to the development of a stress concentration at the GB to maintain the compatibility between the grain and its hard neighbor, which should be relieved by the activation of twinning, a hard slip system (prismatic or pyramidal) or even cracking [190,205,210,374–376]. Koike et al. [61] reported that anomalous ETs with negative twinning SFs are formed to minimize strain incompatibility caused by the greater activity of basal slip in the twinned grain than in the surrounding grains, in agreement with the ML predictions and the experimental result shown in Figure 6.8.

7.2. Conclusions

This thesis was aimed at providing a deeper knowledge of deformation mechanisms (slip and twinning) of wrought Mg alloys with different microstructures at room temperature. With this purpose, various state-of-the-art experimental techniques were used, including the recently developed ST-MLRA and GROD, to evaluate the actual deformation mechanisms. Moreover, in-situ mechanical tests were also carried out. The main conclusions of the results presented in this thesis are the following:

- The combination of state-of-art in-situ EBSD characterization and advanced EBSD-based techniques – such as ST-MLRA and GROD – is very powerful methodology to study the deformation mechanisms in wrought Mg alloys and to review the influence of microstructure on the deformation mechanisms.

- The deformation mechanisms of a dual-textured Mg-6.5Zn alloy were ascertained under tension and compression. Compressive deformation of the grains with the prismatic texture is accommodated by <a> basal slip and ET while tensile deformation promotes <a> basal and <a> non-basal slips, leading to the typical yield asymmetry. However, the rotated grains present the opposite (and much stronger) yield asymmetry because tensile deformation is absorbed by <a> basal slip and ET while compression deformation requires <a> basal slip and CT. This microstructure with appropriate texture distribution (20% area fraction of rotated grains) leads to a negligible tension-compression asymmetry in the yield strength. In addition, the activation of <a> non-basal slips can suppress the transformation of CT to DT.

- The influence of prismatic precipitates on the actual deformation mechanisms of Mg-4.5Zn alloy with a standard prismatic texture was revealed. In the sample without precipitates, planar slip traces were found in 92% of the grains with slip traces, and among them, the primary active slip systems were <a> basal slip and <c + a> II pyramidal slip. However, non-planar slip traces were observed in 76% of the grains with slip traces in the sample with precipitates, and among them, <a> prismatic slip exhibited the highest activity, followed by <c + a> II

pyramidal slip. The change in the dominant active slip systems with precipitation was attributed to the strong hardening induced by precipitates on <a> basal slip. This favored the cross-slip of <a> basal slip dislocations to prismatic plane and plastic deformation progressed by the glide of <a> prismatic slip dislocations parallel to the precipitates.

- The origin of anomalous ETs was explored on Mg-1Al alloy with a standard prismatic texture using in-situ EBSD. Anomalous ETs nucleated mainly at the onset of plastic deformation at or near GB triple junctions. They were associated with the severe strain incompatibility between neighbor grains as a result from the different <a> basal slip-induced lattice rotations. Moreover, the anomalous twins were able to grow with the applied strain due to the continuous activation of <a> basal slip in different neighbor grains, which enhanced the strain incompatibility.

- Coupling with EBSD and ML, 3 different scenarios for twinning in wrought Mg alloys were presented. Twin nucleation is favored in larger grains and in grains with high twinning SFs, but also that twins may form in the grains with very low or even negative SFs for twinning if they have at least one smaller neighbor grain and another one (or the same) that is more hard-to-deform (low <a> basal slip SF). Moreover, twinning of small grains with high twinning SFs is favored if they have low <a> basal slip SFs and have at least one neighbor grain with a high <a> basal slip SF that will deform easily.

7.3. Future work

The following tasks are proposed as future work:

- The analysis of the deformation mechanisms in this thesis is limited to the surface, and the slip / twinning behavior in the bulk may differ from that near the surface because of the lack of constraint. Moreover, twinning is a three-dimensional phenomenon. Thus, future work should try to analyze the deformation mechanisms in the bulk. This can be achieved by means laboratory diffraction contrast tomography and / or in-situ high energy synchrotron X-rays to characterize the deformation behavior of Mg alloys at a three-dimensional scale.

In particular, this information will be very useful to ascertain the nucleation and growth of twins within the bulk and link these results with surface observations.

- Combination of the experimental techniques developed in this thesis with crystal plasticity and / or phase field simulations could provide a comprehensive understanding of the deformation mechanisms of wrought Mg alloys, i.e., the relative activities of various deformation modes during loading, as well as physical origin of some anomalous deformation behaviors near grain / twin boundaries.

- As summarized in chapter 1, there are many other factors, e.g., temperature and strain rate, that also influence the deformation mechanisms of wrought Mg alloys. Further work could be directed to use the experimental techniques developed and applied in this thesis to understand their influence on the deformation behavior of wrought Mg alloys with different microstructures.

Bibliography

[1] A. Dziubińska, A. Gontarz, M. Dziubiński, M. Barszcz, The forming of magnesium alloy forgings for aircraft and automotive applications, Adv. Sci. Technol. Res. J. 10 (2016) 158–168. https://doi.org/10.12913/22998624/64003.

[2] D. Shi, Influence of Al and Zn alloying additions on the deformation mechanisms of Mg alloys, PhD Thesis, Universidad Politécnica de Madrid, 2021. https://doi.org/10.20868/UPM.thesis.69339.

[3] R. John, CRC Handbook of Chemistry and Physics, 99th Edition, CRC Press (2018). https://www.crcpress.com/CRC-Handbook-of-Chemistry-and-Physics-99th-Edition/Rumble/p/book/9781138561632 (accessed June 4, 2019).

[4] W. Michels, Magnesium Alloys and their Applications, Materials Technology 13 (1998) 121–122. https://doi.org/10.1080/10667857.1998.11752784.

[5] E.C. Burke, W.R. Hibbard, Plastic Deformation of Magnesium Single Crystals, JOM 4 (1952) 295–303. https://doi.org/10.1007/BF03397694.

[6] H. Conrad, W.D. Robertson, Effect of temperature on the flow stress and strain-hardening coefficient of magnesium single crystals, JOM 9 (1957) 503–512. https://doi.org/10.1007/BF03397908.

[7] R.E. Reed-Hill, W.D. Robertson, Deformation of magnesium single crystals by nonbasal slip, JOM 9 (1957) 496–502. https://doi.org/10.1007/BF03397907.

[8] K.Y. Xie, Z. Alam, A. Caffee, K.J. Hemker, Pyramidal I slip in c-axis compressed Mg single crystals, Scripta Materialia 112 (2016) 75–78. https://doi.org/10.1016/j.scriptamat.2015.09.016.

[9] J. Wang, J.M. Molina-Aldareguía, J. LLorca, Effect of Al content on the critical resolved shear stress for twin nucleation and growth in Mg alloys, Acta Materialia 188 (2020) 215–227. https://doi.org/10.1016/j.actamat.2020.02.006.

[10] E.W. Kelley, W.F. Hosford, Plane-Strain Compression of Magnesium and Magnesium Alloy Crystals, Transactions of the Metallurgical Society of AIME 242 (1968) 5–13.

[11] J. Koike, Enhanced deformation mechanisms by anisotropic plasticity in polycrystalline Mg alloys at room temperature, Metall Mater Trans A 36 (2005) 1689–1696. https://doi.org/10.1007/s11661-005-0032-4.

[12] A.L. Oppedal, H. El Kadiri, C.N. Tomé, G.C. Kaschner, S.C. Vogel, J.C. Baird, M.F. Horstemeyer, Effect of dislocation transmutation on modeling hardening mechanisms by twinning in magnesium, International Journal of Plasticity 30–31 (2012) 41–61. https://doi.org/10.1016/j.ijplas.2011.09.002.

[13] R.V. Mises, Mechanik der plastischen Formänderung von Kristallen, Zeitschrift Für Angewandte Mathematik Und Mechanik 8 (1928) 161–185. https://doi.org/10.1002/zamm.19280080302.

[14] M.R. Barnett, Twinning and the ductility of magnesium alloys: Part I: "Tension" twins, Materials Science and Engineering: A 464 (2007) 1–7. https://doi.org/10.1016/j.msea.2006.12.037.

[15] M.R. Barnett, Twinning and the ductility of magnesium alloys: Part II. "Contraction" twins, Materials Science and Engineering: A 464 (2007) 8–16. https://doi.org/10.1016/j.msea.2007.02.109.

[16] J.W. Christian, S. Mahajan, Deformation twinning, Progress in Materials Science 39 (1995) 1–157. https://doi.org/10.1016/0079-6425(94)00007-7.
[17] É. Martin, L. Capolungo, L. Jiang, J.J. Jonas, Variant selection during secondary twinning in Mg–3%Al, Acta Materialia 58 (2010) 3970–3983. https://doi.org/10.1016/j.actamat.2010.03.027.
[18] J.F. Nie, K.S. Shin, Z.R. Zeng, Microstructure, Deformation, and Property of Wrought Magnesium Alloys, Metall Mater Trans A 51 (2020) 6045–6109. https://doi.org/10.1007/s11661-020-05974-z.
[19] S. Niknejad, S. Esmaeili, N.Y. Zhou, The role of double twinning on transgranular fracture in magnesium AZ61 in a localized stress field, Acta Materialia 102 (2016) 1–16. https://doi.org/10.1016/j.actamat.2015.09.026.
[20] M. Ruffino, J. Nutter, X. Zeng, D. Guan, W.M. Rainforth, A.T. Paxton, Triple and double twin interfaces in magnesium—the role of disconnections and facets, Sci Rep 13 (2023) 3861. https://doi.org/10.1038/s41598-023-30880-w.
[21] A. Khosravani, D.T. Fullwood, B.L. Adams, T.M. Rampton, M.P. Miles, R.K. Mishra, Nucleation and propagation of {10-12} twins in AZ31 magnesium alloy, Acta Materialia 100 (2015) 202–214. https://doi.org/10.1016/j.actamat.2015.08.024.
[22] L. Jiang, M. Gong, J. Wang, Z. Pan, X. Wang, D. Zhang, Y.M. Wang, J. Ciston, A.M. Minor, M. Xu, X. Pan, T.J. Rupert, S. Mahajan, E.J. Lavernia, I.J. Beyerlein, J.M. Schoenung, Visualization and validation of twin nucleation and early-stage growth in magnesium, Nat Commun 13 (2022) 20. https://doi.org/10.1038/s41467-021-27591-z.
[23] Y. He, B. Li, C. Wang, S.X. Mao, Direct observation of dual-step twinning nucleation in hexagonal close-packed crystals, Nature Communications 11 (2020) 2483. https://doi.org/10.1038/s41467-020-16351-0.
[24] B. Li, E. Ma, Atomic Shuffling Dominated Mechanism for Deformation Twinning in Magnesium, Phys. Rev. Lett. 103 (2009) 035503. https://doi.org/10.1103/PhysRevLett.103.035503.
[25] R.C. Pond, J.P. Hirth, A. Serra, D.J. Bacon, Atomic displacements accompanying deformation twinning: shears and shuffles, Materials Research Letters 4 (2016) 185–190. https://doi.org/10.1080/21663831.2016.1165298.
[26] R. Xin, Z. Liu, Y. Sun, H. Wang, C. Guo, W. Ren, Q. Liu, Understanding common grain boundary twins in Mg alloys by a composite Schmid factor, International Journal of Plasticity 123 (2019) 208–223. https://doi.org/10.1016/j.ijplas.2019.07.018.
[27] N. Thompson, D.J. Millard, XXXVIII. Twin formation, in cadmium, The London, Edinburgh, and Dublin Philosophical Magazine and Journal of Science 43 (1952) 422–440. https://doi.org/10.1080/14786440408520175.
[28] S. Mendelson, Dislocation Dissociations in hcp Metals, Journal of Applied Physics 41 (2003) 1893–1910. https://doi.org/10.1063/1.1659139.
[29] A. Serra, D.J. Bacon, R.C. Pond, The crystallography and core structure of twinning dislocations in H.C.P. metals, Acta Metallurgica 36 (1988) 3183–3203. https://doi.org/10.1016/0001-6160(88)90054-5.
[30] A. Serra, D.J. Bacon, A new model for 1012 twin growth in hcp metals, Philosophical Magazine A 73 (1996) 333–343. https://doi.org/10.1080/01418619608244386.

[31] A. Serra, D.J. Bacon, R.C. Pond, Dislocations in interfaces in the h.c.p. metals—I. Defects formed by absorption of crystal dislocations, Acta Materialia 47 (1999) 1425–1439. https://doi.org/10.1016/S1359-6454(99)00016-6.

[32] R.C. Pond, A. Serra, D.J. Bacon, Dislocations in interfaces in the h.c.p. metals—II. Mechanisms of defect mobility under stress, Acta Materialia 47 (1999) 1441–1453. https://doi.org/10.1016/S1359-6454(99)00017-8.

[33] J. Wang, J.P. Hirth, C.N. Tomé, ($1\bar{0}12$) Twinning nucleation mechanisms in hexagonal-close-packed crystals, Acta Materialia 57 (2009) 5521–5530. https://doi.org/10.1016/j.actamat.2009.07.047.

[34] J. Wang, R.G. Hoagland, J.P. Hirth, L. Capolungo, I.J. Beyerlein, C.N. Tomé, Nucleation of a ($1\bar{0}12$) twin in hexagonal close-packed crystals, Scripta Materialia 61 (2009) 903–906. https://doi.org/10.1016/j.scriptamat.2009.07.028.

[35] J. Wang, S.K. Yadav, J.P. Hirth, C.N. Tomé, I.J. Beyerlein, Pure-Shuffle Nucleation of Deformation Twins in Hexagonal-Close-Packed Metals, Materials Research Letters 1 (2013) 126–132. https://doi.org/10.1080/21663831.2013.792019.

[36] A. Serra, R.C. Pond, D.J. Bacon, Computer simulation of the structure and mobility of twinning disclocations in H.C.P. Metals, Acta Metallurgica et Materialia 39 (1991) 1469–1480. https://doi.org/10.1016/0956-7151(91)90232-P.

[37] A. Serra, D.J. Bacon, Computer simulation of twinning dislocation in magnesium using a many-body potential, Philosophical Magazine A 63 (1991) 1001–1012. https://doi.org/10.1080/01418619108213932.

[38] Y. Kasukabe, J.Y. Yamada, P.J. Lin, L.A. Bursill, Characterization of 1101 twin dislocation structures in evaporated titanium thin films by high-resolution transmission electron microscopy, Philosophical Magazine Letters 67 (1993) 361–368. https://doi.org/10.1080/09500839308240944.

[39] J. Wang, I.J. Beyerlein, J.P. Hirth, C.N. Tomé, Twinning dislocations on {$1\bar{0}11$} and {$1\bar{0}13$} planes in hexagonal close-packed crystals, Acta Materialia 59 (2011) 3990–4001. https://doi.org/10.1016/j.actamat.2011.03.024.

[40] B. Li, E. Ma, Zonal dislocations mediating {$101\bar{1}$} ⟨$101\bar{2}$⟩ twinning in magnesium, Acta Materialia 57 (2009) 1734–1743. https://doi.org/10.1016/j.actamat.2008.12.016.

[41] I. Kim, J. Kim, D.H. Shin, X.Z. Liao, Y.T. Zhu, Deformation twins in pure titanium processed by equal channel angular pressing, Scripta Materialia 48 (2003) 813–817. https://doi.org/10.1016/S1359-6462(02)00513-4.

[42] Z. Kou, Y. Yang, B. Huang, X. Luo, P. Li, G. Zhao, W. Zhang, Observing the dynamic {10-11} twining process in pure Ti at atomic resolution, Scripta Materialia 139 (2017) 139–143. https://doi.org/10.1016/j.scriptamat.2017.06.048.

[43] A. Ostapovets, A. Serra, Slip dislocation and twin nucleation mechanisms in hcp metals, J Mater Sci 52 (2017) 533–540. https://doi.org/10.1007/s10853-016-0351-4.

[44] X.-Y. Li, Y.-F. Guo, Y. Mao, X.-Z. Tang, Nucleation and growth of {101¯1} compression twin in Mg single crystals, International Journal of Plasticity 158 (2022) 103437. https://doi.org/10.1016/j.ijplas.2022.103437.
[45] J.T. Lloyd, A dislocation-based model for twin growth within and across grains, Proceedings of the Royal Society A: Mathematical, Physical and Engineering Sciences 474 (2018) 20170709. https://doi.org/10.1098/rspa.2017.0709.
[46] Y. Hu, V. Turlo, I.J. Beyerlein, S. Mahajan, E.J. Lavernia, J.M. Schoenung, T.J. Rupert, Disconnection-mediated twin embryo growth in Mg, Acta Materialia 194 (2020) 437–451. https://doi.org/10.1016/j.actamat.2020.04.010.
[47] F. Wang, C.D. Barrett, R.J. McCabe, H. El Kadiri, L. Capolungo, S.R. Agnew, Dislocation induced twin growth and formation of basal stacking faults in {101¯2} twins in pure Mg, Acta Materialia 165 (2019) 471–485. https://doi.org/10.1016/j.actamat.2018.12.003.
[48] B. Yang, C. Shi, S. Zhang, J. Hu, J. Teng, Y. Cui, Y. Li, A. Chiba, Quasi-in-situ study on {10-12} twinning-detwinning behavior of rolled Mg-Li alloy in two-step compression (RD)-compression (ND) process, Journal of Magnesium and Alloys 10 (2022) 2775–2787. https://doi.org/10.1016/j.jma.2021.01.006.
[49] S. Godet, L. Jiang, A.A. Luo, J.J. Jonas, Use of Schmid factors to select extension twin variants in extruded magnesium alloy tubes, Scripta Materialia 55 (2006) 1055–1058. https://doi.org/10.1016/j.scriptamat.2006.07.059.
[50] B. Yang, J. Wang, Y. Li, M. Barnett, J. LLorca, Deformation mechanisms of dual-textured Mg-6.5Zn alloy with limited tension-compression yield asymmetry, Acta Materialia 248 (2023) 118766. https://doi.org/10.1016/j.actamat.2023.118766.
[51] N.M. Della Ventura, S. Kalácska, D. Casari, T.E.J. Edwards, A. Sharma, J. Michler, R. Logé, X. Maeder, {10-12} twinning mechanism during in situ micro-tensile loading of pure Mg: Role of basal slip and twin-twin interactions, Materials & Design 197 (2021) 109206. https://doi.org/10.1016/j.matdes.2020.109206.
[52] M.R. Barnett, A. Ghaderi, J. Quinta da Fonseca, J.D. Robson, Influence of orientation on twin nucleation and growth at low strains in a magnesium alloy, Acta Materialia 80 (2014) 380–391. https://doi.org/10.1016/j.actamat.2014.07.013.
[53] A. Chapuis, Y. Xin, X. Zhou, Q. Liu, {10-12} Twin variants selection mechanisms during twinning, re-twinning and detwinning, Materials Science and Engineering: A 612 (2014) 431–439. https://doi.org/10.1016/j.msea.2014.06.088.
[54] M.A. Kumar, B. Clausen, L. Capolungo, R.J. McCabe, W. Liu, J.Z. Tischler, C.N. Tomé, Deformation twinning and grain partitioning in a hexagonal close-packed magnesium alloy, Nature Communications 9 (2018) 4761. https://doi.org/10.1038/s41467-018-07028-w.
[55] C. Liu, F. Roters, D. Raabe, Finite strain crystal plasticity-phase field modeling of twin, dislocation, and grain boundary interaction in hexagonal materials, Acta Materialia 242 (2023) 118444. https://doi.org/10.1016/j.actamat.2022.118444.

[56] I.J. Beyerlein, M. Arul Kumar, The Stochastic Nature of Deformation Twinning: Application to HCP Materials, in: W. Andreoni, S. Yip (Eds.), Handbook of Materials Modeling : Methods: Theory and Modeling, Springer International Publishing, Cham, 2018: pp. 1–39. https://doi.org/10.1007/978-3-319-42913-7_103-1.

[57] H. Abdolvand, M. Majkut, J. Oddershede, S. Schmidt, U. Lienert, B.J. Diak, P.J. Withers, M.R. Daymond, On the deformation twinning of Mg AZ31B: A three-dimensional synchrotron X-ray diffraction experiment and crystal plasticity finite element model, International Journal of Plasticity 70 (2015) 77–97. https://doi.org/10.1016/j.ijplas.2015.03.001.

[58] I.J. Beyerlein, L. Capolungo, P.E. Marshall, R.J. McCabe, C.N. Tomé, Statistical analyses of deformation twinning in magnesium, Philosophical Magazine 90 (2010) 2161–2190. https://doi.org/10.1080/14786431003630835.

[59] D. Guan, B. Wynne, J. Gao, Y. Huang, W.M. Rainforth, Basal slip mediated tension twin variant selection in magnesium WE43 alloy, Acta Materialia 170 (2019) 1–14. https://doi.org/10.1016/j.actamat.2019.03.018.

[60] B. Zhou, L. Wang, P. Jin, H. Jia, H.J. Roven, X. Zeng, Y. Li, Revealing slip-induced extension twinning behaviors dominated by micro deformation in a magnesium alloy, International Journal of Plasticity 128 (2020) 102669. https://doi.org/10.1016/j.ijplas.2020.102669.

[61] J. Koike, Y. Sato, D. Ando, Origin of the Anomalous {10-12} Twinning during Tensile Deformation of Mg Alloy Sheet, Materials Transactions 49 (2008) 2792–2800. https://doi.org/10.2320/matertrans.MRA2008283.

[62] B. Raeisinia, S.R. Agnew, Using polycrystal plasticity modeling to determine the effects of grain size and solid solution additions on individual deformation mechanisms in cast Mg alloys, Scripta Materialia 63 (2010) 731–736. https://doi.org/10.1016/j.scriptamat.2010.03.054.

[63] H.J. Choi, Y. Kim, J.H. Shin, D.H. Bae, Deformation behavior of magnesium in the grain size spectrum from nano- to micrometer, Materials Science and Engineering: A 527 (2010) 1565–1570. https://doi.org/10.1016/j.msea.2009.10.035.

[64] A. Ghaderi, M.R. Barnett, Sensitivity of deformation twinning to grain size in titanium and magnesium, Acta Materialia 59 (2011) 7824–7839. https://doi.org/10.1016/j.actamat.2011.09.018.

[65] P. Dobroň, F. Chmelík, S. Yi, K. Parfenenko, D. Letzig, J. Bohlen, Grain size effects on deformation twinning in an extruded magnesium alloy tested in compression, Scripta Materialia 65 (2011) 424–427. https://doi.org/10.1016/j.scriptamat.2011.05.027.

[66] M. Arul Kumar, L. Capolungo, R.J. McCabe, C.N. Tomé, Characterizing the role of adjoining twins at grain boundaries in hexagonal close packed materials, Sci Rep 9 (2019) 3846. https://doi.org/10.1038/s41598-019-40615-5.

[67] Z.-Z. Shi, Y. Zhang, F. Wagner, P.-A. Juan, S. Berbenni, L. Capolungo, J.-S. Lecomte, T. Richeton, On the selection of extension twin variants with low Schmid factors in a deformed Mg alloy, Acta Materialia 83 (2015) 17–28. https://doi.org/10.1016/j.actamat.2014.10.004.

[68] Z.-Z. Shi, Y. Zhang, F. Wagner, T. Richeton, P.-A. Juan, J.-S. Lecomte, L. Capolungo, S. Berbenni, Sequential double extension twinning in a

magnesium alloy: Combined statistical and micromechanical analyses, Acta Materialia 96 (2015) 333–343. https://doi.org/10.1016/j.actamat.2015.06.029.
[69] A.G. Crocker, Double twinning, The Philosophical Magazine: A Journal of Theoretical Experimental and Applied Physics 7 (1962) 1901–1924. https://doi.org/10.1080/14786436208213854.
[70] I.J. Beyerlein, J. Wang, M.R. Barnett, C.N. Tomé, Double twinning mechanisms in magnesium alloys via dissociation of lattice dislocations, Proceedings of the Royal Society A: Mathematical, Physical and Engineering Sciences 468 (2012) 1496–1520. https://doi.org/10.1098/rspa.2011.0731.
[71] L.W.F. Mackenzie, M. Pekguleryuz, The influences of alloying additions and processing parameters on the rolling microstructures and textures of magnesium alloys, Materials Science and Engineering: A 480 (2008) 189–197. https://doi.org/10.1016/j.msea.2007.07.003.
[72] M. Thirumurugan, S. Kumaran, S. Suwas, T.S. Rao, Effect of rolling temperature and reduction in thickness on microstructure and mechanical properties of ZM21 magnesium alloy and its subsequent annealing treatment, Materials Science and Engineering: A 528 (2011) 8460–8468. https://doi.org/10.1016/j.msea.2011.07.047.
[73] T. Nakata, S. Kamado, Towards tailoring basal texture of rolled Mg alloy sheet by recrystallization for high room-temperature formability: A review, Journal of Magnesium and Alloys 11 (2023) 3992–4010. https://doi.org/10.1016/j.jma.2023.08.006.
[74] H.-Y. Wang, Z.-P. Yu, L. Zhang, C.-G. Liu, M. Zha, C. Wang, Q.-C. Jiang, Achieving high strength and high ductility in magnesium alloy using hard-plate rolling (HPR) process, Sci Rep 5 (2015) 17100. https://doi.org/10.1038/srep17100.
[75] M.-S. Shim, B.-C. Suh, J.H. Kim, N.J. Kim, Effect of differential speed rolling on the texture evolution of Mg-4Zn-1Gd alloy, Met. Mater. Int. 21 (2015) 490–497. https://doi.org/10.1007/s12540-015-4589-1.
[76] Z. Wei, H. Zheng, R. Wu, J. Zhang, H. Wu, S. Jin, Y. Jiao, L. Hou, Interface behavior and tensile properties of Mg-14Li-3Al-2Gd sheets prepared by four-layer accumulative roll bonding, Journal of Manufacturing Processes 61 (2021) 254–260. https://doi.org/10.1016/j.jmapro.2020.11.021.
[77] A. Mehrabi, R. Mahmudi, H. Miura, Superplasticity in a multi-directionally forged Mg–Li–Zn alloy, Materials Science and Engineering: A 765 (2019) 138274. https://doi.org/10.1016/j.msea.2019.138274.
[78] K.B. Nie, K.K. Deng, X.J. Wang, F.J. Xu, K. Wu, M.Y. Zheng, Multidirectional forging of AZ91 magnesium alloy and its effects on microstructures and mechanical properties, Materials Science and Engineering: A 624 (2015) 157–168. https://doi.org/10.1016/j.msea.2014.11.076.
[79] C. Yan, Y. Xin, X.-B. Chen, D. Xu, P.K. Chu, C. Liu, B. Guan, X. Huang, Q. Liu, Evading strength-corrosion tradeoff in Mg alloys via dense ultrafine twins, Nat Commun 12 (2021) 4616. https://doi.org/10.1038/s41467-021-24939-3.
[80] N.P. Papenberg, S. Gneiger, I. Weißensteiner, P.J. Uggowitzer, S. Pogatscher, Mg-Alloys for Forging Applications—A Review, Materials 13 (2020) 985. https://doi.org/10.3390/ma13040985.

[81] H. Miura, T. Maruoka, X. Yang, J.J. Jonas, Microstructure and mechanical properties of multi-directionally forged Mg–Al–Zn alloy, Scripta Materialia 66 (2012) 49–51. https://doi.org/10.1016/j.scriptamat.2011.10.005.
[82] Y. Jiang, Q. Le, Y. Zhu, Q. Liao, T. Wang, L. Bao, P. Wang, Review on forming process of magnesium alloy characteristic forgings, Journal of Alloys and Compounds 970 (2024) 172666. https://doi.org/10.1016/j.jallcom.2023.172666.
[83] Z. Zeng, N. Stanford, C.H.J. Davies, J.-F. Nie, N. Birbilis, Magnesium extrusion alloys: a review of developments and prospects, International Materials Reviews 64 (2019) 27–62. https://doi.org/10.1080/09506608.2017.1421439.
[84] M.R. Barnett, A. Sullivan, N. Stanford, N. Ross, A. Beer, Texture selection mechanisms in uniaxially extruded magnesium alloys, Scripta Materialia 63 (2010) 721–724. https://doi.org/10.1016/j.scriptamat.2010.01.018.
[85] A. Rezaei, R. Mahmudi, C. Cayron, R.E. Logé, Simple shear extrusion versus equal channel angular pressing: A comparative study on the microstructure and mechanical properties of an Mg alloy, Journal of Magnesium and Alloys 11 (2023) 1769–1790. https://doi.org/10.1016/j.jma.2023.05.006.
[86] Q. Yang, B. Jiang, Y. Tian, W. Liu, F. Pan, A tilted weak texture processed by an asymmetric extrusion for magnesium alloy sheets, Materials Letters 100 (2013) 29–31. https://doi.org/10.1016/j.matlet.2013.02.118.
[87] Q. Yang, D. Zhang, P. Peng, G. Wei, J. Zhang, B. Jiang, F. Pan, Asymmetric Extrusion Technology of Mg Alloy: A Review, Materials 16 (2023) 5255. https://doi.org/10.3390/ma16155255.
[88] J. She, P. Peng, A.T. Tang, J.Y. Zhang, J.J. Mao, T.T. Liu, S.B. Zhou, Y. Wang, F.S. Pan, Novel on-line twist extrusion process for bulk magnesium alloys, Materials & Design 182 (2019) 108011. https://doi.org/10.1016/j.matdes.2019.108011.
[89] J. Song, J. She, D. Chen, F. Pan, Latest research advances on magnesium and magnesium alloys worldwide, Journal of Magnesium and Alloys 8 (2020) 1–41. https://doi.org/10.1016/j.jma.2020.02.003.
[90] M. Mohammadi Zerankeshi, R. Alizadeh, E. Gerashi, M. Asadollahi, T.G. Langdon, Effects of heat treatment on the corrosion behavior and mechanical properties of biodegradable Mg alloys, Journal of Magnesium and Alloys 10 (2022) 1737–1785. https://doi.org/10.1016/j.jma.2022.04.010.
[91] X. Zhao, F.-F. Yan, Z.-M. Zhang, P.-C. Gao, S.-C. Li, Influence of Heat Treatment on Precipitation Behavior and Mechanical Properties of Extruded AZ80 Magnesium Alloy, Acta Metall. Sin. (Engl. Lett.) 34 (2021) 54–64. https://doi.org/10.1007/s40195-020-01094-0.
[92] J.-Y. Wang, N. Li, R. Alizadeh, M.A. Monclús, Y.W. Cui, J.M. Molina-Aldareguía, J. LLorca, Effect of solute content and temperature on the deformation mechanisms and critical resolved shear stress in Mg-Al and Mg-Zn alloys, Acta Materialia 170 (2019) 155–165. https://doi.org/10.1016/j.actamat.2019.03.027.
[93] N. Stanford, M.R. Barnett, Solute strengthening of prismatic slip, basal slip and twinning in Mg and Mg–Zn binary alloys, International Journal of Plasticity 47 (2013) 165–181. https://doi.org/10.1016/j.ijplas.2013.01.012.

[94] Y. Chai, D. Yin, S. Hua, G. Huang, H. Zhou, J. Zheng, Q. Wang, Role of yttrium content in twinning behavior of extruded Mg—Y sheets under tension/compression, Transactions of Nonferrous Metals Society of China 32 (2022) 3534–3549. https://doi.org/10.1016/S1003-6326(22)66037-0.
[95] D.D. Yin, C.J. Boehlert, L.J. Long, G.H. Huang, H. Zhou, J. Zheng, Q.D. Wang, Tension-compression asymmetry and the underlying slip/twinning activity in extruded Mg–Y sheets, International Journal of Plasticity 136 (2021) 102878. https://doi.org/10.1016/j.ijplas.2020.102878.
[96] N. Stanford, R.K.W. Marceau, M.R. Barnett, The effect of high yttrium solute concentration on the twinning behaviour of magnesium alloys, Acta Materialia 82 (2015) 447–456. https://doi.org/10.1016/j.actamat.2014.09.022.
[97] M. Arul Kumar, I.J. Beyerlein, R.A. Lebensohn, C.N. Tomé, Role of alloying elements on twin growth and twin transmission in magnesium alloys, Materials Science and Engineering: A 706 (2017) 295–303. https://doi.org/10.1016/j.msea.2017.08.084.
[98] P. Hidalgo-Manrique, J.D. Robson, Interaction Between Precipitate Basal Plates and Tensile Twins in Magnesium Alloys, Metall and Mat Trans A 50 (2019) 3855–3867. https://doi.org/10.1007/s11661-019-05301-1.
[99] B.-Y. Liu, N. Yang, J. Wang, M. Barnett, Y.-C. Xin, D. Wu, R.-L. Xin, B. Li, R.L. Narayan, J.-F. Nie, J. Li, E. Ma, Z.-W. Shan, Insight from in situ microscopy into which precipitate morphology can enable high strength in magnesium alloys, Journal of Materials Science & Technology 34 (2018) 1061–1066. https://doi.org/10.1016/j.jmst.2018.01.017.
[100] S. Si, J. Wu, I.P. Jones, Y.L. Chiu, Influence of precipitates on basal dislocation slip and {01-12} twinning in AZ91 micro-pillars, Philosophical Magazine 100 (2020) 2949–2971. https://doi.org/10.1080/14786435.2020.1802077.
[101] Y. Cui, Y. Li, Z. Wang, X. Ding, Y. Koizumi, H. Bian, L. Lin, A. Chiba, Impact of solute elements on detwinning in magnesium and its alloys, International Journal of Plasticity 91 (2017) 134–159. https://doi.org/10.1016/j.ijplas.2016.09.014.
[102] J.D. Robson, The effect of internal stresses due to precipitates on twin growth in magnesium, Acta Materialia 121 (2016) 277–287. https://doi.org/10.1016/j.actamat.2016.09.022.
[103] F. Liu, R. Xin, C. Wang, B. Song, Q. Liu, Regulating precipitate orientation in Mg-Al alloys by coupling twinning, aging and detwinning processes, Scripta Materialia 158 (2019) 131–135. https://doi.org/10.1016/j.scriptamat.2018.08.049.
[104] C. Liu, P. Shanthraj, J.D. Robson, M. Diehl, S. Dong, J. Dong, W. Ding, D. Raabe, On the interaction of precipitates and tensile twins in magnesium alloys, Acta Materialia 178 (2019) 146–162. https://doi.org/10.1016/j.actamat.2019.07.046.
[105] G. Esteban-Manzanares, R. Alizadeh, I. Papadimitriou, D. Dickel, C.D. Barrett, J. LLorca, Atomistic simulations of the interaction of basal dislocations with MgZn2 precipitates in Mg alloys, Materials Science and Engineering: A 788 (2020) 139555. https://doi.org/10.1016/j.msea.2020.139555.

[106] G. Esteban-Manzanares, A. Ma, I. Papadimitriou, E. Martínez, J. LLorca, Basal dislocation/precipitate interactions in Mg–Al alloys: an atomistic investigation, Modelling Simul. Mater. Sci. Eng. 27 (2019) 075003. https://doi.org/10.1088/1361-651X/ab2de0.

[107] B. Yang, C. Shi, X. Ye, J. Teng, R. Lai, Y. Cui, D. Shi, D. Guan, G. Xie, Y. Li, A. Chiba, A novel strategy to strengthen the hexagonal close-packed (HCP) alloys, Journal of Alloys and Compounds 893 (2022) 162346. https://doi.org/10.1016/j.jallcom.2021.162346.

[108] H. Wang, B. Clausen, L. Capolungo, I.J. Beyerlein, J. Wang, C.N. Tomé, Stress and strain relaxation in magnesium AZ31 rolled plate: In-situ neutron measurement and elastic viscoplastic polycrystal modeling, International Journal of Plasticity 79 (2016) 275–292. https://doi.org/10.1016/j.ijplas.2015.07.004.

[109] Y. Wang, D. Culbertson, Y. Jiang, An experimental study of anisotropic fatigue behavior of rolled AZ31B magnesium alloy, Materials & Design 186 (2020) 108266. https://doi.org/10.1016/j.matdes.2019.108266.

[110] H.F. Alharbi, M. Luqman, E. El-Danaf, N.H. Alharthi, Experimental and Numerical Study of Texture Evolution and Anisotropic Plastic Deformation of Pure Magnesium under Various Strain Paths, Advances in Materials Science and Engineering 2018 (2018) e2867281. https://doi.org/10.1155/2018/2867281.

[111] L. Jiang, J.J. Jonas, R.K. Mishra, A.A. Luo, A.K. Sachdev, S. Godet, Twinning and texture development in two Mg alloys subjected to loading along three different strain paths, Acta Materialia 55 (2007) 3899–3910. https://doi.org/10.1016/j.actamat.2007.03.006.

[112] B. Yang, C. Shi, S. Zhang, J. Hu, J. Teng, Y. Cui, Y. Li, A. Chiba, Quasi-in-situ study on {10-12} twinning-detwinning behavior of rolled Mg-Li alloy in two-step compression (RD)-compression (ND) process, Journal of Magnesium and Alloys 10 (2022) 2775–2787. https://doi.org/10.1016/j.jma.2021.01.006.

[113] A. Chapuis, J.H. Driver, Temperature dependency of slip and twinning in plane strain compressed magnesium single crystals, Acta Materialia 59 (2011) 1986–1994. https://doi.org/10.1016/j.actamat.2010.11.064.

[114] N.M. Della Ventura, P. Schweizer, A. Sharma, M. Jain, T.E.J. Edwards, J.J. Schwiedrzik, C. Peruzzi, R.E. Logé, J. Michler, X. Maeder, Micromechanical response of pure magnesium at different strain rate and temperature conditions: twin to slip and slip to twin transitions, Acta Materialia 243 (2023) 118528. https://doi.org/10.1016/j.actamat.2022.118528.

[115] C.M. Cepeda-Jiménez, J.M. Molina-Aldareguia, M.T. Pérez-Prado, Origin of the twinning to slip transition with grain size refinement, with decreasing strain rate and with increasing temperature in magnesium, Acta Materialia 88 (2015) 232–244. https://doi.org/10.1016/j.actamat.2015.01.032.

[116] R. Plamthottam, S. Lavenstein, J.A. El-Awady, Effect of temperature on the suppression of twinning in textured magnesium, MRS Communications 9 (2019) 1093–1097. https://doi.org/10.1557/mrc.2019.102.

[117] H. Wang, P. Wu, S. Kurukuri, M.J. Worswick, Y. Peng, D. Tang, D. Li, Strain rate sensitivities of deformation mechanisms in magnesium alloys, International Journal of Plasticity 107 (2018) 207–222. https://doi.org/10.1016/j.ijplas.2018.04.005.

[118] S. Xu, W.R. Tyson, R. Eagleson, R. Zavadil, Z. Liu, P.-L. Mao, C.-Y. Wang, S.I. Hill, A.A. Luo, Dependence of flow strength and deformation mechanisms in common wrought and die cast magnesium alloys on orientation, strain rate and temperature, Journal of Magnesium and Alloys 1 (2013) 275–282. https://doi.org/10.1016/j.jma.2013.11.003.
[119] M. Zhao, V. Kannan, K.T. Ramesh, The dynamic plasticity and dynamic failure of a magnesium alloy under multiaxial loading, Acta Materialia 154 (2018) 124–136. https://doi.org/10.1016/j.actamat.2018.05.012.
[120] N.M. Della Ventura, A. Sharma, S. Kalácska, M. Jain, T.E.J. Edwards, C. Cayron, R. Logé, J. Michler, X. Maeder, Evolution of deformation twinning mechanisms in magnesium from low to high strain rates, Materials & Design 217 (2022) 110646. https://doi.org/10.1016/j.matdes.2022.110646.
[121] S.Q. Zhu, H.G. Yan, X.Z. Liao, S.J. Moody, G. Sha, Y.Z. Wu, S.P. Ringer, Mechanisms for enhanced plasticity in magnesium alloys, Acta Materialia 82 (2015) 344–355. https://doi.org/10.1016/j.actamat.2014.09.006.
[122] L. Jiang, J.J. Jonas, A.A. Luo, A.K. Sachdev, S. Godet, Twinning-induced softening in polycrystalline AM30 Mg alloy at moderate temperatures, Scripta Materialia 54 (2006) 771–775. https://doi.org/10.1016/j.scriptamat.2005.11.029.
[123] S. Erich, B. Walter, Kristallplastizität: Mit Besonderer Berücksichtigung der Metalle, 1935. https://link.springer.com/book/10.1007/978-3-662-34532-0 (accessed December 5, 2022).
[124] A. Chapuis, Q. Liu, Investigating the temperature dependency of plastic deformation in a Mg-3Al-1Zn alloy, Materials Science and Engineering: A 725 (2018) 108–118. https://doi.org/10.1016/j.msea.2018.04.019.
[125] Z.R. Zeng, M.Z. Bian, S.W. Xu, C.H.J. Davies, N. Birbilis, J.F. Nie, Effects of dilute additions of Zn and Ca on ductility of magnesium alloy sheet, Materials Science and Engineering: A 674 (2016) 459–471. https://doi.org/10.1016/j.msea.2016.07.049.
[126] S.M. Yin, C.H. Wang, Y.D. Diao, S.D. Wu, S.X. Li, Influence of Grain Size and Texture on the Yield Asymmetry of Mg-3Al-1Zn Alloy, Journal of Materials Science & Technology 27 (2011) 29–34. https://doi.org/10.1016/S1005-0302(11)60021-2.
[127] Z. Zachariah, S.S.V. Tatiparti, S.K. Mishra, N. Ramakrishnan, U. Ramamurty, Tension–compression asymmetry in an extruded Mg alloy AM30: Temperature and strain rate effects, Materials Science and Engineering: A 572 (2013) 8–18. https://doi.org/10.1016/j.msea.2013.02.023.
[128] J. Bohlen, M.R. Nürnberg, J.W. Senn, D. Letzig, S.R. Agnew, The texture and anisotropy of magnesium–zinc–rare earth alloy sheets, Acta Materialia 55 (2007) 2101–2112. https://doi.org/10.1016/j.actamat.2006.11.013.
[129] S.H. Safi-Naqvi, W.B. Hutchinson, M.R. Barnett, Texture and mechanical anisotropy in three extruded magnesium alloys, Materials Science and Technology 24 (2008) 1283–1292. https://doi.org/10.1179/174328408X322204.
[130] J.B. Lin, W.J. Ren, X.Y. Wang, L.F. Ma, Tension–compression asymmetry in yield strength and hardening behaviour of as-extruded AZ31 alloy, Materials Science and Technology 32 (2016) 1855–1860. https://doi.org/10.1080/02670836.2016.1149293.

[131] A. Al-Hadi I. Kobaissy, G. Ayoub, M. Shehadeh, Modeling of the tension-compression asymmetry reduction of ECAPed Mg-3Al-1Zn through grain fragmentation, Computational Materials Science 210 (2022) 111439. https://doi.org/10.1016/j.commatsci.2022.111439.

[132] T. Nakata, C. Xu, R. Ajima, Y. Matsumoto, K. Shimizu, T.T. Sasaki, K. Hono, S. Kamado, Improving mechanical properties and yield asymmetry in high-speed extrudable Mg-1.1Al-0.24Ca (wt%) alloy by high Mn addition, Materials Science and Engineering: A 712 (2018) 12–19. https://doi.org/10.1016/j.msea.2017.11.085.

[133] X. Li, C. Liu, J. Wang, C. Zhang, Tailoring the strength and formability of Mg alloys through rare earth element additions (Gd and Dy) and dynamic recrystallizations, Materials Today Communications 28 (2021) 102627. https://doi.org/10.1016/j.mtcomm.2021.102627.

[134] M.G. Jiang, C. Xu, H. Yan, S.H. Lu, T. Nakata, C.S. Lao, R.S. Chen, S. Kamado, E.H. Han, Correlation between dynamic recrystallization and formation of rare earth texture in a Mg-Zn-Gd magnesium alloy during extrusion, Sci Rep 8 (2018) 16800. https://doi.org/10.1038/s41598-018-35170-4.

[135] A. Imandoust, C.D. Barrett, T. Al-Samman, K.A. Inal, H. El Kadiri, A review on the effect of rare-earth elements on texture evolution during processing of magnesium alloys, J Mater Sci 52 (2017) 1–29. https://doi.org/10.1007/s10853-016-0371-0.

[136] A. Tehranchi, B. Yin, W.A. Curtin, Solute strengthening of basal slip in Mg alloys, Acta Materialia 151 (2018) 56–66. https://doi.org/10.1016/j.actamat.2018.02.056.

[137] B. Yin, Z. Wu, W.A. Curtin, First-principles calculations of stacking fault energies in Mg-Y, Mg-Al and Mg-Zn alloys and implications for 〈c+a〉 activity, Acta Materialia 136 (2017) 249–261. https://doi.org/10.1016/j.actamat.2017.06.062.

[138] W. Rong, Y. Wu, Y. Zhang, M. Sun, J. Chen, L. Peng, W. Ding, Characterization and strengthening effects of γ′ precipitates in a high-strength casting Mg-15Gd-1Zn-0.4Zr (wt.%) alloy, Materials Characterization 126 (2017) 1–9. https://doi.org/10.1016/j.matchar.2017.02.010.

[139] R.G. Li, H.R. Li, H.C. Pan, D.S. Xie, J.H. Zhang, D.Q. Fang, Y.Q. Dai, D.Y. Zhao, H. Zhang, Achieving exceptionally high strength in binary Mg-13Gd alloy by strong texture and substantial precipitates, Scripta Materialia 193 (2021) 142–146. https://doi.org/10.1016/j.scriptamat.2020.10.052.

[140] S. Tang, T. Xin, W. Xu, D. Miskovic, G. Sha, Z. Quadir, S. Ringer, K. Nomoto, N. Birbilis, M. Ferry, Precipitation strengthening in an ultralight magnesium alloy, Nat Commun 10 (2019) 1003. https://doi.org/10.1038/s41467-019-08954-z.

[141] T. Xin, Y. Zhao, R. Mahjoub, J. Jiang, A. Yadav, K. Nomoto, R. Niu, S. Tang, F. Ji, Z. Quadir, D. Miskovic, J. Daniels, W. Xu, X. Liao, L.-Q. Chen, K. Hagihara, X. Li, S. Ringer, M. Ferry, Ultrahigh specific strength in a magnesium alloy strengthened by spinodal decomposition, Science Advances 7 (2021) eabf3039. https://doi.org/10.1126/sciadv.abf3039.

[142] J. Zhang, S. Liu, R. Wu, L. Hou, M. Zhang, Recent developments in high-strength Mg-RE-based alloys: Focusing on Mg-Gd and Mg-Y systems, Journal of Magnesium and Alloys 6 (2018) 277–291. https://doi.org/10.1016/j.jma.2018.08.001.
[143] W. Yu, Z. Chen, N. Cheng, B. Gan, H. He, X. Li, J. Hu, High-strength wrought magnesium alloy with dense nano-scale spherical precipitate, CHINESE SCI BULL 52 (2007) 1867–1871. https://doi.org/10.1007/s11434-007-0250-9.
[144] Q. Wang, J. Chen, Z. Zhao, S. He, Microstructure and super high strength of cast Mg-8.5Gd-2.3Y-1.8Ag-0.4Zr alloy, Materials Science and Engineering: A 528 (2010) 323–328. https://doi.org/10.1016/j.msea.2010.09.004.
[145] N. Stanford, J. Geng, Y.B. Chun, C.H.J. Davies, J.F. Nie, M.R. Barnett, Effect of plate-shaped particle distributions on the deformation behaviour of magnesium alloy AZ91 in tension and compression, Acta Materialia 60 (2012) 218–228. https://doi.org/10.1016/j.actamat.2011.10.001.
[146] C.M. Cepeda-Jiménez, M. Castillo-Rodríguez, M.T. Pérez-Prado, Origin of the low precipitation hardening in magnesium alloys, Acta Materialia 165 (2019) 164–176. https://doi.org/10.1016/j.actamat.2018.11.044.
[147] J. Jain, W.J. Poole, C.W. Sinclair, M.A. Gharghouri, Reducing the tension–compression yield asymmetry in a Mg–8Al–0.5Zn alloy via precipitation, Scripta Materialia 62 (2010) 301–304. https://doi.org/10.1016/j.scriptamat.2009.11.024.
[148] J.F. Nie, Precipitation and Hardening in Magnesium Alloys, Metall and Mat Trans A 43 (2012) 3891–3939. https://doi.org/10.1007/s11661-012-1217-2.
[149] Y. Yang, V. Massardier, M.R.G. Ferdowsi, L. Jiang, J. Wang, T. Dorin, S.R. Kada, M.R. Barnett, M. Perez, Revisiting Precipitation kinetics in Mg-Zn alloy – a multi-characterization and modeling study, Acta Materialia 260 (2023) 119276. https://doi.org/10.1016/j.actamat.2023.119276.
[150] G. Mima, Y. Tanaka, Mechanism of Precipitation Hardening of Magnesium-Zinc Alloys, Transactions of the Japan Institute of Metals 12 (1971) 323–328. https://doi.org/10.2320/matertrans1960.12.323.
[151] J.B. Clark, Transmission electron microscopy study of age hardening in a Mg-5 wt.% Zn alloy, Acta Metallurgica 13 (1965) 1281–1289. https://doi.org/10.1016/0001-6160(65)90039-8.
[152] J. Wang, N. Stanford, Investigation of precipitate hardening of slip and twinning in Mg5%Zn by micropillar compression, Acta Materialia 100 (2015) 53–63. https://doi.org/10.1016/j.actamat.2015.08.012.
[153] J. Wang, M.R.G. Ferdowsi, S.R. Kada, P.A. Lynch, Z. Wang, J.A. Kimpton, M.R. Barnett, Stress relaxations during cyclic loading-unloading in precipitation hardened Mg-4.5Zn, Acta Materialia 205 (2021) 116531. https://doi.org/10.1016/j.actamat.2020.116531.
[154] J.D. Robson, N. Stanford, M.R. Barnett, Effect of precipitate shape on slip and twinning in magnesium alloys, Acta Materialia 59 (2011) 1945–1956. https://doi.org/10.1016/j.actamat.2010.11.060.
[155] N. Stanford, M.R. Barnett, Effect of particles on the formation of deformation twins in a magnesium-based alloy, Materials Science and

Engineering: A 516 (2009) 226–234. https://doi.org/10.1016/j.msea.2009.04.001.
[156] R. Alizadeh, J. LLorca, Interactions between basal dislocations and β1′ precipitates in Mg–4Zn alloy: Mechanisms and strengthening, Acta Materialia 186 (2020) 475–486. https://doi.org/10.1016/j.actamat.2020.01.028.
[157] J.D. Robson, N. Stanford, M.R. Barnett, Effect of particles in promoting twin nucleation in a Mg–5wt.% Zn alloy, Scripta Materialia 63 (2010) 823–826. https://doi.org/10.1016/j.scriptamat.2010.06.026.
[158] P. Hidalgo-Manrique, J.D. Robson, M.T. Pérez-Prado, Precipitation strengthening and reversed yield stress asymmetry in Mg alloys containing rare-earth elements: A quantitative study, Acta Materialia 124 (2017) 456–467. https://doi.org/10.1016/j.actamat.2016.11.019.
[159] E.O. Hall, The Deformation and Ageing of Mild Steel: III Discussion of Results, Proc. Phys. Soc. B 64 (1951) 747. https://doi.org/10.1088/0370-1301/64/9/303.
[160] P.N. J, The cleavage strength of polycrystals, J. Iron Steel Inst. 174 (1953) 25–28.
[161] H. Somekawa, T. Mukai, Hall–Petch relation for deformation twinning in solid solution magnesium alloys, Materials Science and Engineering: A 561 (2013) 378–385. https://doi.org/10.1016/j.msea.2012.10.040.
[162] N. Hansen, The effect of grain size and strain on the tensile flow stress of aluminium at room temperature, Acta Metallurgica 25 (1977) 863–869. https://doi.org/10.1016/0001-6160(77)90171-7.
[163] R. Armstrong, I. Codd, R.M. Douthwaite, N.J. Petch, The plastic deformation of polycrystalline aggregates, The Philosophical Magazine: A Journal of Theoretical Experimental and Applied Physics 7 (1962) 45–58. https://doi.org/10.1080/14786436208201857.
[164] R.W. Armstrong, Engineering science aspects of the Hall–Petch relation, Acta Mech 225 (2014) 1013–1028. https://doi.org/10.1007/s00707-013-1048-2.
[165] S.M. Razavi, D.C. Foley, I. Karaman, K.T. Hartwig, O. Duygulu, L.J. Kecskes, S.N. Mathaudhu, V.H. Hammond, Effect of grain size on prismatic slip in Mg–3Al–1Zn alloy, Scripta Materialia 67 (2012) 439–442. https://doi.org/10.1016/j.scriptamat.2012.05.017.
[166] A.E. Davis, J.D. Robson, M. Turski, Reducing yield asymmetry and anisotropy in wrought magnesium alloys – A comparative study, Materials Science and Engineering: A 744 (2019) 525–537. https://doi.org/10.1016/j.msea.2018.12.060.
[167] B. Kim, S.-M. Baek, H.Y. Jeong, J.G. Lee, S.S. Park, Grain refinement and reduced yield asymmetry of extruded Mg–5Sn–1Zn alloy by Al addition, Journal of Alloys and Compounds 660 (2016) 304–309. https://doi.org/10.1016/j.jallcom.2015.11.133.
[168] Z.R. Zeng, Y.M. Zhu, R.L. Liu, S.W. Xu, C.H.J. Davies, J.F. Nie, N. Birbilis, Achieving exceptionally high strength in Mg3Al1Zn-0.3Mn extrusions via suppressing intergranular deformation, Acta Materialia 160 (2018) 97–108. https://doi.org/10.1016/j.actamat.2018.08.045.

[169] C.M. Cepeda-Jiménez, J.M. Molina-Aldareguia, M.T. Pérez-Prado, Effect of grain size on slip activity in pure magnesium polycrystals, Acta Materialia 84 (2015) 443–456. https://doi.org/10.1016/j.actamat.2014.10.001.
[170] R. Zheng, J.-P. Du, S. Gao, H. Somekawa, S. Ogata, N. Tsuji, Transition of dominant deformation mode in bulk polycrystalline pure Mg by ultra-grain refinement down to sub-micrometer, Acta Materialia 198 (2020) 35–46. https://doi.org/10.1016/j.actamat.2020.07.055.
[171] M.R. Barnett, A rationale for the strong dependence of mechanical twinning on grain size, Scripta Materialia 59 (2008) 696–698. https://doi.org/10.1016/j.scriptamat.2008.05.027.
[172] J. Bohlen, P. Dobron, E. Meza Garcia, F. Chmelík, P. Lukáč, D. Letzig, K.U. Kainer, The Effect of Grain Size on the Deformation Behaviour of Magnesium Alloys Investigated by the Acoustic Emission Technique, Advanced Engineering Materials 8 (2006) 422–427. https://doi.org/10.1002/adem.200600023.
[173] J. Bohlen, P. Dobroň, J. Swiostek, D. Letzig, F. Chmelík, P. Lukáč, K.U. Kainer, On the influence of the grain size and solute content on the AE response of magnesium alloys tested in tension and compression, Materials Science and Engineering: A 462 (2007) 302–306. https://doi.org/10.1016/j.msea.2006.02.470.
[174] K. Wei, R. Hu, D. Yin, L. Xiao, S. Pang, Y. Cao, H. Zhou, Y. Zhao, Y. Zhu, Grain size effect on tensile properties and slip systems of pure magnesium, Acta Materialia 206 (2021) 116604. https://doi.org/10.1016/j.actamat.2020.116604.
[175] I.A. Ovid'ko, R.Z. Valiev, Y.T. Zhu, Review on superior strength and enhanced ductility of metallic nanomaterials, Progress in Materials Science 94 (2018) 462–540. https://doi.org/10.1016/j.pmatsci.2018.02.002.
[176] E.W. Hart, Theory of the tensile test, Acta Metallurgica 15 (1967) 351–355. https://doi.org/10.1016/0001-6160(67)90211-8.
[177] D. Jia, Y.M. Wang, K.T. Ramesh, E. Ma, Y.T. Zhu, R.Z. Valiev, Deformation behavior and plastic instabilities of ultrafine-grained titanium, Applied Physics Letters 79 (2001) 611–613. https://doi.org/10.1063/1.1384000.
[178] R. Zheng, T. Bhattacharjee, A. Shibata, T. Sasaki, K. Hono, M. Joshi, N. Tsuji, Simultaneously enhanced strength and ductility of Mg-Zn-Zr-Ca alloy with fully recrystallized ultrafine grained structures, Scripta Materialia 131 (2017) 1–5. https://doi.org/10.1016/j.scriptamat.2016.12.024.
[179] S. You, Y. Huang, K.U. Kainer, N. Hort, Recent research and developments on wrought magnesium alloys, Journal of Magnesium and Alloys 5 (2017) 239–253. https://doi.org/10.1016/j.jma.2017.09.001.
[180] X. Zeng, C. Liu, C. Zhao, J. Dong, F. Roters, D. Guan, Three-dimensional study of grain scale tensile twinning activity in magnesium: A combination of microstructure characterization and mechanical modeling, Acta Materialia 255 (2023) 119043. https://doi.org/10.1016/j.actamat.2023.119043.
[181] B. Shi, C. Yang, Y. Peng, F. Zhang, F. Pan, Anisotropy of wrought magnesium alloys: A focused overview, Journal of Magnesium and Alloys 10 (2022) 1476–1510. https://doi.org/10.1016/j.jma.2022.03.006.

[182] X. Xu, D. Lunt, R. Thomas, R.P. Babu, A. Harte, M. Atkinson, J.Q. da Fonseca, M. Preuss, Identification of active slip mode in a hexagonal material by correlative scanning electron microscopy, Acta Materialia 175 (2019) 376–393. https://doi.org/10.1016/j.actamat.2019.06.024.

[183] D. Lunt, R. Thomas, M.D. Atkinson, A. Smith, R. Sandala, J.Q. da Fonseca, M. Preuss, Understanding the role of local texture variation on slip activity in a two-phase titanium alloy, Acta Materialia 216 (2021) 117111. https://doi.org/10.1016/j.actamat.2021.117111.

[184] B. Zhou, L. Wang, W. Liu, X. Zeng, Y. Li, Revealing the Subsurface Basal <a> Dislocation Activity in Magnesium Through Lattice Rotation Analysis, Metall Mater Trans A 51 (2020) 4414–4421. https://doi.org/10.1007/s11661-020-05907-w.

[185] C. Marichal, H. Van Swygenhoven, S. Van Petegem, C. Borca, {110} Slip with {112} slip traces in bcc Tungsten, Sci Rep 3 (2013) 2547. https://doi.org/10.1038/srep02547.

[186] G. Zhu, L. Wang, H. Zhou, J. Wang, Y. Shen, P. Tu, H. Zhu, W. Liu, P. Jin, X. Zeng, Improving ductility of a Mg alloy via non-basal slip induced by Ca addition, International Journal of Plasticity 120 (2019) 164–179. https://doi.org/10.1016/j.ijplas.2019.04.020.

[187] B. Yang, C. Shi, X. Ye, J. Teng, R. Lai, Y. Cui, D. Guan, H. Cui, Y. Li, A. Chiba, Underlying slip/twinning activities of Mg-xGd alloys investigated by modified lattice rotation analysis, Journal of Magnesium and Alloys 11 (2023) 998–1015. https://doi.org/10.1016/j.jma.2021.06.008.

[188] C. He, Z. Li, D. Kong, X. Zhao, H. Chen, J.-F. Nie, Origin of profuse {11-21} deformation twins in Mg-Gd alloys, Scripta Materialia 191 (2021) 62–66. https://doi.org/10.1016/j.scriptamat.2020.08.041.

[189] C.M. Cepeda-Jiménez, J.M. Molina-Aldareguia, M.T. Pérez-Prado, EBSD-Assisted Slip Trace Analysis During In Situ SEM Mechanical Testing: Application to Unravel Grain Size Effects on Plasticity of Pure Mg Polycrystals, JOM 68 (2016) 116–126. https://doi.org/10.1007/s11837-015-1521-6.

[190] Y. Guo, D.M. Collins, E. Tarleton, F. Hofmann, A.J. Wilkinson, T.B. Britton, Dislocation density distribution at slip band-grain boundary intersections, Acta Materialia 182 (2020) 172–183. https://doi.org/10.1016/j.actamat.2019.10.031.

[191] C. Xiang, Y. Yang, N. Gupta, High Strain Rate Compressive Behavior of As-Cast and Heat Treated Magnesium-Rare Earth Alloy at Low Temperatures, J. Dynamic Behavior Mater. 6 (2020) 197–206. https://doi.org/10.1007/s40870-020-00238-8.

[192] D. Fullwood, B. Adams, J. Basinger, T. Ruggles, A. Khosravani, C. Sorensen, J. Kacher, Microstructure Detail Extraction via EBSD: An Overview, in: Strain and Dislocation Gradients from Diffraction, IMPERIAL COLLEGE PRESS, 2013: pp. 405–437. https://doi.org/10.1142/9781908979636_0012.

[193] S.I. Wright, M.M. Nowell, A Review of In Situ EBSD Studies, in: A.J. Schwartz, M. Kumar, B.L. Adams, D.P. Field (Eds.), Electron Backscatter Diffraction in Materials Science, Springer US, Boston, MA, 2009: pp. 329–337. https://doi.org/10.1007/978-0-387-88136-2_24.

[194] S. Hémery, C. Tromas, P. Villechaise, Slip-stimulated grain boundary sliding in Ti-6Al-4 V at room temperature, Materialia 5 (2019) 100189. https://doi.org/10.1016/j.mtla.2018.100189.
[195] G. Zhu, L. Wang, J. Wang, J. Wang, J.-S. Park, X. Zeng, Highly deformable Mg–Al–Ca alloy with Al2Ca precipitates, Acta Materialia 200 (2020) 236–245. https://doi.org/10.1016/j.actamat.2020.09.006.
[196] C.M. Cepeda-Jiménez, J.M. Molina-Aldareguia, M.T. Pérez-Prado, EBSD-Assisted Slip Trace Analysis During In Situ SEM Mechanical Testing: Application to Unravel Grain Size Effects on Plasticity of Pure Mg Polycrystals, JOM 68 (2016) 116–126. https://doi.org/10.1007/s11837-015-1521-6.
[197] Z. Huang, L. Wang, B. Zhou, T. Fischer, S. Yi, X. Zeng, Observation of non-basal slip in Mg-Y by in situ three-dimensional X-ray diffraction, Scripta Materialia 143 (2018) 44–48. https://doi.org/10.1016/j.scriptamat.2017.09.011.
[198] A. Githens, S. Ganesan, Z. Chen, J. Allison, V. Sundararaghavan, S. Daly, Characterizing microscale deformation mechanisms and macroscopic tensile properties of a high strength magnesium rare-earth alloy: A combined experimental and crystal plasticity approach, Acta Materialia 186 (2020) 77–94. https://doi.org/10.1016/j.actamat.2019.12.012.
[199] T.R. Bieler, R. Alizadeh, M. Peña-Ortega, J. Llorca, An analysis of (the lack of) slip transfer between near-cube oriented grains in pure Al, International Journal of Plasticity 118 (2019) 269–290. https://doi.org/10.1016/j.ijplas.2019.02.014.
[200] F. Bachmann, R. Hielscher, H. Schaeben, Texture Analysis with MTEX – Free and Open Source Software Toolbox, Solid State Phenomena 160 (2010) 63–68. https://doi.org/10.4028/www.scientific.net/SSP.160.63.
[201] D.E. Laughlin, K. Hono, Physical Metallurgy, 5th ed, Newnes, 2014.
[202] B. Zhou, L. Wang, P. Jin, H. Jia, H.J. Roven, X. Zeng, Y. Li, Revealing slip-induced extension twinning behaviors dominated by micro deformation in a magnesium alloy, International Journal of Plasticity 128 (2020) 102669. https://doi.org/10.1016/j.ijplas.2020.102669.
[203] B. Yang, C. Shi, R. Lai, D. Shi, D. Guan, G. Zhu, Y. Cui, G. Xie, Y. Li, A. Chiba, J. LLorca, Identification of active slip systems in polycrystals by Slip Trace - Modified Lattice Rotation Analysis (ST-MLRA), Scripta Materialia 214 (2022) 114648. https://doi.org/10.1016/j.scriptamat.2022.114648.
[204] Z. Chen, S.H. Daly, Active Slip System Identification in Polycrystalline Metals by Digital Image Correlation (DIC), Exp Mech 57 (2017) 115–127. https://doi.org/10.1007/s11340-016-0217-3.
[205] S. Haouala, R. Alizadeh, T.R. Bieler, J. Segurado, J. LLorca, Effect of slip transmission at grain boundaries in Al bicrystals, International Journal of Plasticity 126 (2020) 102600. https://doi.org/10.1016/j.ijplas.2019.09.006.
[206] E. Nieto-Valeiras, S. Haouala, J. LLorca, On the effect of slip transfer at grain boundaries on the strength of FCC polycrystals, European Journal of Mechanics - A/Solids 91 (2022) 104427. https://doi.org/10.1016/j.euromechsol.2021.104427.

[207] E. Bayerschen, A.T. McBride, B.D. Reddy, T. Böhlke, Review on slip transmission criteria in experiments and crystal plasticity models, J Mater Sci 51 (2016) 2243–2258. https://doi.org/10.1007/s10853-015-9553-4.
[208] J. Luster, M.A. Morris, Compatibility of deformation in two-phase Ti-Al alloys: Dependence on microstructure and orientation relationships, Metall Mater Trans A 26 (1995) 1745–1756. https://doi.org/10.1007/BF02670762.
[209] R. Alizadeh, M. Peña-Ortega, T.R. Bieler, J. LLorca, A criterion for slip transfer at grain boundaries in Al, Scripta Materialia 178 (2020) 408–412. https://doi.org/10.1016/j.scriptamat.2019.12.010.
[210] M.T. Andani, A. Lakshmanan, V. Sundararaghavan, J. Allison, A. Misra, Quantitative study of the effect of grain boundary parameters on the slip system level Hall-Petch slope for basal slip system in Mg-4Al, Acta Materialia 200 (2020) 148–161. https://doi.org/10.1016/j.actamat.2020.08.079.
[211] V. Tong, E. Wielewski, B. Britton, Characterisation of slip and twinning in high rate deformed zirconium with electron backscatter diffraction, (2018). https://doi.org/10.48550/arXiv.1803.00236.
[212] D.M. Henderson, Euler angles, quaternions, and transformation matrices, 1977. https://ntrs.nasa.gov/citations/19770024290 (accessed October 10, 2023).
[213] M. Wu, Y. Hou, L. Hua, H. Ma, X. Li, S. Xiong, On the deformation behavior of heterogeneous microstructure and its effect on the mechanical properties of die cast AZ91D magnesium alloy, Journal of Magnesium and Alloys 10 (2022) 1981–1993. https://doi.org/10.1016/j.jma.2021.09.006.
[214] F. Pedregosa, G. Varoquaux, A. Gramfort, V. Michel, B. Thirion, O. Grisel, M. Blondel, P. Prettenhofer, R. Weiss, V. Dubourg, J. Vanderplas, A. Passos, D. Cournapeau, M. Brucher, M. Perrot, É. Duchesnay, Scikit-learn: Machine Learning in Python, Journal of Machine Learning Research 12 (2011) 2825–2830.
[215] G. Ducamp, C. Gonzales, P.-H. Wuillemin, aGrUM/pyAgrum : a toolbox to build models and algorithms for Probabilistic Graphical Models in Python, in: 2020: p. 609. https://hal.science/hal-03135721 (accessed July 12, 2023).
[216] Y. Freund, R.E. Schapire, A Decision-Theoretic Generalization of On-Line Learning and an Application to Boosting, Journal of Computer and System Sciences 55 (1997) 119–139. https://doi.org/10.1006/jcss.1997.1504.
[217] J.H. Friedman, Stochastic gradient boosting, Computational Statistics & Data Analysis 38 (2002) 367–378. https://doi.org/10.1016/S0167-9473(01)00065-2.
[218] L. Breiman, Random Forests, Machine Learning 45 (2001) 5–32. https://doi.org/10.1023/A:1010933404324.
[219] H. Zhang, The Optimality of Naive Bayes, Proceedings of 17th International Florida Artificial Intelligence Research Society Conference (2004) 562–567.
[220] J. Pearl, Bayesian Networks: A Model of Self-activated Memory for Evidential Reasoning, UCLA Computer Science Department, 1985.
[221] J.A. Hanley, B.J. McNeil, The meaning and use of the area under a receiver operating characteristic (ROC) curve, Radiology 143 (1982) 29–36. https://doi.org/10.1148/radiology.143.1.7063747.

[222] A.P. Bradley, The use of the area under the ROC curve in the evaluation of machine learning algorithms, Pattern Recognition 30 (1997) 1145–1159. https://doi.org/10.1016/S0031-3203(96)00142-2.
[223] T. Fawcett, An introduction to ROC analysis, Pattern Recognition Letters 27 (2006) 861–874. https://doi.org/10.1016/j.patrec.2005.10.010.
[224] A. Vinogradov, D. Orlov, A. Danyuk, Y. Estrin, Deformation mechanisms underlying tension–compression asymmetry in magnesium alloy ZK60 revealed by acoustic emission monitoring, Materials Science and Engineering: A 621 (2015) 243–251. https://doi.org/10.1016/j.msea.2014.10.081.
[225] E.A. Ball, P.B. Prangnell, Tensile-compressive yield asymmetries in high strength wrought magnesium alloys, Scripta Metallurgica et Materialia; (United States) 31:2 (1994). https://doi.org/10.1016/0956-716X(94)90159-7.
[226] C.M. Cepeda-Jiménez, M.T. Pérez-Prado, Microplasticity-based rationalization of the room temperature yield asymmetry in conventional polycrystalline Mg alloys, Acta Materialia 108 (2016) 304–316. https://doi.org/10.1016/j.actamat.2016.02.023.
[227] V. Herrera-Solaz, P. Hidalgo-Manrique, M.T. Pérez-Prado, D. Letzig, J. Llorca, J. Segurado, Effect of rare earth additions on the critical resolved shear stresses of magnesium alloys, Materials Letters 128 (2014) 199–203. https://doi.org/10.1016/j.matlet.2014.04.144.
[228] P. Hidalgo-Manrique, S.B. Yi, J. Bohlen, D. Letzig, M.T. Pérez-Prado, Effect of Nd Additions on Extrusion Texture Development and on Slip Activity in a Mg-Mn Alloy, Metall Mater Trans A 44 (2013) 4819–4829. https://doi.org/10.1007/s11661-013-1823-7.
[229] H. Borkar, M. Hoseini, M. Pekguleryuz, Effect of strontium on the texture and mechanical properties of extruded Mg–1%Mn alloys, Materials Science and Engineering: A 549 (2012) 168–175. https://doi.org/10.1016/j.msea.2012.04.029.
[230] I.J. Beyerlein, S. Xu, J. Llorca, J.A. El-Awady, J.R. Mianroodi, B. Svendsen, Alloy design for mechanical properties: Conquering the length scales, MRS Bulletin 44 (2019) 257–265. https://doi.org/10.1557/mrs.2019.67.
[231] D.L. Yin, J.T. Wang, J.Q. Liu, X. Zhao, On tension–compression yield asymmetry in an extruded Mg–3Al–1Zn alloy, Journal of Alloys and Compounds 478 (2009) 789–795. https://doi.org/10.1016/j.jallcom.2008.12.033.
[232] H. Chen, T. Liu, Y. Zhang, B. Song, D. Hou, F. Pan, The yield asymmetry and precipitation behavior of pre-twinned ZK60 alloy, Materials Science and Engineering: A 652 (2016) 167–174. https://doi.org/10.1016/j.msea.2015.11.092.
[233] A.E. Davis, J.D. Robson, M. Turski, The effect of multiple precipitate types and texture on yield asymmetry in Mg-Sn-Zn(-Al-Na-Ca) alloys, Acta Materialia 158 (2018) 1–12. https://doi.org/10.1016/j.actamat.2018.07.044.
[234] C.M. Cepeda-Jiménez, C. Prado-Martínez, M.T. Pérez-Prado, Understanding the high temperature reversed yield asymmetry in a Mg-rare earth alloy by slip trace analysis, Acta Materialia 145 (2018) 264–277. https://doi.org/10.1016/j.actamat.2017.12.021.

[235] M.R. Barnett, Z. Keshavarz, A.G. Beer, D. Atwell, Influence of grain size on the compressive deformation of wrought Mg–3Al–1Zn, Acta Materialia 52 (2004) 5093–5103. https://doi.org/10.1016/j.actamat.2004.07.015.
[236] H. Wang, L. Zhang, W. Chen, D. Fang, W. Zhang, G. Cui, Improved tension/compression asymmetry achieved in high-strength magnesium alloys via compression-extrusion process, Materials Science and Engineering: A 736 (2018) 239–247. https://doi.org/10.1016/j.msea.2018.08.110.
[237] H. Yu, Y. Xin, A. Chapuis, X. Huang, R. Xin, Q. Liu, The different effects of twin boundary and grain boundary on reducing tension-compression yield asymmetry of Mg alloys, Sci Rep 6 (2016) 29283. https://doi.org/10.1038/srep29283.
[238] Y. Xin, X. Zhou, Q. Liu, Suppressing the tension–compression yield asymmetry of Mg alloy by hybrid extension twins structure, Materials Science and Engineering: A 567 (2013) 9–13. https://doi.org/10.1016/j.msea.2012.12.094.
[239] M. Jahedi, B.A. McWilliams, P. Moy, M. Knezevic, Deformation twinning in rolled WE43-T5 rare earth magnesium alloy: Influence on strain hardening and texture evolution, Acta Materialia 131 (2017) 221–232. https://doi.org/10.1016/j.actamat.2017.03.075.
[240] L.B. Tong, M.Y. Zheng, S. Kamado, D.P. Zhang, J. Meng, L.R. Cheng, H.J. Zhang, Reducing the tension–compression yield asymmetry of extruded Mg–Zn–Ca alloy via equal channel angular pressing, Journal of Magnesium and Alloys 3 (2015) 302–308. https://doi.org/10.1016/j.jma.2015.08.007.
[241] J.D. Robson, N. Stanford, M.R. Barnett, Effect of precipitate shape on slip and twinning in magnesium alloys, Acta Materialia 59 (2011) 1945–1956. https://doi.org/10.1016/j.actamat.2010.11.060.
[242] G. Mann, J.R. Griffiths, C.H. Cáceres, Hall-Petch parameters in tension and compression in cast Mg–2Zn alloys, Journal of Alloys and Compounds 378 (2004) 188–191. https://doi.org/10.1016/j.jallcom.2003.12.052.
[243] Z. Wu, W.A. Curtin, The origins of high hardening and low ductility in magnesium, Nature 526 (2015) 62–67. https://doi.org/10.1038/nature15364.
[244] S. Sandlöbes, S. Zaefferer, I. Schestakow, S. Yi, R. Gonzalez-Martinez, On the role of non-basal deformation mechanisms for the ductility of Mg and Mg–Y alloys, Acta Materialia 59 (2011) 429–439. https://doi.org/10.1016/j.actamat.2010.08.031.
[245] N. Stanford, M.R. Barnett, Solute strengthening of prismatic slip, basal slip and $\{10\bar{1}2\}$ twinning in Mg and Mg–Zn binary alloys, International Journal of Plasticity 47 (2013) 165–181. https://doi.org/10.1016/j.ijplas.2013.01.012.
[246] M. Zhang, H. Zhang, A. Ma, J. LLorca, Experimental and numerical analysis of cyclic deformation and fatigue behavior of a Mg-RE alloy, International Journal of Plasticity 139 (2021) 102885. https://doi.org/10.1016/j.ijplas.2020.102885.
[247] S. Amukarimi, M. Mozafari, Biodegradable magnesium - based biomaterials: An overview of challenges and opportunities, MedComm (2020) 2 (2021) 123–144. https://doi.org/10.1002/mco2.59.
[248] G. Garces, P. Perez, S. Cabeza, H.K. Lin, S. Kim, W. Gan, P. Adeva, Reverse tension/compression asymmetry of a Mg–Y–Zn alloys containing LPSO

phases, Materials Science and Engineering: A 647 (2015) 287–293. https://doi.org/10.1016/j.msea.2015.09.003.
[249] Y.Q. Chi, X.H. Zhou, X.G. Qiao, H.G. Brokmeier, M.Y. Zheng, Tension-compression asymmetry of extruded Mg-Gd-Y-Zr alloy with a bimodal microstructure studied by in-situ synchrotron diffraction, Materials & Design 170 (2019) 107705. https://doi.org/10.1016/j.matdes.2019.107705.
[250] W. Rong, Y. Zhang, Y. Wu, Y. Chen, M. Sun, J. Chen, L. Peng, The role of bimodal-grained structure in strengthening tensile strength and decreasing yield asymmetry of Mg-Gd-Zn-Zr alloys, Materials Science and Engineering: A 740–741 (2019) 262–273. https://doi.org/10.1016/j.msea.2017.09.125.
[251] S. Lyu, R. Zheng, W. Xiao, Y. Huang, S. Gavras, N. Hort, G. Li, C. Ma, Abnormal extrusion texture and reversed yield asymmetry in a Mg–Y-Sm-Zn-Zr alloy, Materials Science and Engineering: A 760 (2019) 426–430. https://doi.org/10.1016/j.msea.2019.06.029.
[252] L. Zhao, B. Guan, Y. Xin, X. Huang, C. Liu, P. Wu, Q. Liu, A quantitative study on mechanical behavior of Mg alloys with bimodal texture components, Acta Materialia 214 (2021) 117013. https://doi.org/10.1016/j.actamat.2021.117013.
[253] J. Wang, M.R.G. Ferdowsi, S.R. Kada, S. Babaniaris, B. Hutchinson, P.A. Lynch, M.R. Barnett, Appearance of textures with a c-axis parallel to the extrusion direction in Mg alloys, Scripta Materialia 210 (2022) 114422. https://doi.org/10.1016/j.scriptamat.2021.114422.
[254] K. Tesař, H. Somekawa, A. Singh, Achieving Yield Symmetry in an Extruded Mg-Zn-Y Alloy by More Effective Dispersion of Quasicrystalline i-Phase, Metall Mater Trans A 52 (2021) 2185–2194. https://doi.org/10.1007/s11661-021-06209-5.
[255] S. Lyu, W. Xiao, G. Li, D. Xia, Y. Huang, S. Gavras, N. Hort, R. Zheng, C. Ma, Formation mechanism of the abnormal texture during extrusion in Mg-Y-Sm-Zn-Zr alloy, Journal of Alloys and Compounds 821 (2020) 153477. https://doi.org/10.1016/j.jallcom.2019.153477.
[256] Y.P. Wu, X.M. Zhang, Y.L. Deng, C.P. Tang, Y.Y. Zhong, Effect of secondary extrusion on the microstructure and mechanical properties of a Mg–RE alloy, Materials Science and Engineering: A 616 (2014) 148–154. https://doi.org/10.1016/j.msea.2014.08.022.
[257] R. Alizadeh, R. Mahmudi, A.H.W. Ngan, T.G. Langdon, An Unusual Extrusion Texture in Mg–Gd–Y–Zr Alloys, Advanced Engineering Materials 18 (2016) 1044–1049. https://doi.org/10.1002/adem.201500516.
[258] J. Wang, M.R.G. Ferdowsi, P.A. Lynch, S.R. Kada, M.R. Barnett, Influence of precipitation on tension and compression twinning in Mg-6.5Zn alloy, Scripta Materialia 207 (2022) 114253. https://doi.org/10.1016/j.scriptamat.2021.114253.
[259] R. Hielscher, H. Schaeben, A novel pole figure inversion method: specification of the *MTEX* algorithm, J Appl Crystallogr 41 (2008) 1024–1037. https://doi.org/10.1107/S0021889808030112.
[260] M.R. Barnett, Z. Keshavarz, A.G. Beer, X. Ma, Non-Schmid behaviour during secondary twinning in a polycrystalline magnesium alloy, Acta Materialia 56 (2008) 5–15. https://doi.org/10.1016/j.actamat.2007.08.034.

[261] M.R. Barnett, M.D. Nave, A. Ghaderi, Yield point elongation due to twinning in a magnesium alloy, Acta Materialia 60 (2012) 1433–1443. https://doi.org/10.1016/j.actamat.2011.11.022.
[262] D.F. Shi, A. Ma, M.T. Pérez-Prado, C.M. Cepeda-Jiménez, Activation of second-order pyramidal slip and other secondary mechanisms in solid solution Mg-Zn alloys and their effect on tensile ductility, Acta Materialia 244 (2022) 118555. https://doi.org/10.1016/j.actamat.2022.118555.
[263] C.H. Caceres, G.E. Mann, J.R. Griffiths, Grain Size Hardening in Mg and Mg-Zn Solid Solutions, Metall Mater Trans A 42 (2011) 1950–1959. https://doi.org/10.1007/s11661-010-0599-2.
[264] J. Wang, Impact of aging on monotonic and cyclic loading of extruded Mg-Zn alloys, thesis, Deakin University, 2019. https://dro.deakin.edu.au/articles/thesis/Impact_of_aging_on_monotonic_and_cyclic_loading_of_extruded_Mg-Zn_alloys/21118072/1 (accessed November 8, 2022).
[265] C. Lou, X. Zhang, Y. Ren, Non-Schmid-based {10-12} twinning behavior in polycrystalline magnesium alloy, Materials Characterization 107 (2015) 249–254. https://doi.org/10.1016/j.matchar.2015.07.022.
[266] N. Li, C. Wang, M.A. Monclús, L. Yang, J.M. Molina-Aldareguia, Solid solution and precipitation strengthening effects in basal slip, extension twinning and pyramidal slip in Mg-Zn alloys, Acta Materialia 221 (2021) 117374. https://doi.org/10.1016/j.actamat.2021.117374.
[267] J. Jain, P. Cizek, W.J. Poole, M.R. Barnett, The role of back stress caused by precipitates on {10-12} twinning in a Mg-6Zn alloy, Materials Science and Engineering: A 647 (2015) 66–73. https://doi.org/10.1016/j.msea.2015.08.091.
[268] M. Ghazisaeidi, L.G. Hector, W.A. Curtin, Solute strengthening of twinning dislocations in Mg alloys, Acta Materialia 80 (2014) 278–287. https://doi.org/10.1016/j.actamat.2014.07.045.
[269] W. Taylor, A. Moore, Tensile deformation modes in polycrystalline beryllium near the ductile-brittle transition, Journal of Nuclear Materials 13 (1964) 23–27. https://doi.org/10.1016/0022-3115(64)90062-5.
[270] Y.B. Chun, C.H.J. Davies, The Evolution of In-Grain Misorientation Axes (IGMA) During Deformation of Wrought Magnesium Alloy AZ31, in: Springer International Publishing, Cham, 2016: pp. 345–349. https://doi.org/10.1007/978-3-319-48099-2_55.
[271] L. Wang, Z. Zheng, H. Phukan, P. Kenesei, J.-S. Park, J. Lind, R.M. Suter, T.R. Bieler, Direct measurement of critical resolved shear stress of prismatic and basal slip in polycrystalline Ti using high energy X-ray diffraction microscopy, Acta Materialia 132 (2017) 598–610. https://doi.org/10.1016/j.actamat.2017.05.015.
[272] M. Yamasaki, K. Hagihara, S. Inoue, J.P. Hadorn, Y. Kawamura, Crystallographic classification of kink bands in an extruded Mg–Zn–Y alloy using intragranular misorientation axis analysis, Acta Materialia 61 (2013) 2065–2076. https://doi.org/10.1016/j.actamat.2012.12.026.
[273] M. Sarebanzadeh, A. Orozco-Caballero, J. LLorca, Accurate determination of active slip systems for improved geometrical criteria of basal-to-basal slip

transfer at grain boundaries in pure Mg, Acta Materialia 243 (2023) 118536. https://doi.org/10.1016/j.actamat.2022.118536.
[274] W. Gong, T. Kawasaki, R. Zheng, T. Mayama, B. Sun, K. Aizawa, S. Harjo, N. Tsuji, Compressive deformation behavior of AZ31 alloy at 21K: an in-situ neutron diffraction study, Scripta Materialia 225 (2023) 115161. https://doi.org/10.1016/j.scriptamat.2022.115161.
[275] D. Ando, J. Koike, Relationship between Deformation-Induced Surface Relief and Double Twinning in AZ31 Magnesium Alloy, J. Japan Inst. Metals 71 (2007) 684–687. https://doi.org/10.2320/jinstmet.71.684.
[276] D. Ando, J. Koike, Y. Sutou, Relationship between deformation twinning and surface step formation in AZ31 magnesium alloys, Acta Materialia 58 (2010) 4316–4324. https://doi.org/10.1016/j.actamat.2010.03.044.
[277] B. Liu, J. Yang, X. Zhang, Q. Yang, J. Zhang, X. Li, Development and application of magnesium alloy parts for automotive OEMs: A review, Journal of Magnesium and Alloys 11 (2023) 15–47. https://doi.org/10.1016/j.jma.2022.12.015.
[278] J.-L. Wang, J.-K. Xu, C. Hopkins, D.H.-K. Chow, L. Qin, Biodegradable Magnesium-Based Implants in Orthopedics—A General Review and Perspectives, Advanced Science 7 (2020) 1902443. https://doi.org/10.1002/advs.201902443.
[279] J.A. Yasi, L.G. Hector, D.R. Trinkle, First-principles data for solid-solution strengthening of magnesium: From geometry and chemistry to properties, Acta Materialia 58 (2010) 5704–5713. https://doi.org/10.1016/j.actamat.2010.06.045.
[280] Z. Wu, R. Ahmad, B. Yin, S. Sandlöbes, W.A. Curtin, Mechanistic origin and prediction of enhanced ductility in magnesium alloys, Science 359 (2018) 447–452. https://doi.org/10.1126/science.aap8716.
[281] F. Pan, M. Yang, X. Chen, A Review on Casting Magnesium Alloys: Modification of Commercial Alloys and Development of New Alloys, Journal of Materials Science & Technology 32 (2016) 1211–1221. https://doi.org/10.1016/j.jmst.2016.07.001.
[282] Q. Zhu, Y. Li, F. Cao, D. Qiu, Y. Yang, J. Wang, H. Zhang, T. Ying, W. Ding, X. Zeng, Towards development of a high-strength stainless Mg alloy with Al-assisted growth of passive film, Nat Commun 13 (2022) 5838. https://doi.org/10.1038/s41467-022-33480-w.
[283] D. Bian, X. Chu, J. Xiao, Z. Tong, H. Huang, Q. Jia, J. Liu, W. Li, H. Yu, Y. He, L. Ma, X. Wang, M. Li, T. Yang, W. Huang, C. Zhang, M. Yao, Y. Zhang, Z. Xu, S. Guan, Y. Zheng, Design of single-phased magnesium alloys with typically high solubility rare earth elements for biomedical applications: Concept and proof, Bioactive Materials 22 (2023) 180–200. https://doi.org/10.1016/j.bioactmat.2022.09.018.
[284] P. Hidalgo-Manrique, V. Herrera-Solaz, J. Segurado, J. Llorca, F. Gálvez, O.A. Ruano, S.B. Yi, M.T. Pérez-Prado, Origin of the reversed yield asymmetry in Mg-rare earth alloys at high temperature, Acta Materialia 92 (2015) 265–277. https://doi.org/10.1016/j.actamat.2015.03.053.
[285] H. Ovri, J. Markmann, J. Barthel, M. Kruth, H. Dieringa, E.T. Lilleodden, Mechanistic origin of the enhanced strength and ductility in Mg-rare earth

alloys, Acta Materialia 244 (2023) 118550. https://doi.org/10.1016/j.actamat.2022.118550.
[286] K. Kishida, H. Yokobayashi, H. Inui, A formation criterion for Order-Disorder (OD) phases of the Long-Period Stacking Order (LPSO)-type in Mg-Al-RE (Rare Earth) Ternary Systems, Sci Rep 7 (2017) 12294. https://doi.org/10.1038/s41598-017-12506-0.
[287] J. Shao, Z. Chen, T. Chen, Z. Hu, X. Zhou, C. Liu, The effect of LPSO on the deformation mechanism of Mg–Gd–Y–Zn–Zr magnesium alloy, Journal of Magnesium and Alloys 4 (2016) 83–88. https://doi.org/10.1016/j.jma.2016.03.001.
[288] C. Xu, T. Nakata, X.G. Qiao, M.Y. Zheng, K. Wu, S. Kamado, Ageing behavior of extruded Mg–8.2Gd–3.8Y–1.0Zn–0.4Zr (wt.%) alloy containing LPSO phase and γ′ precipitates, Scientific Reports 7 (2017) 43391. https://doi.org/10.1038/srep43391.
[289] Y. Wan, B. Tang, Y. Gao, L. Tang, G. Sha, B. Zhang, N. Liang, C. Liu, S. Jiang, Z. Chen, X. Guo, Y. Zhao, Bulk nanocrystalline high-strength magnesium alloys prepared via rotary swaging, Acta Materialia 200 (2020) 274–286. https://doi.org/10.1016/j.actamat.2020.09.024.
[290] A. Ghaderi, M.R. Barnett, Sensitivity of deformation twinning to grain size in titanium and magnesium, Acta Materialia 59 (2011) 7824–7839. https://doi.org/10.1016/j.actamat.2011.09.018.
[291] H. Fan, S. Aubry, A. Arsenlis, J.A. El-Awady, Grain size effects on dislocation and twinning mediated plasticity in magnesium, Scripta Materialia 112 (2016) 50–53. https://doi.org/10.1016/j.scriptamat.2015.09.008.
[292] J.U. Lee, Y.J. Kim, S.-H. Kim, J.H. Lee, M.-S. Kim, S.-H. Choi, B.G. Moon, Y.M. Kim, S.H. Park, Texture tailoring and bendability improvement of rolled AZ31 alloy using {10-12} twinning: The effect of precompression levels, Journal of Magnesium and Alloys 7 (2019) 648–660. https://doi.org/10.1016/j.jma.2019.09.002.
[293] S.H.C. Park, Y.S. Sato, H. Kokawa, Effect of micro-texture on fracture location in friction stir weld of Mg alloy AZ61 during tensile test, Scripta Materialia 49 (2003) 161–166. https://doi.org/10.1016/S1359-6462(03)00210-0.
[294] R. Li, R. Xin, Q. Liu, A. Chapuis, S. Liu, G. Fu, L. Zong, Effect of grain size, texture and density of precipitates on the hardness and tensile yield stress of Mg-14Gd-0.5Zr alloys, Materials & Design 114 (2017) 450–458. https://doi.org/10.1016/j.matdes.2016.10.074.
[295] I. Basu, K.G. Pradeep, C. Mießen, L.A. Barrales-Mora, T. Al-Samman, The role of atomic scale segregation in designing highly ductile magnesium alloys, Acta Materialia 116 (2016) 77–94. https://doi.org/10.1016/j.actamat.2016.06.024.
[296] Q. Deng, Y. Wu, Y. Luo, N. Su, X. Xue, Z. Chang, Q. Wu, Y. Xue, L. Peng, Fabrication of high-strength Mg-Gd-Zn-Zr alloy via selective laser melting, Materials Characterization 165 (2020) 110377. https://doi.org/10.1016/j.matchar.2020.110377.
[297] K.K. Alaneme, E.A. Okotete, Enhancing plastic deformability of Mg and its alloys—A review of traditional and nascent developments, Journal of

Magnesium and Alloys 5 (2017) 460–475. https://doi.org/10.1016/j.jma.2017.11.001.
[298] R. Ahmad, B. Yin, Z. Wu, W.A. Curtin, Designing high ductility in magnesium alloys, Acta Materialia 172 (2019) 161–184. https://doi.org/10.1016/j.actamat.2019.04.019.
[299] U. Masood Chaudry, S. Tekumalla, M. Gupta, T.-S. Jun, K. Hamad, Designing highly ductile magnesium alloys: current status and future challenges, Critical Reviews in Solid State and Materials Sciences 47 (2022) 194–281. https://doi.org/10.1080/10408436.2021.1947185.
[300] C.W. Ha, S.J. Choi, N.J. Park, Effect of Alloying Elements on Microstructure, Texture Development, and Mechanical Properties of Magnesium Alloys, AMM 217–219 (2012) 382–385. https://doi.org/10.4028/www.scientific.net/AMM.217-219.382.
[301] H.K. Lim, D.H. Kim, J.Y. Lee, W.T. Kim, D.H. Kim, Effects of alloying elements on microstructures and mechanical properties of wrought Mg–MM–Sn alloy, Journal of Alloys and Compounds 468 (2009) 308–314. https://doi.org/10.1016/j.jallcom.2007.12.098.
[302] J. Xie, J. Zhang, Z. You, S. Liu, K. Guan, R. Wu, J. Wang, J. Feng, Towards developing Mg alloys with simultaneously improved strength and corrosion resistance via RE alloying, Journal of Magnesium and Alloys 9 (2021) 41–56. https://doi.org/10.1016/j.jma.2020.08.016.
[303] S. Sandlöbes, Z. Pei, M. Friák, L.-F. Zhu, F. Wang, S. Zaefferer, D. Raabe, J. Neugebauer, Ductility improvement of Mg alloys by solid solution: Ab initio modeling, synthesis and mechanical properties, Acta Materialia 70 (2014) 92–104. https://doi.org/10.1016/j.actamat.2014.02.011.
[304] F. Khomamizadeh, B. Nami, S. Khoshkhooei, Effect of rare-earth element additions on high-temperature mechanical properties of AZ91 magnesium alloy, Metall Mater Trans A 36 (2005) 3489–3494. https://doi.org/10.1007/s11661-005-0022-6.
[305] J. Wang, Y. Chen, Z. Chen, J. Llorca, X. Zeng, Deformation mechanisms of Mg-Ca-Zn alloys studied by means of micropillar compression tests, Acta Materialia 217 (2021) 117151. https://doi.org/10.1016/j.actamat.2021.117151.
[306] Q. Peng, B. Ge, H. Fu, Y. Sun, Q. Zu, J. Huang, Nanoscale coherent interface strengthening of Mg alloys, Nanoscale 10 (2018) 18028–18035. https://doi.org/10.1039/C8NR04805C.
[307] S. Sandlöbes, M. Friák, S. Korte-Kerzel, Z. Pei, J. Neugebauer, D. Raabe, A rare-earth free magnesium alloy with improved intrinsic ductility, Sci Rep 7 (2017). https://doi.org/10.1038/s41598-017-10384-0.
[308] P. Peng, J. She, A. Tang, J. Zhang, S. Zhou, M. Rashad, J. Kim, A.A. Luo, F. Pan, A new dilute Mg–Mn–Al alloy with exceptional rollability and ductility at room temperature, Materials Science and Engineering: A 859 (2022) 144229. https://doi.org/10.1016/j.msea.2022.144229.
[309] I. Basu, M. Chen, J. Wheeler, R.E. Schäublin, J.F. Löffler, Segregation-driven exceptional twin-boundary strengthening in lean Mg–Zn–Ca alloys, Acta Materialia 229 (2022) 117746. https://doi.org/10.1016/j.actamat.2022.117746.

[310] W. Fu, P. Dang, S. Guo, Z. Ren, D. Fang, X. Ding, J. Sun, Heterogeneous fiberous structured Mg-Zn-Zr alloy with superior strength-ductility synergy, Journal of Materials Science & Technology 134 (2023) 67–80. https://doi.org/10.1016/j.jmst.2022.06.021.

[311] Y. Li, A. Zhang, C. Li, H. Xie, B. Jiang, Z. Dong, P. Jin, F. Pan, Recent advances of high strength Mg-RE alloys: Alloy development, forming and application, Journal of Materials Research and Technology 26 (2023) 2919–2940. https://doi.org/10.1016/j.jmrt.2023.08.055.

[312] J.F. Nie, Effects of precipitate shape and orientation on dispersion strengthening in magnesium alloys, Scripta Materialia 48 (2003) 1009–1015. https://doi.org/10.1016/S1359-6462(02)00497-9.

[313] J.D. Robson, N. Stanford, M.R. Barnett, Effect of Precipitate Shape and Habit on Mechanical Asymmetry in Magnesium Alloys, Metall Mater Trans A 44 (2013) 2984–2995. https://doi.org/10.1007/s11661-012-1466-0.

[314] J. Jain, P. Cizek, W.J. Poole, M.R. Barnett, Precipitate characteristics and their effect on the prismatic-slip-dominated deformation behaviour of an Mg–6 Zn alloy, Acta Materialia 61 (2013) 4091–4102. https://doi.org/10.1016/j.actamat.2013.03.033.

[315] F. Wang, J.J. Bhattacharyya, S.R. Agnew, Effect of precipitate shape and orientation on Orowan strengthening of non-basal slip modes in hexagonal crystals, application to magnesium alloys, Materials Science and Engineering: A 666 (2016) 114–122. https://doi.org/10.1016/j.msea.2016.04.056.

[316] R. Alizadeh, J. Wang, J. LLorca, Precipitate strengthening of pyramidal slip in Mg–Zn alloys, Materials Science and Engineering: A 804 (2021) 140697. https://doi.org/10.1016/j.msea.2020.140697.

[317] B. Yang, L. Javier, Origin of nucleation and growth of extension twins in grains unsuitably oriented for twinning during deformation of Mg-1%Al, Journal of Magnesium and Alloys (2024) In press. https://doi.org/10.1016/j.jma.2024.02.013.

[318] D.F. Shi, M.T. Pérez-Prado, C.M. Cepeda-Jiménez, Effect of solutes on strength and ductility of Mg alloys, Acta Materialia 180 (2019) 218–230. https://doi.org/10.1016/j.actamat.2019.09.018.

[319] F.J. Humphreys, Review Grain and subgrain characterisation by electron backscatter diffraction, Journal of Materials Science 36 (2001) 3833–3854. https://doi.org/10.1023/A:1017973432592.

[320] V. Randle, Electron backscatter diffraction: Strategies for reliable data acquisition and processing, Materials Characterization 60 (2009) 913–922. https://doi.org/10.1016/j.matchar.2009.05.011.

[321] J. Xu, B. Guan, Y. Xin, G. Huang, P. Wu, Q. Liu, Revealing the role of pyramidal slip in the high ductility of Mg-Li alloy, Journal of Magnesium and Alloys (2021). https://doi.org/10.1016/j.jma.2021.11.012.

[322] H.-S. Jang, B.-J. Lee, Effects of Zn on 〈c + a〉 slip and grain boundary segregation of Mg alloys, Scripta Materialia 160 (2019) 39–43. https://doi.org/10.1016/j.scriptamat.2018.09.022.

[323] A. Akhtar, E. Teghtsoonian, Solid solution strengthening of magnesium single crystals—I alloying behaviour in basal slip, Acta Metallurgica 17 (1969) 1339–1349. https://doi.org/10.1016/0001-6160(69)90151-5.

[324] A. Akhtar, E. Teghtsoonian, Solid solution strengthening of magnesium single crystals—ii the effect of solute on the ease of prismatic slip, Acta Metallurgica 17 (1969) 1351–1356. https://doi.org/10.1016/0001-6160(69)90152-7.
[325] N. Stanford, M.R. Barnett, Effect of Zn Concentration and Grain Size on Prismatic Slip in Mg-Zn Binary Alloys, in: S.N. Mathaudhu, W.H. Sillekens, N.R. Neelameggham, N. Hort (Eds.), Magnesium Technology 2012, Springer International Publishing, Cham, 2012: pp. 207–211. https://doi.org/10.1007/978-3-319-48203-3_39.
[326] W. Xu, N. Birbilis, G. Sha, Y. Wang, J.E. Daniels, Y. Xiao, M. Ferry, A high-specific-strength and corrosion-resistant magnesium alloy, Nature Materials 14 (2015) 1229–1235. https://doi.org/10.1038/nmat4435.
[327] J. Bai, Y. Yang, C. Wen, J. Chen, G. Zhou, B. Jiang, X. Peng, F. Pan, Applications of magnesium alloys for aerospace: A review, Journal of Magnesium and Alloys 11 (2023) 3609–3619. https://doi.org/10.1016/j.jma.2023.09.015.
[328] B. Yang, J. Wang, Y. Li, M. Barnett, J. LLorca, Suppressed transformation of compression twins to double twins in Mg by activation of <a> non-basal slip, Scripta Materialia 235 (2023) 115620. https://doi.org/10.1016/j.scriptamat.2023.115620.
[329] P. Chen, B. Li, D. Culbertson, Y. Jiang, Contribution of extension twinning to plastic strain at low stress stage deformation of a Mg-3Al-1Zn alloy, Materials Science and Engineering: A 709 (2018) 40–45. https://doi.org/10.1016/j.msea.2017.10.038.
[330] D. Drozdenko, J. Bohlen, S. Yi, P. Minárik, F. Chmelík, P. Dobroň, Investigating a twinning–detwinning process in wrought Mg alloys by the acoustic emission technique, Acta Materialia 110 (2016) 103–113. https://doi.org/10.1016/j.actamat.2016.03.013.
[331] Y. Pei, A. Godfrey, J. Jiang, Y.B. Zhang, W. Liu, Q. Liu, Extension twin variant selection during uniaxial compression of a magnesium alloy, Materials Science and Engineering: A 550 (2012) 138–145. https://doi.org/10.1016/j.msea.2012.04.046.
[332] C. Guo, R. Xin, J. Xu, B. Song, Q. Liu, Strain compatibility effect on the variant selection of connected twins in magnesium, Materials & Design 76 (2015) 71–76. https://doi.org/10.1016/j.matdes.2015.03.041.
[333] X. Liu, J.J. Jonas, B.W. Zhu, T. Wang, L.X. Li, Variant selection of primary extension twins in AZ31 magnesium deformed at 400°C, Materials Science and Engineering: A 649 (2016) 461–467. https://doi.org/10.1016/j.msea.2015.10.020.
[334] M. Arul Kumar, I.J. Beyerlein, C.N. Tomé, Effect of local stress fields on twin characteristics in HCP metals, Acta Materialia 116 (2016) 143–154. https://doi.org/10.1016/j.actamat.2016.06.042.
[335] L. Jiang, M.A. Kumar, I.J. Beyerlein, X. Wang, D. Zhang, C. Wu, C. Cooper, T.J. Rupert, S. Mahajan, E.J. Lavernia, J.M. Schoenung, Twin formation from a twin boundary in Mg during in-situ nanomechanical testing, Materials Science and Engineering: A 759 (2019) 142–153. https://doi.org/10.1016/j.msea.2019.04.117.

[336] C. Liu, P. Shanthraj, M. Diehl, F. Roters, S. Dong, J. Dong, W. Ding, D. Raabe, An integrated crystal plasticity–phase field model for spatially resolved twin nucleation, propagation, and growth in hexagonal materials, International Journal of Plasticity 106 (2018) 203–227. https://doi.org/10.1016/j.ijplas.2018.03.009.

[337] T. Liu, Q. Yang, N. Guo, Y. Lu, B. Song, Stability of twins in Mg alloys – A short review, Journal of Magnesium and Alloys 8 (2020) 66–77. https://doi.org/10.1016/j.jma.2020.02.002.

[338] S.-G. Hong, S.H. Park, C.S. Lee, Role of {10-12} twinning characteristics in the deformation behavior of a polycrystalline magnesium alloy, Acta Materialia 58 (2010) 5873–5885. https://doi.org/10.1016/j.actamat.2010.07.002.

[339] D.F. Shi, A. Ma, M.T. Pérez-Prado, C.M. Cepeda-Jiménez, Activation of second-order pyramidal slip and other secondary mechanisms in solid solution Mg-Zn alloys and their effect on tensile ductility, Acta Materialia 244 (2023) 118555. https://doi.org/10.1016/j.actamat.2022.118555.

[340] B.-C. Suh, M.-S. Shim, D.-W. Kim, N.J. Kim, Twinning behavior of Mg–4Zn–1Gd alloy sheet during longitudinal tensile deformation, Scripta Materialia 69 (2013) 465–468. https://doi.org/10.1016/j.scriptamat.2013.05.043.

[341] B. Yang, V. Vassilev-Galindo, J. LLorca, Application of machine learning to assess the influence of microstructure on twin nucleation in Mg alloys, Npj Comput. Mater. 10 (2023) 26. https://doi.org/10.1038/s41524-024-01212-x.

[342] W.B. Hutchinson, M.R. Barnett, Effective values of critical resolved shear stress for slip in polycrystalline magnesium and other hcp metals, Scripta Materialia 63 (2010) 737–740. https://doi.org/10.1016/j.scriptamat.2010.05.047.

[343] O. Lacombe, C. Parlangeau, N.E. Beaudoin, K. Amrouch, Calcite Twin Formation, Measurement and Use as Stress–Strain Indicators: A Review of Progress over the Last Decade, Geosciences 11 (2021) 445. https://doi.org/10.3390/geosciences11110445.

[344] R. Sánchez-Martín, M.T. Pérez-Prado, J. Segurado, J. Bohlen, I. Gutiérrez-Urrutia, J. Llorca, J.M. Molina-Aldareguia, Measuring the critical resolved shear stresses in Mg alloys by instrumented nanoindentation, Acta Materialia 71 (2014) 283–292. https://doi.org/10.1016/j.actamat.2014.03.014.

[345] M. Arul Kumar, I.J. Beyerlein, R.J. McCabe, C.N. Tomé, Grain neighbour effects on twin transmission in hexagonal close-packed materials, Nature Communications 7 (2016) 13826. https://doi.org/10.1038/ncomms13826.

[346] M.A. Kumar, R.J. McCabe, V. Taupin, C.N. Tomé, L. Capolungo, Statistical characterization of twin transmission across grain boundaries in magnesium, Materials Characterization 194 (2022) 112457. https://doi.org/10.1016/j.matchar.2022.112457.

[347] Y.Q. Chai, C.J. Boehlert, Y.F. Wan, G.H. Huang, H. Zhou, J. Zheng, Q.D. Wang, D.D. Yin, Anomalous Tension Twinning Activity in Extruded Mg Sheet During Hard-Orientation Loading at Room Temperature, Metall Mater Trans A 52 (2021) 449–456. https://doi.org/10.1007/s11661-020-06093-5.

[348] L. Capolungo, I.J. Beyerlein, Nucleation and stability of twins in hcp metals, Phys. Rev. B 78 (2008) 024117. https://doi.org/10.1103/PhysRevB.78.024117.

[349] M. Gong, G. Liu, J. Wang, L. Capolungo, C.N. Tomé, Atomistic simulations of interaction between basal dislocations and three-dimensional twins in magnesium, Acta Materialia 155 (2018) 187–198. https://doi.org/10.1016/j.actamat.2018.05.066.
[350] J. Jeong, M. Alfreider, R. Konetschnik, D. Kiener, S.H. Oh, In-situ TEM observation of {10-12} twin-dominated deformation of Mg pillars: Twinning mechanism, size effects and rate dependency, Acta Materialia 158 (2018) 407–421. https://doi.org/10.1016/j.actamat.2018.07.027.
[351] U.M. Chaudry, H.M.R. Tariq, M. Zubair, N. Ansari, T.-S. Jun, Implications of twinning on the microstructure development, crystallographic texture and mechanical performance of Mg alloys- a critical review, Journal of Magnesium and Alloys (2023). https://doi.org/10.1016/j.jma.2023.09.023.
[352] S.H. Park, J.H. Lee, B.G. Moon, B.S. You, Tension–compression yield asymmetry in as-cast magnesium alloy, Journal of Alloys and Compounds 617 (2014) 277–280. https://doi.org/10.1016/j.jallcom.2014.07.164.
[353] D. Xie, Z. Lyu, Y. Li, P.K. Liaw, H.B. Chew, Y. Ren, Y. Chen, K. An, Y. Gao, In situ monitoring of dislocation, twinning, and detwinning modes in an extruded magnesium alloy under cyclic loading conditions, Materials Science and Engineering: A 806 (2021) 140860. https://doi.org/10.1016/j.msea.2021.140860.
[354] M.R. Barnett, J. Wang, S.R. Kada, A. de Vaucorbeil, A. Stevenson, M. Fivel, P.A. Lynch, Grain scale bursts of plasticity in Mg-4Zn via high energy X-rays: Towards twin observation in real-time, Acta Materialia 264 (2024) 119549. https://doi.org/10.1016/j.actamat.2023.119549.
[355] E. Nieto-Valeiras, E. Ganju, N. Chawla, J. LLorca, Assessment of slip transfer criteria for prismatic-to-prismatic slip in pure Ti from 3D grain boundary data, Acta Materialia 262 (2024) 119424. https://doi.org/10.1016/j.actamat.2023.119424.
[356] C. Bing, T.R. Bieler, P. Eisenlohr, A computational study of how surfaces affect slip family activity, Acta Materialia 259 (2023) 119246. https://doi.org/10.1016/j.actamat.2023.119246.
[357] A. Venkatraman, S. Mohan, V.R. Joseph, D.L. McDowell, S.R. Kalidindi, A new framework for the assessment of model probabilities of the different crystal plasticity models for lamellar grains in \alpha+\beta Titanium alloys, Modelling Simul. Mater. Sci. Eng. 31 (2023) 044001. https://doi.org/10.1088/1361-651X/accdf4.
[358] D. Zhao, F. Witte, F. Lu, J. Wang, J. Li, L. Qin, Current status on clinical applications of magnesium-based orthopaedic implants: A review from clinical translational perspective, Biomaterials 112 (2017) 287–302. https://doi.org/10.1016/j.biomaterials.2016.10.017.
[359] M. Li, F. Benn, T. Derra, N. Kröger, M. Zinser, R. Smeets, J.M. Molina-Aldareguia, A. Kopp, J. LLorca, Microstructure, mechanical properties, corrosion resistance and cytocompatibility of WE43 Mg alloy scaffolds fabricated by laser powder bed fusion for biomedical applications, Materials Science and Engineering: C 119 (2021) 111623. https://doi.org/10.1016/j.msec.2020.111623.

[360] J.-H. Cho, S.-B. Kang, Deformation and Recrystallization Behaviors in Magnesium Alloys, in: P. Wilson (Ed.), Recent Developments in the Study of Recrystallization, InTech, 2013. https://doi.org/10.5772/55597.
[361] X. Song, J. Luo, Z. Shi, L. Zhuang, Y. Qiao, J. Zhang, Quantitative prediction of grain boundary misorientation effect on twin transmission in hexagonal metals, Materials & Design 192 (2020) 108745. https://doi.org/10.1016/j.matdes.2020.108745.
[362] A. Akhtar, E. Teghtsoonian, Substitutional solution hardening of magnesium single crystals, The Philosophical Magazine: A Journal of Theoretical Experimental and Applied Physics 25 (1972) 897–916. https://doi.org/10.1080/14786437208229311.
[363] C. Zhao, X. Chen, F. Pan, J. Wang, S. Gao, T. Tu, C. Liu, J. Yao, A. Atrens, Strain hardening of as-extruded Mg-xZn (x = 1, 2, 3 and 4 wt%) alloys, Journal of Materials Science & Technology 35 (2019) 142–150. https://doi.org/10.1016/j.jmst.2018.09.015.
[364] S. Ganeshan, S.L. Shang, Y. Wang, Z.-K. Liu, Effect of alloying elements on the elastic properties of Mg from first-principles calculations, Acta Materialia 57 (2009) 3876–3884. https://doi.org/10.1016/j.actamat.2009.04.038.
[365] N. Bertin, C.N. Tomé, I.J. Beyerlein, M.R. Barnett, L. Capolungo, On the strength of dislocation interactions and their effect on latent hardening in pure Magnesium, International Journal of Plasticity 62 (2014) 72–92. https://doi.org/10.1016/j.ijplas.2014.06.010.
[366] X. Ma, Q. Jiao, L.J. Kecskes, J.A. El-Awady, T.P. Weihs, Effect of basal precipitates on extension twinning and pyramidal slip: A micro-mechanical and electron microscopy study of a Mg–Al binary alloy, Acta Materialia 189 (2020) 35–46. https://doi.org/10.1016/j.actamat.2020.02.037.
[367] Z. Huang, J.E. Allison, A. Misra, Interaction of Glide Dislocations with Extended Precipitates in Mg-Nd alloys, Sci Rep 8 (2018) 3570. https://doi.org/10.1038/s41598-018-20629-1.
[368] J.J. Bhattacharyya, F. Wang, N. Stanford, S.R. Agnew, Slip mode dependency of dislocation shearing and looping of precipitates in Mg alloy WE43, Acta Materialia 146 (2018) 55–62. https://doi.org/10.1016/j.actamat.2017.12.043.
[369] P.D. Ispánovity, D. Ugi, G. Péterffy, M. Knapek, S. Kalácska, D. Tüzes, Z. Dankházi, K. Máthis, F. Chmelík, I. Groma, Dislocation avalanches are like earthquakes on the micron scale, Nat Commun 13 (2022) 1975. https://doi.org/10.1038/s41467-022-29044-7.
[370] J.S. Chun, J.G. Byrne, Precipitate strengthening mechanisms in magnesium zinc alloy single crystals, J Mater Sci 4 (1969) 861–872. https://doi.org/10.1007/BF00549777.
[371] P.B. Hirsch, F.J. Humphreys, The deformation of single crystals of copper and copper-zinc alloys containing alumina particles - I. Macroscopic properties and workhardening theory, Proceedings of the Royal Society of London. A. Mathematical and Physical Sciences 318 (1997) 45–72. https://doi.org/10.1098/rspa.1970.0133.

[372] Z. Huang, C. Yang, J.E. Allison, L. Qi, A. Misra, Dislocation cross-slip in precipitation hardened Mg–Nd alloys, Journal of Alloys and Compounds 859 (2021) 157858. https://doi.org/10.1016/j.jallcom.2020.157858.
[373] M. Liao, B. Li, M.F. Horstemeyer, Interaction Between Basal Slip and a Mg17Al12 Precipitate in Magnesium, Metall Mater Trans A 45 (2014) 3661–3669. https://doi.org/10.1007/s11661-014-2284-3.
[374] T. Benjamin Britton, A.J. Wilkinson, Stress fields and geometrically necessary dislocation density distributions near the head of a blocked slip band, Acta Materialia 60 (2012) 5773–5782. https://doi.org/10.1016/j.actamat.2012.07.004.
[375] M.D. Sangid, H.J. Maier, H. Sehitoglu, The role of grain boundaries on fatigue crack initiation – An energy approach, International Journal of Plasticity 27 (2011) 801–821. https://doi.org/10.1016/j.ijplas.2010.09.009.
[376] A. Jamali, A. Ma, J. LLorca, Quantitative assessment of the microstructural factors controlling the fatigue crack initiation mechanisms in AZ31 Mg alloy, Acta Materialia 239 (2022) 118263. https://doi.org/10.1016/j.actamat.2022.118263.

Annex A. Mg-4.5Zn alloy

Figure A.1. Large EBSD of Mg-4.5Zn alloy

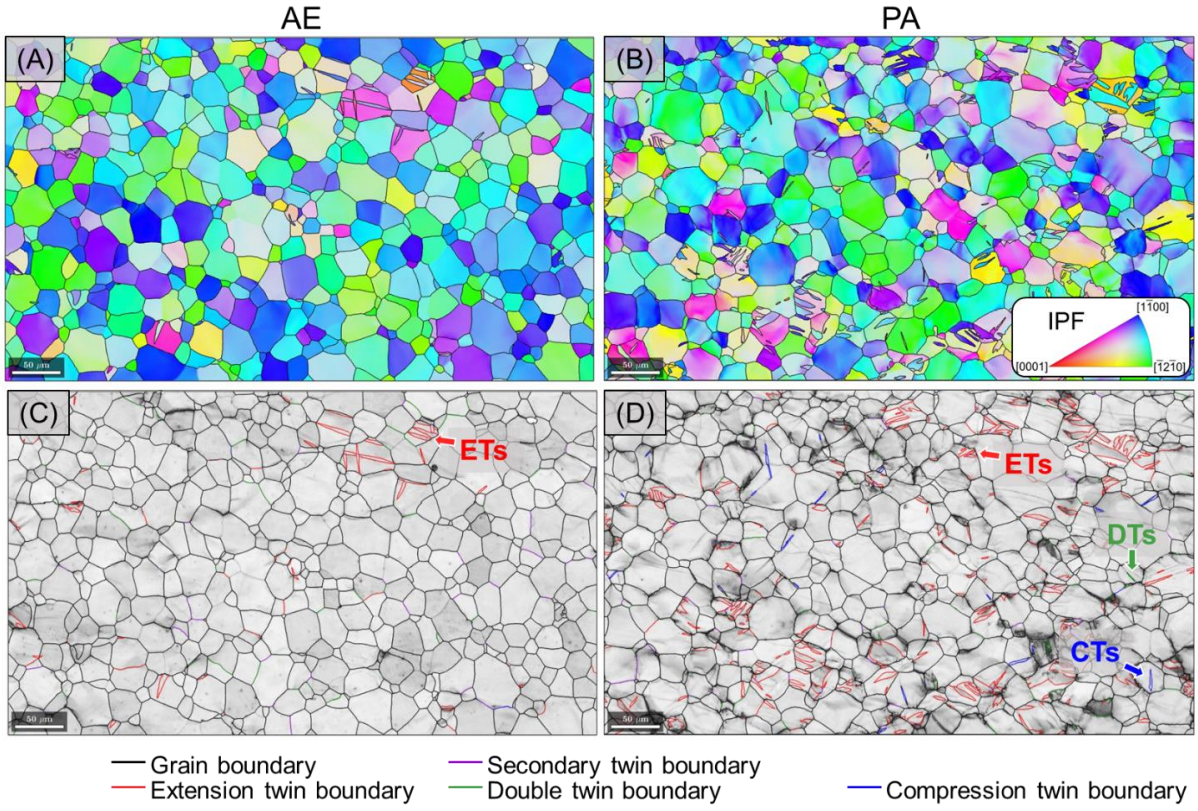

Figure A.1: The microstructures of (A, C) AE and (B, D) PA after deformation in a bigger area. EBSD orientation map in terms of (A-B) IPF and (C-D) BC. The reference direction of IPF is the horizontal direction, and all GBs were overlaid in black. ET, CT, secondary twin, and DT boundaries were highlighted in red, blue, purple, and green, respectively, in the BC maps. Note that their identification was performed by measuring the RA - misorientation angle of every boundary. The RA & angle pairs for ET, CT, secondary twin and DT are $<2\bar{1}\bar{1}0>$ & 86.30°, $<2\bar{1}\bar{1}0>$ & 56.15°, $<1\bar{1}00>$ & 60.00°, and $<2\bar{1}\bar{1}0>$ & 37.50°, respectively. The threshold misorientation angle was set to 5°.

Annex B. Mg-1Al alloy

Figure B.1. Twinning propensity of the large size grains after deformation

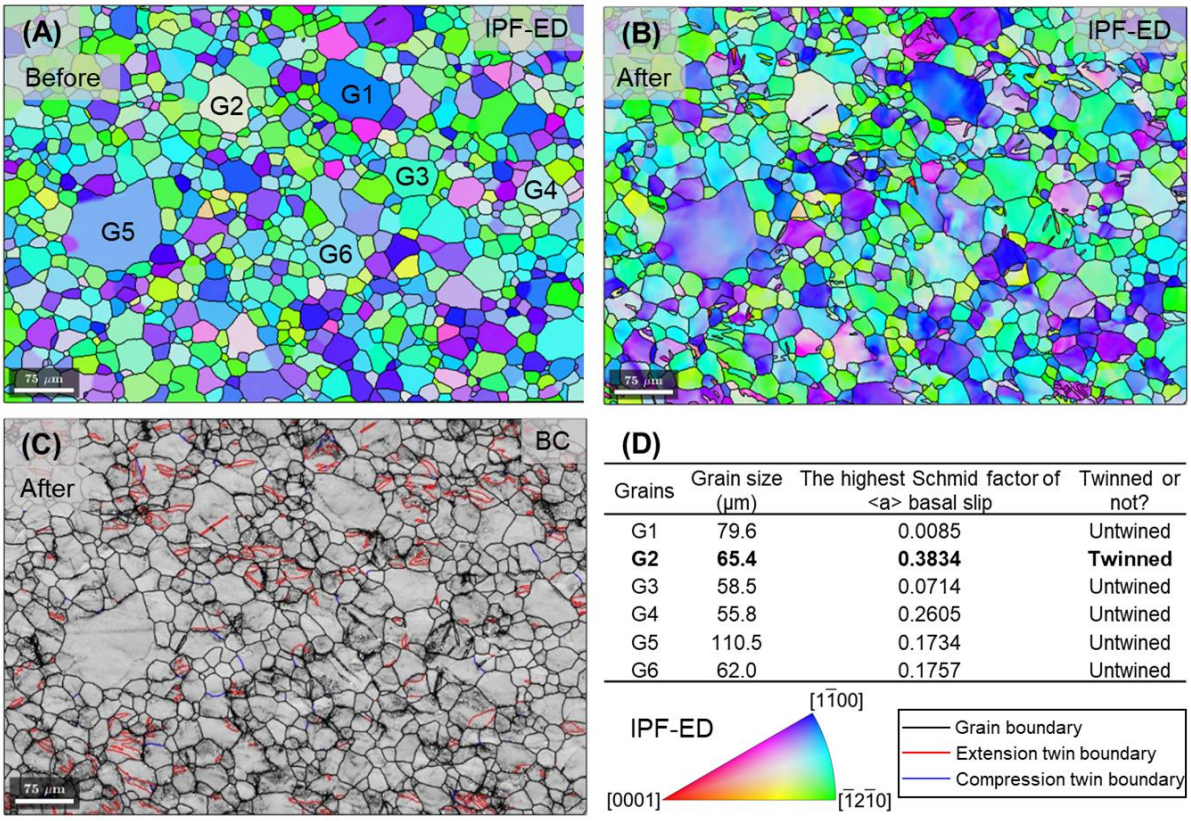

Grains	Grain size (μm)	The highest Schmid factor of <a> basal slip	Twinned or not?
G1	79.6	0.0085	Untwined
G2	**65.4**	**0.3834**	**Twinned**
G3	58.5	0.0714	Untwined
G4	55.8	0.2605	Untwined
G5	110.5	0.1734	Untwined
G6	62.0	0.1757	Untwined

Figure B.1: Examination of twinning behaviour in large size grains of Mg-1Al alloy using quasi-in situ EBSD. Microstructures of Mg-1Al samples (A) before and after deformation up to the (B, C) 6% engineering strain. D) Table summarizing the features of abnormal size grains. The reference direction of EBSD IPF maps is the ED. All GBs were overlaid in black. ET and secondary twin boundaries were highlighted in red and blue, respectively, in the BC maps. Note that their identification was performed by measuring the RA - misorientation angle of every boundary. The RA & angle pairs for ET and secondary twin are <2$\bar{1}\bar{1}$0> & 86.30°, and <1$\bar{1}$00> & 60.00°, respectively. The twinned grain was bold in Figure B.1(D).

Figure B.2. Evolution of the grains in Figure 5.9 at various strains

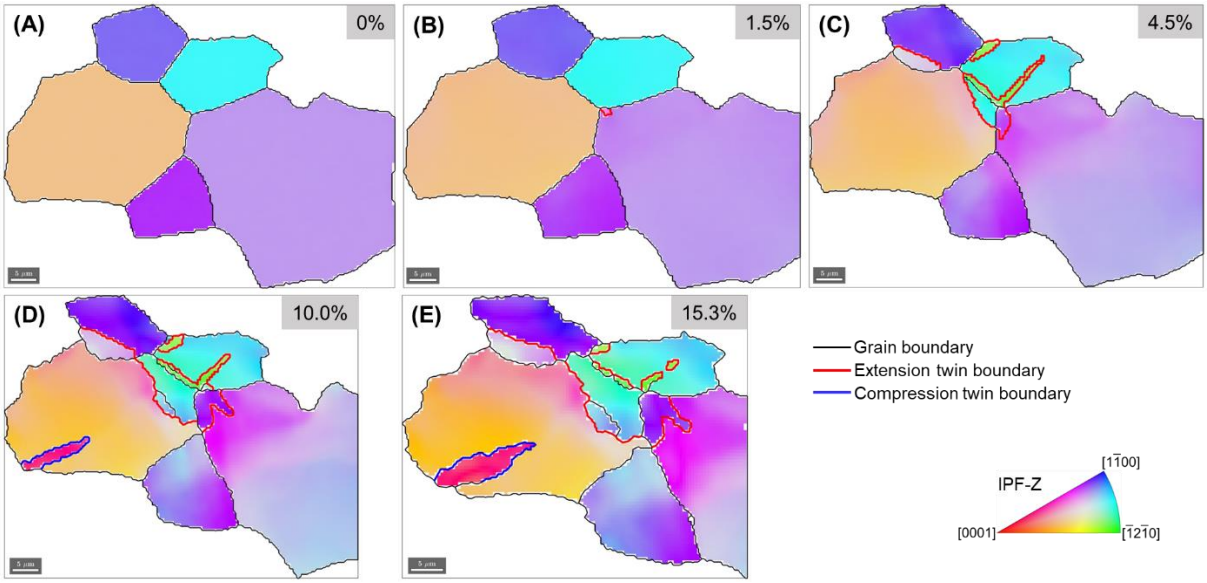

Figure B.2: EBSD IPF maps of the microstructural evolution of the grains in Fig. 9 during tensile deformation. (A) 0%, (B) 1.5%, (C) 4.5%, (D) 10.0%, (E) 15.3%. The number of twins at 15.3% strain is lower than that at 10% strain probably due to the difficulties of indexing thin twins after large deformation.

Table B.1. Evolution of the length of twinned grains along tensile direction as a function of the applied strain

Table B.1: Length of the grains in Fig. 9 along the loading direction as a function of the applied strain. The grain size is defined as the equivalent circle diameter. Note that grain G146 was located near the edge of EBSD before the evolution of its length during deformation, thus its length could not be measured.

Grains	Grain size (μm)	Grain length in μm and (longitudinal strain)				
		0%	1.5%	4.5%	10.0%	15.3%
G87	15.7	18.5	18.5	19.0 (2.7%)	19.5 (5.4%)	20.0 (8.1%)
G92	17.2	24.0	24.0	23.0 (-4.2%)	20.5 (-14.6%)	19.5 (-18.8%)
G121	29.9	35.5	36.0 (1.4%)	36.5 (2.8%)	37.0 (4.2%)	38.0 (7.0%)
G132	14.9	18.0	17.5 (-2.8%)	17.0 (-5.6%)	18.0 (0%)	18.5 (2.8%)
G146				Unknown		

Annex C. Machine learning

Figure C.1. Microstructure of AZ31 Mg alloy

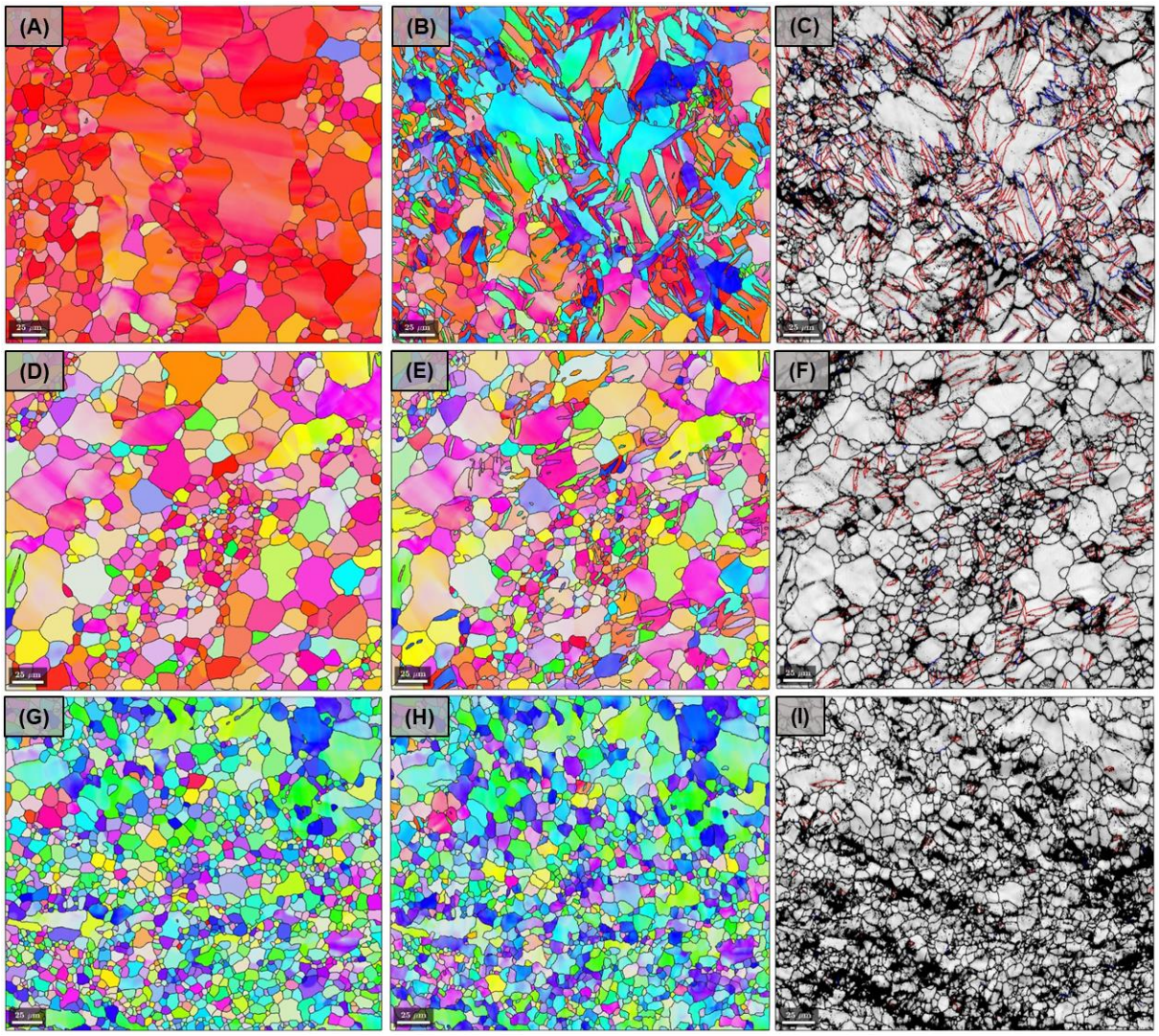

Figure C.1: Microstructures of samples (A-C) S0, (D-F) S45, and (G-I) S90 before and after deformation. EBSD IPF maps in the horizontal direction of samples (A, D, G) before and (B, E, H) after deformation. EBSD BC maps of samples (C, F, I) after deformation. All GBs were overlaid in black. ETs and secondary twin boundaries were highlighted in red and blue, respectively, in the BC maps. Note that their identification was performed by measuring the RA - misorientation angle of every boundary. The RA & angle pairs for ET and secondary twin are $<2\bar{1}\bar{1}0>$ & 86.30°, and $<1\bar{1}00>$ & 60.00°, respectively.

Figure C.2. Microstructure of Mg-1Al alloy

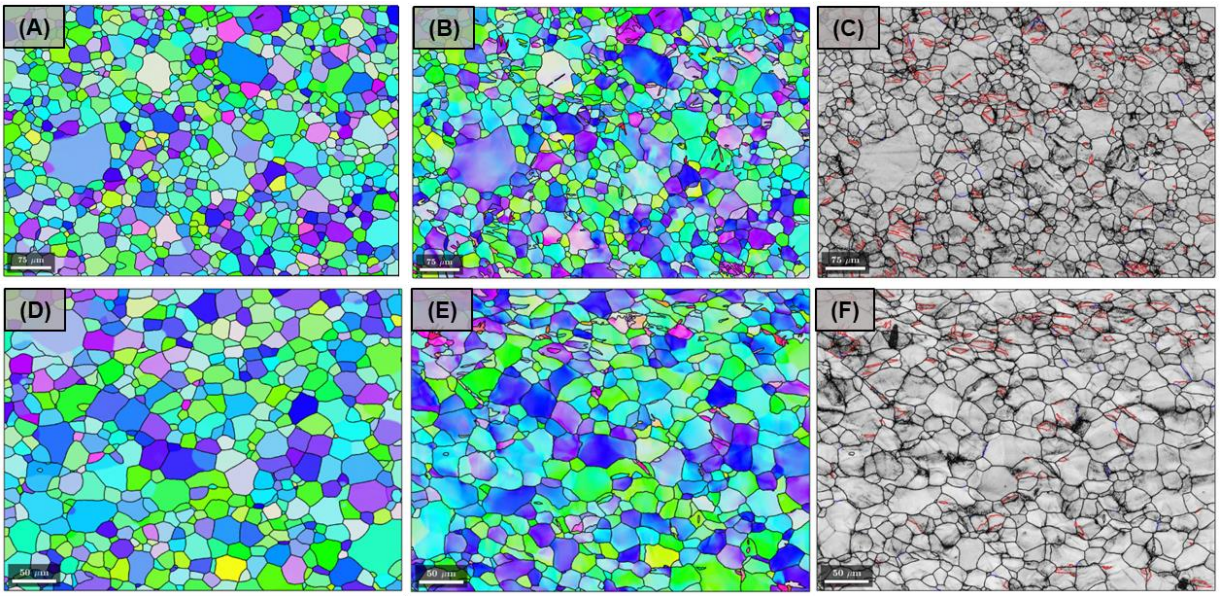

Figure C.2: Microstructures of Mg-1Al samples (A, D) before and after deformation up to (B, C) 6%, and (E, F) 10% engineering strains. The reference direction of EBSD IPF maps is the ED. All GBs were overlaid in black. ET and secondary twin boundaries were highlighted in red and blue, respectively, in the BC maps. Note that their identification was performed by measuring the RA - misorientation angle of every boundary. The RA & angle pairs for ET and secondary twin are $<2\bar{1}10>$ & 86.30°, and $<1\bar{1}00>$ & 60.00°, respectively.

Figure C.3. Difference of textures for AZ31 and Mg-1Al alloy

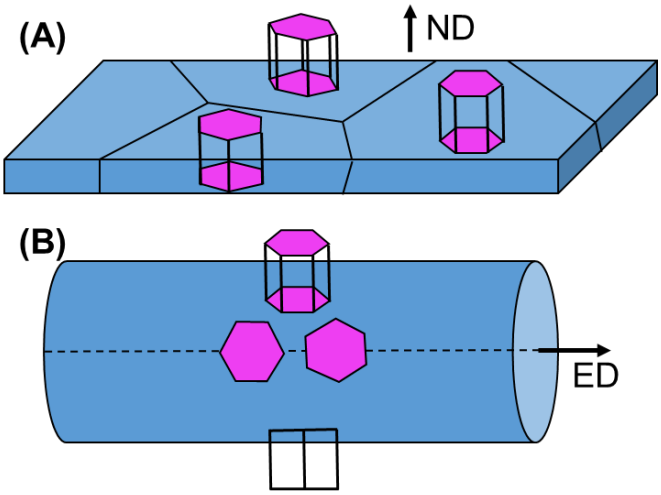

Figure C.3: Schematic illustration of (A) strong basal texture of AZ31 Mg alloy and (B) strong prismatic texture of Mg-1Al alloy.

Figure C.4. Active slip analysis using grain reference orientation deviation

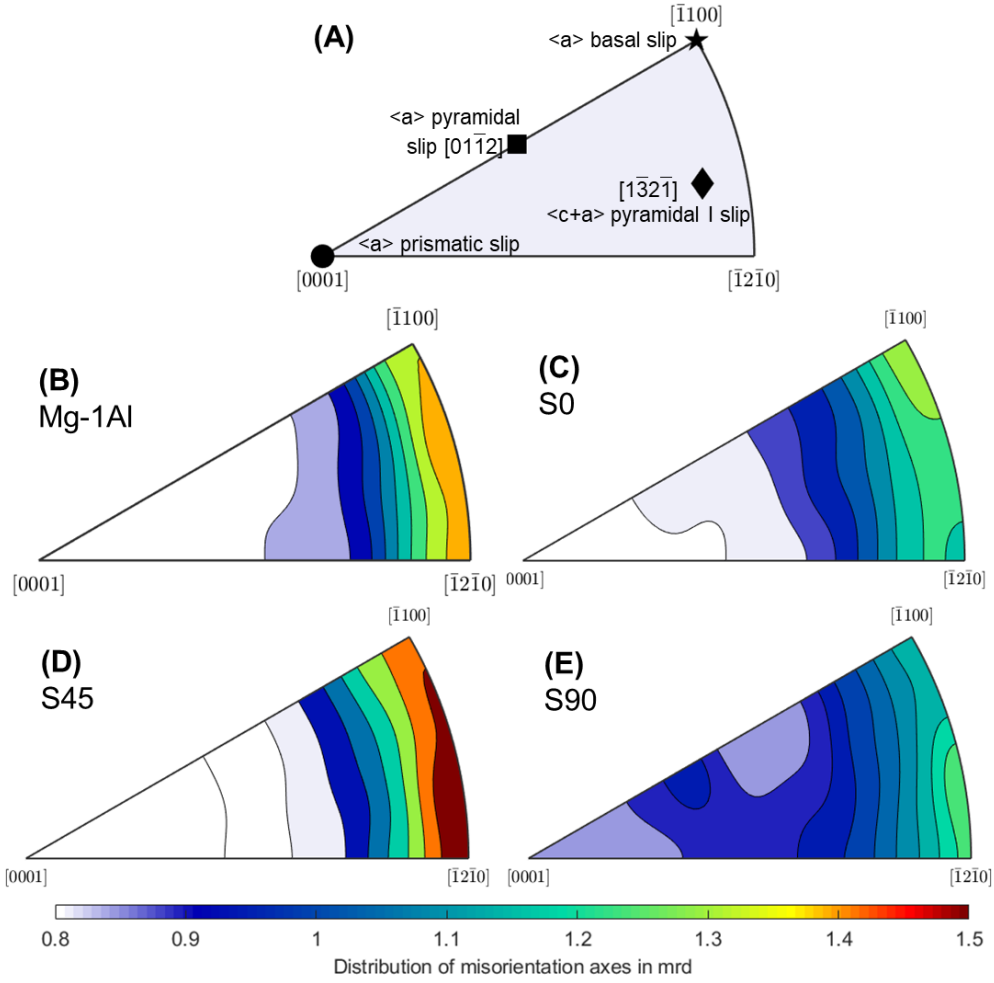

Figure C.4: Slip behavior analysis of deformed Mg-1Al (9.5% true strain) and AZ31 alloy (6% true strain). (A) RAs associated with dislocation slip along different systems in HCP Mg. Evolution of the distribution of intragranular misorientation axes in the crystal coordinate system (expressed in mrd) of Mg alloy during tensile deformation along different directions. (B) Mg-1Al, (C) S0, (D) S45, and (E) S90.

Methods C.1. Optimal hyperparameters of the Bayesian network models

1) AZ31

learningMethod = 'GHC'

discretizationNbBins = 3

discretizationStrategy = 'quantile'

UsePR = False

2) AZ31 MB (for both *Max_deltaBSF* and *S_SF1*)

learningMethod= 'MIIC'

discretizationNbBins = 3

discretizationStrategy = 'quantile'

UsePR = False

3) AZ31 [T_SF1 < 0.16]

learningMethod = 'MIIC'

discretizationNbBins = 3

discretizationStrategy = 'quantile'

UsePR = True

4) Mg-1Al

learningMethod = 'Tabu'

discretizationNbBins = 3

discretizationStrategy = 'quantile'

UsePR = False

5) AZ31 [*T_SF1* < 0.16] MB

learningMethod = 'NaiveBayes'

discretizationNbBins = 3

discretizationStrategy == 'quantile'

UsePR = False

6) Mg-1Al MB

learningMethod = 'TAN'

discretizationNbBins = 3

discretizationStrategy = 'quantile'

UsePR = False

7) AZ31 [*T_SF1* < 0.16] MB (*Min_deltaGs)*

learningMethod = 'MIIC'

discretizationNbBins = 3

discretizationStrategy = 'quantile'

UsePR = False

8) Mg-1Al MB (*Grain_size*)

learningMethod = 'Chow-Liu'

discretizationNbBins = 3

discretizationStrategy = 'quantile'

UsePR = True